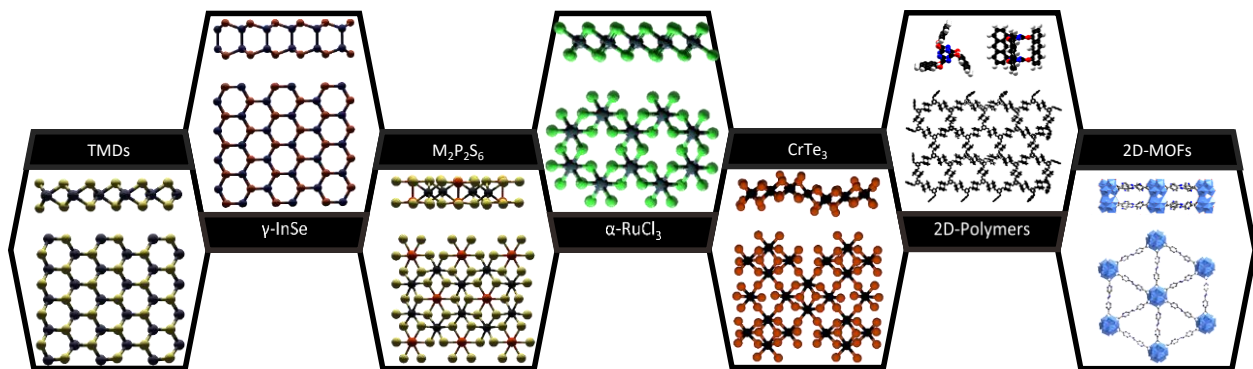

LIQUID PHASE EXFOLIATION AND SIZE-DEPENDENT PROPERTIES OF VAN DER WAALS CRYSTALS

Kevin Synnatschke

Thesis for the degree of
Doctor Rerum Naturalium



Department of Chemistry
Heidelberg University

LIQUID PHASE EXFOLIATION
AND
SIZE-DEPENDENT PROPERTIES
OF VAN DER WAALS CRYSTALS

Combined Faculty of Natural Sciences and Mathematics
Heidelberg University, Germany

Dissertation for the degree of
Doctor Rerum Naturalium (Dr. rer. nat.)

Presented by
Kevin Synnatschke

Submitted at 13.01.2021

Date of oral exam:

1. Examiner: Dr. Claudia Backes

26.02.2021

2. Examiner: Prof. Dr. Jonathan Coleman

“The science of today is the technology of tomorrow.”

- Edward Teller

Acknowledgements

Advances in science can hardly be achieved by a single person. First, I would like to express my gratitude to Dr. Claudia Backes who supervised and guided me. Thanks for the countless hours of patient discussions, suggestions and advices, often in combination with a cold beverage to boost and refresh the cognitive performance. The past years of working rather with than for you as a PhD student were truly inspiring and encouraging and I am looking forward to future discussions. Many thanks is also credited to all my colleagues from the Backes and the Zaumseil group. Especially to Maik Matthiesen, Marcel Alings, Martin Held, Maximilian Brohmann, Sebastian Grieger and Stefan Grimm for all the joint discussions including non-scientific regards and the occasional reminder to stay hydrated after a long day in the lab. Many thanks to Jana Zaumseil who was not only sharing her facilities with our group but also heaps of knowledge, ideas and advices on various topics.

Second, as many aspects discussed in this thesis have been highly collaborative, I would like to thank all collaborators who contributed to this work. Without all the provided materials, most of the work presented in this thesis would not have been possible. I would like to thank Bettina Lotsch and Sourav Laha (MPI Stuttgart), Dieter Schlüter and Ralf Lange (ETA Zürich), Wolfgang Bensch, Jonas van Dinter and Anna-Lena Hansen (Kiel University), Norbert Stock and Jonas Gosch and Zdenek Sofer (Prague University) for their fruitful supply of new 2D-materials to play with. Furthermore, I would like to thank Rüdiger Klingeler, Lena Spiellecke and Martin Jonak (Heidelberg University) for magnetic measurements which could not be included in the framework of this thesis. Many thanks to Sarah Haigh, Shouqi Shao and Daniel Kelly (Manchester University) as well as Ute Kaiser and Haoyuan Qi (Ulm University) for your efforts with transmission electron microscopy. Also thanks to Yana Vaynzof, Yvonne Hofstetter (Dresden University), Georg Duesberg and Beata Szydłowska (Munich University) for the XPS measurements. Also, I have to thank Janina Maultzsch, Narine Moses Badlyan, Stefan Wolff and Hans Tornatzky (Erlangen University) for the experimental and theoretic support with Raman measurements. You all literally shed light into my samples and experiments.

Third, I am grateful for the work contributed by students under my supervision. A special thanks goes out for Guillermo Lozano Onrubia and Alina Müller who worked under a cracking whip on time dependent measurements. Without taking turns with you, some experiments would not have been possible. Thanks also to Julian Petry who helped me with various experiments as a student assistant. Many thanks should also be dedicated to Angelina Jovic, who untiringly worked on improving the experimental details on the layer selective floating. Also, to Pascal Merten who explored experimental challenges with the method and helped to tackle them. Additional thanks to Andreas Albers, Elena Papalozzi, Johannes Dreizler, Karsten Hengefeld, Nico Zeitter, Robert Kindler and Simon Settele. Hard work is not always rewarded. While not every project had a positive and conclusive outcome, many challenges and experimental procedures you studied were used as basis for further

analysis and experimental refinements which can be considered as a corner stone for further investigations. Hence, none of the information you provided is wasted and some projects are still ongoing and could not be included here. I would like to thank Leonhard Karger, Guillermo Lozano Onrubia and Sabrina Steffens for their thrust in my guidance for their master theses. Especially Leonhard who was continuously questioning and reconsidering his own results and literature was rewarded by fascinating findings. These results are beyond the framework of this thesis but will certainly get the attention they deserve in upcoming reports.

At last, on a personal note, I would like to thank my friends and family. Many thanks to Aaron, Andreas, Patrick, Christian, Fabian, Jan, Johannes, Matthias and at least three Maxes. I would not be who I am today without you. Also, thanks to the Schenk family, who kept reminding me that no matter how much work piles up, there always is time for a joint beer (or two). Furthermore, I am deeply grateful to my Family (especially my parents and grandparents) for their support in any situation of my life and would like to thank my girlfriend for her motivation and tremendous patience as well as her parents for being incredibly understanding hosts during the writing process.

Abstract

Van der Waals crystals exhibit comparatively strong, typically covalent bonds in two dimensions and comparatively weak, typically non-covalent bonds between the two-dimensional lattice. This enables to separate individual two-dimensional layers of a van der Waals crystal which can be thinned down to atomic thickness in a process called exfoliation. The resulting nanosheets typically exhibit completely different properties compared to their corresponding bulk counterparts which can be exploited for various applications in advanced devices. Different methods have been presented for preparation of two-dimensional nanomaterials each with their respective up- and downsides. While some techniques can provide materials of highest quality, suitable for fundamental studies of inherent material properties, they typically lack scalability. Other methods focus on a high production rate of the nanomaterial, but introduce imperfections to the material due to the harsh conditions required. In recent years, exfoliation in the liquid phase has emerged to a widely used production technique due to the scalability and its wide applicability.

While the industrial relevance of two-dimensional nanomaterials is somewhat linked to the quality of the material that can be prepared by high throughput methods, a deeper understanding of underlying fundamentals for the nanosheet preparation is required to improve state-of-the-art techniques. In the case of liquid-exfoliated nanosheets, this can be achieved by statistical studies of the nanomaterial dimensions that can be prepared and isolated by size selection techniques. In this work, sonication-assisted liquid phase exfoliation using different conditions and solvents and subsequent size selection was applied to a total of 17 different van der Waals crystals. The material dimensions of all fractions were quantified through statistical atomic force microscopy. The findings presented in this work demonstrate a fundamental correlation between the nanomaterial lateral size and thickness which is ascribed to equipartition of energy between processes of nanosheet delamination and tearing. This provides an experimental proxy to determine the ratio between the in-plane binding strength and the out-of-plane interlayer attraction.

Isolation of different size-fractions of the same material and the knowledge over the nanomaterial dimensions in these fractions enables to study size-dependent changes of material properties in a quantitative manner. Measurements of optical properties on different sizes of dispersed nanosheets reveal systematic changes of the spectra with nanosheet size and enable to derive spectroscopic metrics for the size, thickness and concentration for different van der Waals nanomaterials, typically using extinction and absorbance spectroscopy. Structurally and compositionally different materials show similar changes in their optical response with changing material size which can be ascribed to a combination of confinement and dielectric screening effects, as well as changing contributions from scattering and electronically different material edges. Unifying principles across various materials were identified for the changes of the optical spectra with material dimensions.

The knowledge of material dimensions and the understanding of the optical spectra enables to study the stability of different nanomaterial systems as function of time using optical spectroscopy

such as extinction, absorbance or photoluminescence. A dependence of the speed and degree of the material decomposition on the storage temperature and the water content of the solvent is conveniently accessible for different material dimensions.

The results presented within this work provide an advanced understanding of the exfoliation of layered crystals, unifying principles of optical properties as function of nanomaterial dimensions and proof-of-concept experiments for quantification of the material decomposition.

Zusammenfassung

Van der Waals Materialien zeichnen sich durch typischerweise vergleichsweise starke, kovalente Bindungen entlang zweier Richtungen und vergleichsweise schwache, meist nichtkovalente Bindungen zwischen dem zwei-dimensionalen Gitter aus. Dies ermöglicht die Isolation einzelner zwei-dimensionaler Schichten eines van der Waals Kristalls, welche bis zu atomarer Dicke reduziert werden können mittels eines Prozesses, den man als Exfoliierung bezeichnet. Die resultierenden Nanoplaten weisen unterschiedliche Eigenschaften im Vergleich zu den jeweiligen makroskopischen Gegenständen auf, was nicht nur ein spannendes Gebiet der Grundlagenforschung darstellt, sondern interessant sein kann für eine große Bandbreite von Anwendungen. Verschiedene Methoden zur Darstellung von zwei-dimensionalen Nanomaterialien wurden in den vergangenen Jahren berichtet, welche jeweils eigene Vor- und Nachteile haben. Während einige dieser Techniken Materialien höchster Qualität für fundamentale Untersuchungen inhärenter Materialeigenschaften zugänglich machen, sind diese jedoch nicht in großem Maßstab umsetzbar. Andere Methoden setzen sich die Optimierung der Produktionsrate zum Ziel, was allerdings zu Fehlern in der Kristallstruktur führen kann, da zu diesem Zweck für gewöhnlich harsche Bedingungen benötigt werden. Die Exfoliierung in der flüssigen Phase gehört heute zu einer der am weitesten verbreitenden Methoden, was auf die Skalierbarkeit des Prozesses und die breite Anwendbarkeit zurück geht.

Da die industrielle Relevanz der zwei-dimensionalen Nanomaterialien zum Teil auch mit der Qualität des Materials einhergeht, welches durch Techniken mit hohem Durchsatz erzeugt werden kann, ist es notwendig zugrundeliegende Prinzipien der Nanomaterial Herstellung besser zu verstehen um derzeit verwendete Methodiken zu verbessern. Im Fall von flüssigphasen-exfoliierten Nanoschichten kann dies durch statistische Evaluation der Nanomaterial Dimensionen nach Größenselektion erreicht werden. In dieser Arbeit wurden insgesamt 17 verschiedene van der Waals Kristalle in der flüssigen Phase unter verschiedenen Bedingungen exfoliiert, durch Zentrifugationstechniken der Größe nach getrennt und die jeweiligen Größenverteilungen in den Fraktionen mittels statistischer Rasterkraftmikroskopie bestimmt. Die Ergebnisse zeigen einen fundamentalen Zusammenhang zwischen der lateralen Größe und Dicke der Nanomaterialien auf. Dies beruht auf einer Gleichverteilung des Energieeintrags, der sowohl in kovalente Bindungsbrüche, als auch zur Delaminierung der Schichten eingeht. Der Zusammenhang zwischen Schichtgröße und Dicke stellt somit eine experimentelle Näherung für das Verhältnis zwischen der Bindungsstärke entlang der Ebene einer Schicht und der Anziehung zwischen den Schichten dar.

Die Isolation von Fraktionen verschiedener Größen eines Material und die Kenntnis über die Dimensionen der Nanoschichten in diesen Fraktionen ermöglicht es größenabhängige Änderungen der Materialeigenschaften zu quantifizieren. Optische Messungen (vor allem Extinktion und Absorption) an den größenselektierten Dispersionen zeigen systematische Variationen der Spektren, was die

Herleitung von Metriken für die laterale Größe, Dicke und Konzentration des Nanomaterials ermöglicht. Materialien mit unterschiedlicher Struktur und Zusammensetzung zeigen vergleichbare Änderungen der optischen Signatur, was auf eine Kombination von Effekten basierend auf Lokalisierung und dielektrischer Abschirmung der Exzitonen, sowie Beiträgen durch Lichtstreuung und elektronisch unterschiedlichen Materialkanten zurück geht. Allgemein gültige Prinzipien wurden somit hinsichtlich der Änderungen optischer Spektren mit der Materialgröße identifiziert.

Die Kombination aus der Kenntnis über die Materialgrößen und dem Verständnis der optischen Spektren ermöglicht es, die Stabilität verschiedener Nanomaterialien in Abhängigkeit der Zeit zu untersuchen, beispielsweise, mittels Extinktions-, Absorptions- oder Photolumineszenz-Messungen. Eine Abhängigkeit zwischen der Geschwindigkeit, sowie Vollständigkeit der Materialzersetzung mit der Temperatur and dem Wassergehalt des Lösungsmittels ist somit für verschiedene Materialgrößen mittels relativ einfacher Methoden zugänglich.

Die Ergebnisse, die im Rahmen dieser Arbeit präsentiert werden, tragen signifikant zu einem tieferen Verständnis der Exfoliierung von van der Waals Kristallen bei. Zudem werden erste Indizien allgemeiner, materialübergreifender Eigenschaften identifiziert, in diesem Fall in Bezug auf die optische Signatur als Funktion der Nanoschichtgröße. Die breite Anwendbarkeit einfacher experimenteller Konzepte zur vergleichenden Materialzersetzung wird ebenfalls demonstriert.

Table of Contents

Index of Abbreviations.....	1
1 Introduction	3
2 Background	5
2.1 Van der Waals Crystals	5
2.2 Liquid Phase Exfoliation	6
2.2.1 Turbulence-Assisted Shear Force Exfoliation	7
2.2.2 Sonication-Assisted Exfoliation.....	9
2.2.3 Colloidal Stability of Nanomaterial Dispersions	13
2.3 Nanomaterial Size Selection.....	20
2.3.1 Fundamental Principles of Centrifugation	21
2.3.2 Liquid Cascade Centrifugation	24
2.3.3 Density Gradient Ultracentrifugation	26
2.4 Size-Dependent Material Properties	27
2.5 Nanomaterial Stability	29
3 Exfoliability of Different Van der Waals Crystals.....	33
Liquid Phase Exfoliation of	34
3.1 Transition Metal Dichalcogenides	34
3.2 Indium Selenide, γ -InSe	41
3.3 Transition Metal Hexathiohypo Diphosphates, $M_2P_2S_6$	47
3.4 Ruthenium Chloride, α - $RuCl_3$	53
3.5 Chromium Telluride, $CrTe_3$	57
3.6 Organic Sheet Stacks, Exfoliation of 2D-Polymers	61
3.7 Metal Organic Frameworks.....	74
3.8 Material Exfoliability in Comprehensive Comparison	78
4. Size-Dependent Nanomaterial Properties	85
Size Effects on	87
4.1 Transition Metal Dichalcogenides	87
4.2 Indium Selenide.....	98
4.3 Transition Metal Hexathiohypo Diphosphates.....	103

4.4 Ruthenium Chloride.....	107
4.5 Chromium Telluride	110
4.6 Organic 2D-Polymers	112
4.7 Unifying Principles for Size-Dependent Phenomena in 2D-Materials	120
5 Environmental Stability of LPE Nanosheets	125
Stability of.....	125
5.1 Transition Metal Dichalcogenide Nanosheets	125
5.2 Indium Selenide	132
5.3 Transition Metal Hexathiohypo Diphosphates	136
5.4 Ruthenium Chloride.....	145
5.5 Chromium Telluride	150
5.5 Quantitative Assessment of the Environmental Stability for Van der Waals Nanoparticles	154
6 Conclusion and Future Perspectives	157
7 Methods	161
7.1 Liquid Phase Exfoliation.....	161
7.2 Size Selection.....	162
7.3 Material Characterisation.....	163
7.4 Computational Methods.....	166
7.5 Index of Chemicals and Materials	167
8 Appendix.....	169
9 Bibliography	217

Index of Abbreviations

2D	two-dimensional
Abs	absorbance
AFM	atomic force microscopy
aq.	aqueous
BP	black phosphorus
CTAB	cetyltrimethylammonium bromide
CMC	critical micelle concentration
CVD	chemical vapor deposition
DCM	dichloromethane
DGU	density gradient ultracentrifugation
<i>e.g.</i>	<i>exempli gratia</i> (for example)
<i>g</i>	earth's g gravitational field
Em	emission
<i>etc.</i>	<i>et cetera</i> (and so forth)
<i>et al.</i>	<i>et alii / et aliae / et alia</i> (and others)
Ex	excitation
Ext	extinction
GBL	<i>gamma</i> -butyrolactone
<i>h</i> -BN	hexagonal boron nitride
<i>i.a.</i>	<i>inter alia</i> (among other things)
IBU	inorganic building units
<i>i.e.</i>	<i>id est</i> (which means / in other words)
IPA	isopropyl alcohol
ITO	indium tin oxide
L	length

LCC	liquid cascade centrifugation
LPE	liquid phase exfoliation
LSF	layer selective floating
ME	micromechanically-exfoliated
ML	monolayer
N	layer number
Nf	number fraction
nIR	near infrared
PBI	perylene bisimide
PL(E)	photoluminescence (emission / excitation)
PMA	poly(methacrylate)
PVA	poly(vinyl alcohol)
RCF	relative centrifugal force
RPM	revolutions per minute
SC	sodium cholate
SDS	sodium dodecyl sulfate
STM	scanning tunnelling microscopy
TEM	transmission electron microscopy
THF	tetrahydrofuran
TMD	transition metal dichalcogenide
UV	ultra violet
Vf	volume fraction
Vis	visual
vol%	volume percent
vs.	<i>versus</i>
W	width
⟨□⟩	arithmetic average of □

1 Introduction

Many advances in technology are associated with scientific progress and the understanding of matter. Phenomena rationalised on the basis of experiments are the foundation of technological achievements and further improvements of state-of-the-art technology which enables to exploit material properties – also in various aspects of our daily life. Different materials are used in such practical devices which are steadily decreasing in size and become lighter which ideally makes them easier to handle and requires less material for fabrication. While current challenges lie in precise processing of nanoscopic structures, additional limitations of inherent material properties currently used in such devices are found due to quantum effects. Such size-effects constrain the applicability of these systems in progressively smaller device structures. Therefore, exploring new materials is an important topic of today's research. While quantum effects limit the application potential of some bulk material systems, they open the door to study all kinds of nanomaterials which exhibit interesting properties due to their reduced dimensionality. To this end, nanoscience has received ever-growing attention over the past three decades, as materials with unique mechanical, electronical and optical characteristics have been identified which can be prepared and applied with continually improving precision.

Such nanomaterials are often classified by their geometry, where spherical particles with all dimensions in the nanometre range are considered as zero-dimensional (0D), tubular nanomaterials, where all except one dimension are nanometre-sized, are considered one-dimensional (1D) and planar materials with only one dimension being in the nanometre size are considered two-dimensional (2D) materials. Quantum confinement effects arise from a reduction of one, two or for all three dimensions of the same material, but typically result in different properties for materials of the same chemical composition but of a different dimensionality (*e.g.* nanospheres, -fibres and -surfaces of silicon or carbon allotropes).¹⁻³ While all three classes of nanomaterials show intriguing properties, the framework of this thesis is limited to discussions on two-dimensional materials. While 2D-materials down to a single layer can cover comparatively large areas, the fabrication of such films made of a single "macromolecule" is typically not scalable. Techniques for preparation of different 2D-materials in a large scale in a liquid environment have been demonstrated previously,⁴⁻⁶ but are overall crude and can introduce defects to the nanomaterial. Hence, a deeper understanding of aspects influencing the quality of the nanomaterial upon preparation and processing is required to exploit their full potential regardless of the application area.

In this thesis, new insights into fundamentals of nanomaterial preparation and their stability in the liquid phase are presented. The contents of the thesis are organised as described in the following.

In Chapter 2, theoretical and experimental work of the current state of research is summarised. In particular, different approaches of nanomaterial preparation and further processing in the liquid phase are discussed. The colloidal and environmental material stability are addressed for intensively

Chapter 1 - Introduction

studied materials such as graphite, transition metal dichalcogenides (TMDs) and black phosphorus (BP).

Chapter 3 presents experimental data on the exfoliation of 17 van der Waals crystals that were exfoliated and size-selected through centrifugation within this work. Note that many of these crystals have not been previously exfoliated in the liquid phase so that an in-depth characterisation is required. The focus is laid on quantifying the nanosheet dimensions (*i.e.* lateral size and thickness) based on extensive statistical microscopy experiments. A common, fundamental behaviour across all materials under study was identified which demonstrates that the material dimensions are associated with inherent binding strength anisotropy of the materials along the different crystallographic axis.

In Chapter 4, the quantified material dimensions for fractions of all 17 different nanomaterials are correlated to their optical response which enables to derive spectroscopic metrics for the nanosheet concentration, average layer number and lateral size. A comparison of the observed changes in extinction and absorbance spectra for different materials enabled to identify unifying principles for the optical transitions with changing material dimensions.

Chapter 5 reports and quantifies the environmental stability of the different 2D-nanomaterials. Importantly, even under realistic conditions typically applied for further material processing, most materials are prone to degradation. This degradation is quantified through time and temperature-dependent spectroscopy to extract degradation kinetics and, in some cases, activation energies.

The thesis concludes in Chapter 6 with a summary of the achieved findings and gives a perspective for future research.

Finally, the utilized experimental methods applied throughout this work are described in detail in Chapter 7.

The advances presented this work can be considered as proof-of-concept studies which can readily be applied to additional materials to further improve the fundamental understanding of nanomaterials' chemistry.

2 Background

In this Chapter a general background on properties and methods for production as well as processing of the two-dimensional (2D) materials being covered in this thesis is introduced. At first, van der Waals crystals and different concepts of material delamination for scalable production of 2D-nanomaterials are presented. Second, different size selection techniques for polydisperse mixtures of different nanomaterial sizes are discussed, including a brief overview of changing properties with material dimensions. At last, the nanomaterial stability is discussed for two well-known examples: graphite and black phosphorus.

2.1 Van der Waals Crystals

In recent years, the class of two-dimensional materials attracted increasing attention in material sciences, initiated by the demonstration of successful delamination of graphite down to a single layer of atomic thickness in 2004.⁷ Since then, thousands of layered materials, known for decades already, have been rediscovered. Those materials have one particular property in common: all comprise comparatively strong, mostly covalent bonds in two dimensions forming a planar crystal lattice. The individual layers are stacked and held on top of one another by non-covalent forces forming a layered material, a so-called van der Waals crystal. Separating individual layers of such a crystal leads to changes of fundamental material properties, such as mechanical flexibility and strength, but also affects the band structure and thus the electronic and optical response. In addition, the effective surface area of the nanomaterial is much larger which is of great advantage for electrodes in supercapacitors or batteries as well as in catalysis. With these novel properties arising upon material delamination, called exfoliation, a scientific gold-rush started, rediscovering already known materials, in search of new properties upon layer separation. Various approaches have been developed for material delamination, yielding nanomaterials in different quantities and of varying quality. To date, the highest quality of nanosheets can be prepared by micromechanical exfoliation, (ME) where the material is delaminated using adhesive tape to peel off layers from a van der Waals single crystal. The material layer number can be adjusted by repeatedly applying the same technique on the material sticking to the tape. While nanosheets prepared by this method enable to study the change of fundamental material properties with decreasing layer number, a major drawback of the process is its lack of scalability. The first scalable example of exfoliation of layered crystals down to a single layer in the liquid phase without chemical treatment or intercalation was demonstrated in 2008, providing a versatile and easily applicable method based on a simple principle: the delamination of the crystal in a liquid medium can be achieved using high energy processes to overcome the attractive interlayer forces. Consequently, colloidal stabilisation is necessary to prevent reaggregation of the nanomaterial, using appropriate solvents or surfactant solutions as the exfoliation medium. The process, coined liquid phase

Chapter 2 - Background

exfoliation (LPE), is widely used for preparation of 2D-nanomaterials and will be detailed in the following Chapter.

2.2 Liquid Phase Exfoliation

Following the example of Coleman *et al.*⁴ that monolayers of graphite (*i.e.* graphene) can be produced in liquid media, liquid phase exfoliation gained increasing attention for preparation of 2D-nanomaterials. According to the current understanding, the process is divided into two steps:

- 1) Delamination of the sheet stacks induced by exposing the crystals to high energies.
- 2) Colloidal stabilisation of the dispersed nanomaterial.

For both steps, various methods have been established. The delamination can be realised by different energy sources such as sonication induced cavitation or the application of shear forces. Colloidal stabilisation of the nanosheets is achieved using different solvents, solvent mixtures or surfactant and polymer solutions (Figure 2.2-1).

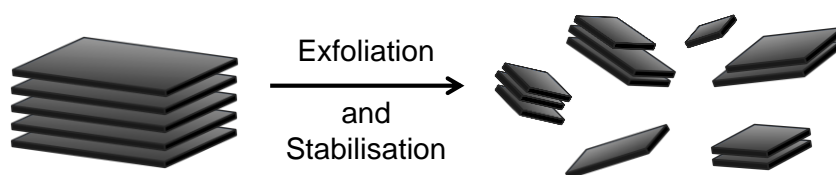


Figure 2.2-1: Schematic illustration of liquid phase exfoliation employed to produce nanosheets of different size and thickness.

Both steps involve multiple processes and will be described in more detail in the following Chapters, giving an overview over widely applied techniques for 2D-nanomaterial preparation, developed over the past decade. The versatility of the process has made LPE an important methodology for nanomaterial preparation. To date, more than 15 classes of layered materials are reported to be successfully exfoliated into 2D-nanostructures, including transition metal dichalcogenides (TMDs),⁸⁻¹⁰ transition metal hexathiohypo diphosphates (MPS₃),¹¹ III-VI and IV-VI semiconductors,¹²⁻¹⁴ pnictogens,¹⁵⁻¹⁷ silicates,¹⁸ oxides,^{19, 20} hydroxides,²¹ minerals,²² as well as synthetic structures, such as organic polymers (2D-Pol),²³ covalent organic frameworks (2D-COFs)²⁴ and others. Note that the majority of the more exotic structures were exfoliated only very recently, *i.e.* over the past three years. For each material, only little fine-tuning of the exfoliation parameters is needed to formulate inks containing nanosheets,²⁵ ready for further processing or deposition for various applications. Depending on the respective layer number of the obtained 2D-material, nanosheets with substantially different electronic structures are dispersed ranging from metallic over semiconducting and luminescent up to insulating properties. So far, a large variety of techniques for liquid phase exfoliation is available, all exhibiting different advantages over one another, as well as challenges that are still to be

overcome. However, all methods have in common that they rely on overcoming the interlayer attraction either by applying shear or normal forces to the material, as indicated in Figure 2.2-2.

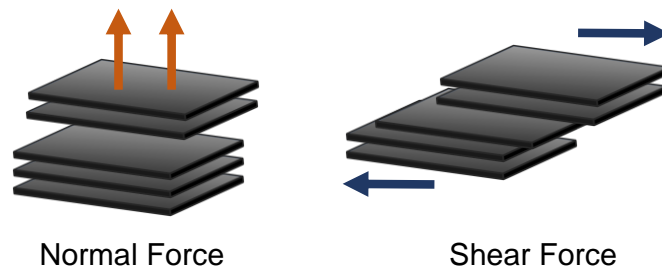


Figure 2.2-2: Schematic illustration of normal (left) and shear forces (right) exerting on a layered crystal during exfoliation.

2.2.1 Turbulence-Assisted Shear Force Exfoliation

Applying shear and normal forces to dispersed material can be achieved using devices as simple as a kitchen blender, generating hydrodynamic forces *via* rotating blades.^{26, 27} The working principle was first presented for the delamination of 2D-materials in 2014 by two different groups independently, using a rotor/stator shear force mixer.^{28, 29} It should be noted that the same approach has been applied to disperse other nanomaterials before, such as carbon nanotubes.^{30, 31} In this particular setup, a rotating blade, closely spaced to a fixed part, termed stator, turbulences the liquid (Figure 2.2-3). The dispersed material is dragged towards the rotating mixing head through small perforations in the stator. While portions of the liquid are driven back and forth into the residual solvent volume through the holes in the stator, strong shear forces act on the material in the dispersion. In addition to the shear forces, collision of particles with any surface in the reaction vessel and with other particles assists the exfoliation by weakening interlayer attraction and possibly partial intercalation of solvent or surfactant molecules in between the individual layers of the van der Waals crystal. Furthermore, secondary effects from collapsing cavitation bubbles can play a role in the exfoliation process. Due to pressure differences between the liquid in the inner and outer region of the rotor/stator combination, jet cavitation can occur, as indicated in Figure 2.2-3 D (a detailed description of the impact of cavitation is given in Chapter 2.2.2). However, this effect presumably has only a minor impact on the turbulence-assisted exfoliation process, as the pressure difference is too low for a continuous formation and collapse of cavitation bubbles.

Interestingly, turbulent energy dissipation, as defined for rotor/stator mixers,³² is not a requirement for the exfoliation *per se*. Coleman *et al.* have shown, that shear rates in the region of laminar flow are sufficient, at least for preparation of few-layered graphite. Furthermore, comprehensive experiments on the exfoliation parameters show, that the mixing speed has no impact on the production

Chapter 2 - Background

rate of the nanomaterial, after reaching a certain threshold, for material exfoliation.²⁹ Similar experiments on MoS₂ and WS₂ support the observations made for graphite, although higher shear rates, still being in the laminar flow regime, are necessary.³³

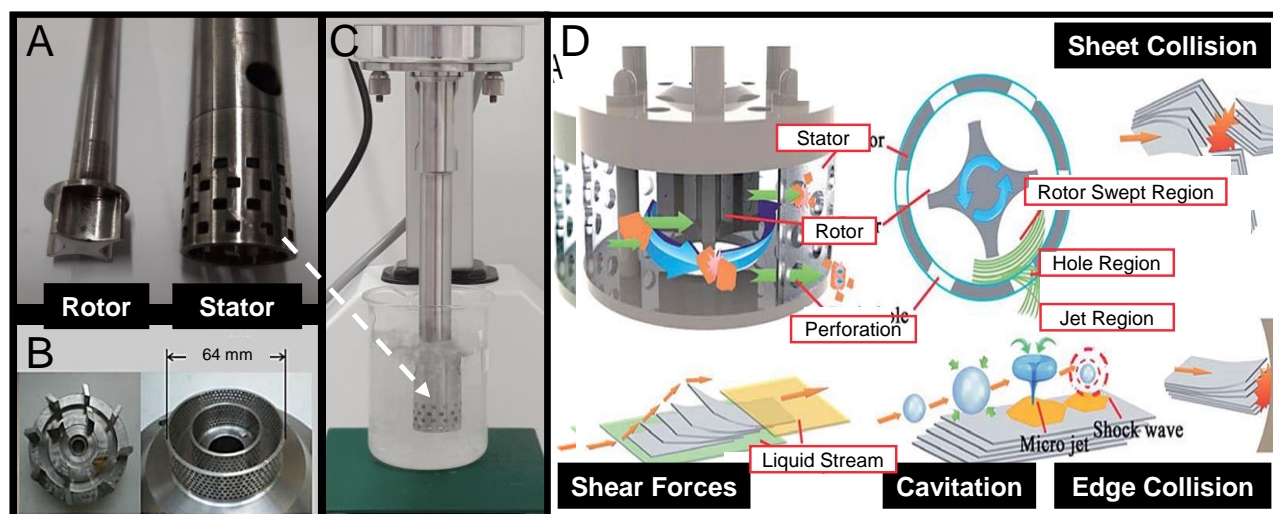


Figure 2.2-3: Working principle of a shear force mixer. (A) The mixer consists of two parts: a rotating part, termed rotor (left) and a fixed part, termed stator (right). (B) Different sizes and geometries of rotor/stator combinations can be realised to tailor exerting forces to the required application. (C) Typical setup of a shear force mixer in laboratory scale. (D) Schematic illustration of forces exerting on a layered crystal upon shear force mixing. Reproduced and adapted with permission from ^{28, 34, 35}.

However, for this conceivably simple setup, a huge parameter space has to be explored for process optimisation, including geometric aspects, such as the volume of the mixer, stator perforation size and periodicity, vessel and rotor geometry, as well as mixing speed, material concentration, choice of solvent, temperature and mixing times. The impact of this parameter space on the resulting nanomaterial would ideally be verified by tedious statistical approaches. In addition to that, new techniques with a different parameter space have been reported.

Related methods that introduce high energy into liquid systems, employing a combination of shear and normal forces have been developed in recent years. Promising approaches are based on high pressure liquid or gas streams, which act on the nanomaterial for example by pumping fluid through a microscopic channel at high pressure.^{36, 37} Another, particularly interesting technique for material delamination makes use of a compressed gas flow at high velocity, capable of intercalating in between individual layers of the material. The high velocity and expansion of the gas, streaming into the reaction chamber which contains the layered material causes high shear energies, delaminating individual layers of the material. A detailed description of the process is given by Kaner *et al.*³⁸ To date, this is the first example of material delamination in the gas-phase, which prevents undesired side reactions from solvents and surfactants, triggered by the energy added to the system for the material exfoliation.

2.2.2 Sonication-Assisted Exfoliation

A harsher, yet widely applied approach for layer separation of 2D-materials in the liquid phase is by sonication. While colloiddally stable dispersions of “water containing powders of MoS₂ and WSe₂”, prepared by sonication have already been reported in 1989,³⁹ the first intentional exfoliation of a 2D-material down to a single layer was described by Coleman *et al.* in 2008 for the delamination of graphite, in various solvents.⁴ The sonication assisted exfoliation method is widely employed in the laboratory scale, as it promises comparatively high monolayer contents with only little fine tuning of the processing parameters, using easily accessible techniques at low costs. To date, a large variety of different van der Waals crystals has been exfoliated, using sonication aided exfoliation methods.

The commonly assumed mechanism for the material delamination *via* sonication is the collapse of cavitation bubbles, formed by negative pressure waves which can be generated by ultrasound (*i.e.* sonication baths or horn sonicators) which propagate through the medium at kilohertz frequencies. These cavitation bubbles grow as the inside pressure falls below the vapor pressure of the fluid and fills with vaporised solvent until they eventually collapse violently. Consequently, high local temperatures and pressures are created and translated into tensile stress, acting on the dispersed material. The cavitation bubbles can have long or short lifetimes (*i.e.* stable and inertial cavitation) and lead to isotropic or anisotropic stress waves upon bubble collapse (*i.e.* shockwaves or microjets), which in turn leads to delamination of the material (Figure 2.2-4 A). The lifetime of the cavitation bubbles is inversely proportional to the energy of their collapse due to pressure modulation by continuous solvent evaporation. In addition, the concentration of the formed cavitation bubbles in a certain medium can play an important role as damping of the energy propagation by other bubbles can occur due to interference effects (Figure 2.2-4 B-C). This effect is usually observed at high acoustic power, where higher concentrations of cavitation bubbles in the fluid are generated (Figure 2.2-4 C).⁴⁰⁻⁴³

Chapter 2 - Background

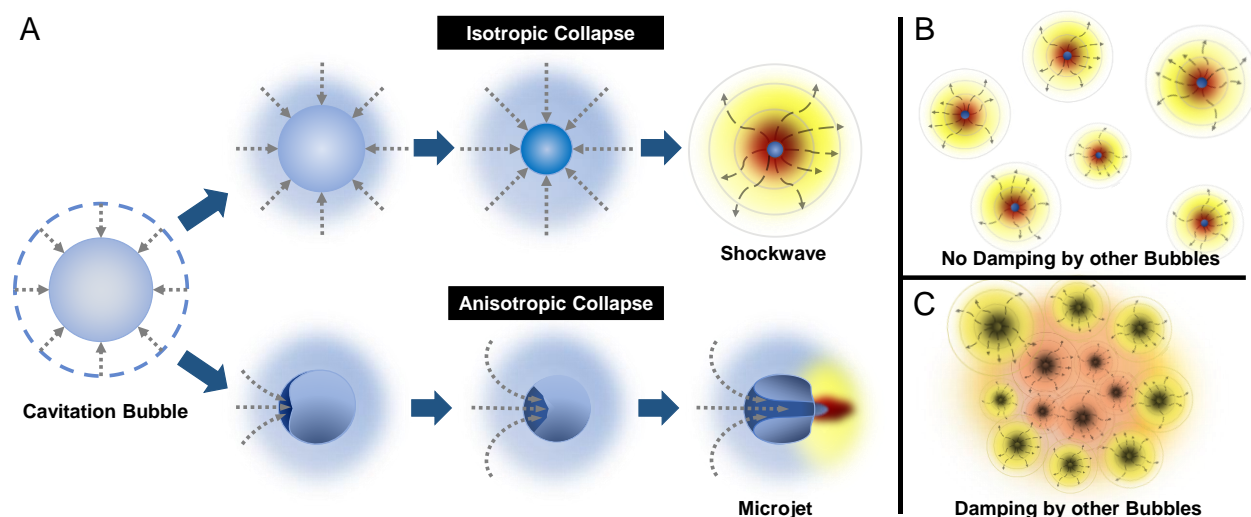


Figure 2.2-4: Simplified mechanisms of cavitation bubble collapse. (A) Isotropic (upper pathway) and anisotropic (lower pathway) cavitation bubble collapse leads to homogeneous (*i.e.* shockwaves) or directed (*i.e.* microjets) energy dissipation. (B) Effective (undamped) energy propagation at low cavitation bubble concentrations, (C) Damped energy propagation at high cavitation bubble concentrations due to interference.

However, the exact mechanisms are still not fully understood and significant discrepancies throughout literature are reported. One possible explanation for this is the low degree of control over the cavitation dose in commercially available sonicators. However, further process optimisation with regard to scalable and reproducible production of nanomaterials requires a meaningful analysis of all parameters influencing the energy dose, acting on the material and thus the quality of the nanosheets. It is well known that the frequency determines the energy of a propagating wave. This was recently confirmed experimentally for the exfoliation of graphite by Anthopoulos *et al.*⁴⁴ using a multi-frequency cavitating vessel. Nevertheless, systematic studies, taking other aspects such as the vessel geometry, material and filling height, temperature and solvent parameters (surface energy, viscosity, *etc.*) into account which have a significant impact on the resulting forces acting on the material, are not reported yet.

While the increasing demand on 2D-nanomaterials will require high throughput exfoliation techniques without introducing significant amounts of defects to the material, further studies on the influences of all process parameters are absolutely necessary. Important progress on the understanding of LPE has been made in 2019, as it was demonstrated experimentally that the exfoliation of graphite occurs in three progressive steps (Figure 2.2-5 A).⁴⁵

- 1) Kink band formation on the van der Waals crystal
- 2) Peeling off graphite strips
- 3) Delamination and tearing into nanosheets

The formation of wrinkles and kink bands can be observed on the surface of a graphite crystal after a few seconds already (Figure 2.2-5 B) and can be considered as a starting point of subsequent peeling steps. Large graphite crystals are ruptured into smaller pieces which can form additional kink bands (Figure 2.2-5 C), leading to continuously smaller graphite strips (Figure 2.2-5 D). Those steps

(1 and 2) can be observed for crystallites down to a limit of ~ 30 layers. From that point on, layer separation preferentially occurs that is accompanied by tearing of the nanostructures (Figure 2.2-5 E). To the current understanding, the sheet delamination and tearing of covalent bonds happens simultaneously, while the ratio of the occurrence of the two processes depends, in a simplified picture, on the ratio of the covalent in-plane to the non-covalent out-of-plane binding strengths.⁴⁶

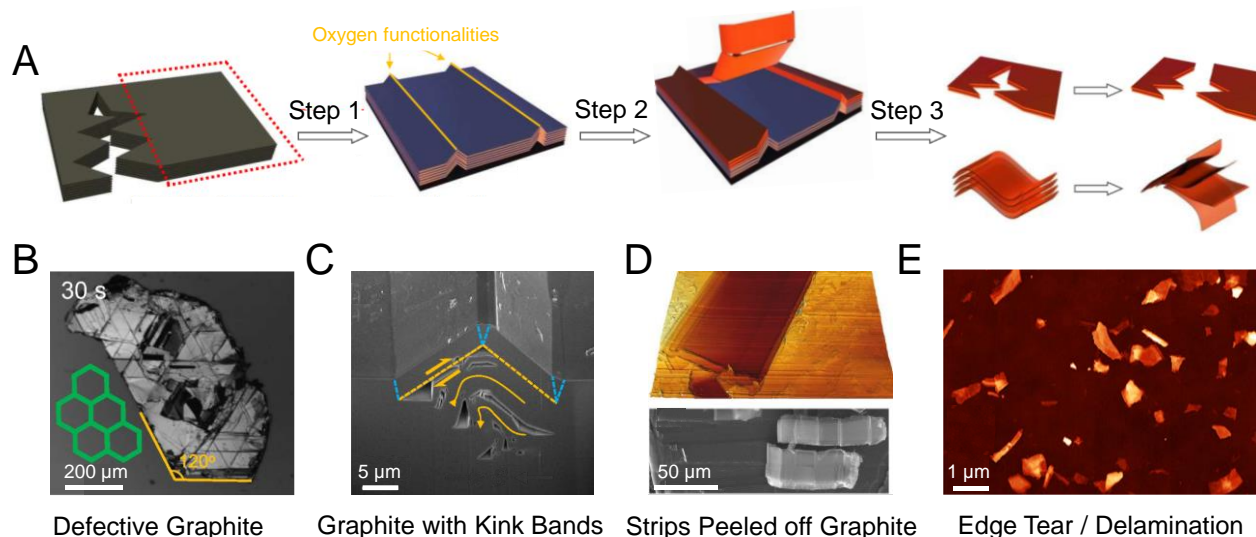


Figure 2.2-5: Exfoliation of graphite. (A) Schematic illustration of the three steps observed during sonication-assisted LPE of graphite. From left to right: rupture into smaller pieces of the starting material and kink band formation (step 1), strip-peeling (step 2) and delamination and simultaneous tearing into nanosheets (step 3). (B) Optical micrograph of a graphite crystal subjected to bath sonication for 30 seconds. (C) Scanning electron microscopy (SEM) image of a kink-band formed upon sonication. (D) Upper part: 3D-atomic force microscopy (AFM) image of a trench on the surface of a graphite crystal after peeling of graphite strips. Lower part: SEM micrograph of incompletely peeled graphite strips. (E) Typical AFM image of different sizes of nanosheets after LPE. Reproduced and adapted with permission from^{45,47}.

A relation between the processes of delamination and tearing (*i.e.* the ratio between material size and thickness) was reported in 2019 by O'Regan *et al.*⁴⁷ This comparative study on material exfoliation includes data on the exfoliation of 12 different layered materials. The experimental data show a power law scaling of the nanosheet area with the nanosheet thickness in the fractions of the size selection for all materials (Figure 2.2-6 A). The work suggests that energy equipartition holds between material exfoliation and scission, at least for sonication-based approaches, where high energies are introduced to the system. To understand these results quantitatively, a model is presented, which correlates the characteristic lateral size of a single layer (D_{ML}) divided by the crystallographic thickness (h_0) to the edge to surface energy ratio, which can be approximated by the in-plane and out-of-plane Young's modulus ratio ($Y_{In-plane}/Y_{Out-of-plane}$). The latter can conveniently be computed from DFT calculations.⁴⁷

However, to fully understand the model, it is important to mention, that D_{ML} is calculated from the square root of the average nanosheet area ($\langle LW \rangle$) divided by the average layer number ($\langle N \rangle$). While the experimental nanosheet area is approximated as the sheet length multiplied with the width, assuming a rectangular shape of the sheets, which is reported to be a good proxy for the given statistic

Chapter 2 - Background

distribution of different geometric nanosheet structures resulting after LPE,⁴⁸ the theoretical model assumes an ellipse as shape. In reality, the LPE nanosheets show polydisperse geometries which poses an intrinsic limitation to these considerations. Nonetheless, the correlation between experimental values of D_{ML} and the calculated Young's modulus ratio shows a linear scaling, as shown in Figure 2.2-6 B, which supports equipartition of energy between scission and delamination.

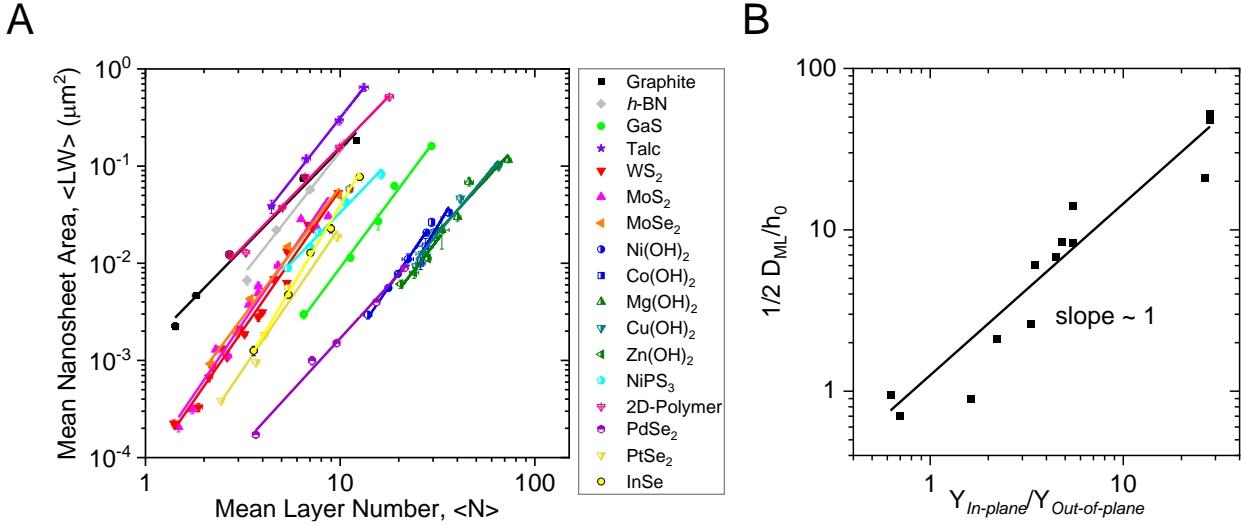


Figure 2.2-6: Experimental metrics for exfoliation efficiency. (A) Correlation between the arithmetic mean nanosheet area and layer number for different 2D-materials. The nanosheet area increases with layer number, following a power law, as indicated by the linear fit (solid lines) on the logarithmic scale. Extrapolation to the single layer serves as quantitative proxy for the exfoliation efficiency, D_{ML} . Materials of the same class exhibit a similar exfoliation behaviour (*e.g.* layered hydroxides and transition metal dichalcogenides). (B) Relation between D_{ML} of different materials and the calculated in-plane to out-of-plane modulus ratio. A linear correlation is observed between the two magnitudes. Reproduced and adapted with permission from ⁴⁷.

According to the model, the size/thickness ratio (k) for arbitrarily thick nanomaterial is reflected in equation 1.

$$k = \frac{\sqrt{\langle LW \rangle}}{\langle N \rangle h_0} = \frac{D_{ML}}{h_0} = 2a \frac{E_E}{E_S} \langle N \rangle^{b-1} \quad (\text{Eq. 1})$$

Where E_E and E_S are the in-plane and out-of-plane bonding energy, respectively. The factor a is introduced, assuming that the respective energies required for tearing and delamination do not explicitly depend on the sheet shape, which suggests a constant ratio for both events. The factor 2 is needed, as exfoliation of a crystal generates two new surfaces and b is required to simplify multi-parameter means, as shown in equation 2. A complete model derivation is given in reference ⁴⁷.

$$\langle N \sqrt{LW} \rangle = \sqrt{\langle LW \rangle} \langle N \rangle^b \quad (\text{Eq. 2})$$

Because experimental data as well as theoretical modelling results in a -values reasonably close to unity and b is empirically found to be ~ 1 as well, k seems to be directly proportional to

E_E/E_S , independent of the layer number, which implies an important fundamental limitation of the process, as it suggests k to be material-dependent parameter, independent of the morphology of the starting material. This is further corroborated by an experimental study on the exfoliation of different crystallite sizes and morphologies of MoS₂.⁴⁹ The proposed model describes an important correlation for the exfoliation of different materials but the implications are yet to be validated experimentally to find its limitations and to develop further insights into the process dynamics.

2.2.3 Colloidal Stability of Nanomaterial Dispersions

After successful material delamination in a liquid medium, an important aspect of LPE is the subsequent stabilisation of the nanomaterial to prevent aggregation and random restacking. Empirical exfoliation experiments show, that some solvents or additives efficiently stabilise certain materials, while other materials tend to aggregate in the exact same solvent systems. To understand the aspects of colloidal stabilisation or destabilisation of nanomaterials, a general logic can be applied: a colloiddally stable dispersion is obtained if the interactions between the solvent and the nanomaterial are stronger than the solvent/solvent interactions or the inter-nanosheet attraction. For solvent stabilisation of the nanomaterial in charge neutral systems, the Gibbs free energy of mixing (ΔG_{mix}) gives a fundamental relation for the energy difference between the respective isolated species and their mixture. For $\Delta G_{mix} < 0$, mixing of the components is energetically favoured. ΔG_{mix} can be described as the difference between the enthalpy of mixing (ΔH_{mix}) and product of the entropy of mixing (ΔS_{mix}) and the absolute temperature (T) as shown in equation 3, also known as Gibbs Helmholtz equation.

$$\Delta G_{mix} = \Delta H_{mix} - \Delta S_{mix}T \quad (\text{Eq. 3})$$

Thus, to favour mixing of the components, ΔH_{mix} should be minimised and ΔS_{mix} should be maximised. As macromolecules, such as proteins, polymers or, 2D-nanomaterials are comparatively rigid, the contribution of the entropy of mixing to the Gibbs free energy of mixing is expected to be negligible, which makes minimisation of ΔH_{mix} a key parameter for the mixing. Thus, a better understanding of the factors determining ΔH_{mix} should provide valuable insights for given solvent/solute combinations.

According to Hildebrand and Scatchard, ΔH_{mix} can be described as a function of the Hildebrand solubility parameters of the solvent (δ_S) and the solute (δ_N), the volume fraction of the solute (ϕ) and the volume of mixing (V_{mix}). While the relation, shown in equation 4 is strictly limited to smaller (*i.e.* not macromolecular) solutes, additional approximations have to be made for larger molecules. However, in this form it suggests, that the enthalpy of mixing is minimised when δ_S and δ_N match.

Chapter 2 - Background

$$\Delta H_{mix} = V_{mix}(\phi - \phi^2)(\delta_S - \delta_N)^2 \quad (\text{Eq. 4})$$

ΔH_{mix} denotes the energy difference between the energy required for separation of all molecules in the mixture until no interactions take place (*i.e.* separation to infinity) and the energy to form a solvent/solute mixture containing separated molecules but with sheet stacks of decreased thickness. In case of mixing a layered crystal with a solvent, considering, that the number and size of the sheet packages change upon exfoliation, ΔH_{mix} can be expressed by the sum of five energetic components: the respective energies required to separate the solvent molecules (E_S^{Sep}) to separate the individual layers of the crystal (E_N^{Sep}) the energy to form a solvent matrix containing voids to accommodate the sheet packages from infinitively separated solvent molecules (E_S^{Void}), the energy retrieved by reconstituting sheet stacks of reduced thicknesses (E_N^{Const}) and the interfacial energy for placing the sheet stacks into the voids of the solvent matrix ($E_{S,N}^{Inter}$), as shown in equation 5.

$$\Delta H_{mix} = E_S^{Sep} + E_N^{Sep} - (E_S^{Void} + E_N^{Const} + E_{S,N}^{Inter}) \quad (\text{Eq. 5})$$

Coleman *et al.* formulated and rearranged these respective energies for the first time in 2008 to describe the enthalpy of mixing for platelet-like objects, in their case for the exfoliation of graphite.⁴ Based on a number of approximations, the equation can be rearranged in order to relate ΔH_{mix} to the surface energies of the solvent (γ_S) and the solute (γ_N) and the thickness of the sheet stacks (t_N), in good agreement with the expression introduced by Hildebrand and Scatchard (Eq. 4), as shown in equation 6.

$$\Delta H_{mix} \approx \frac{2V_{mix}}{t_N} (\sqrt{\gamma_S} - \sqrt{\gamma_N})^2 \phi \quad (\text{Eq. 6})$$

However, this model is strictly limited to materials, in which only dispersive interactions (*i.e.* no polar or hydrogen interactions) occur, which is assumed to be the case for graphite nanosheets. It is expected, that solvents with surface energies matching the surface energy of graphite, which is per definition the required amount of energy per unit area to overcome the van der Waals interactions between the individual sheets, would result in a low enthalpy of mixing that is favourable for solvation of the nanosheets. In this regard, graphite was exfoliated *via* bath sonication in a number of different solvents to confirm the applicability of the model. The amount of dispersed material can be determined by optical absorbance measurements on the exfoliated nanosheets after mild centrifugation to remove macroscopic aggregates. For quantification, gravimetric filtering of the dispersion allows to calculate the concentration of the nanomaterial in different solvents, using the Beer-Lambert law. The experiments indeed show a peak of the graphite concentration for solvent surface energies of $\sim 65 \text{ mJ/m}^2$ (Figure 2.2-6 A), which is in accordance with the surface energy of graphite experimentally determined by inverse gas chromatography (Figure 2.2-6 B).⁵⁰⁻⁵²

It is evident from the experimental data that not all solvents with matching surface energies with respect to the nanomaterial efficiently stabilise the dispersion. This is reasonable, as the approximation does not account for dipolar interactions that cannot be neglected for most solvents.

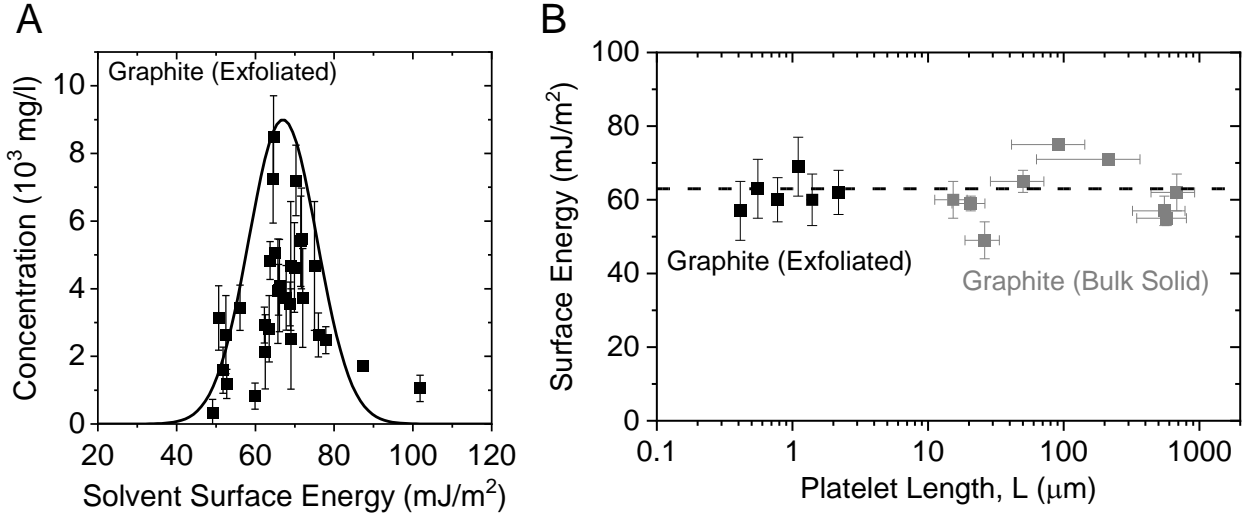


Figure 2.2-6: Correlation between solvent surface energy and nanosheet concentration after exfoliation. (A) Concentration of exfoliated graphite determined by absorption measurements after removal of unexfoliated particles. The concentration over the solvent surface energy follows a Gaussian envelope, as suggested by the model. (B) Surface energy of graphite nanosheets and bulk crystals as determined by inverse gas chromatography. Reproduced and adapted with permission from ^{4, 51, 52}.

Based on these findings, generalised solubility parameters for nanostructures of different dimensionalities (spherical, cylindrical or platelet-like) have been presented in follow-up reports.^{53, 54} For example for carbon nanotubes (cylindrical, 1D-nanomaterial), the maximum dispersed volume fraction (ϕ_{cyl}) was found to follow an exponential relation, as described in equation 7:

$$\phi_{cyl} \propto \exp \left[-\frac{\overline{v}_{cyl}}{RT} \frac{\partial \Delta H_{mix}/V_{mix}}{\partial \phi} \right] \quad (\text{Eq. 7})$$

with \overline{v}_{cyl} being the molar volume of cylindrical particles and R the gas constant. A quantitative prediction of the concentration of dispersed solute as function of the respective surface energies could be derived in subsequent work by combining equation 6 and 7. In this approach, 2D-nanomaterials are approximated as disks (*i.e.* cylinders with extremely low aspect ratio), as shown in equation 8:

$$c \propto \exp \left[-\frac{\pi D_N^2}{8\gamma_N k_B T} (\gamma_S - \gamma_N)^2 \right] \quad (\text{Eq. 8})$$

where c is the concentration of dispersed nanomaterial, k_B is the Boltzmann constant and D_N is the diameter of the nanodisks. This represents an important relation between the nanomaterial concentration and the solvent surface energy and predicts the dependence of the concentration on the solvent surface energy to follow a Gaussian function. As this is the case for graphite (Figure 2.2-6 A), the model was tested in subsequent work on four different group-VI transition metal dichalcogenides (TMDs), which support the model applicability.⁵⁰ Furthermore, a comparison of the Gaussian-peak

Chapter 2 - Background

positions on the concentration as function of the surface energy shows, that the surface energies of the four different TMDs are not only very close to one another, but also similar to the surface energy of exfoliated graphite.^{4, 50}

As many reports correlate the dispersed material in terms of solvent surface tensions (Γ_S), it should be mentioned at this point, that the surface energy is linked to the surface tension by the simple expression:

$$\Gamma_S = \gamma_S - TS_S \quad (\text{Eq. 9})$$

where TS_S is the product of the surface entropy and the absolute temperature, which is found to be $\sim 29 \text{ mJ/m}^2$ for most liquids at room temperature.^{55, 56} The graphs showing the dispersed concentration, represented by absorption of the different TMD dispersions over the solvent surface tension are presented below (Figure 2.2-7). Similar to exfoliated graphite (Figure 2.2-6), the data is quite scattered. However, considerable amounts of material are only dispersed for matching surface energies of the solvent (\approx surface tension $+29 \text{ mJ/m}^2$) and the solute. The discrepancy, that many datapoints are significantly below the Gaussian envelope function implies, that the model does not accurately describe all interactions between the nanomaterial and the solvent but it serves as indicator to identify appropriate solvents for colloidal nanomaterial stabilisation.

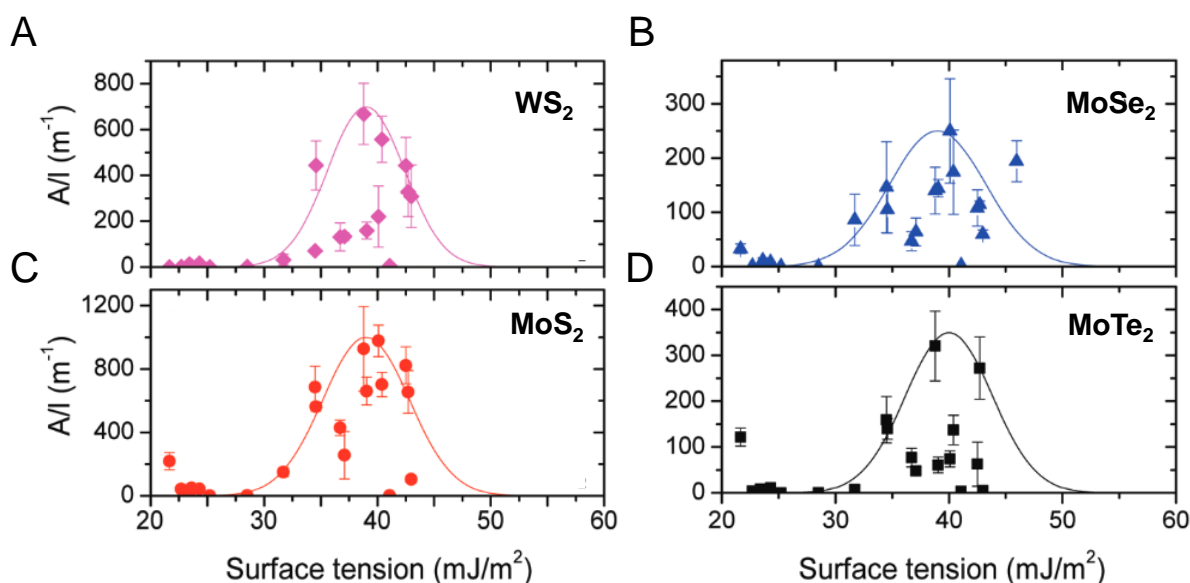


Figure 2.2-7: Nanosheet concentration expressed in absolute optical absorption of different nanosheet dispersions as function of the solvent surface tension. The experimental data follows a Gaussian envelope as suggested by the model (Eq. 8). The fitted concentration of WS₂ (A), MoSe₂ (B), MoS₂ (C) and MoTe₂ (D) peak at similar surface tensions. Reproduced and adapted with permission from⁵⁰.

As mentioned above, one reason for the observed deviations from the model is that only dispersive interactions are considered. Especially as dipolar and hydrogen bonding interactions are ubiquitous, those additional influences have to be considered to account for adequate solubility thermodynamics. In polymer physics, the enthalpy of mixing is commonly expressed by the Hildebrand

Chapter 2 - Background

solubility parameter (δ_T), which is defined as the amount of energy required to separate two objects to infinite distance, or otherwise denoted as square root of the total cohesive energy density. According to Hansen,⁵⁷ the total energy for attractive interactions in a liquid is given by the sum of three energetic contributions arising from dispersive forces (δ_D), polar forces (δ_P) and hydrogen bonding (δ_H) which are also known as Hansen parameters. The Hildebrand solubility parameter can be obtained from the root mean square (rms) of the three Hansen parameters:

$$\delta_T = (\delta_D^2 + \delta_P^2 + \delta_H^2)^{\frac{1}{2}} \quad (\text{Eq. 10})$$

which allows, in consideration of equation 8, to express the dispersed nanomaterial concentration as function of all three Hansen parameters:

$$c \propto \exp \left[- \left\{ (\delta_{D,S} - \delta_{D,N})^2 + (\delta_{P,S} - \delta_{P,N})^2 + (\delta_{H,S} - \delta_{H,N})^2 \right\} \right] \quad (\text{Eq. 11})$$

It is evident from the equation, that for the concentration to be maximised, all three Hansen parameters have to match the respective parameters of the nanomaterial, which explains the deviation from the Gaussian envelope if only one parameter (*i.e.* the surface energy) is analysed. It was demonstrated, that the matching of all three parameters is the case for the solvents achieving the highest concentrations of nanomaterial.⁵⁸ In case of graphite and MoS₂, similar solubility parameters are found. The data implies, that a good solvent for the exfoliation should exhibit a dispersive Hansen parameter ($\delta_{D,S}$) of $\sim 18 \text{ MPa}^{1/2}$, a polar Hansen parameter ($\delta_{P,S}$) of $\sim 9 \text{ MPa}^{1/2}$, and a hydrogen bonding parameter ($\delta_{H,S}$) of $\sim 7.5 \text{ MPa}^{1/2}$, which is a surprising result, as MoS₂ and graphite are expected to show different surface chemistries. While the exact reasons for this behaviour remain unclear, it is evident, that additional factors might interplay with solvent stabilisation thermodynamics.

Apart from these aspects, the model gives an important guideline to identify suitable solvents for material stabilisation. In addition, solvent parameters can be adjusted by the use of solvent mixtures, as shown by Tan *et al.*⁴² which also highlight the importance of solvent viscosity normalised centrifugation times for removal of aggregates and unexfoliated material in advance of determination of the dispersed nanomaterial concentration. This is a crucial point, which was not considered in the work of Coleman and co-workers and will be addressed in more detail in Chapter 2.3.1.

In addition to stabilisation of nanomaterials in pure solvents and solvent mixtures, a stabilisation of colloids can be achieved by adding stabilisers to the liquid medium. This avoids the use of toxic/hazardous solvents or solvent blends, which may complicate further processing substantially also due to high, or in case of blends usually non-azeotropic, boiling points. In this regard, typical stabilisers are surfactants, which usually exhibit amphiphilicity (*i.e.* they consist of a polar and a nonpolar part). Depending on the chemical structure, the stabilisers can be charged (cationic or anionic) but this is not a necessary criterion for efficient stabilisation of the dispersed material. Depending on the solvent, stable dispersions can be formed if an interaction between the stabiliser and the nanomaterial is strong enough to prevent aggregation, as reported for carbon nanotubes in organic

Chapter 2 - Background

solvents (*e.g.* toluene).³⁴ However, for many materials, stabilisation in aqueous solution is possible, offering a green alternative for nanomaterial processing.

Basically, all surfactants for stabilisation of nanomaterials in aqueous dispersions have one property in common: they consist of polar and nonpolar groups. While the surfactant molecules (at low concentrations) will move towards any nonpolar site available in the dispersion container (*e.g.* water/air interface or nanomaterial surface), a solvation of the nanomaterial can be achieved. In this regard, the nonpolar part of the stabiliser interacts preferably with the usually hydrophobic surface of the nanomaterial and the polar part is solvated by water molecules, forming a stable dispersion. Surfactant stabilised dispersions containing monolayer structures of a 2D-material have first been reported in 2009 for exfoliated graphite.⁵⁹⁻⁶¹

However, this stabilisation mechanism is only surface selective for nanomaterials in a certain concentration range, that is below the critical micelle concentration (CMC). Above this threshold, the surfactant molecules form stable aggregates, where the nonpolar groups converge and form micelles either free in solution or around the nano- and the raw material. With a stabiliser coating the surface of the nanomaterial, aggregation is prevented by the steric hindrance and the solvation shell. In case of ionic structures, an additional Coulombic repulsion has to be considered, which is expected to have a stronger impact on the stabilisation of the dispersion than purely steric aspects. Depending on the chemical structure of the stabiliser molecules, different types of interactions are considered to play a role (Figure 2.2-8).⁶²

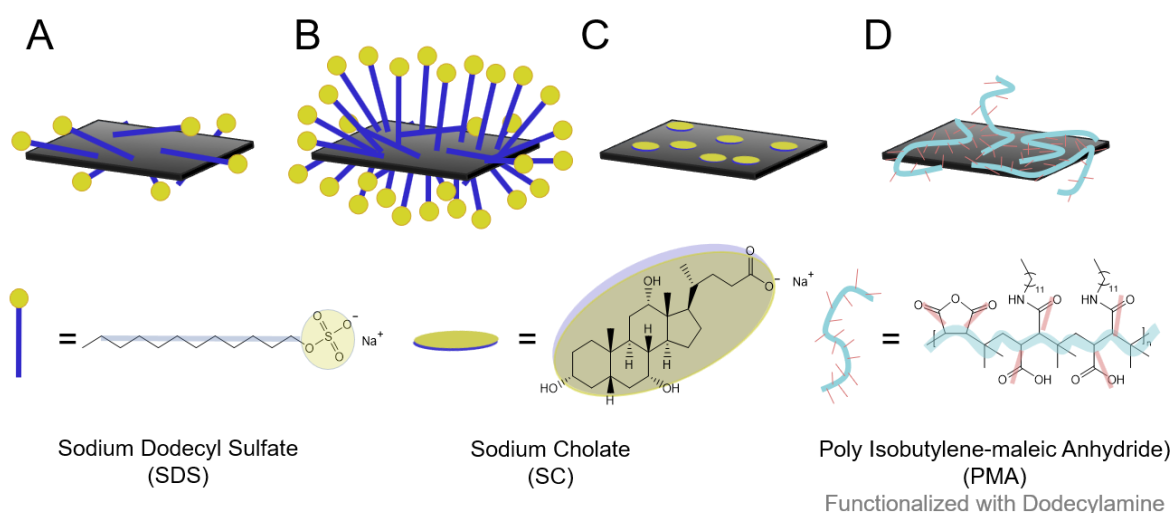


Figure 2.2-8: Schematic illustration of different interactions between a stabiliser molecule and a 2D-material, depending on the structure and concentration of the stabiliser. (A-B) Interactions of a linear amphiphile and a 2D-nanosheet at low (A) and at high concentrations (B). (C) Interaction between a nanosheet and a facial amphiphile. (D) Possible interaction between a stabilising polymer and a 2D-nanosheet. Exemplary chemical structures of the different types of amphiphiles are shown below.

For linear surfactants, with a polar head-group and a nonpolar, typically aliphatic tail (*e.g.* cetyltrimethylammonium bromide, CTAB or sodium dodecylsulfate, SDS), the aliphatic part of the molecule is expected to interact with the sheet surface, while the polar part points towards the

surrounding solvent. As mentioned above, depending on the concentration of the stabiliser, the interaction is expected to be either tails-on (below the CMC, Figure 2.2-8 A) or micellar (above the CMC, Figure 2.2-8 B). In case of facial amphiphiles (*e.g.* sodium cholate, SC), the surfactant is expected to lie flat on the nanomaterial surface, with the nonpolar part of the molecule facing the nanosheet surface (Figure 2.2-8 C). In addition, polymer chains can wrap around the sheets (Figure 2.2-8 D). However, for this kind of wrapping to be favoured, polymers used for stabilisation should exhibit nonpolar parts on the polymer chain with polar side groups for solvation in the medium (*e.g.* poly(vinyl alcohol), PVA or poly(methyl methacrylate), PMA).⁶³ To date, various stabilisers have been reported, rationally designed to exhibit specifically high affinities to different nanomaterials (*e.g.* *via* π - π interactions) and side groups tailored to ensure maximum solubility in the chosen medium (Figure 2.2-9).^{64, 65} In addition, extensive studies on the exfoliation of TMDs using different stabilisers in an aqueous medium have demonstrated that the chemical structure of the stabiliser has a minor impact on the dimensions of the resulting nanomaterial while the concentration seems to play an important role in this regard.⁶⁶

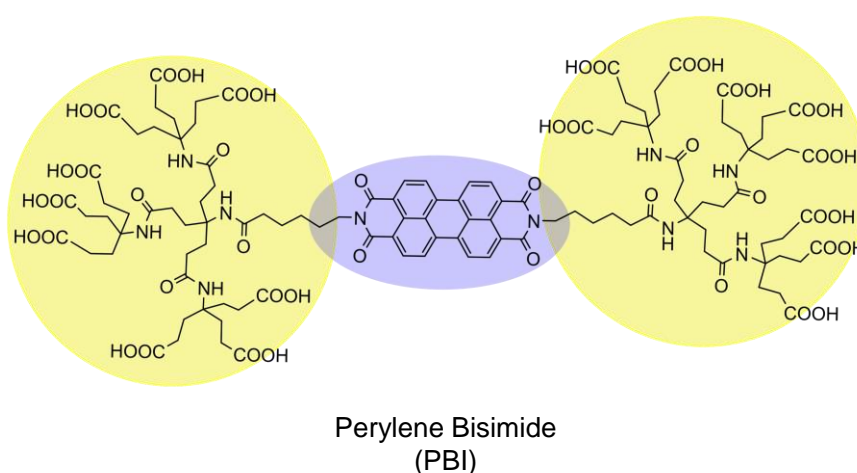


Figure 2.2-9: Example of a designed surfactant for colloidal nanomaterial stabilisation in aqueous solutions. Perylene bisimide (blue) with two water solubilising moieties (highlighted in yellow) as bolaamphiphilic stabiliser.

Surfactant stabilisation has widely been applied to dispersions of different nanostructures. However, similar challenges arise for surfactant-stabilised dispersions of nanomaterial as for the use of pure solvents. It is unclear, to what extent stabilisers or high boiling point solvents can be removed for subsequent deposition of the nanomaterial to thin-films.

2.3 Nanomaterial Size Selection

Dispersions of nanosheets produced by liquid phase exfoliation typically contain nanomaterial ensembles of different sizes and thicknesses. This provides the advantage that bulk information is available in a single measurement, which allows to average spectroscopic information over a statistical material size distribution. This is not the case for micromechanical exfoliation, as typically only single flakes are subjected to analysis. A major drawback of LPE nanosheets is that as exfoliated samples are too polydisperse for most applications as the nanomaterial dimensions predetermine its properties. In order to exploit the full potential of the nanomaterial, it is important to enrich certain material sizes by removal of the undesired material. An ideal methodology would allow for independent selection of material lateral size and material thickness. However, as mentioned in Chapter 2.2.2, the accessible size-range of materials produced by LPE is intrinsically limited by the ratio of in-plane to out-of-plane binding strengths.

Different methods have been established to achieve size selection of nanomaterials (Figure 2.2-10). Among various techniques such as nanopore-filtering³⁹ (Figure 2.2-10 A), colloidal destabilisation^{48, 66} (Figure 2.2-10 B) and chromatographic approaches⁶⁷ (Figure 2.2-10 C), centrifugation based techniques are widely applied in this regard.

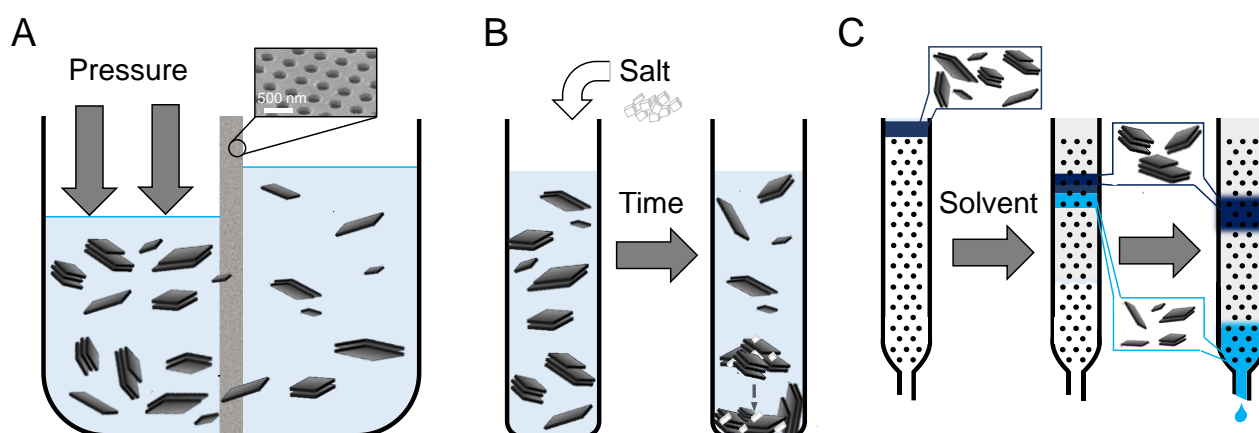


Figure 2.2-10: Different techniques for nanomaterial size selection. (A) Filtering of nanosheets through nanopores. (B) Size selective precipitation *via* colloidal destabilisation by increasing the ionic strength of the dispersion. (C) Size selection by different moving speeds of different nanosheet sizes in column chromatography. Reproduced and adapted with permission from ⁶⁸.

Centrifugation-based approaches have become an important topic of ongoing research on nanomaterial size selection and various concepts have been established in recent years.^{9, 48} A brief introduction on two different approaches which have proven to be particularly effective is given in the following Chapters. However, in order to rationalise these techniques, an understanding of the fundamental principle of centrifugation is necessary. A brief description will thus be given below.

2.3.1 Fundamental Principles of Centrifugation

For polydisperse nanosheet ensembles, centrifugation-based techniques have proven to be efficient for nanomaterial size selection⁴⁸ as different nanosheet sizes show a different sedimentation behaviour. The movement of a particle in a centrifugal field is given by the combination of four forces:

- 1) the centrifugal force, \vec{F}_c
- 2) the frictional force, \vec{F}_f
- 3) the buoyant force, \vec{F}_b
- 4) the gravitational force, \vec{F}_g

The centrifugal force can be described by the velocity of the angular motion ($\vec{\omega}$) with respect to the rotational axis (\vec{r}) and the mass of the particle (m) as shown in equation 12.

$$\vec{F}_c = -m\vec{\omega} \times (\vec{\omega} \times \vec{r}) \quad (\text{Eq. 12})$$

While the centrifugal force always works outwards from the rotational axis, the frictional force works in the opposite direction of the particle movement and the buoyant force works (approximately) towards the rotational axis (*i.e.* against the combination of the centrifugal force and the gravitational force, acting on the surrounding fluid). As the centrifugal force typically outweighs the gravitational force by orders of magnitude, the contribution of the earth gravitational force can be neglected, which typically acts in orthogonal direction to \vec{F}_c . This allows to describe the forces acting on the particles in the centrifuge in one dimension, towards or outwards the centre of the rotation and enables to describe the centrifugal force pulling down a particle in a centrifugal field with magnitude

$$F_c = mr\omega^2 \quad (\text{Eq. 13})$$

often expressed as relative centrifugal force (RCF) in multiples of the earth gravitational field (g). The common expression how fast a circular object spins is revolutions per minute (RPM), which only contains information about the angular velocity of the spinning object. In addition to the angular velocity, knowledge over the radius of the rotor is necessary to convert the revolutions per minute, which is often quoted as only parameter in literature, to an actual force acting on the particles. This is important to keep in mind if comparing results obtained for different centrifuges or even for using different rotors.

The frictional force originates in the movement of particles in a medium and is directly proportional to the product of the velocity of the moving particle (v) and a frictional coefficient (c_f), with the latter being dependent on the shape and size of the object in movement as well as the viscosity of the medium.

Chapter 2 - Background

$$F_f = v c_f \quad (\text{Eq. 14})$$

The buoyant force represents the force, exerted on a particle by the liquid and is equal to the acceleration of the mass of displaced liquid. The contribution of the buoyant force is given by the product of the density of the medium (ρ_S), the volume of the particle (V_N) and depends, neglecting the earth's gravitational field, on the centrifugal acceleration applied ($r\omega^2$).

$$F_b = V_N \rho_S r \omega^2 \quad (\text{Eq. 15})$$

According to these considerations, the direction of the particle movement is given by the balance of F_c and F_b , while the particle velocity is additionally influenced by F_f . Sedimentation of particles can thus only occur if F_c outweighs F_b . However, for all the forces acting on the material, it is worthwhile to mention, that the size and the rigidity of the solvation shell have an additional influence. Thus, the larger the difference of the so-called buoyant density of the particle including the surrounding solvation shell and the density of the medium, the higher the sedimentation velocity. Overall, the sedimentation behaviour can be described by the sum of all relevant forces exerting on the particle as shown in equation 16 (Figure 2.2-11).

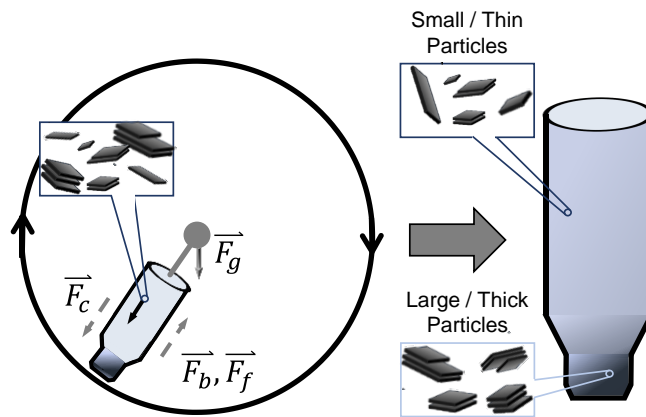


Figure 2.2-11: Centrifugation-based size selection. Different forces exerting on the nanosheets, depending on the size and shape of the sheets. Centrifugal forces acting on large and thick material are typically stronger than on small and thin particles.

$$F_{ges} = \sum_i F_i = F_c + F_f + F_b \quad (\text{Eq. 16})$$

Rearranging the equations discussed above allows to extract a sedimentation coefficient (c_{sed}), which is represented by the ratio of the sedimentation velocity of a particle (v) and the strength of the centrifugal field ($r\omega^2$) in units of Svedberg ($1 \text{ S} = 10^{-13} \text{ s}$) as shown in equation 17.⁶⁹

$$c_{sed} = \frac{v}{r\omega^2} = \frac{m(1 - V_N \rho_S)}{c_f} \quad (\text{Eq. 17})$$

In view of a polydisperse mixture of different nanosheet sizes and thicknesses (*i.e.* anisotropic in shape), the sedimentation behaviour strongly depends on the frictional coefficient of the sheets, which depends on the drag coefficient of the nanostructures and their solvation shell. In addition, the particle density and volume, as well as the viscosity and density of the medium have a strong impact on the efficiency of the size selection. Especially the viscosity of the solvent (included in c_f) has a major impact on the sedimentation velocity of the particles. Many reports do not take this factor into account, which makes comparison of results obtained from different groups difficult. However, awareness in this regard is increasing and normalisation of the centrifugation time to the solvent viscosity (Figure 2.2-12) enables a more consistent comparison of the efficiency of the size selection and gives additional insights into solvent stabilization of nanosheets as the determination of the material concentration after centrifugation is more reliable.⁴²

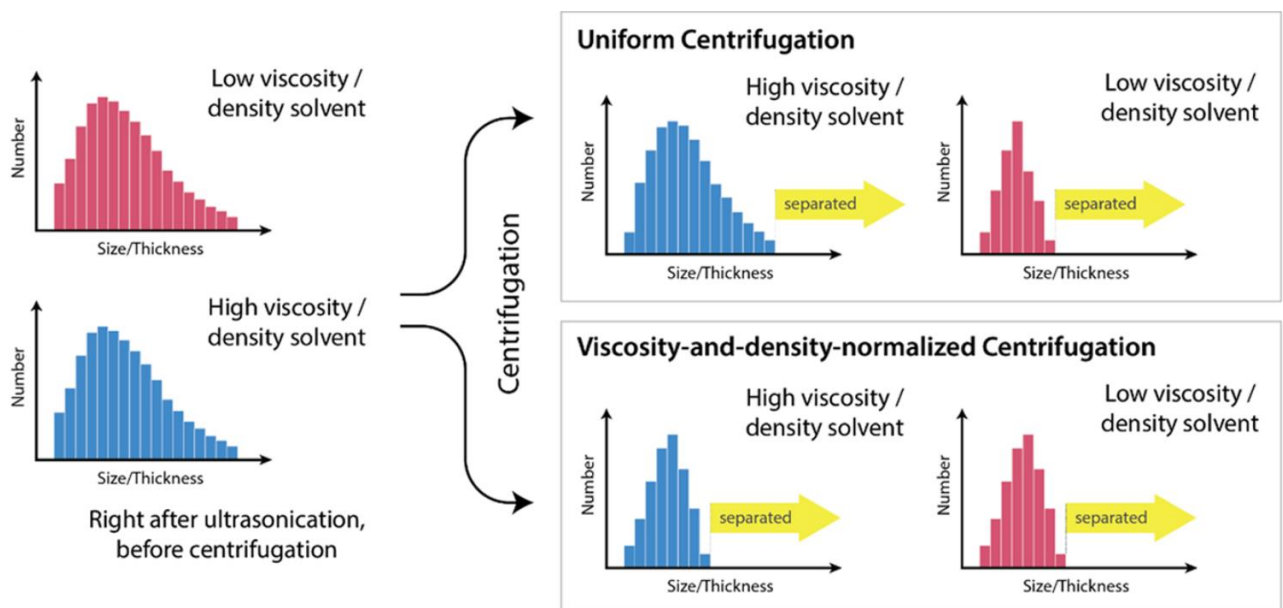


Figure 2.2-12: Impact of solvent viscosity on nanosheet sedimentation. Centrifugation times normalised to viscosity and density of the solvent allows to reproducibly select similar nanosheet size distributions in different solvents. Reproduced with permission from ⁴².

In the simplest scenario of sedimentation-based size selection of nanosheets *via* centrifugation, the polydisperse nanosheet ensemble is centrifuged for a defined time at a constant centrifugation speed. After centrifugation, the supernatant can be separated from the sediment, which results in two fractions of different material sizes, depending on the sedimentation behaviour. According to various reports, sedimentation of large and thick nanosheets occurs faster than sedimentation of comparatively smaller and thinner structures. Thus, the sediment fraction contains qualitatively larger and thicker nanosheets than the supernatant fraction.

The procedure described above can be referred to as single-step homogenous centrifugation. In addition to the solvent and nanomaterial parameters, mentioned in the previous Chapter, additional factors, such as the length of the centrifuge tube and its filling height (*i.e.* particle travel distance) have an impact on the result of the size selection. Moreover, the travel distance of the particles, often

Chapter 2 - Background

neglected in literature, is an important parameter for two reasons. Firstly, an increased travel distance leads to prolonged sedimentation times (Figure 2.2-13 A). Second, the centrifugal field increases directly proportional to the distance from the centre of rotation ($F_c \propto r$) which means that the forces, exerting on particles in a short centrifuge tube are different from those in a large tube (Figure 2.2-13 B).

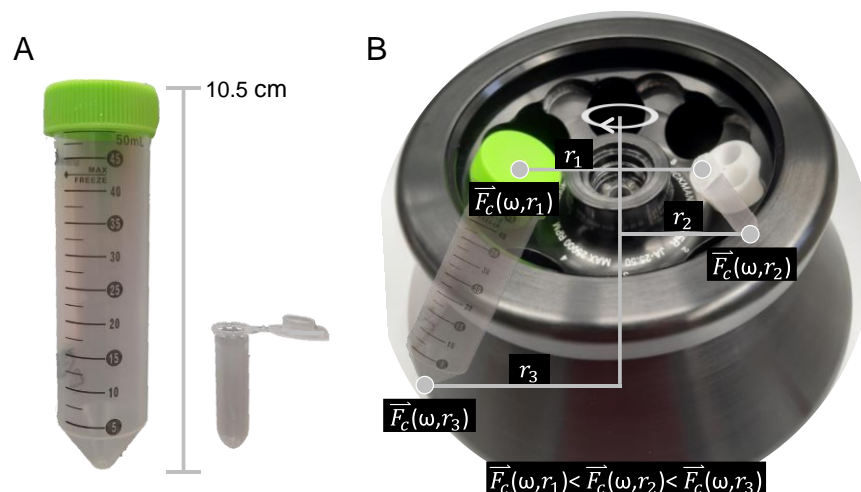


Figure 2.2-13: Impact of centrifuge tubes and rotor geometry on the sedimentation behaviour. (A) Two different centrifuge tubes of different dimensions. **(B)** Fixed angle rotor (Beckmann JA-25.50) equipped with both centrifuge tubes in comparison. The geometry of the tube and the rotor has an impact on the exerting forces and the travel distance of the particles.

These considerations also imply that sufficiently long centrifugation times are required for adequate material separation. Typically applied centrifugation times are 2 hours for filling heights of ~ 8.5 cm in aqueous surfactant dispersions.^{10, 47, 63, 70-73} It is important to keep these aspects in mind if the size selection contains more than one centrifugation step in order to reproducibly isolate fractions of certain sizes of a nanomaterial.

2.3.2 Liquid Cascade Centrifugation

Selecting different sizes of liquid phase-exfoliated nanosheet ensembles allows to investigate size-dependent material properties of, ideally narrow distributions of different material dimensions. In this regard, liquid cascade centrifugation (LCC) has been established⁷¹ and has proven to achieve successful separation of different nanomaterial sizes for various classes of 2D-materials.^{10, 12, 20, 21, 23, 63, 70-72, 74, 75} The basic principle is based on multiple centrifugation steps at increasing centrifugal acceleration. After each step, the supernatant is decanted and used for the subsequent step, while the sediment is collected in a reduced volume of fresh solvent.⁷¹ Thus, an iterative size selection is achieved, with each sediment fraction containing different size distributions of the nanomaterial. The size-range of each sediment fraction is determined by the centrifugation speeds applied between two steps and can be tuned depending on the required size-range for the desired application. Typically,

the sediment after the first centrifugation step at low centrifugal acceleration, as well as the supernatant after the last step at high centrifugal acceleration are discarded, because these fractions usually contain large amounts of unexfoliated and defective material and soluble impurities, respectively.^{66, 71} The process is schematically illustrated in Figure 2.2-14.

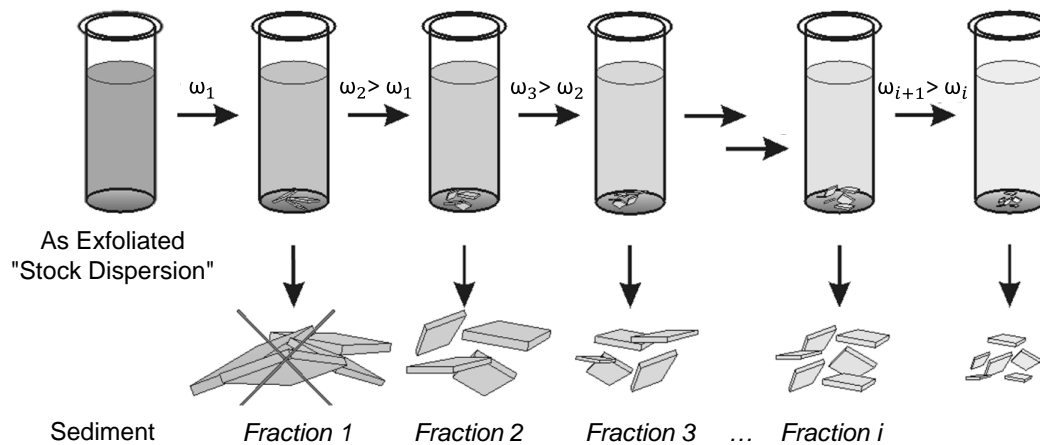


Figure 2.2-14: Schematic illustration of liquid cascade centrifugation (LCC). Sedimentation of nanomaterial in consecutive centrifugation steps of increasing centrifugal acceleration leads separation of large and thick from small and thin particles. The number of steps and the centrifugation time have an impact on the efficiency of the size selection.

In order to accomplish decent size separation, it is crucial to decant the supernatant from the sediment as carefully but at the same time as completely as possible. The size selection process itself is time consuming but bears the advantage of low material wastage, as all fractions can be collected for analysis and further processing to study size effects on fundamental material properties or device performance. Another advantage of this technique is the high concentration of nanomaterials in the sediment fractions. Thus, the desired dispersion concentration for subsequent investigations can be readily adjusted by the added volume of fresh solvent. At the same time, the concentration of the stabiliser can be reduced significantly through repeated washing steps followed by redispersion in fresh solvent or by solvent exchange, leaving minor contributions of the residual solvent in the sediment. This is important especially for thin-film deposition techniques, such as cast- or printing processes, for which the rheological properties of the ink exhibit a major impact on the material deposition.^{25, 76, 77}

Until now, LCC has been applied to a large variety of materials, using organic solvents, solvent blends, aqueous surfactant or polymer-stabilized systems and requires only little fine tuning of the process parameters (*e.g.* centrifugation speed) to achieve size selection. However, using this approach large/thick nanosheets are separated from smaller/thinner counterparts, *i.e.* no layer-dependent separation is possible. While so-called secondary cascades⁷⁸ have been suggested to partially overcome this problem, it will always be a limitation in sedimentation-based techniques.

2.3.3 Density Gradient Ultracentrifugation

An alternative, yet well-established route to size selection of materials is isopycnic centrifugation. The method, described by Vinograd *et al.*⁷⁹ is commonly applied to biomolecules and makes use of density differences of solutions or gels to accomplish size selection, while the material passes through different layers of varying density of the medium⁸⁰ (*i.e.* density gradient, Figure 2.2-15 A). The material moves through the medium in a strong centrifugal field until the density of the medium equals the buoyant density of the material, which leads to separation into bands of relative density (Figure 2.2-15 B). The efficiency of the size selection by isopycnic centrifugation depends on the density profile of the medium, which has to be adjusted to the respective buoyant density of the nanomaterial for successful size separation. Thus, the result strongly depends on the number of layers of different densities in the medium and the homogeneity of the buoyant density differences of the material subjected to centrifugation.

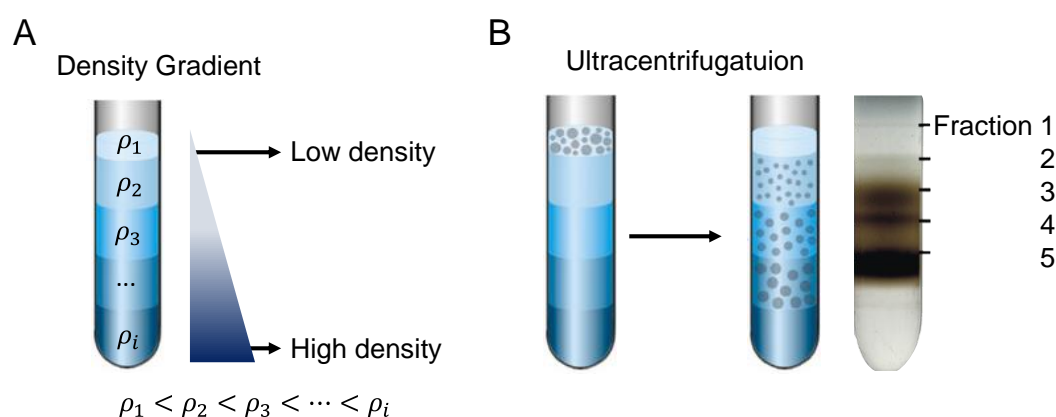


Figure 2.2-15: Schematic illustration of the principle of density gradient ultracentrifugation (DGU). (A) Different concentrations (*i.e.* densities, ρ) of a gradient medium layered in a centrifuge tube. A density gradient is formed with increasing density from top to bottom. (B) Left: illustration of the working principle. Ultracentrifugation leads to size selection if the buoyant density of the particles matches to a density within the gradient (*i.e.* isopycnic point). Right: experimental result of size-selected WS₂ *via* DGU after combined adjustment of the gradient medium and the buoyant density of the particles. Reproduced and adapted with permission from ⁸¹.

The approach deems particularly promising for layered materials, as the solvation shell has a larger impact on the buoyant density of thin compared to thicker structures, due to an increasing surface per particle mass for decreasing nanosheet layer number.

In order to tailor the density of the medium to the densities of the desired nanomaterial size or in case of 2D-materials, thickness, so-called density gradient media are used. These enable the formation of a density gradient and increase the inherent density of the fluid. Common gradient media are aqueous solutions of salt (*e.g.* CsI, CsCl) or sugar (*e.g.* sucrose, iodixanol) at different concentrations, which can be stacked layer by layer in a centrifuge tube to form a density gradient. This allows to tailor the densities of the individual layers of fluid to the buoyant densities of different nanosheet layer numbers by careful adjustment of the concentration of the gradient medium. The technique was

successfully applied to aqueous dispersions of graphite⁸² and *h*-BN⁸³ in sodium cholate, using an aqueous iodixanol gradient and results in visual bands of preferentially mono-layered and bi-layered material, respectively. For materials exhibiting a higher inherent density, such as TMDs, the surfactant coverage with sodium cholate did not sufficiently lower the buoyant density of the nanosheets to match the accessible density range in aqueous iodixanol solution. However, it was possible to enrich fractions containing few- and mono-layered species of MoS₂ and WS₂ after adjustment of the buoyant density of the nanomaterial by stabilisation with a block copolymer with large solvateable side-chains.⁸⁴ In subsequent reports, mixtures of iodixanol and CsCl qualified DGU for size selection of ReS₂ nanosheets.⁸⁵

Although these results demonstrate the applicability of DGU for size selection of various 2D-nanostructures and show, that the buoyant density of materials can be adjusted with respect to the chemical structure of the stabiliser, isopycnic centrifugation is still not widely used to this end for different reasons: using the methodology for size selection requires expertise and the appropriate equipment (*i.e.* an ultracentrifuge with a swinging bucket type rotor) to reproduce reported results. Tedious fine-tuning of the medium is necessary to optimise the density gradient to a specific material, especially for materials with a high inherent density. In addition, the accessible nanosheet concentrations of mono- and bilayer fractions are diluted upon centrifugation, as the volume of material subjected to the size selection is comparatively low in contrast to the volume of the gradient medium, which is furthermore hard to completely remove from the nanomaterial as high concentrations of the gradient medium (up to 40 vol%) are required. At last, using salts in the medium can cause significant nanosheet aggregation due to colloidal destabilisation which influences the buoyant density of the material.

2.4 Size-Dependent Material Properties

Inherent material properties change when going from bulk solid to nano-dimensional structures of the same chemical composition.⁸⁶ This includes changes of the mechanical properties (*e.g.* elasticity, ductility), as well as alternations of the electrical (*e.g.* conductivity) and optical (*e.g.* photoluminescence) response. In addition to changes of fundamental material properties, the chemical reactivity of the nanomaterial is increased due to its higher effective surface area. While these so-called surface- and confinement effects limit applicability of bulk materials with decreasing size in smaller (*i.e.* nanoscopic) device structures, due to the presence of dangling bonds, they open the door for van der Waals crystals.

The physical and chemical properties of van der Waals crystals strongly depend on the number of layers in a sheet stack. Graphite shows significant changes of the electronic properties upon changes in the layer number, especially for isolated single layers (*i.e.* graphene).⁸⁷ Furthermore, novel properties arise for the monolayer: charge carriers act as massless fermions,⁸⁸ the Born-Oppenheimer

Chapter 2 - Background

approximation is no longer applicable,⁸⁹ and many other unexpected features are observed upon layer separation.^{87,90} Motivated by these novel properties for atomically thin graphite, other layered compounds were rediscovered and investigated for layer-dependent changes of the corresponding nanomaterials. In 2010, it was shown, that different TMDs, commonly used as lubricants due to their layered structure and heat resistance, show photoluminescence (PL) in the monolayer limit (Figure 2.2-16 A), whereas thicker sheets exhibit an indirect band gap (Figure 2.2-16 B).

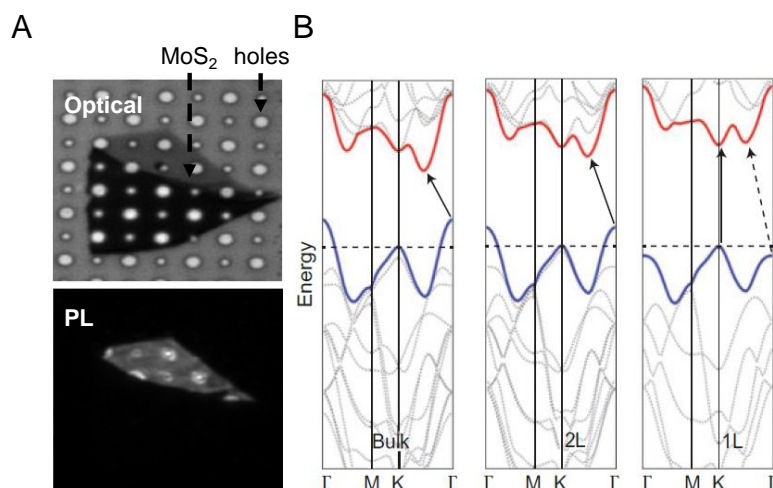


Figure 2.2-16: Confinement effects observed for MoS₂. (A) Upper part: optical micrograph of an incompletely exfoliated MoS₂ nanosheet. Lower part: radiative decay of excited states is only observed for the mono-layered part of the nanosheet. (B) Calculated band structures of bulk, bi- and mono-layered MoS₂. Only the mono-layered material exhibits a direct band gap. Reproduced and adapted with permission from ^{91,92}.

While the emerging PL can be attributed to confinement effects, which can manifest with varying degree for different materials,⁹³ other changes in optical properties are predominantly associated with geometric effects.⁴⁸ The impact of the particle size on extinction spectra of TMDs was first observed by Guitérrez and Henglein in 1989 for different sizes of pore filtered dispersions of MoS₂ and WSe₂.³⁹ However, the available technical equipment did not allow for a quantitative analysis at that time. 35 years later, geometric effects on exfoliated TMD nanosheets were investigated systematically on size-selected samples of different semiconducting TMDs, namely MoS₂, WS₂, MoSe₂ and WSe₂.⁴⁸ Nanosheet size and thickness distributions of the different size fractions have been quantified by a combination of statistic transmission electron microscopy (TEM) and atomic force microscopy (AFM) which enables the correlation of observed changes (*e.g.* peak intensity ratios) in the extinction and absorption behaviour to the respective mean nanosheet sizes. The intensity ratios of the spectra systematically change with the average lateral dimensions of the nanosheets which is mainly attributed to two different electronic contributions from nanosheet edges and basal planes. With variations in nanosheet lateral size, the ratio of the electronic edge to basal plane contribution changes as well (Figure 2.2-17 A). This connection can be described by a simple model, approximating the nanosheets as rectangles of a combination of an edge and a centre region, where both of which exhibit different absorption coefficients ($\alpha_E(\lambda)$ and $\alpha_C(\lambda)$, respectively):

$$\frac{Abs(\lambda_1)}{Abs(\lambda_2)} = \frac{\alpha_C(\lambda_1) \cdot \langle L \rangle + 2 \cdot \{\langle LW^{-1} \rangle + 1\} \cdot \{\alpha_E(\lambda_1) - \alpha_C(\lambda_1)\}}{\alpha_C(\lambda_2) \cdot \langle L \rangle + 2 \cdot \{\langle LW^{-1} \rangle + 1\} \cdot \{\alpha_E(\lambda_2) - \alpha_C(\lambda_2)\}} \quad (\text{Eq. 18})$$

Here, $\frac{Abs(\lambda_1)}{Abs(\lambda_2)}$ represents the extinction intensity ratio, $\langle L \rangle$ is the mean nanosheet length extracted from statistical microscopy and $\langle LW^{-1} \rangle$ is the average nanosheet length/width aspect ratio. Note, that a similar model can be applied to extinction measurements. In addition to changes with nanosheet length, a systematic blueshift of the lowest energy excitonic transition is observed with decreasing layer number of the nanosheets (*i.e.* confinement of excited states, Figure 2.2-17 B).

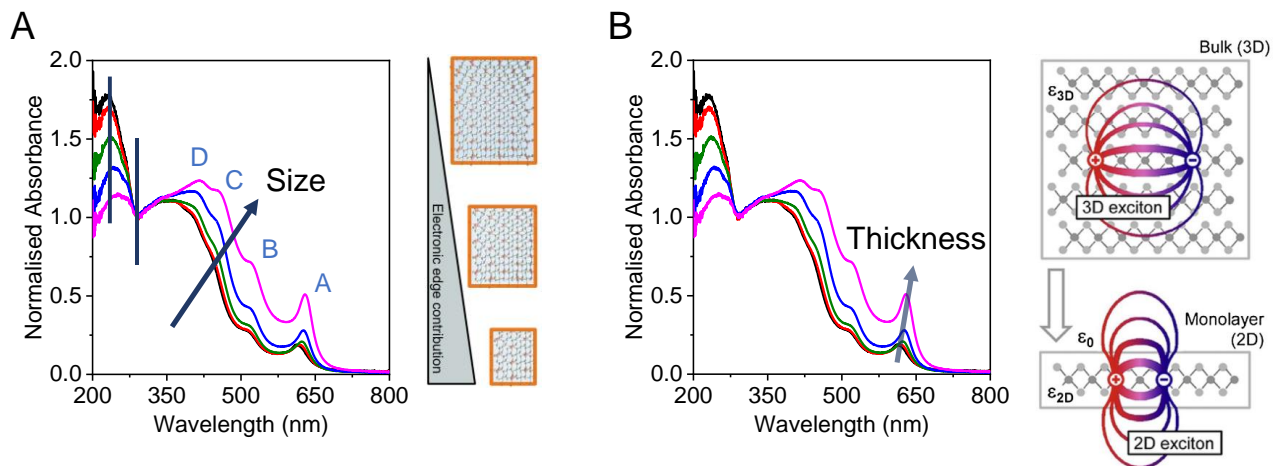


Figure 2.2-17: Size effects observed for WS₂. (A) Size-dependent changes of absorbance spectra of WS₂. (A) Left: changes of peak intensity ratio depending on the different nanomaterial lateral dimensions. Different excitonic transitions are indicated by capital letters. Right: changes are attributed to different ratios of edge and basal plane contribution for different nanosheet sizes. (B) Left: absorbance spectra of different sizes of WS₂. Position of the A-exciton shifts systematically with nanomaterial thickness. Right: shifts can be attributed to confinement effects leading to localisation of excited excitons. Reproduced and adapted with permission from ^{48, 71, 94}.

These findings are important, as they enable quick determination of the average nanosheet dimensions by standard spectroscopy and suggest that the changes of the spectra for different nanosheet sizes follow a general principle for 2D-materials, which was shown to hold for black phosphorus,⁷⁵ GaS¹² and many other examples.^{11, 23} However, it is far from understood in which way other electronic contributions (*e.g.* from defects or oxidation) or changes of the dielectric environment influence the optical spectra. Thus, the applicability of spectroscopic metrics is limited as yet.

2.5 Nanomaterial Stability

In perspective of finding novel wonder materials for basically any desirable application, the materials' stability is often a widely accepted condition. Furthermore, for many intended applications, persistent performance of resulting devices is required. As mentioned in the previous Chapter, layer separation leads to an increase of the effective nanosheet surface, which can be advantageous for

Chapter 2 - Background

applications in catalysis. However, an increase of a materials surface area also leads to an increased chemical reactivity. Graphite and TMDs are considered as stable materials in ambient conditions⁹⁵ and are therefore widely used in applications as dry lubricants in high temperature mechanics.⁹⁶ Yet, when exfoliated into nanosheets, colloiddally stable dispersions of graphite and MoS₂ nanosheets can be formed in pure water if exfoliated at elevated temperatures (at 40°C and 60°C, respectively) due to formation of solvateable surface oxide functionalities.⁹⁷ It is unclear whether the increased temperature leads to functionalisation of readily available defect sites in the bulk material or if new defects are formed. However, it was shown, that defects on the material surface can act as starting points for further degradation and the awareness about decreased stability of the nanomaterials compared to their bulk counterparts is increasing.⁹⁸ A systematic study on micromechanically-exfoliated TMD nanosheets demonstrates the progressive nanosheet decomposition on the supposedly stable nanomaterial by scanning tunnelling microscopy.⁹⁸

While exfoliation of light, air and water sensitive 2D-materials that exhibit promising properties for optoelectronic (black phosphorus, antimony),^{99, 100} spintronic (RuCl₃, CrI₃)^{101, 102} or water splitting (FePS₃, NiPS₃)^{11, 103} applications have been reported, in particular the stability of these systems has to be delicately considered. In spite of these proof-of-concept reports, chemical sensitivity limits the widespread application of such materials. For most of these 2D-materials, the decomposition is poorly investigated or at least insufficiently commented. However, black phosphorus (BP) seems to be an exception in this regard. Various studies show rapid decomposition of the nanosheets of the single element 2D-material in presence of oxygen.^{104, 105} The sensitivity of these materials to environmental effects makes their use in state-of-the-art devices challenging.

In order to retain the desired inherent material properties, inhibition of the degradation is necessary. Sutter *et al.* report stable BP nanosheets by encapsulation with degassed water.¹⁰⁶ Other groups suggest the passivation of the material by non-covalent functionalisation with specifically designed small molecules exhibiting strong interactions with the 2D-material's surface¹⁰⁷ or by another inert 2D-material, such as *h*-BN or graphite,^{108, 109} or by embedding the material in a polymer matrix, depending on the designated purpose of the nanomaterial (Figure 2.2-18).

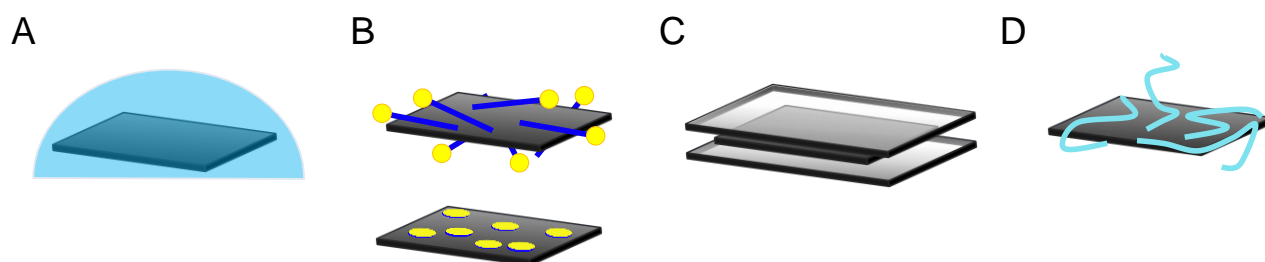


Figure 2.2-18: Simplified schematic illustration of possible routes to passivation of 2D-materials. (A) Shielding from oxygen in a degassed solvent. **(B)** Surface passivation by non-covalent interactions with a solvent or stabiliser molecule. **(C)** Shielding from chemical environmental by encapsulation with inert 2D-materials (*e.g.* *h*-BN). **(D)** Embedding of the nanomaterial in a polymer matrix.

Chapter 2 - Background

It is important to consider that most reports on nanosheet decomposition and passivation focus on micromechanically cleaved 2D-materials which are typically much larger than for example sonication assisted liquid-exfoliated nanosheets. Hence, edge-effects may have a significantly different impact on the material decomposition for smaller nanosheets which can be prepared by high throughput approaches. Large-number statistics cannot be provided from studies on ME nanosheets, where large flake to flake deviations can be observed. In addition, most reports discuss 2D-materials deposited on a substrate, such as *h*-BN, gold or silicon/silicon oxide which has an additional impact on the degradation behaviour of the nanomaterial as reported recently.¹¹⁰ Reported studies on the nanomaterial decomposition can therefore not be considered as representative for the respective nanomaterials. In contrast, liquid phase-exfoliated nanomaterials allow to probe an ensemble of nanosheets in a homogenous chemical environment. This enables to study the material stability averaged over billions of nanosheets in a single measurement if the spectroscopic response is sufficiently understood.

With regard of all the aspects discussed in the previous Chapters, many open questions remain before exfoliated van der Waals crystals can be used in large scale devices and applications. Robust benchmarking will be required to unravel technologic advances of layered crystals. It is unclear whether or not 2D-materials supersede currently utilised materials in state-of-the-art applications. However, the toolbox of hundreds of layered materials, each with its own properties, allows to render the scientific advances of 2D-materials as important progress in material science. A better understanding of these systems and controlled deposition will allow rational design of combined hierarchical structures with new properties, specifically tailored depending on the desired application. Synergistic effects of constructed superstructures might again lead to new material properties. Future perspectives of 2D-materials remain an open question but exciting insights are still to be explored.

Chapter 2 - Background

The following Chapter reports on the exfoliability of different van der Waals Crystals. In addition to reported results, new insights on the size and thickness relationship of various layered materials are reported and supplemental data on the exfoliation of different van der Waals crystals is presented. Parts of this Chapter are published in *ACS Nano* (2019), 13; *Chem. Mat.* (2019), 24; *Chem. Mat.* (2019), 31; *Angew. Chem.* (2020), 59 and in *JACS* (2020), 142. Presented reprints are shown in combination with a citation in the caption text and are reproduced or modified with permission from the respective publishers.

3 Exfoliability of Different Van der Waals Crystals

Van der Waals crystals are versatile starting materials for new nanostructures when exfoliated into nanosheets which is predominantly attributed to confinement effects in two dimensions. This effect amplifies with decreasing layer number and is most pronounced for single layers. While the degree of confinement predetermines the properties of the nanomaterial, exfoliation into mono-layered species is not always necessary. In comparative studies across various material classes, it might become possible to identify common aspects of size and thickness-dependent properties which can then be exploited in various application areas in a rational way. As future perspective, designing material properties by means of exfoliation and restacking of different materials into mixed structures (*i.e.* heterostacks) is appealing. The understanding of such superstructures is limited as mostly experimental challenges are still to be overcome but synergistic effects have readily been reported.¹¹¹⁻¹¹⁴ To achieve this, it is first required to create a toolbox to create the individual building blocks on demand by various means, including but not limited to liquid phase exfoliation. As such, it is important to understand the fundamental limitations of the exfoliation process.

In this work, different van der Waals crystals have been tested for their exfoliability by means of sonication-assisted exfoliation in the liquid phase followed by size selection to facilitate characterisation. The nanomaterial dimensions were measured by statistic evaluation of drop-cast nanosheets *via* atomic force microscopy (AFM). Exfoliated nanosheets were size-selected by liquid cascade centrifugation and the different fractions (*i.e.* material sizes) were evaluated individually. This protocol was applied for two reasons: when using AFM for quantification of the nanosheet dimensions, measurement parameters have to be adjusted to the particle size to reliably account for pixilation effects and cantilever broadening. AFM measurements thus generally overestimate the nanosheet size by an approximately constant factor if the field of view is adjusted to the nanosheet sizes. This can be corrected by a correlation of the average nanosheet sizes of a number of samples measured with both AFM with statistic and TEM statistics, as reported before.⁷¹ In the framework of this thesis, nanomaterial sizes were corrected by an empirical correlation of mean lengths of the same sample extracted by statistic AFM and TEM as discussed in more detail in the following Chapter. Separating fractions of different material dimensions additionally allows to investigate size-dependent material properties (Chapter 4). For all materials under study, a comparison to liquid phase-exfoliated graphite is shown, which serves as reference material.

Chapter 3 - Exfoliability

Liquid Phase Exfoliation of

3.1 Transition Metal Dichalcogenides

Layered transition metal dichalcogenides (TMDs) are a well-known class of 2D-materials that consist of over 40 different materials, such as WS_2 and MoSe_2 . The sulfides are non-toxic and find application as lubricants as the crystals can be sheared parallel to the stacking direction and exhibit a high temperature resistance.⁹⁶ The crystal structure of 2H-TMDs is schematically shown in Figure 3.1-1 A. The bulk crystals used for the following experiments have been purchased from a commercial source. Representative scanning electron microscopy (SEM) images, X-ray diffraction (XRD) pattern and Raman spectra are shown in Figure 3.1-1 B-D and confirm the structural integrity and high quality of the bulk material.

However, when exfoliated into nanosheets, new properties arise. Group-VI TMDs are semiconductors with an indirect bandgap for bulk and few-layered species. If exfoliated into monolayers, a direct gap is formed, which leads to radiative decay of excitonic inter-band transitions in the visible and near infrared (nIR) range.¹¹⁵ The emerging photoluminescence renders group-VI TMD monolayers interesting materials for optoelectronics.^{116, 117} Optical properties, such as the exciton binding energy of TMDs have been investigated extensively on micromechanically-exfoliated single nanosheets.^{48, 78, 115, 118-120} However, quantitative reports of fundamental properties are quite scattered which is likely due to extrinsic and environmental impact such as strain or dielectric inhomogeneities.¹²¹ It should be noted that the majority of studies focus on individual nanosheets on a substrate. Using liquid phase exfoliation in combination with size selection by cascade centrifugation is a complementary approach which allows to study an ensemble of nanosheets and average the properties over millions of nanosheets in a homogenous dielectric environment. In spite of the fact, that such a correlation of properties to average nanosheet size and thickness information requires tedious statistic evaluation of the material dimensions, promising insights are expected if the nanosheet size distribution is accurately determined and controlled.

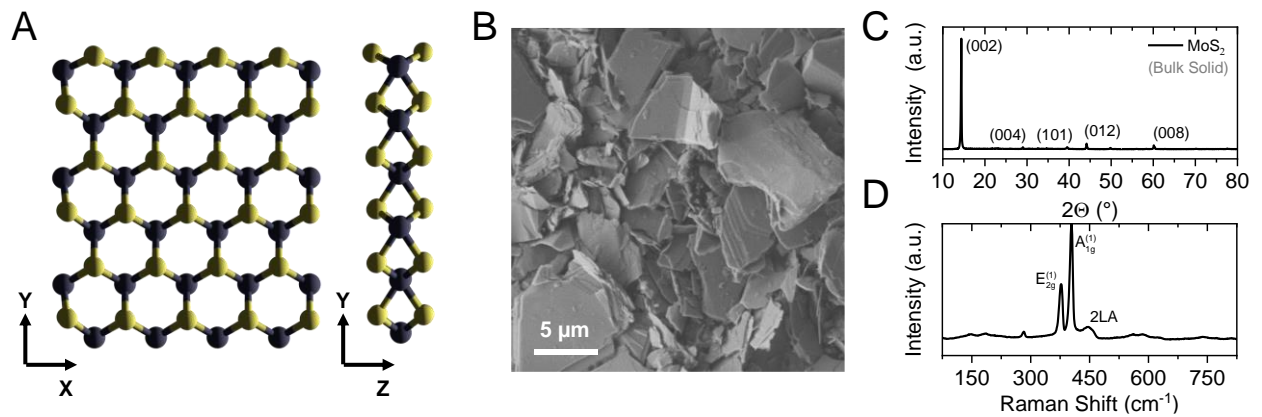


Figure 3.1-1: Character of bulk MoS₂. (A) Schematic crystal structure of 2H-TMDs, such as MoS₂ (black: transition metal, yellow: chalcogen). (B) Low magnification SEM image of MoS₂ crystallites. Images reveal crystallite sizes in range of 2-20 μm. The layered character of the material is clearly resolved. (C) Diffraction pattern of powdered MoS₂. (D) Raman spectrum acquired for MoS₂ using an excitation wavelength of 532 nm. Reproduced and adapted with permission from ^{49, 122}.

In this regard, four different group-VI TMDs (WS₂, MoS₂, WSe₂ and MoSe₂) were subjected to liquid phase exfoliation by tip sonication in aqueous sodium cholate solution (for experimental details see Chapter 7.1). The nanosheet stock dispersion as obtained after exfoliation was size-selected by liquid cascade centrifugation to reduce the sample polydispersity. This enables to separate fractions of different sizes of nanosheets. The cascade centrifugation sequence was kept constant for all four TMDs and consists of seven consecutive centrifugation steps with each step being performed at higher speeds than the previous one. The centrifugal acceleration for the respective size selection steps were 100 g, 400 g, 1000 g, 5000 g, 10000 g, 22000 g and 74000 g, expressed in multiples of the earth's gravitational field (g). Applying this procedure results in fractions containing nanosheets of decreasing size and thickness as schematically illustrated in Figure 3.1-2. After each centrifugation step, the supernatant is separated from the sediment. While the latter is redispersed in reduced volume of fresh solvent and used for analysis, the supernatant is taken for the subsequent step of the centrifugation sequence. It is important to note that collecting the sediment in small volumes of solvent is crucial for the analysis as the sheets can be redispersed at higher concentration. The sediment after the first step and the supernatant after the last step were discarded as these two fractions contain mostly unexfoliated or defective material, respectively. Isolated fractions are labelled by the lower and upper centrifugal acceleration used for sedimentation in accordance to previous work for better comparability of materials addressed throughout this work and to literature. Hence, the expression "0.1-0.4k g" (Figure 3.1-2) describes parameters for nanomaterial separation between two consecutive centrifugation steps. In this example, the sample was obtained by sedimentation of nanosheets at 400 g from a supernatant obtained after centrifugation at 100 g. The central g-force used in Figure 3.1-4 results from the mean centrifugal acceleration between two steps (in this example: 0.25k g).

Chapter 3 - Exfoliability

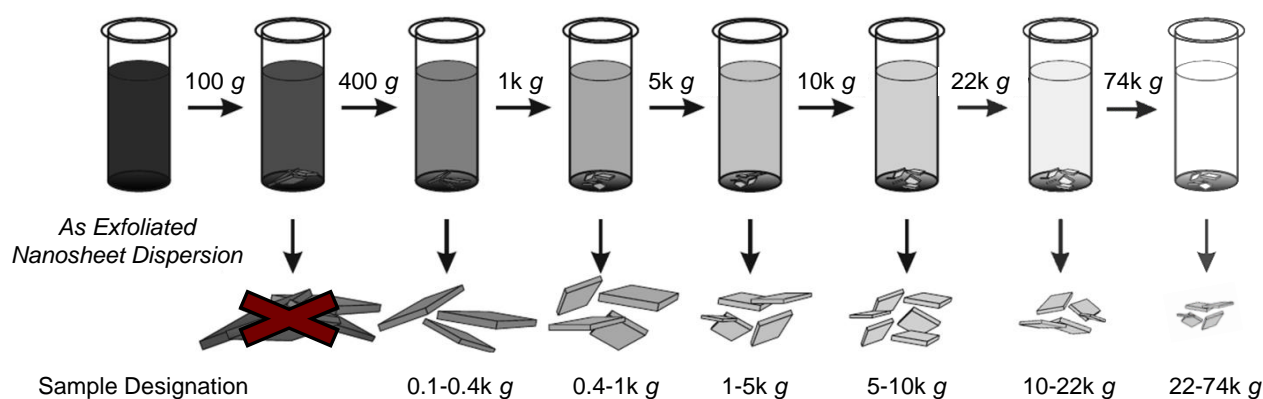


Figure 3.1-2: Schematic illustration of nanomaterial size selection by liquid cascade centrifugation. The graph shows the centrifugation sequence used for the size selection of the as prepared stock dispersion of TMDs in aqueous sodium cholate. The sediment received after each step is collected and redispersed in reduced volume of fresh solvent, while the supernatant is used for the next step at higher centrifugal acceleration. The steps chosen for the size selection of all TMD nanosheets were 100 g, 400 g, 1000 g, 5000 g, 10000 g, 22000 g and 74000 g for 2 hours, respectively. The unit "g" represents the relative centrifugal force (RCF in multiples of the earth's gravitational force). Samples are labelled by the upper and lower centrifugation boundary, as indicated in the graph.

To accurately address the size-range of the nanosheets in each size-selected fraction, statistical AFM measurements were performed on drop-cast nanosheets. A small amount of the high concentrated sediments was collected and diluted in ultrapure water and subsequently deposited on a Si/SiO₂ wafer by flash evaporation for this purpose (for experimental details see Chapter 7.3). For each sample, the longest dimension (length), dimension perpendicular (width) and thickness of 200-300 individual nanosheets was manually measured and statistically evaluated as will be described in more detail below.

To account for pixilation and cantilever broadening, the size distribution each fraction was additionally determined by statistical TEM measurements (Appendix 3.1-1). Figure 3.1-3 A shows the arithmetic mean nanosheet length, determined from AFM ($\langle L \rangle_{AFM}$) as function of the average length measured with TEM ($\langle L \rangle_{TEM}$) for the four TMDs. The data is fit to a linear function resulting in an empiric correction of the measured length extracted from atomic force microscopy: $L_{TEM} = L_{cor} = (L_{AFM} - 21 \text{ nm}) / 1.05$. The subtraction of 21 nm accounts for tip broadening effects and the division by 1.05 corrects for pixilation. For the evaluation of the nanosheet layer number from the measured AFM thickness, additional contributions from solvent leftovers and the measurement parameters have to be considered.⁷¹ The measured height is thus typically overestimated, but proportional to the real height. For conversion, step height analysis on incompletely exfoliated nanosheets can be performed. In this approach, the apparent AFM height of a single layer is determined by measuring line profiles along nanosheet steps and terraces (Figure 3.1-3 B) and sorted in ascending order. Regular steps with a height of multiples of 1.9 nm are observed for MoS₂ (Figure 3.1-3 C). Hence, the measured nanosheet height is divided by 1.9 nm to extract the layer number.⁶

Furthermore, for a later correlation of the average material dimensions with spectroscopic data, it makes sense to weigh the layer number with the nanosheet volume fraction (V_f) of each sheet

to account for the increased contribution of large and thick particles in spectroscopy, where the volume and not number average is probed. Here, the volume fraction weighted layer number is termed $\langle N \rangle_{Vf}$ which differs from $\langle N \rangle$ similarly as weight- and number-averaged molecular weight in polymer chemistry^{10, 96, 123} and can be calculated from the nanosheet length, width and layer number as indicated by equation 19.

$$\langle N \rangle_{Vf} = \frac{\sum_{i=1}^n N_i^2 L_i W_i}{\sum_{i=1}^n N_i L_i W_i} \quad (\text{Eq. 19})$$

It should be noted, that throughout this thesis, the nanosheet length (L) is defined as longest dimension of a sheet, while the width (W) is defined as the dimension perpendicular to the length ($L > W$ and $L \perp W$). The correlation between $\langle N \rangle_{Vf}$ and $\langle N \rangle$ is empirically found to be $\langle N \rangle_{Vf} = 1.46\langle N \rangle - 0.48$ for the TMDs under study, as shown in Figure 3.1-3 D.

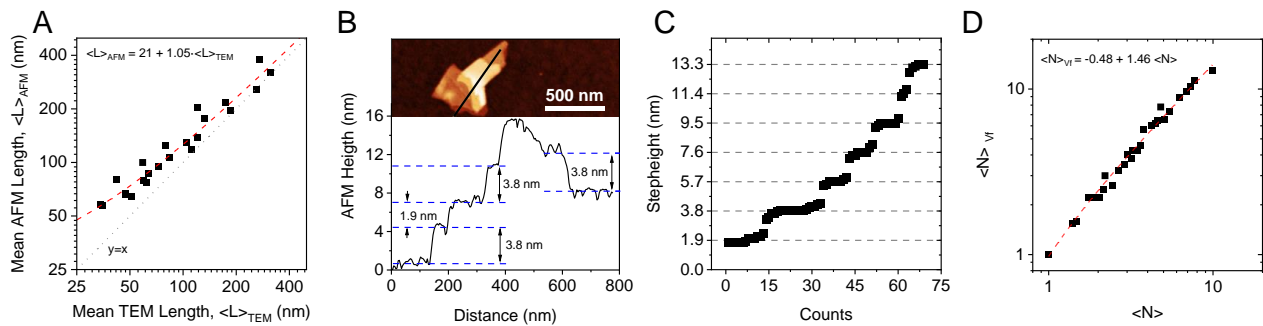


Figure 3.1-3: Corrections required for statistic evaluation of TMD nanosheet dimensions. (A) Correction of the lateral nanosheet dimensions determined by atomic force microscopy as suggested by statistic evaluation of the same dispersions in transmission electron microscopy and AFM. (B) Height profile of an incompletely exfoliated MoS₂ nanosheet. The black line indicates where the profile is measured. Terraces of incompletely exfoliated material are resolved and analysed to determine the apparent AFM thickness of a single layer. (C) Statistic distribution of step heights such as the ones extracted from the nanosheet in (B) plotted in ascending order. The step height is found to be a multiple of 1.9 nm, which is the apparent height of a single layer of TMDs and can be used to convert the measured height to the nanosheet layer number.⁷¹ (D) Correlation between volume fraction weighted layer number and arithmetic mean layer number of nanosheets to account for increased spectroscopic weight for thicker structures. Reproduced and adapted with permission from^{10, 48}.

Representative images of nanosheets from a large (0.4-1k g) and a small (10-22k g) size fraction are shown exemplarily for MoS₂ in Figure 3.1-4 A-B (for the complete dataset see Appendix 3.1-2). Histograms of the corrected lateral sizes and the nanosheet layer number distributions of the same two fractions are shown in direct comparison in Figure 3.1-4 C-D. The nanosheets isolated between 10-22k g are characterised by lateral sizes ranging from 20 to 100 nm and layer numbers between 1 and 4, while the nanosheets isolated at the beginning of the cascade (0.1-0.4k g) are significantly larger (with L ranging from 100 to 500 nm) and thicker (2-15 layers). From such size distribution of the nanosheets, the arithmetic mean nanosheet dimensions, *i.e.* volume fraction weighted layer number, $\langle N \rangle_{Vf}$ and the arithmetic mean nanosheet length, $\langle L \rangle$ are extracted for the different size fractions of all four materials. To assess the size selection, $\langle N \rangle_{Vf}$ and $\langle L \rangle$ are plotted as a function of

Chapter 3 - Exfoliability

the central centrifugal forces exerted on the material between two consecutive steps in centrifugation cascade (Figure 3.1-4 E-F). The mean sizes of the different materials roughly fall on the same curve for both $\langle N \rangle_{Vf}$ and $\langle L \rangle$, following a power law dependence with the central centrifugal force (\overline{RCF}): $\langle N \rangle_{Vf} \propto \overline{RCF}^{-0.38}$ and $\langle L \rangle \propto \overline{RCF}^{-0.4}$. This emphasizes, that the size selection mechanism is not necessarily dominated by the particle mass, as the four materials exhibit similar nanosheet sizes, but significantly different inherent densities.

In addition to the average material dimensions determined from size and thickness distributions, knowledge over the layer number and lateral size distribution allows to extract the volume fraction of monolayers, Vf_{ML} in the dispersions. The resultant data is shown as function of central RCF in Figure 3.1-4 G. Again, the data for all four TMDs fall on a master curve, similar to $\langle L \rangle$ and $\langle N \rangle_{Vf}$. As the monolayer content is insignificant in fractions isolated at low centrifugal force, solid statistics (evaluation of >300 nanosheets) are required to reliably extract these trends. Nonetheless, some scatter for these fractions is observed, which reduces for fractions isolated at higher centrifugal force (*i.e.* higher monolayer content). Empirical fitting of the data allows to describe Vf_{ML} as function of \overline{RCF} giving the relation: $Vf_{ML} = [1.2 + 70(\overline{RCF})^{-1.3}]^{-1}$, where the monolayer volume fraction increases with the central centrifugal force applied upon size selection before eventually leveling off. As $\langle N \rangle_{Vf}$ should be somewhat related to Vf_{ML} , a correlation between the two quantities is shown in Figure 3.1-4 H. Fitting the data results in a solid relation between Vf_{ML} and $\langle N \rangle_{Vf}$ (and thus $\langle N \rangle$), as shown in equation 20:

$$Vf_{ML} = \left[\frac{\langle N \rangle_{Vf}^{3.4}}{10} + 0.9 \right]^{-1} \quad (\text{Eq. 20})$$

This is useful, as it allows to estimate the monolayer content from arithmetic mean layer number, which can be determined from significantly fewer AFM counts than required for the monolayer volume fraction and, as discussed in Chapter 4 even from absorbance/extinction spectroscopy.

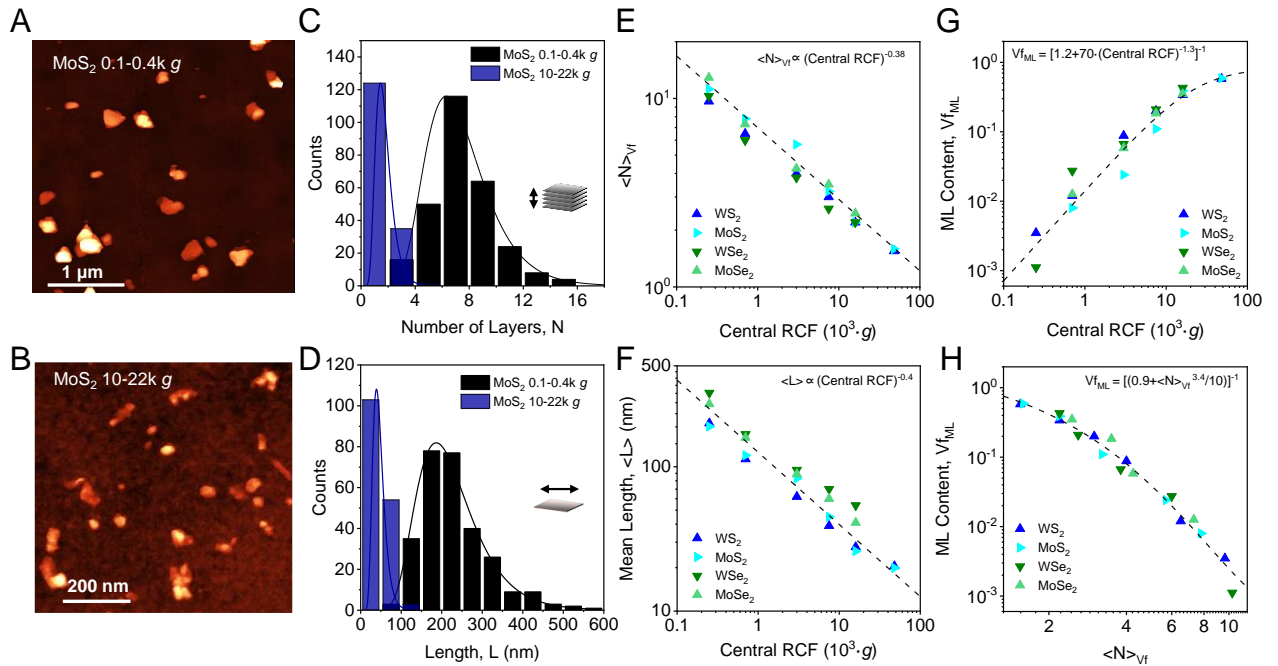


Figure 3.1-4: Statistic evaluation of MoS₂ nanosheet dimensions for different fractions of the size selection. (A-B) AFM images of drop-cast nanosheets for two fractions containing relatively large, $RCF = 0.1-0.4k\text{ g}$ (A) and small nanosheets, $RCF = 10-22k\text{ g}$ (B). (C-D) Histograms of the nanosheet layer number (C) and lateral sheet size (D) distribution for the two fractions shown in (A-B). (E) Mean volume fraction weighted layer number, $\langle N \rangle_{Vf}$ of TMD nanosheets across all fractions as function of central RCF plotted on a logarithmic scale. (F) Mean nanosheet length, $\langle L \rangle$ of the same nanosheet fractions as function of central RCF on a logarithmic scale. Both, $\langle N \rangle_{Vf}$ and $\langle L \rangle$ show a power law decrease with increasing centrifugation centrifugal acceleration as indicated by the dashed lines. (G-H) Monolayer content, Vf_{ML} as function of central centrifugal field (G) and as function of $\langle N \rangle_{Vf}$ (H), respectively. Reproduced and adapted with permission from ¹⁰.

As mentioned in Chapter 2.2.2, a relation of the in-plane to out-of-plane binding strength ratio is represented in the nanosheets area per layer number for various layered crystals exfoliated by LPE due to both exfoliation and scission occurring during the exfoliation process with an equipartition in energy.⁴⁷ The four TMDs under study share a similar structure. Thus, only minor differences of the binding strengths are expected. This is the case for three of the four TMDs (WS₂, MoS₂ and MoSe₂), which fall of the same curve when plotting the arithmetic mean nanosheet area versus mean layer number plot (Figure 3.1-5 A). It is unclear, why the exfoliated WSe₂ deviates from this behaviour. It should be noted that exceptionally large mono- and bilayers were found in this sample batch suggesting that scission was somewhat suppressed over exfoliation for reasons that could not be identified.

However, in consideration of experimental variations during centrifugation across batches (intrinsic such as design of rotor, vial and filling height or extrinsic *e.g.* upon decanting), it makes sense to evaluate the data in a different way. If the nanosheet area systematically changed with the layer number as function of the in-plane to out-of-plane binding strength ratio, the same relation should be evident from stock-like dispersions, containing all sizes and thicknesses of the nanomaterial produced during LPE. However, due to technical difficulties mentioned above, statistic evaluation of

Chapter 3 - Exfoliability

such polydisperse mixtures is barely feasible. Nevertheless, the population of all nanosheet sizes produced is roughly represented in the different size fractions isolated in the size selection (Figure 3.1-5 B, data of the other TMDs is shown in Appendix 3.1-3). It should be noted that such a plot of LW vs. N with data for all fractions combined can contain some bias, as it would be required to weigh the nanosheet population in a certain fraction by the mass in this fraction to work out the actual population in the stock. However, this is hardly feasible. Nonetheless, to mitigate the centrifugation-based variations, this data cloud can be analysed by averaging the mean area of a certain nanosheet thickness range as indicated by the dashed boxes in Figure 3.1-5 B to extract a more robust representation of the scaling of area with thickness. For the adjusted evaluation (referred to as $\langle N \rangle$ -averaged), the area of nanosheets with a similar thickness was summed up and averaged in packages of at least 70 counts. This leads to two effects: the number of datapoints is significantly increased and the fitted exponents of all TMDs equalise to 1.2, which is identical to the exponent extracted for graphite (evaluated similarly, Figure 3.1-5 C). While the applicability of the modified evaluation is still to be tested for other material systems, a clear improvement of the data quality is observed. However, the different exponent (1.2) compared to the fraction-averaged data (~ 2)⁴⁷ will require re-evaluation of the suggested model for the relationship between material size and thickness and the in-plane to out-of-plane binding strength ratio based on energy equipartition.

In addition to analysing the scaling of area with layer number, it can be of interest to investigate changes in the length/width aspect ratio ($\langle LW^{-1} \rangle$), as this can contain some information about the exfoliation/scission process. For example, for graphite it was observed that thinner nanosheets are elongated compared to thicker ones which was explained in terms of a three stage exfoliation/scission process initiated by kinks in the parent graphite.⁴⁵ In contrast to graphite, where the length/width aspect ratio increases with decreasing layer number, no changes are observed for the TMDs and $\langle LW^{-1} \rangle$ remains mostly constant if the $\langle N \rangle$ -averaging analysis is applied to the respective LW^{-1} vs. N data cloud (Figure 3.1-5 D). This is in contrast to the reported increase of the TMD fraction averaged length/width aspect ratio which was found to increase with increasing centrifugal acceleration.⁴⁷ This discrepancy between $\langle N \rangle$ -averaged and fraction-averaged data is interesting, as it is apparently a shape filtering effect occurring during centrifugation: the drag coefficient (*i.e.* shape) of the nanomaterial has an impact on the sedimentation velocity of the particles in addition to the mass/density and is which is reflected in changes in the average length/width aspect ratio. This nicely illustrates the importance of analysing the data in different ways. With aid of the $\langle N \rangle$ -averaging, it is clear the exfoliation/scission in graphite is distinct from the TMDs. Possibly, no kink band formation occurs in TMDs. Alternatively, the changes in $\langle LW^{-1} \rangle$ with $\langle N \rangle$ in the case of graphite can be interpreted as anisotropic bonding in the graphene lattice (zigzag vs. armchair edges). Then, Figure 3.1-5 D would suggest that this is not the case in transition metal dichalcogenides. In any way, for a conclusive discussion, results for additional materials need to be considered.

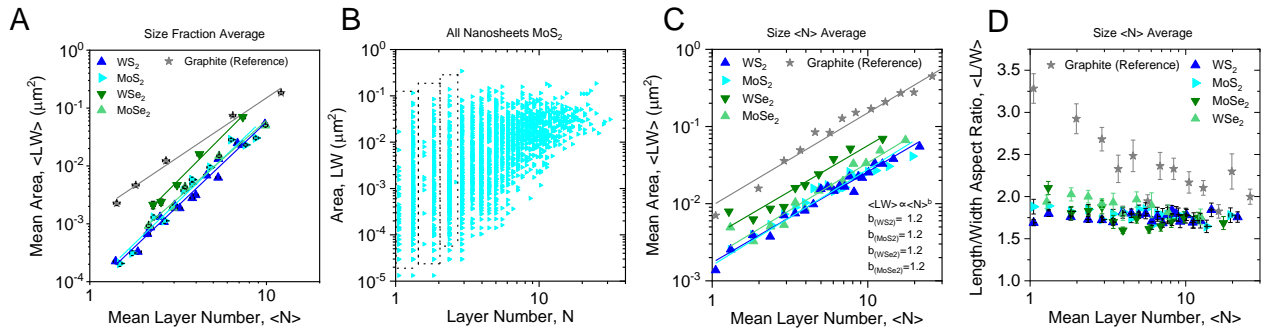


Figure 3.1-5: Accessible nanosheet dimensions for LPE group-VI TMDs. (A) Average TMD nanosheet area (*i.e.* length \times width) as function of mean layer number for fractions isolated upon size selection.⁴⁷ (B) Scatter plot of measured nanosheet area versus layer number. Nanosheets from all fractions of the size selection are combined. (C-D) TMD nanosheet area as function of mean layer number (C) and nanosheet length/width aspect ratio (D) averaged for nanosheets in a certain thickness bin. Reproduced and adapted with permission from ⁴⁷.

In summary, statistic evaluation of size-selected TMD nanosheet ensembles allows to average and quantify size-dependent properties which will be discussed in more detail in Chapter 4. However, apart from the knowledge over material size distributions isolated in different fractions of the cascade centrifugation, fundamental insights into material exfoliation and sedimentation behaviour can be derived from extensive datasets. Considering the sum of all nanosheets from different size fractions as representative for the accessible material dimensions produced by LPE, binding strength ratios and the characteristic material monolayer size can be extrapolated experimentally. This is useful as the position of the material dimensions on the $\langle N \rangle$ -averaged nanosheet area per layer number can serve as figure of merit for material exfoliability and enables a quantitative comparison to other materials as will be shown in the following.

3.2 Indium Selenide, γ -InSe

In addition to TMDs, many other 2D-materials exhibit interesting properties for a range of applications. For example, with regard to optical and optoelectronic applications, direct bandgap semiconductors are of great relevance. Examples of layered materials showing photoluminescence without the limitation to monolayers are black phosphorus (BP) and indium selenide (γ -InSe, structure in Figure 3.2-1 A). Both of these materials are semiconductors which show layer-dependent shifts of the PL emission in the NIR range of the electromagnetic spectrum due to their small, yet layer-dependent direct band gap.^{75, 124-126} A major drawback in view of the applicability of BP is that the material is highly sensitive to environmental impacts and rapidly degrades in ambient conditions.^{104, 106, 127, 128} While the mechanisms and influences of the material decomposition are well understood^{128, 129} and approaches for passivation of the degradation mechanisms are under study, either material properties are drastically influenced by means of passivation due to strong interactions with the stabiliser (*e.g.* PL quenching)^{75, 107} or the processes are not scalable (*e.g.* encapsulation with *h*-BN),¹³⁰ which limits their application potential. In contrast to BP, indium selenide shows ambient stability

Chapter 3 - Exfoliability

over weeks,¹³¹ which renders the 2D-material an interesting compound for a range of applications. However, reports on fundamental material properties are mainly focused on micromechanically cleaved γ -InSe nanosheets. In spite of the high quality of nanosheets produced by micromechanical cleavage, it is important to investigate such properties on nanosheets prepared by means of scalable exfoliation techniques, such as LPE.

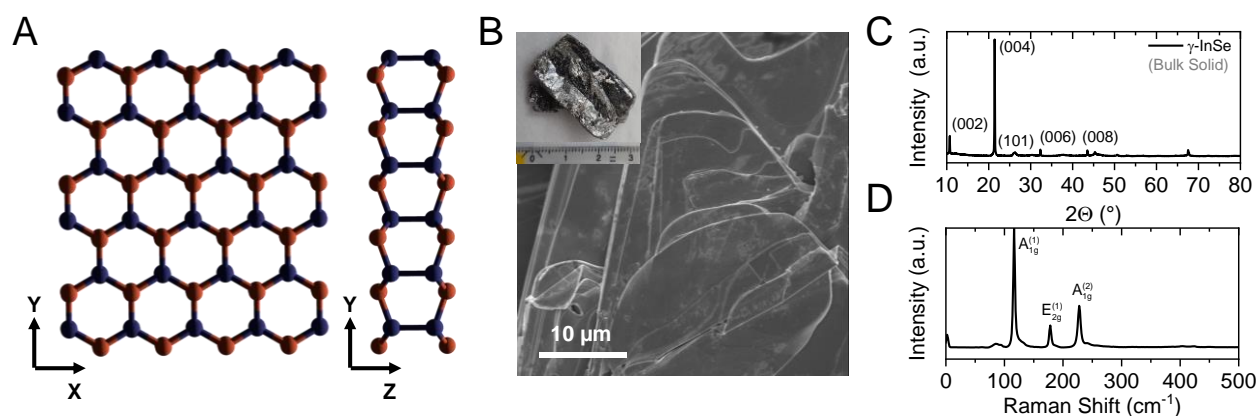


Figure 3.2-1: Character of bulk γ -InSe. (A) Schematic crystal structure of III-VI semiconductors, such as γ -InSe (blue: indium, red: selenium). (B) Low magnification SEM image of a γ -InSe crystal. The layered character of the material is clearly resolved. The inset shows a photograph of the crystal used for the experiments. (C) X-ray diffraction pattern of a γ -InSe single crystal. (D) Raman spectrum acquired for γ -InSe using an excitation wavelength of 532 nm. Reproduced and adapted with permission from ¹²².

To obtain further insights into solvent processibility of 2D-materials, and to additionally test whether the optical properties of γ -InSe are retained in sonication-assisted LPE, different sizes of γ -InSe nanosheets were prepared, following a complementary protocol as used for the TMD exfoliation described in Chapter 3.1. The bulk crystals were supplied by Zdenek Sofer (University of Chemistry and Technology, Prague). Representative SEM images, XRD pattern and Raman spectra are shown in Figure 3.2-1 B-D and confirm the structural integrity and high quality of the bulk material.

After initial aggregation problems for the exfoliation of γ -InSe in aqueous sodium cholate, the exfoliation medium was fixed to *N*-methyl-2-pyrrolidone (NMP), which solved issues with colloidal destabilisation. The resulting stock dispersion after exfoliation of the layered crystal was size-selected using LCC to reduce the polydispersity of the nanosheets. Different sizes of γ -InSe nanosheets were separated in seven consecutive centrifugation steps at 50 g, 100 g, 300 g, 700 g, 2000 g, 5000 g and 30000 g, respectively (experimental details are given in Chapter 7.2). The supernatant after each centrifugation step is used for the subsequent step, while the sediment is collected and redispersed in reduced volume of fresh solvent for analysis. Similar to the size selection applied to TMDs in the previous Chapter, the sediment obtained after the first step is discarded as it contains mostly unexfoliated material, as well as the supernatant after the last step with predominantly defective material remaining in the dispersion after centrifugation at high speeds (*i.e.* at 30000 g). Samples are labelled by the centrifugal acceleration applied between two steps, in accordance to other material systems addressed throughout this thesis and previous reports.^{47, 49, 66, 132, 133}

The size and thickness distribution of the γ -InSe nanosheet fractions resulting after the size selection were determined by statistical AFM on drop-cast material. The same setup and cantilevers have been used as in Chapter 3.1. Thus, the same corrections for the AFM length can be applied (Figure 3.1-3 A). Similar to previous reports, the apparent AFM height was converted into layer number by step height analysis. Statistical analysis of line profiles on steps and terraces of incompletely exfoliated nanosheets plotted in ascending order reveals discrete steps of 1.5 nm (Figure 3.2-2 A-B), which is thus considered as the apparent height of a monolayer of γ -InSe exfoliated in NMP. Thus, the nanosheet layer number is obtained by dividing the measured height by 1.5 nm. In addition to the arithmetic mean layer number, the volume fraction weighted average will be of interest for further correlations with spectroscopic data as discussed for TMDs in Chapter 3.1. When plotting these two representations of the layer number *versus* each other for γ -InSe dispersions (Figure 3.2-2 C), a well-defined correlation between the volume fraction weighed layer number, $\langle N \rangle_{vf}$ and the arithmetic mean layer number, $\langle N \rangle$ is observed. Importantly, the correlation widely follows the one obtained for TMDs which suggests that this scaling might be material independent and can thus be an indicator for the reliability of the overall statistical analysis. A universal fit with all data included will therefore be presented at the end of Chapter 3.

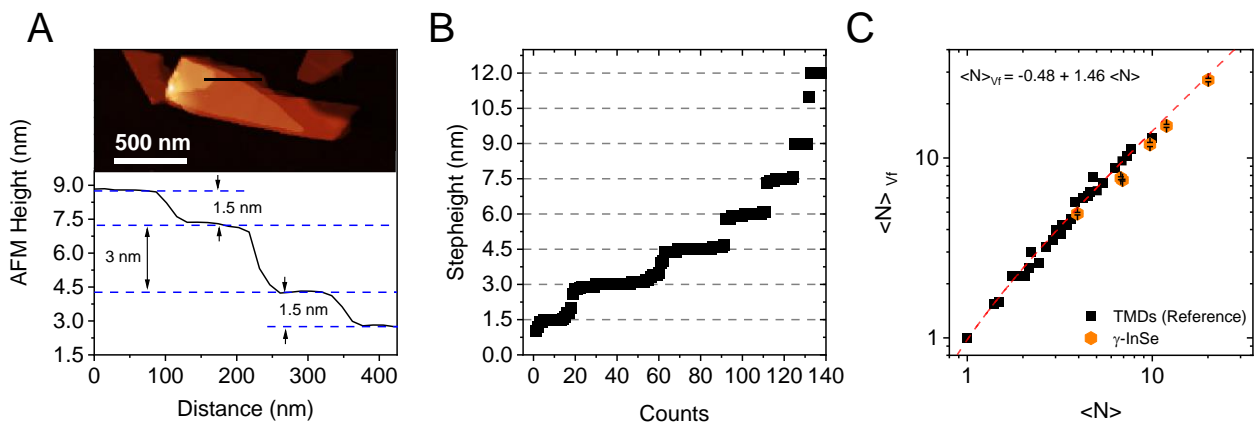


Figure 3.2-2 Corrections required for statistic evaluation of γ -InSe nanosheet dimensions. (A) Height profile of an incompletely exfoliated γ -InSe nanosheet. The black line indicates where the profile is measured. Terraces of incompletely exfoliated material are resolved and analysed to determine the apparent AFM thickness of a single layer. (B) Statistic distribution of step heights such as the ones extracted from the nanosheet in (A) plotted in ascending order. The step height is found to be a multiple of 1.5 nm, which is the apparent height of a single layer of γ -InSe and can be used to convert the measured height to the nanosheet layer number.⁷¹ (C) Correlation between volume fraction weighted layer number and arithmetic mean layer number of nanosheets. The TMD data is included for comparison.

Representative AFM images of nanosheets from a large and thick and a small and thin fraction are shown in Figure 3.2-3 A-B. The layer number and the corrected nanosheet lateral length distribution histograms of the same two fractions are shown in comparison in Figure 3.2-3 C-D, respectively. The nanosheets isolated between 5-30k g are characterised by lateral sizes ranging from 20 to 150 nm and layer numbers between 1 and 8, while the nanosheets isolated at the beginning of the cascade (0.1-0.3k g) are significantly larger (with L ranging from 100 to 750 nm) and thicker (3-35 layers).

Chapter 3 - Exfoliability

Histograms for all nanosheet sizes extracted within the size selection can be found in Appendix 3.2-1. From the distributions, the volume fraction weighted mean layer number, $\langle N \rangle_{Vf}$ and arithmetic mean nanosheet sheet length, $\langle L \rangle$ for all samples were calculated and plotted as function of the midpoint centrifugal acceleration between two consecutive centrifugation steps on a logarithmic scale in Figure 3.2-3 E-F. In both cases, a clear decrease of both observables can be seen, following a power law dependence with increasing centrifugal acceleration (linear on the logarithmic scale), as $\langle N \rangle_{Vf} \propto \overline{RCF}^{-0.37}$ and $\langle L \rangle \propto \overline{RCF}^{-0.42}$. The exponent is similar to the exponents extracted for TMDs, where $\langle N \rangle_{Vf} \propto \overline{RCF}^{-0.38}$ and $\langle L \rangle \propto \overline{RCF}^{-0.4}$. Note that an exponent of -0.5 is expected for $\langle L \rangle$ due to the relationship of $\langle L \rangle$ and the cut size which was found to be proportional to the inverse rotation rate.^{78, 134} Due to the relationship between $\langle N \rangle$ and $\langle L \rangle$ and $\langle N \rangle$ with $\langle N \rangle_{Vf}$, it is also not surprising that the scaling exponent of $\langle N \rangle_{Vf}$ with RCF is lower than that for $\langle L \rangle$. Overall, the observed data is thus widely consistent with centrifugation theory, even though the current models are relatively crude for particles with anisotropic shape, *e.g.* platelets as is the case here.^{71, 134, 135}

Monolayer contents are not quantitatively evaluated in the case of γ -InSe. This is due to multiple reasons. Firstly, in contrast to TMDs, γ -InSe exhibits a direct band gap for all layer numbers. Thus, the focus of the exfoliation was not on monolayer enrichment but on generating a better understanding on the exfoliability of new materials, as well as on the colloidal and material stability. Additional insights in this regard are given in Chapter 5 (5.2 for γ -InSe). Secondly, the required solvent choice limits both the production, as well as the isolation of monolayers. The organic solvent NMP has a factor of 1.6 higher dynamic viscosity (2.6 mPa·s at 4°C)¹³⁶ than the aqueous sodium cholate solution,¹³⁷ used for the TMD exfoliation. Note, that the sodium cholate only has a minor impact on the viscosity of the aqueous dispersion in the concentration range used for the exfoliation¹³⁸ and is thus neglected. The higher viscosity has two implications. Firstly, the absolute energy transferred to the material upon sonication should be decreased for similar exfoliation conditions in a solvent of higher viscosity.¹³⁹ Secondly, for reasons of processing time, the centrifugation time was not normalised to the viscosity (nor to the density) of the solvent. This has the effect, that the size distribution of each fraction is broader than for centrifugation of the same material in a solvent of lower viscosity. However, as aggregation of the nanomaterial was observed for exfoliation in aqueous sodium cholate, the centrifugation times were kept identical, to compare the outcome using a different solvent with similar processing times.

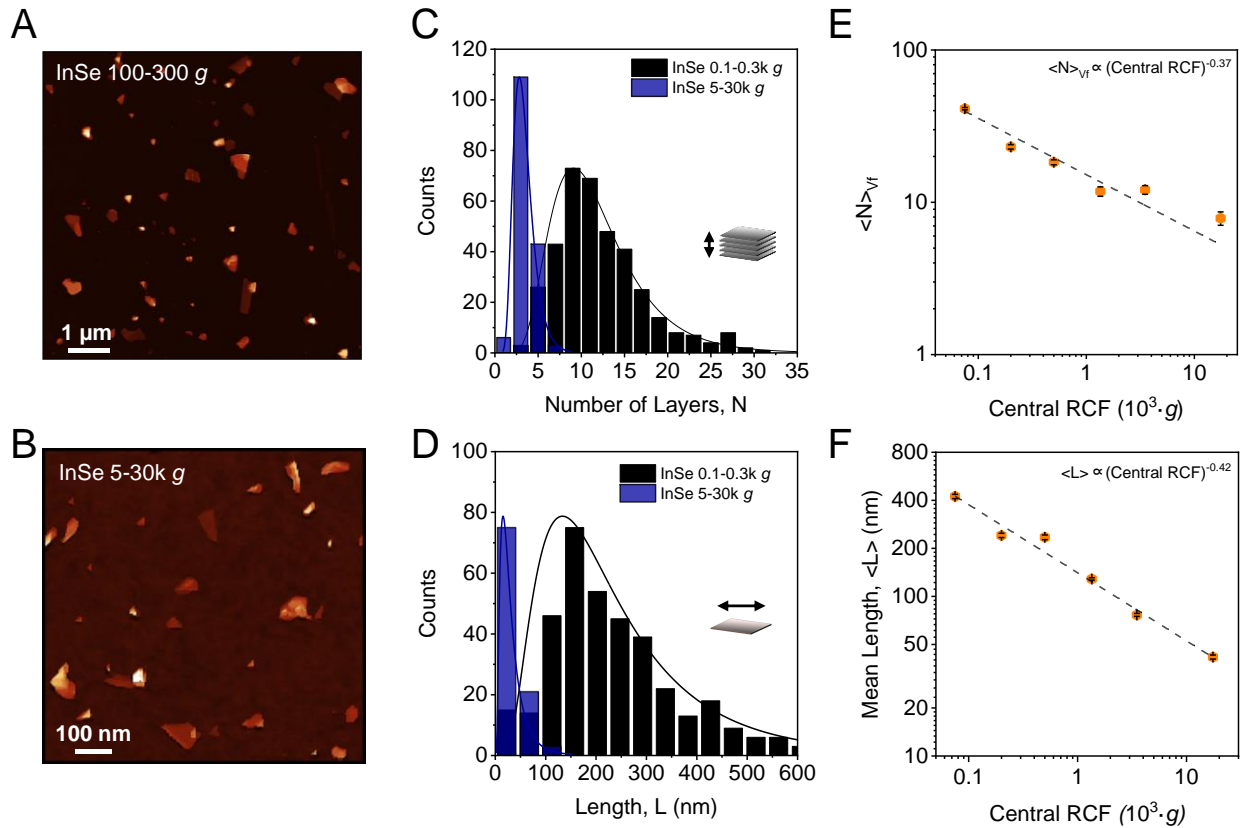


Figure 3.2-3: Statistic evaluation of γ -InSe nanosheet dimensions for different fractions of the size selection. (A-B) AFM images of drop-cast nanosheets for two fractions containing relatively large, RCF = 0.1-0.3k g (A) and small nanosheets, RCF = 5-30k g (B). (C-D) Histograms of the nanosheet layer number (C) and lateral sheet size (D) distribution for the two fractions shown in (A-B). (E) Mean volume fraction weighted layer number, $\langle N \rangle_{vf}$ of γ -InSe nanosheets across all fractions on a logarithmic scale. (F) Mean nanosheet length, $\langle L \rangle$ of the same nanosheet fractions on a logarithmic scale. Both, $\langle N \rangle_{vf}$ and $\langle L \rangle$ show a power law decrease with increasing centrifugation speed as indicated by the dashed lines. Reproduced and adapted with permission from ¹⁰.

To further evaluate the applicability of the model mentioned in Chapter 2.2.2 which suggests predetermined material dimensions of nanosheets prepared by sonication-assisted LPE depending on the in-plane to out-of-plane binding strength ratio,⁴⁷ the area of all γ -InSe nanosheets (regardless of the fraction) are plotted as a function of their layer number in a scatter plot (Figure 3.2-4 A). In order to visualise trends more clearly, the mean dimensions of nanosheet packages of at least 70 individual sheets of a similar layer number were summarised in one data point (N -average instead of fraction average). The mean area of these packages shows a power law increase with increasing layer number, as shown in Figure 3.2-4 B. Published data on graphite nanosheets exfoliated in NMP have been re-evaluated in the same way as reference (grey stars).⁴⁷ Linear fitting of the data results in exponents of $\langle LW \rangle \propto \langle N \rangle^{1.3}$ in strong analogy to graphite exfoliated using similar conditions, where $\langle LW \rangle \propto \langle N \rangle^{1.2}$. This gives a convenient possibility to approximate the characteristic mono-layer size of the material through extrapolation which is 41.4 nm in this case, *i.e.* lower than for graphene (97.2 nm) and comparable to TMDs (39.8 nm for WS₂, 41.5 nm for MoS₂, 61.1 nm for WSe₂ and 44.9 nm for MoSe₂). This is particularly useful for γ -InSe, as nanosheets are comparably

Chapter 3 - Exfoliability

thick and thus a low number of monolayers was produced so that this quantity is not directly accessible.

In the previous Chapter, it was outlined that the length/width aspect ratio might also be an interesting parameter to describe the exfoliation process. Therefore, in Figure 3.2-4 C, the scaling of the length/width aspect ratio with layer number is shown for γ -InSe in comparison to graphene. In spite of some scatter, a higher aspect ratio is observed for thin nanosheets which systematically decreases with increasing layer number and levels off for nanosheets with more than ~ 10 layers. The decrease in the thickness range below 10 layers seems to follow a linear trend (the dashed lines in Figure 3.2-4 C are a guide for the eye). This is in line with graphite, but in contrast to observations made with TMDs, where no differences of the aspect ratio with changing layer number were observed. This supports the claim, that a covalent binding strength anisotropy of different in-plane crystal directions has an impact on the lateral dimensions of the nanosheets as the sedimentation behaviour of the different materials seems to be identical. However, the data on the in-plane dimensions is not conclusive yet and requires additional experiments, including theoretic studies.

One can argue that a weakness of the comparison of the nanosheet dimensions across materials is the use of different exfoliation media. While data in NMP and aqueous surfactant is available for graphene, this might not be accessible for all materials which can potentially limit a comparative study. However, it should be pointed out that identical exponents are found for exfoliation in aqueous sodium cholate and in NMP in the case of graphene and additional data for exfoliated graphite using a different source of ultrasonic energy (*i.e.* bath sonication), is shown in Appendix 3.2-2. As all data points collapse on a master curve, all individual nanosheets from the three different datasets were combined and evaluated independent of the production methodology. The combined data again falls on the same curve as the others, resulting in a universal relation of the graphite nanosheet area to the layer number: $\langle LW \rangle \propto \langle N \rangle^{1.2}$. The independence of the material dimensions on the exfoliation conditions strongly suggests the applicability of the binding strength anisotropy model, at least for the applicable size and thickness range under study, and thus allows to use the combined data on graphite as reference for other 2D-materials exfoliated in other solvents. Furthermore, the same applies for the nanosheet length/width aspect ratio, as the different datasets on the nanosheet aspect ratio of exfoliated graphite collapse on the same curve (Appendix 3.2-2).

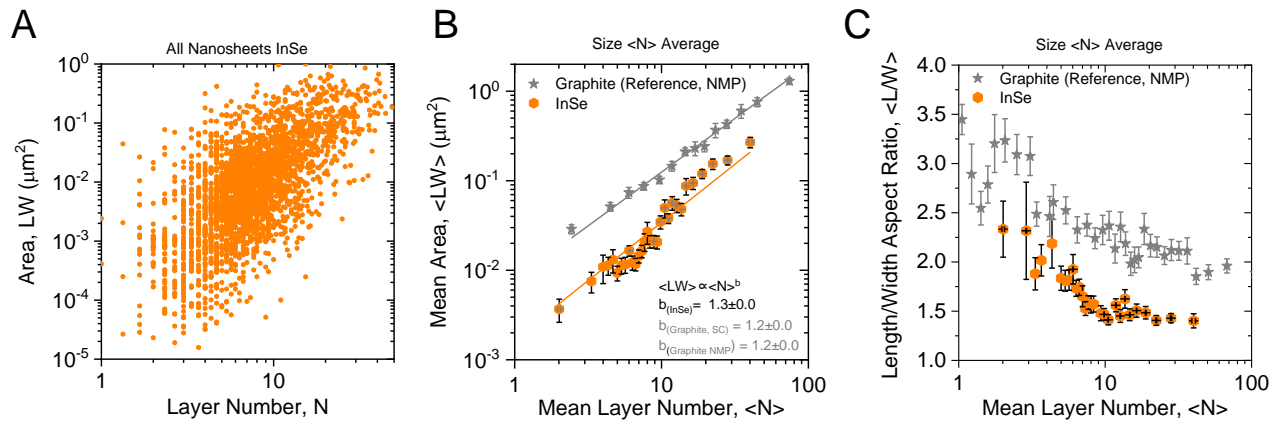


Figure 3.2-4: Accessible Nanosheet dimensions for LPE γ -InSe. (A) Scatter plot of measured γ -InSe nanosheet area versus layer number. Nanosheets from all fractions of the size selection are combined. (B-C) Mean γ -InSe nanosheet area as function of mean layer number (B) and mean nanosheet length/width aspect ratio (C) averaged for nanosheets exhibiting a similar thickness.

Overall, the exfoliation of γ -InSe gives additional insights into 2D-nanomaterial preparation and supports current assumptions made for model development and further improvement. The data produced on each new layered crystal helps understanding fundamental limits of the process and will be discussed comprehensively for all materials under study in Chapter 3.8. Size-dependent optical properties and degradation of γ -InSe will be addressed in Chapters 4.2 and 5.2.

3.3 Transition Metal Hexathiohypo Diphosphates, $\text{M}_2\text{P}_2\text{S}_6$

Another class of layered materials that received increasing attention in recent years are metal hexathiohypo diphosphates exhibiting a structure of covalently linked $\text{M}_2^{(\text{II})}\text{P}_2\text{S}_6$ units, alternatively coined MPS_3 (structure see Figure 3.3-1). Similar to most other 2D-materials, this class of materials has been known for decades already and was rediscovered together with many other van der Waals crystals. Transition metal hexathiohypo diphosphates have first been reported as $\text{Fe}^{(\text{II})}$ salt of the $\text{P}_2\text{S}_6^{4-}$ anion in 1894¹⁴⁰ and built up a large family of layered compounds which show an enormous variety of properties by the exchange of the metal atom in the honeycomb arrangement of the monoclinic C2/m crystal lattice (Figure 3.3-1 A). The layered character of $\text{M}^{(\text{II})}\text{PS}_3$ (resolved by SEM on NiPS_3 crystals in Figure 3.3-1 B) supports the possibility for Li^+ -ion storage (*i.e.* intercalation) in between individual layers, which makes them particularly interesting as cathode or electrolyte material in lithium ion accumulators.¹⁴¹ Varying the metal ions in the hexathiohypo diphosphate lattice gives rise to different physical properties and allows to tailor the band gap, and/or the magnetic response of these materials. The band gap for example can be adjusted by exchanging the metal atom ranging from insulator, to direct or indirect semiconductors.¹⁴² In addition to that, the corresponding nanomaterials were investigated for their intercalation chemistry, nonlinear optical material behavior¹⁴³ or as solid electrolytes suitable for lithium batteries.¹⁴⁴

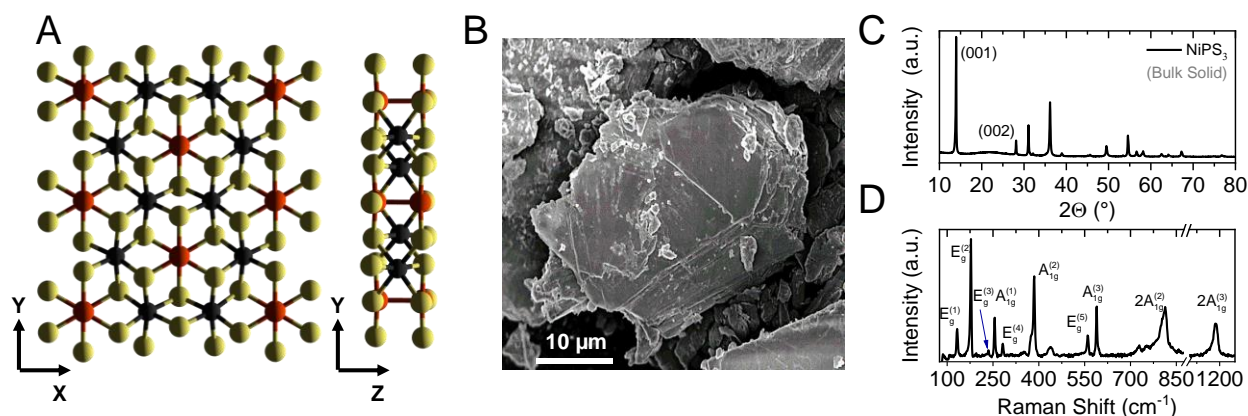


Figure 3.3-1: Character of bulk NiPS₃. (A) Schematic crystal structure of transition metal hexathiohypo diphosphates (black: transition metal, red: phosphorus, yellow: sulfur). (B) Low magnification SEM image of a NiPS₃ crystals. Images reveal crystallite sizes in range of 5-50 μm. The layered character of the material is clearly resolved. (C) X-ray diffraction pattern of powdered NiPS₃. (D) Raman spectrum acquired for NiPS₃ crystals using an excitation wavelength of 532 nm. Reproduced and adapted with permission from ^{11, 122}.

While those properties render the nanomaterial particularly interesting for energy storage, especially as the accessible intercalation yield should be increased compared to bulk crystals,^{145, 146} only little is known about the performance of exfoliated material in actual devices. To address this, crystals of different MPS₃-species were exfoliated in liquid phase. Different groups report on aqueous exfoliation of various metal hexathiohypo diphosphates.^{147, 148} However, preliminary exfoliation experiments showed that dispersions of nanosheets produced by LPE in aqueous sodium cholate with similar conditions as applied to TMDs, seem to be instable according to UV-Vis experiments, as discussed in more detail in Chapter 5.3.¹¹ In addition to obvious aggregation, AFM measurements on produced nanosheets of NiPS₃ and FePS₃ show, that the edges of the nanomaterial are jagged and the sheet surface is not planar suggesting degradation.

In order to avoid nanosheet degradation, the exfoliation of three different hexathiohypo diphosphates (NiPS₃, FePS₃ and MnPS₃) was performed by bath sonication in dried and degassed N-Cyclohexyl-2-pyrrolidone (CHP) in inert gas conditions (for experimental details see Chapter 7.1). The starting materials supplied by the group of Wolfgang Bensch (Kiel University) showed the expected features of the crystalline layered materials (as exemplarily shown by SEM, XRD and Raman on bulk NiPS₃ in Figure 3.3-1B-D) After it was shown that the resulting nanomaterial dispersion was stable and did not show any signs of degradation in preliminary AFM or UV-Vis measurements, a size selection by LCC. To validate the robustness of the exfoliation and size selection by LCC in the highly viscous solvent CHP (dynamic viscosity 11.6 mPa·s at 25°C),¹⁴⁹ two batches of the respective nanomaterial were size-selected with slightly different centrifugation speeds (termed cascade 1 and 2). The centrifugal accelerations of the first and the second centrifugation sequence were 50 g, 100 g, 400 g, 1000 g, 5000 g, 10000 g and 50000 g for cascade 1 and 600 g, 3000 g, 10000 g and 30000 g for cascade 2.

The supernatant after each centrifugation step was used for the subsequent step, while the sediment was redispersed and subjected to analysis similar to other material systems discussed within this thesis. The first sediment contains mostly unexfoliated material and the supernatant after the last step is comprised of defective material. These two fractions are thus not considered for the statistical analysis. The sample labelling is consistent with Chapter 3.1 and 3.2.

For size and thickness determination, similar corrections as discussed in Chapter 3.1 have to be taken into account. The statistic distribution of the nanosheets length and thickness in the different size fractions were quantified from statistic AFM measurements. In case of transition metal hexathiohypo diphosphates, the apparent step height of a single layer was determined to be 1.5 nm by measuring line profiles on incompletely exfoliated nanosheets (Figure 3.3-2 A-B). To account for the over-estimation of the measured height from the AFM, the layer number of nanosheets was calculated from the measured height *via* division by 1.5 nm. For later considerations of spectroscopic trends with material size (Chapter 4.3), the arithmetic mean layer number was weighted with the nanosheet volume of each sheet to correct for the increased impact of thicker structures (Figure 3.3-2 C). As observed for γ -InSe as well, a well-defined correlation between the volume fraction weighed layer number, $\langle N \rangle_{Vf}$ and the arithmetic mean layer number, $\langle N \rangle$ is observed in agreement with the data extracted from TMDs, shown as reference.

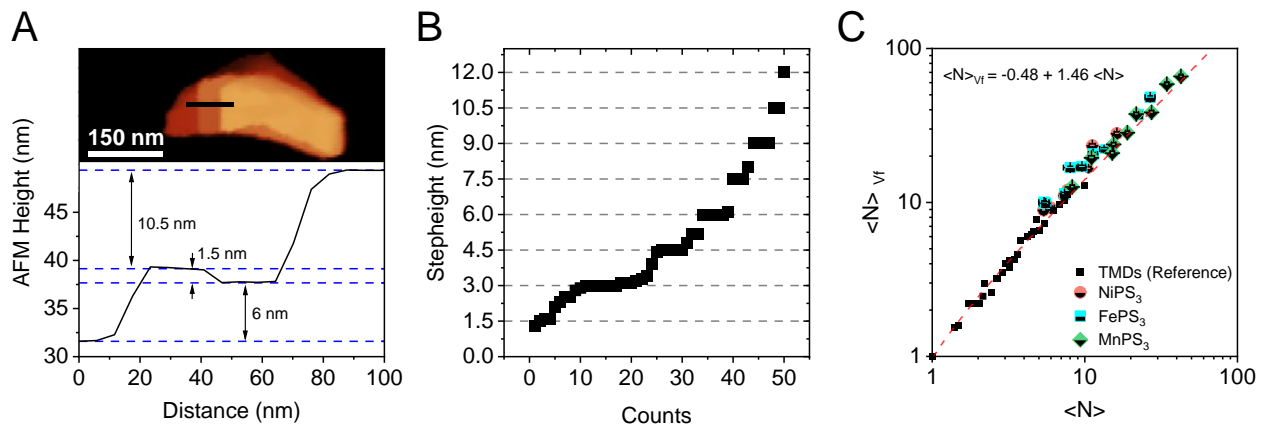


Figure 3.3-2: Corrections required for statistic evaluation of transition metal hexathiohypo diphosphate nanosheet dimensions measured by AFM. (A) Height profile of an incompletely exfoliated NiPS₃ nanosheet. The black line indicates where the profile is measured. Terraces of incompletely exfoliated material are resolved and analyzed to determine the apparent AFM thickness of a single layer. (B) Statistic distribution of step heights such as the ones extracted from the nanosheet in (A) plotted in ascending order. The step height is found to be a multiple of 1.5 nm, which is the apparent height of a single layer of NiPS₃ and can be used to convert the measured height to the nanosheet layer number.⁷¹ (C) Correlation between volume fraction weighted layer number and arithmetic mean layer number of NiPS₃, FePS₃ and MnPS₃ nanosheets. The TMD data is included for comparison. Reproduced and adapted with permission from ¹¹

Nanosheets from AFM measurements on drop-cast NiPS₃ are shown for two different fractions after the size selection (0.1-0.4k g and 10-30k g) in Figure 3.3-3 A-B. The two fractions are shown as representative for comparably large (100-400 g) and small (10-30k g) nanosheets, respec-

Chapter 3 - Exfoliability

tively. The actual size and thickness distribution of the same two fractions are shown in Figure 3.3-3 C-D (for other sizes and materials see Appendix 3.3). The nanosheets isolated between 10-30k g are characterised by lateral sizes ranging from 50 to 250 nm and layer numbers between 1 and 16, while the nanosheets isolated at the beginning of the cascade (0.1-0.4k g) are significantly larger (with L ranging from 100 nm to 1 μm) and thicker (5-55 layers). To express changes of the size and thickness distributions in the respective fractions quantitatively, the volume fraction weighted layer number and the nanosheet length are both shown as function the midpoint centrifugal acceleration between two consecutive centrifugation steps on a logarithmic scale. For all materials, a clear decrease of size and thickness is observed with increasing centrifugation speed (Figure 3.3-3 E-F). Generally, a linear trend (*i.e.* power law) with an identical slope but a different intercept is observed on both plots. Thus, linear fitting was performed for each material individually (Table 3.3-2). Interestingly, the exponents extracted from the fit are similar for the different MPS₃ species but dissimilar to the exponents describing the sedimentation behaviour of materials discussed in previous Chapters. Note that also the exponent for $\langle L \rangle$ is significantly lower than -0.5 which is expected from centrifugation theory. Such a deviation has been observed before in the case of *h*-BN in aqueous surfactant,⁷² but no explanation was given. It could be argued that the size quantification by AFM statistics can be error prone. However, as will be shown later in this thesis the MPS₃ datasets are self-consistent (also including a correlation of nanosheet sizes to spectroscopic data). In addition, the scaling of arithmetic and volume fraction-weighted $\langle N \rangle$ which was identified as quality indicator in Chapter 3.2 suggests that the deviation in the exponent is not related to inaccurate size distribution statistics. It should be noted that for the exfoliation of the different MPS₃ species, a highly viscous solvent was used, which is known to efficiently stabilise nanomaterial dispersions and simultaneously suppress material degradation: *N*-cyclohexyl-2-pyrrolidone (CHP). The solvents viscosity is significantly higher (by a factor of 13, *i.e.* 11.6 mPa·s at 25°C)¹⁴⁹ compared to aqueous solutions, which might have an impact on the resulting exponents. However, since a strong deviation from the expected exponent of -0.5 was also observed for *h*-BN in aqueous surfactant, this seems not to be a likely reason.⁷²

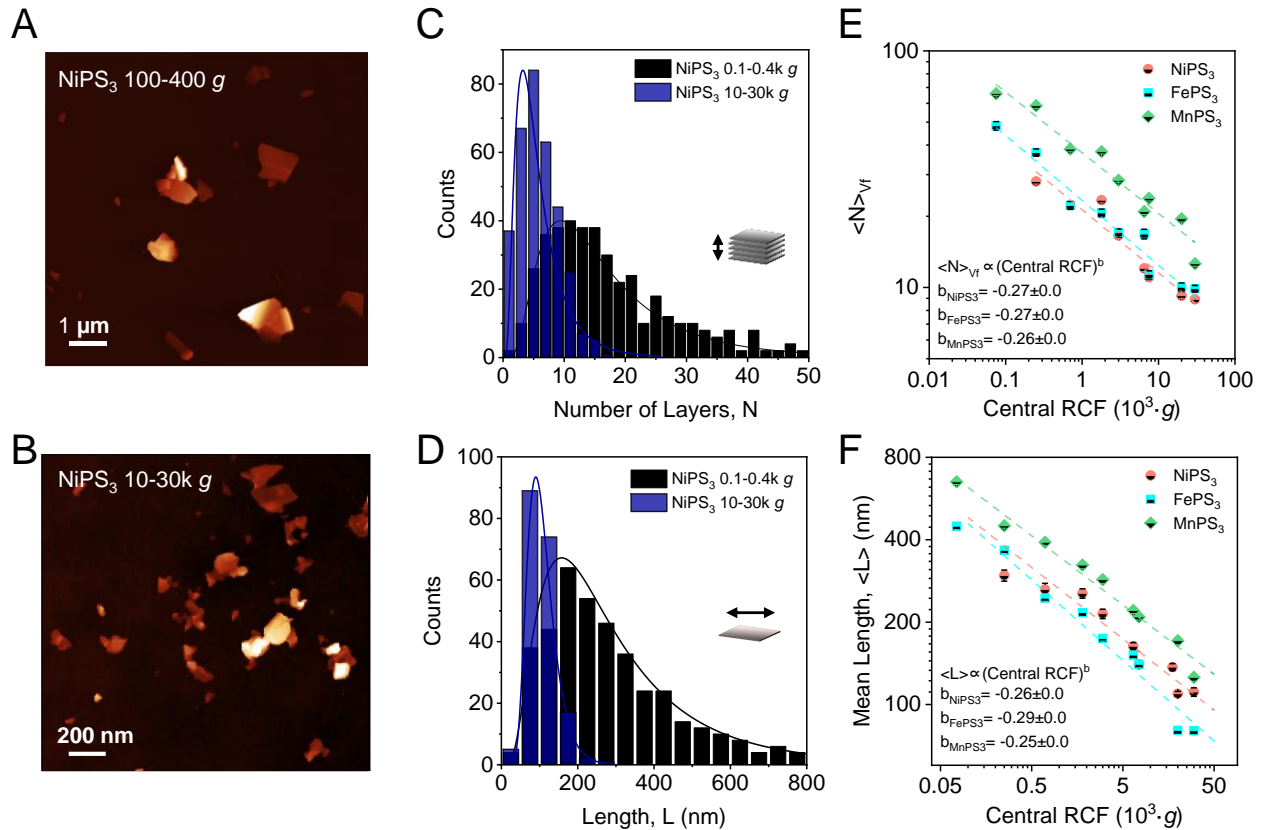


Figure 3.3-3: Statistic evaluation of MPS₃ nanosheet dimensions for different fractions of the size selection. (A-B) AFM images of drop-cast nanosheets for two fractions of NiPS₃ containing relatively large, RCF = 0.1-0.4k g (A) and small nanosheets, RCF = 10-30k g (B). (C-D) Histograms of the nanosheet layer number (C) and lateral sheet size (D) distribution for the two fractions shown in (A-B). (E) Mean volume fraction weighted layer number, $\langle N \rangle_{vf}$ of NiPS₃, FePS₃ and MnPS₃ nanosheets across all fractions on a logarithmic scale. (F) Mean nanosheet length, $\langle L \rangle$ of the same nanosheet fractions on a logarithmic scale. Both, $\langle N \rangle_{vf}$ and $\langle L \rangle$ show a power law decrease with increasing centrifugation speed as indicated by the dashed lines. Reproduced and adapted with permission from ¹¹.

Table 3.3-2: Relation between the arithmetic mean layer number and the volume fraction weighed layer number for different metal hexathiohyposphates.

NiPS ₃	$\langle N \rangle_{vf} \propto \overline{RCF}^{-0.27}$	$\langle L \rangle \propto \overline{RCF}^{-0.26}$
FePS ₃	$\langle N \rangle_{vf} \propto \overline{RCF}^{-0.27}$	$\langle L \rangle \propto \overline{RCF}^{-0.29}$
MnPS ₃	$\langle N \rangle_{vf} \propto \overline{RCF}^{-0.26}$	$\langle L \rangle \propto \overline{RCF}^{-0.25}$

Nonetheless, the high solvent viscosity will impact the outcome of exfoliation and size selection. Since the centrifugation time was kept identical with respect to aqueous systems for reasons of material sensitivity in ambient conditions (see Chapter 5), the isolated nanomaterial fractions are more polydisperse than for a size selection of the same material in aqueous dispersion. In addition, the increased viscosity has an impact on the exfoliation energy.¹³⁹ Thus, larger and thicker structures are produced than in an appropriate solvent of lower viscosity. However, as also with γ -InSe, mono-

Chapter 3 - Exfoliability

layered structures and narrow size distributions are not required for MPS_3 : while an increased effective surface area should increase the application potential of metal hexathiohypo diphosphates in energy storage applications, monolayers are not suitable for intercalation chemistry.

As discussed in Chapter 3.1, the combined dimensions of nanosheets contained in all size fractions can still be viewed as representative for the nanosheet dimensions produced in sonication-assisted LPE (Figure 3.3-4 A). While the size selection mechanism cannot fully be understood at the current stage, the statistical AFM data is extremely valuable, as it gives fundamental limitations of the available nanosheet sizes using LPE in combination with LCC and allows to quantitatively assess the exfoliability of the material systems. For a quantitative analysis, the arithmetic mean nanosheet area of sheets with a similar layer number are shown as function of their layer number in Figure 3.3-4 B. In agreement with the model described in Chapter 2.2.2,⁴⁷ a power law dependence of the area with the sheet thickness is observed. Furthermore, the datapoints of all three materials collapse on the same curve, resulting in a universal exponent for the three different hexathiohypo diphosphates under study: $\langle LW \rangle \propto \langle N \rangle^{1.3}$, which is almost identical to the exponents extracted for graphene, TMDs and $\gamma\text{-InSe}$. Extrapolation of the data yields a characteristic monolayer length of 38.6 nm which is slightly smaller than for TMDs and $\gamma\text{-InSe}$. To check for changes of the lateral material dimensions (*i.e.* the length/width aspect ratio) with layer number, the mean aspect ratio is plotted as function of layer number in Figure 3.3-4 C. Similar to observations made for TMDs, the aspect ratio remains constant for all layer numbers. Assuming that the model holds for changing binding strengths along different directions of the 2D-plane, this would suggest that the covalent binding strength in the 2D-plane is isotropic for TMDs and for MPS_3 -species. However, this explanation will require additional experimental evidence for verification.

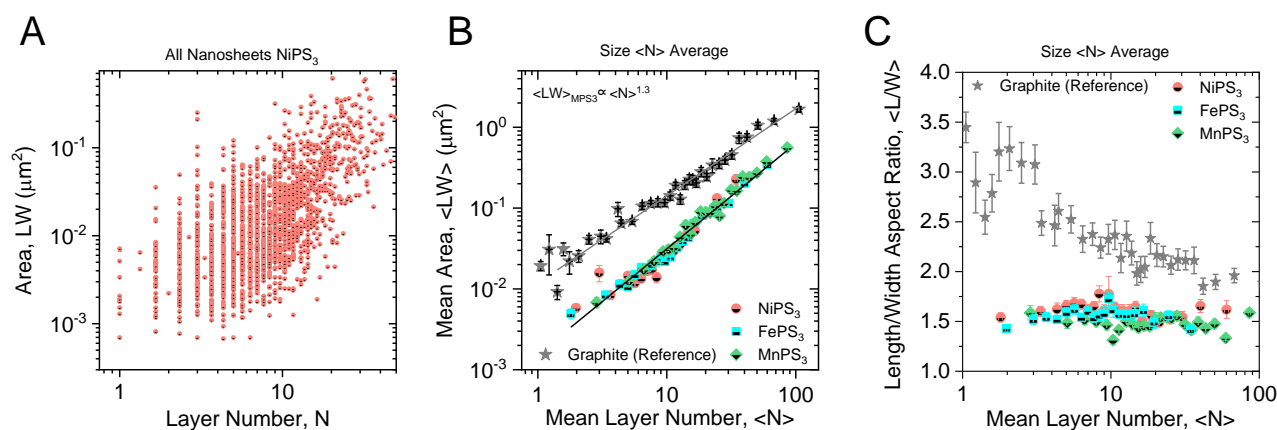


Figure 3.3-4: Accessible nanosheet dimensions for different LPE MPS_3 species. (A) Scatter plot of measured NiPS_3 nanosheet area *versus* layer number. Nanosheets from all fractions of the size selection are combined. (B-C) MPS_3 nanosheet area as function of mean layer number (B) and nanosheet length/width aspect ratio (C) averaged for nanosheets exhibiting a similar thickness in comparison to the combined graphite data (from different exfoliation runs in aqueous surfactant and NMP).

The data collected for different transition metal hexathiohypo diphosphates provides additional insights into material exfoliability. The robustness of the exfoliation and size selection in a

highly viscous solvent was confirmed by combination of two individual datasets using different centrifugation conditions. The datapoints of both centrifugation cascades show complementary results for the average population of material dimensions. Changes of material dimensions with centrifugal acceleration qualitatively represent trends observed for other materials but show different exponents. The reason for this remains elusive, but might be related to material and colloidal stability in different solvents, which is discussed in more detail in Chapter 5.3.

3.4 Ruthenium Chloride, α -RuCl₃

The emergence of 2D-materials has started a hunt for new exfoliable materials with novel properties arising due to confinement. However, this is not strictly limited to mechanic or electronic considerations. In view of exotic magnetic transitions in the 2D-plane, potentially emerging upon exfoliation due to reduced interference with out-of-plane magnetic ordering, α -RuCl₃ renders a promising candidate for applications in quantum computing (structure see Figure 3.4-1 A). The material exfoliation in the liquid phase was first presented in 2016.¹⁰² In this approach, lithium ion intercalation was used to decrease the interlayer attraction to ease the exfoliation. However, electron transfer processes and thus changes of the material characteristics cannot be avoided using this method. To date, no charge-balanced exfoliation of the exotic magnet was reported in the liquid phase.

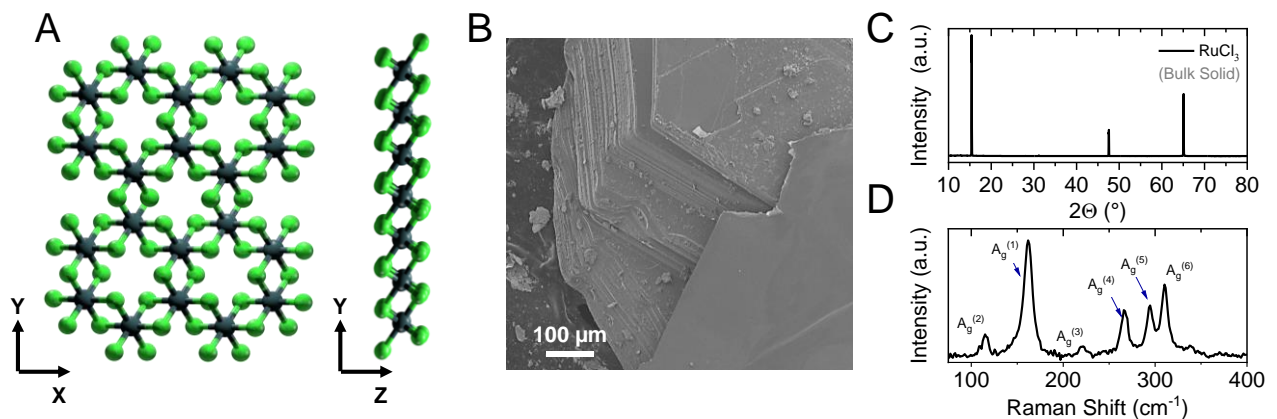


Figure 3.4-1: Character of bulk α -RuCl₃. (A) Schematic crystal structure of α -RuCl₃ (dark green: ruthenium, green: chlorine). (B) Low magnification SEM image of a α -RuCl₃ crystal. Images reveal crystallite sizes in range of several 100's of μm . The layered character of the material is clearly resolved. (C) X-ray diffraction pattern of powdered α -RuCl₃. (D) Raman spectrum acquired for α -RuCl₃ crystals using an excitation wavelength of 532 nm. Reproduced and adapted with permission from ¹²².

To address the exfoliability and stability of the exotic layered antiferromagnet in aqueous surfactant dispersions, ground α -RuCl₃ was first subjected to tip sonication in aqueous sodium cholate. The bulk material was supplied by the group of Bettina Lotsch (MPI Stuttgart) and was found to show the expected layered character (SEM, Figure 3.4-1B) and crystallinity (XRD and Raman, Fig-

Chapter 3 - Exfoliability

ure 3.4-1 C-D). Since significant aggregation and material decomposition was observed in the aqueous medium, the exfoliation protocol was adjusted to exfoliation under inert gas conditions in dried and degassed CHP, using similar conditions as for the exfoliation of metal hexathiohypo diphosphates (for experimental details see Chapter 7.1). The as obtained dispersion of nanosheets was size-selected using established cascade centrifugation protocols as described in previous Chapters of this thesis and elsewhere.^{10, 71, 132} The centrifugation speeds applied for size selection of α -RuCl₃ were 100 g, 400 g, 1000 g, 3000 g, 6000 g, 12000 g, 22000 g and 50000 g, respectively. In agreement with other material systems, the sediment of the first centrifugation step and the supernatant after the last step contain mostly unexfoliated and defective material, respectively. Consequently, both fractions were not subjected to analysis. The sample labelling represents the centrifugation conditions in which a sample was prepared, consistent with other materials addressed within this thesis and with previous reports.^{10, 71, 132} In agreement to other material systems, size and thickness corrections for the AFM measurements have to be applied to address the material dimensions accurately. For the lateral sizes, the corrections presented in Chapter 3.1 can be applied. To address the overestimation of the AFM thickness, originating from solvent contributions and measurement parameters, step height analysis has to be performed for each material and solvent combination, respectively. To do this, line profiles on incompletely exfoliated nanosheets are measured (Figure 3.4-2 A). Step heights are shown in ascending order to estimate the apparent thickness of a monolayer (Figure 3.4-2 B), which is 1.5 nm in case of α -RuCl₃ exfoliated in CHP. Thus, the apparent AFM height is divided by 1.5 nm to convert the measured height of nanosheets into their layer number. As for other materials discussed above, the correlation between arithmetic and volume fraction-weighted mean layer number can serve as quality indicator for the statistical evaluation. The scaling between the two quantities shown in Figure 3.4-2 C is similar to the TMDs thus further confirming that this is a universal scaling.

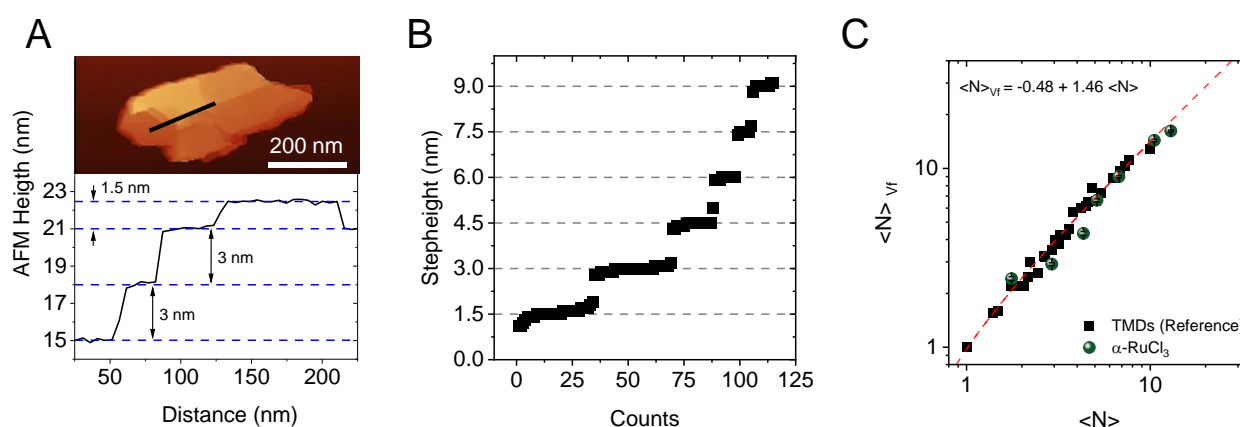


Figure 3.4-2: Corrections required for statistic evaluation of α -RuCl₃ nanosheet dimensions. (A) Height profile of an incompletely exfoliated α -RuCl₃ nanosheet. The black line indicates where the profile is measured. Terraces of incompletely exfoliated material are resolved and analysed to determine the apparent AFM thickness of a single layer. (B) Statistic distribution of step heights such as the ones extracted from the nanosheet in (A) plotted in ascending order. The step height is found to be a multiple of 1.5 nm, which is the apparent height of a single layer of α -RuCl₃ and can be used to convert the measured height to the nanosheet layer number.⁷¹ (C) Correlation between volume fraction weighted layer number and arithmetic mean layer number of α -RuCl₃ nanosheets in comparison to TMDs.

AFM images of representative nanosheets from a fraction containing comparably large (100-400 g) and small (22-50k g) are shown in comparison (Figure 3.4-3 A-B). Corresponding size and thickness distributions of nanosheets from the same two fractions are shown in Figure 3.4-3 C-D (the complete dataset is shown in Appendix 3.4-1). Changes of the arithmetic mean material dimensions are displayed as function of the midpoint centrifugal acceleration between two consecutive centrifugation steps in Figure 3.4-3 E-F. As expected, a systematic change of $\langle N \rangle_{Vf}$ and $\langle L \rangle$ is observed with the centrifugation speed, following a power law dependence in both cases. This provides a quantitative relation for both observables with centrifugation parameters: $\langle N \rangle_{Vf} \propto \overline{RCF}^{-0.42}$ and $\langle L \rangle \propto \overline{RCF}^{-0.31}$. While similar conditions for the exfoliation and size selection were chosen as used for the metal hexathiohypo diphosphates, different exponents are observed, which suggests additional influences on the material sedimentation velocity beyond the current understanding of centrifugation theory.^{71, 135} However, as fractions of different centrifugation conditions are discussed, an experimental error (*e.g.* non-uniform decanting in the glovebox for different centrifugation steps) cannot be excluded even though this is not expected to have an impact on the scaling of the exponents with RCF . Nonetheless, it is possible that defined exponents for material systems handled in inert gas conditions might be difficult to compare due to additional processing steps, which are a potential source of experimental errors (*e.g.* shaking of centrifuged samples when passing through the glovebox antechamber).

Chapter 3 - Exfoliability

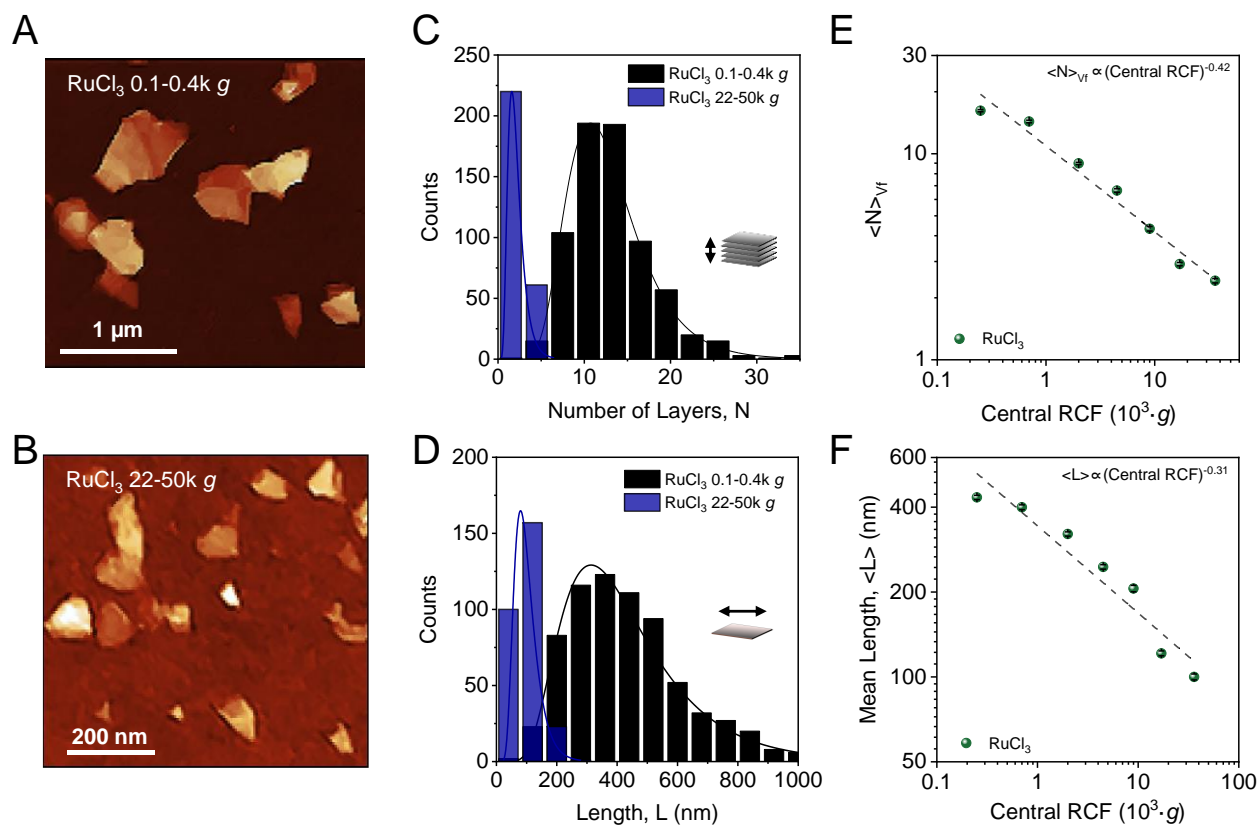


Figure 3.4-3: Statistic evaluation of α -RuCl₃ nanosheet dimensions for different fractions of the size selection.

(A-B) AFM images of drop-cast nanosheets for two fractions containing relatively large, RCF = 0.1-0.4k g (A) and small nanosheets, RCF = 22-50k g (B). (C-D) Histograms of the nanosheet layer number (C) and lateral sheet size (D) distribution for the two fractions shown in (A-B). (E) Mean volume fraction weighted layer number, $\langle N \rangle_{Vf}$ of α -RuCl₃ nanosheets across all fractions on a logarithmic scale. (F) Mean nanosheet length, $\langle L \rangle$ of the same nanosheet fractions on a logarithmic scale. Both, $\langle N \rangle_{Vf}$ and $\langle L \rangle$ show a power law decrease with increasing centrifugation speed as indicated by the dashed lines.

In contrast to the fraction-averaged data, the combined data of all nanosheet sizes and thicknesses (Figure 3.4-4 A) produced by LPE does not contain errors from varying experimental practice. For analysis, nanosheets dimensions of similar thickness are averaged and changes of the nanosheet area are followed as function of the sheet thickness (Figure 3.4-4 B). This results in a linear trend on the double logarithmic scale (*i.e.* power law), as observed for all other material systems under study. In case of α -RuCl₃, the nanosheet dimensions are of similar size at a given thickness as for graphite nanosheets, which is the current figure of merit for material exfoliability. The nanosheet sizes produced for α -RuCl₃ in CHP follow a power law behaviour as function of their thickness with an exponent of 1.3 ($\langle LW \rangle \propto \langle N \rangle^{1.3}$). This is in perfect agreement with observations made for other material systems and supports the energy equipartition hypothesis as described in Chapter 2.2.2. The extrapolated characteristic monolayer length is 77.3 nm, which is larger than for TMDs, InSe or MPS₃. The nanosheet aspect ratio shows no trend with material thickness (Figure 3.4-4 C). Similar observations have been made for exfoliated TMDs and MPS₃ species. While different trends have been observed for graphite and γ -InSe, no clear conclusion can be drawn without additional experimental evidence.

However, the results do not disagree with an in-plane binding strength anisotropy being responsible for these observations.

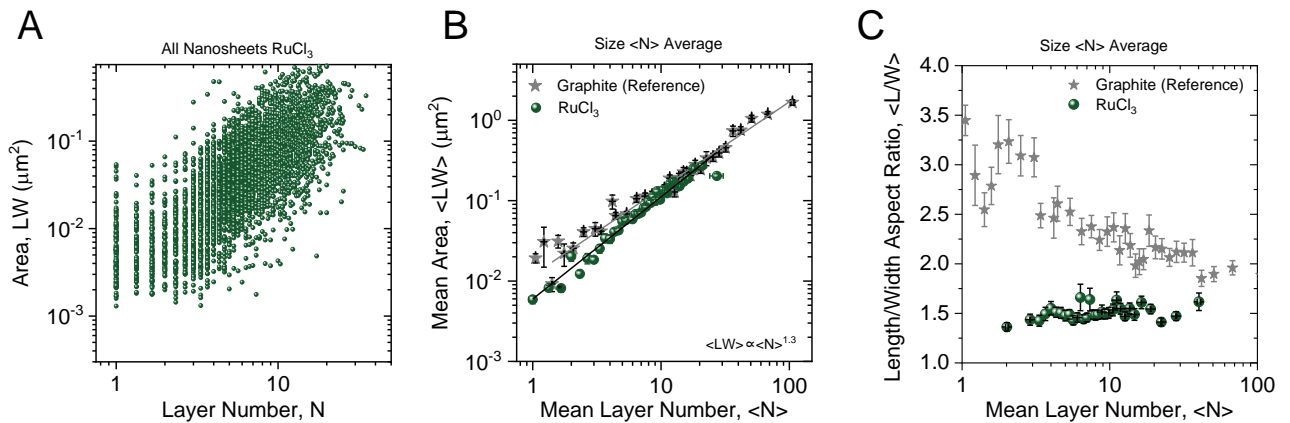


Figure 3.4-4: Accessible nanosheet dimensions for LPE α -RuCl₃. (A) Scatter plot of measured α -RuCl₃ nanosheet area *versus* layer number. Nanosheets from all fractions of the size selection are combined. (B-C) α -RuCl₃ nanosheet area as function of mean layer number (B) and nanosheet length/width aspect ratio (C) averaged for nanosheets exhibiting a similar thickness in comparison to the combined graphite data from various exfoliation runs.

Observations made for inert gas exfoliated α -RuCl₃ in CHP fit to trends obtained for other 2D-materials. While a power law dependence is observed as scaling behaviour of dimensions with centrifugal acceleration, fitting results in dissimilar exponents. The deviations for α -RuCl₃ compared to other materials might have an origin in the processing methodology. However, experimental proof is difficult as sensitivity of the material system to ambient conditions was found in the form of colloidal and nanomaterial instability when exposed to oxygen and water. While this limits the potential of the nanomaterial in applications, it is an important assessment which will be discussed more quantitative in Chapter 5.4. Overall, α -RuCl₃ shows a higher area/thickness aspect ratio than TMDs, or other semiconductors investigated in the framework of this thesis with an exfoliability comparable to graphite.

3.5 Chromium Telluride, CrTe₃

In recent years, magnetic 2D-materials gained increasing attention. While theoretic predictions help to identify interesting materials, synthesis and exfoliation of such material systems are extremely challenging for some of these compounds. A layered antiferromagnet, CrTe₃ was first reported in 1979 (structure see Figure 3.5-1A).¹⁵⁰ Theoretic considerations predict the material to be interesting for studies on magnetic ordering in low-dimensional structures.¹⁵¹ However, only little is known about the characteristics of the nanomaterials due to experimental challenges associated with phase pure synthesis and poor material stability. To this end, CrTe₃ was subjected to LPE and size selection. The bulk material (supplied by the group of Wolfgang Bensch, Kiel University) shows the characteristic layered structure, albeit with relatively small crystals (SEM Figure 3.5-1B) and the expected XRD pattern (Figure 3.5-1C). The Raman spectrum (532 nm excitation) is shown in Figure 3.5-1D.

Chapter 3 - Exfoliability

Note that the Raman spectra of CrTe_3 have not been investigated in detail in literature to date so that the modes cannot be assigned.

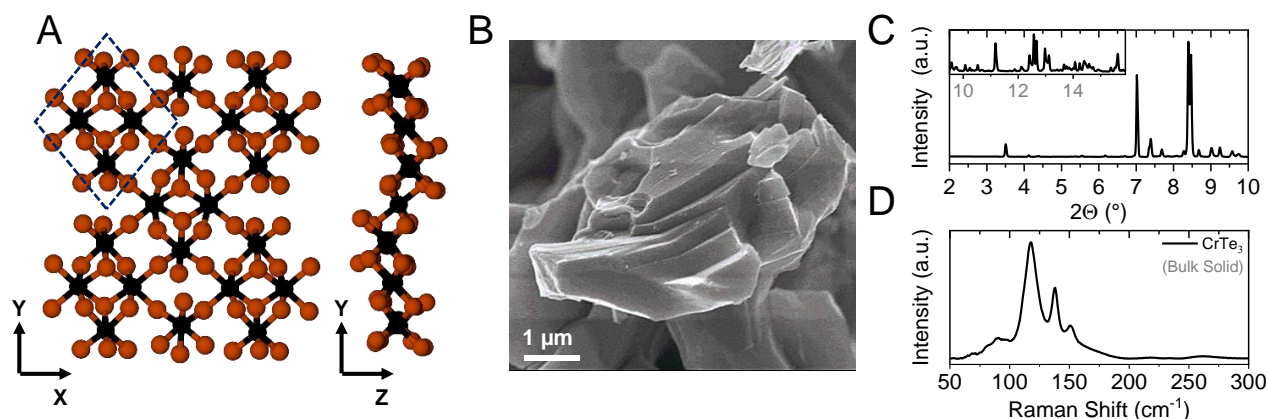


Figure 3.5-1: Character of bulk CrTe_3 . (A) Schematic crystal structure of CrTe_3 (black: chromium, red: tellurium). (B) Low magnification SEM image of a CrTe_3 crystal. Images reveal crystallite sizes in range of 5-10 μm . The layered character of the material is resolved. (C) X-ray diffraction pattern of powdered CrTe_3 . (D) Raman spectrum acquired for CrTe_3 powder using an excitation wavelength of 532 nm. Raman modes of the structure are not reported in literature as yet. Reproduced and adapted with permission from ¹²².

To test the exfoliability of CrTe_3 , LPE was first performed by tip sonication, using aqueous sodium cholate as stabiliser. Similar to observations made for NiPS_3 and for RuCl_3 , strong aggregation and material decomposition can be noticed in preliminary AFM measurements. Thus, the exfoliation was performed in inert gas conditions, using CHP as medium (for experimental details see Chapter 7.1). The resulting dispersion was size-selected by cascade centrifugation,^{10, 71, 132} using similar conditions as applied to other materials prone to ambient conditions. The respective steps for the size selection of CrTe_3 were 100 g, 400 g, 1000 g, 5000 g, 10000 g and 30000 g. In consistence with size selection performed for other material systems, the supernatant after each step is taken for the subsequent step and the respective sediment is redispersed in fresh solvent and subjected to analysis. As the first sediment and the last supernatant typically contain predominantly unexfoliated and defective material, respectively, these two fractions were discarded. Isolated fractions of different size are labelled by the centrifugation speed applied between two consecutive centrifugation steps to enable comparison to other materials, isolated at different centrifugal accelerations. For nanomaterial size and thickness determination, statistic AFM measurements have been performed, applying corrections for tip broadening and pixilation effects for lateral material dimensions and height corrections as suggested by step height analysis on incompletely exfoliated nanosheets (Figure 3.5-2 A). Thus, to convert the apparent AFM height of a nanosheet into layer number, the measured height is divided by 1.9 nm (Figure 3.5-2 B). In addition, similar to other materials discussed in previous Chapters, the correlation between arithmetic and volume fraction-weighted mean layer number can be used as measure for the quality of the statistical evaluation. The scaling between the two quantities shown in Figure 3.5-2 C is similar to TMDs which are shown as reference, thus further confirming that this is indeed a universal scaling.

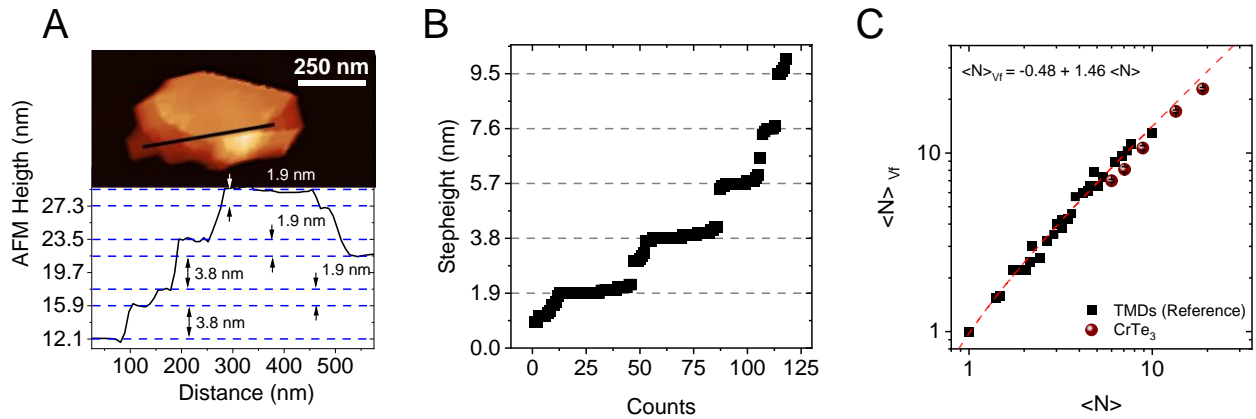


Figure 3.5-2: Corrections required for statistic evaluation of CrTe₃ nanosheet dimensions. (A) Height profile of an incompletely exfoliated CrTe₃ nanosheet. The black line indicates where the profile is measured. Terraces of incompletely exfoliated material are resolved and analysed to determine the apparent AFM thickness of a single layer. (B) Statistic distribution of step heights such as the ones extracted from the nanosheet in (A) plotted in ascending order. The step height is found to be a multiple of 1.9 nm, which is the apparent height of a single layer of CrTe₃ and can be used to convert the measured height to the nanosheet layer number.⁷¹ (C) Correlation between volume fraction weighed layer number and arithmetic mean layer number of CrTe₃ nanosheets.

For accurate assessment of the nanosheet dimensions of each fraction, more than 300 nanosheets have been counted for each centrifugation step. Representative nanosheets of the largest (0.1-0.4k g) and the smallest isolated size fraction (10-30k g) are shown in Figure 3.5-3 A-B. Histograms of the corresponding nanosheet thickness and lateral size distribution are shown in Figure 3.5-3 C-D (the complete dataset is shown in Appendix 3.5-1). To visualise trends of the material dimensions with centrifugal acceleration quantitatively, the mean volume fraction weighted nanosheet thickness and the arithmetic mean nanosheet length of each size are extracted from the different size distributions. Plots of both parameters are shown on a double logarithmic scale as function of the midpoint of the centrifugal acceleration applied between two consecutive centrifugation steps (Figure 3.5-3 E-F). As with other materials, the typical power law dependence is observed, which suggests a quantitative relation of the two quantities as $\langle N \rangle_{Vf} \propto \overline{RCF}^{-0.28}$ and $\langle L \rangle \propto \overline{RCF}^{-0.35}$. In case of CrTe₃, the exponent extracted for $\langle N \rangle_{Vf}$ is closely related to the ones observed for the different MPS₃ species, exfoliated and size-selected in similar conditions. However, the exponent for $\langle L \rangle$ is slightly increased in comparison. While the same argumentation as for RuCl₃ holds for CrTe₃ as well, the origin of these variations is yet unclear and need additional experimental evidence. The exact quantitative relation between the exponents and the forces exerting upon centrifugation is not understood to date and additional data on different material systems and solvents might provide additional insights in this regard. However, it is important to note, that the materials with lower exponents of the $\langle L \rangle$ vs. RCF scaling than the expected -0.5 are sensitive to ambient conditions (with the exception of *h*-BN described in literature).⁷² A distinct sedimentation velocity is expected if the material surface potentially decomposes in presence of oxygen or water due to changes of the solvation shell and thus the buoyant density. If this process occurs during the centrifugation, the exponent would also be affected. Furthermore, more complex considerations have to be made if material

Chapter 3 - Exfoliability

edges and basal planes show a different chemical reactivity. In addition, aggregation during centrifugation would also affect the scaling exponent.

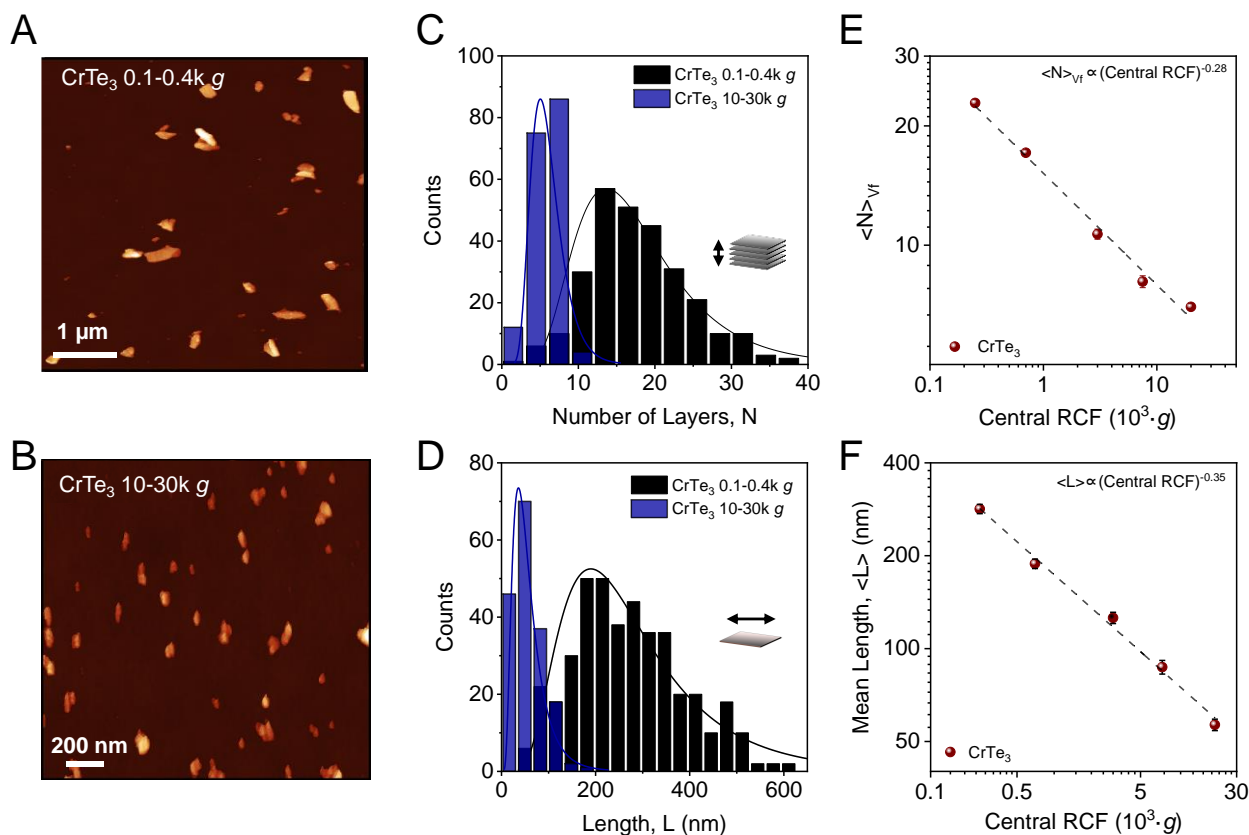


Figure 3.5-3: Statistic evaluation of CrTe₃ nanosheet dimensions for different fractions of the size selection. (A-B) AFM images of drop-cast nanosheets for two fractions containing relatively large, RCF = 0.1-0.4k g (A) and small nanosheets, RCF = 10-30k g (B). (C-D) Histograms of the nanosheet layer number (C) and lateral sheet size (D) distribution for the two fractions shown in (A-B). (E) Mean volume fraction weighted layer number, $\langle N \rangle_{vf}$ of CrTe₃ nanosheets across all fractions on a logarithmic scale. (F) Mean nanosheet length, $\langle L \rangle$ of the same nanosheet fractions on a logarithmic scale. Both, $\langle N \rangle_{vf}$ and $\langle L \rangle$ show a power law decrease with increasing centrifugation speed as indicated by the dashed lines.

In contrast to fraction-averaged material dimensions which are dependent on the sedimentation behaviour, the overall population of sizes and thicknesses measured in all material fractions can be regarded as representative for the accessible size and thickness range of CrTe₃ produced by sonication-assisted LPE. As discussed throughout this Chapter, this gives a measure of the material exfoliability. To this end, the area of all individual nanosheets is shown as function of their thickness in a scatterplot (Figure 3.5-4 A). To quantify the trends, the material dimensions of nanosheet packages exhibiting similar thickness are averaged and plotted as function of layer number (Figure 3.5-4 B). Consistent with other materials discussed, the average dimensions follow a power law dependence for decreasing layer number with the nanosheet area: $\langle LW \rangle \propto \langle N \rangle^{1.3}$. Note, that the exponents are identical for all other material systems but show a different intercept, which will be discussed in more detail in Chapter 3.8. Extrapolation allows to determine the characteristic monolayer size of CrTe₃, which is 28.4 nm. In addition to the nanosheet area, the length/width aspect ratio is shown as function

of the layer number (Figure 3.5-4 C). Similar to TMDs, MPS_3 and RuCl_3 , no obvious change in the aspect ratio is observed.

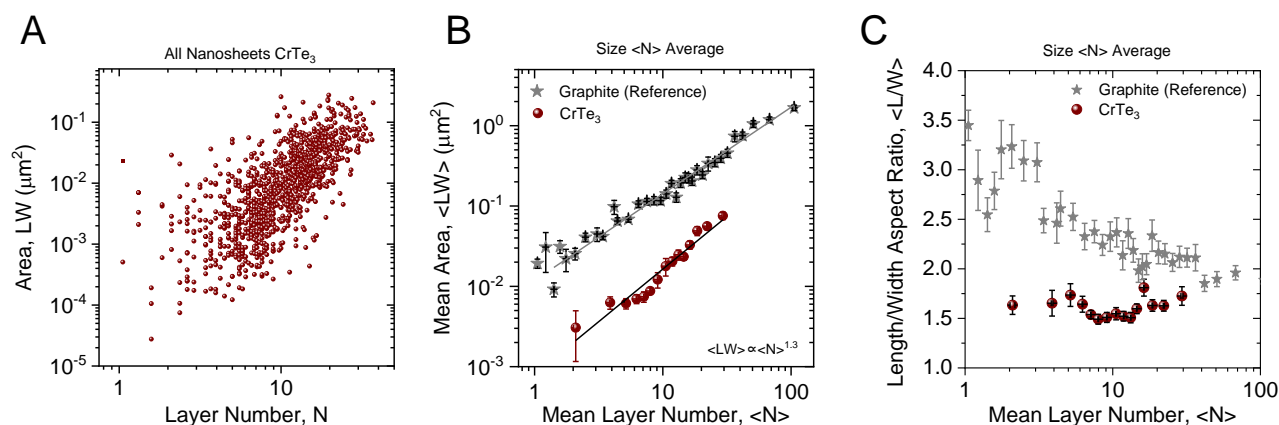


Figure 3.5-4: Accessible nanosheet dimensions for LPE CrTe₃. (A) Scatter plot of measured CrTe₃ nanosheet area *versus* layer number. Nanosheets from all fractions of the size selection are combined. (B-C) CrTe₃ nanosheet area as function of mean layer number (B) and nanosheet length/width aspect ratio (C) averaged for nanosheets exhibiting a similar thickness compared to the graphite reference.

Successful exfoliation of CrTe₃ can be achieved in dry solvent in inert gas conditions. The results shown required tremendous experimental effort as the material aggregates in all solvent systems tested as yet. Stabilisation of the colloidal dispersion was achieved in a highly viscous solvent, CHP, which does not stop, but slow down the aggregation sufficiently to enable size selection and characterisation. To refresh the nanomaterial solvation, brief sonication can be applied to the aggregated material. A more detailed discussion on the stability of CrTe₃ is given in Chapter 5.5. For material characterisation, processing steps were performed without interruptions to pursue changes of pristine nanomaterial properties over time.

3.6 Organic Sheet Stacks, Exfoliation of 2D-Polymers

Recent advances in the synthesis of organic van der Waals structures allow the selective growth of new materials with the possibility of tailoring the material properties to the desired application. The synthetic procedures, usually performed under mild conditions, allows to introduce all kinds of chemical functionalities through the rich organic synthesis. While different growth mechanisms for these synthetic, purely organic materials are reported, a general classification into two different groups can be made: 2D-polymers (2D-Pol) and 2D-covalent organic frameworks (2D-COFs). The former, per definition, has to be constituted of covalent bonds to yield a material of single-crystalline nature with topological planarity and additionally has to be no thicker than a molecular repeat unit (or at least cleavable into such a “monolayer”) to be classified as 2D-polymer.¹⁵² Not all organic 2D-materials fulfil these five criteria. In particular, 2D-COFs are typically polycrystalline due to their synthesis conditions relying on reversible bond formation.¹⁵³ In general, the synthesis of such systems

Chapter 3 - Exfoliability

underlies certain limitations to implement genuine polymerisation in strictly two dimensions: the monomer has to be at least trifunctional and should be shape-persistent upon polymerisation. Additionally, minimal mass transport can enhance the long-range order of such systems.

Schlüter *et al.* have reported on the photochemical synthesis of different 2D-polymers, meeting all these criteria. In their approach, a covalent 2D-network is formed upon photochemical cycloaddition of a preorganised single crystal of an appropriate monomer. The conversion is schematically shown in Figure 3.6-1 A. Possible monomer structures, that have successfully been transformed into a 2D-polymer are shown in Figure 3.6-1 B-C. In both systems, the polymerisation occurs, forming a 2D-polymer single crystal from a single crystal of preorganised monomers without mass transport and minimal structural distortion. However, in the case of the first 2D-polymer (2D-Pol (1), prepared by Kory *et al.*), not all monomers undergo the cycloaddition reaction. Within each layer of the crystal, one out of three monomer molecules serve as template (Figure 3.6-1 B, depicted in red), which is not included in the covalent network. This gives rise to a porous hexagonal lattice (Figure 3.6-1 B, depicted in green). In a different example, a similar porous hexagonal structure could be realised starting from a single crystalline monomer, providing full conversion of all monomers into a covalent polymer lattice. To achieve this, a styryl pyrylium heterostilben was used, which crystallises in preferential orientation of the monomers due to the steric hindrance of the *tert*-butyl moieties, as indicated in Figure 3.6-1 C.

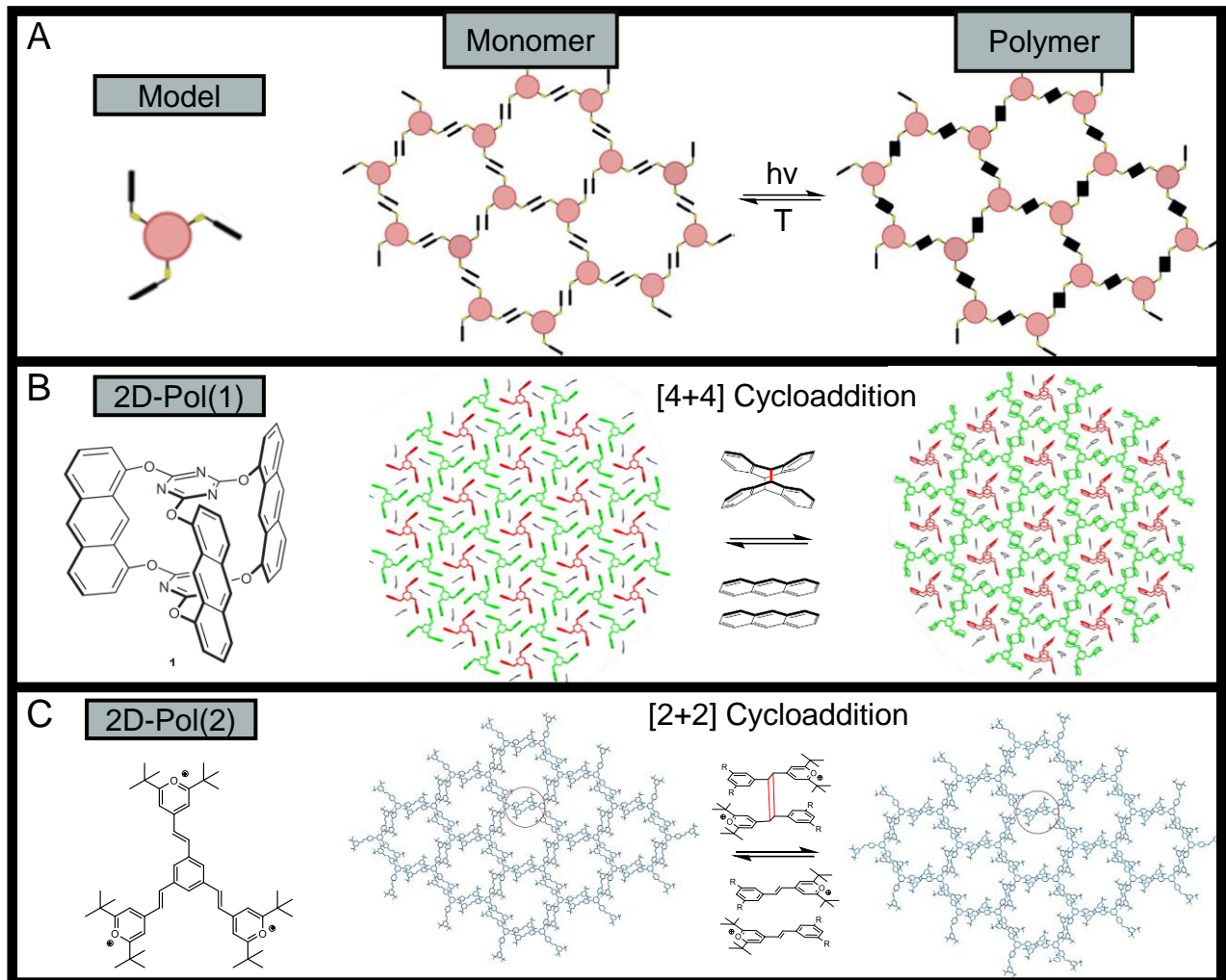


Figure 3.6-1: Photochemical single crystal approach for 2D-polymer synthesis. (A) Model reaction with a tri-functional linker molecule. The linker has to be crystallised in a linkage-preferential orientation before polymerisation. Monomer single crystals can then photochemically polymerise into polymer single crystals. (B-C) Chemical structure of the monomer molecule, crystal structure of the pre-oriented monomer and crystal structure of the resulting 2D-polymer after photocyclization reaction for 2D-Pol (1) (A) and 2D-Pol (2) (B), respectively. Reproduced and adapted with permission from ^{154, 155}.

Both of these material systems exhibit an evenly spaced porous structure over the entire sheet plane (if the template molecule is removed), which renders them interesting materials as membrane for gas and ion separation. However, before such an application can be realised, delamination of the individual layers has to be achieved. While exfoliation of 2D-Pol(2) was previously demonstrated (both in the liquid phase and micromechanically),¹⁵⁵ exfoliation down to monolayers were rare events not sufficient for further studies. To improve this, single crystals of both 2D-polymers were subjected to LPE and size selection in aqueous surfactant solution (sodium cholate, SC) which has proven to result in larger quantities of monolayers compared to organic solvent systems in the case of graphite.⁴⁷ Both bulk materials were supplied by the group of Dieter Schlüter (ETH Zürich). The structure of 2D-Pol(1) is exemplarily shown in Figure 3.6-2 A (without the template molecule to illustrate the porous character of the covalent network) along with an SEM image (Figure 3.6-2 B) revealing rela-

Chapter 3 - Exfoliability

tively large, almost monodisperse hexagonal platelets underlining the aesthetics of such a single crystal to single crystal synthesis. The chemical composition is verified by NMR spectroscopy (Figure 3.6-2 C) and the crystallinity through XRD (Figure 3.6-2 D).

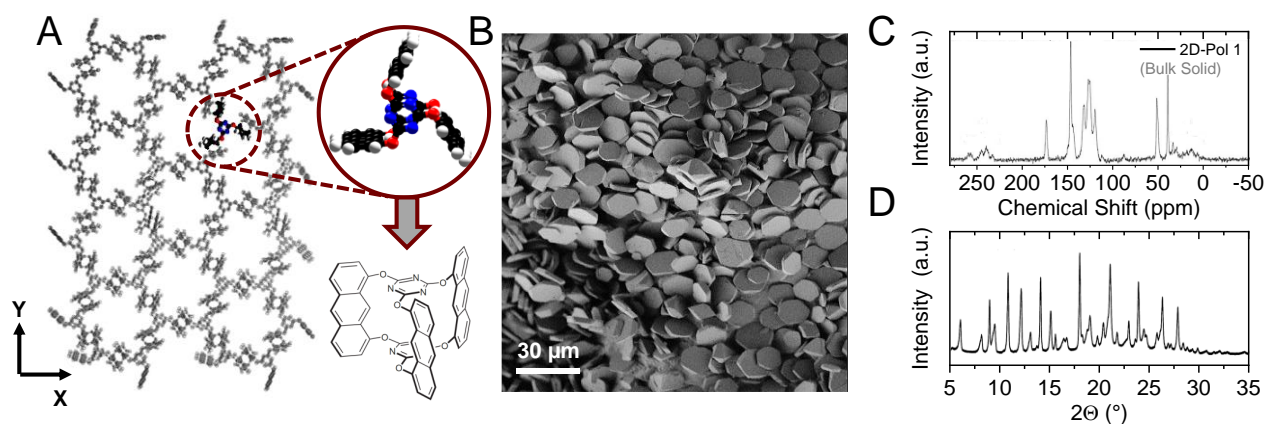


Figure 3.6-2: Character of bulk 2D-Pol(1). (A) Schematic crystal structure of the covalent lattice of the 2D-polymer without the incorporated template molecules (black: carbon, red: oxygen, blue: nitrogen, white: hydrogen). (B) Low magnification SEM image of 2D-Pol(1) single crystals. Images reveal a homogenous crystal size distribution in range of 10-20 μm . The layered character of the material could not be resolved due to charging effects. (C) ^{13}C -cross polarization/magic angle spinning nuclear magnetic resonance spectra (CP/MAS NMR) of 2D-Pol(1). (D) X-ray diffraction pattern of powdered 2D-Pol(1). Long-range order for the polymerised species is evident from low-angle reflexes. Reproduced and adapted with permission from ¹⁵⁴.

In the case of both 2D-Pol(1) and 2D-Pol(2), aggregation of the nanomaterial was observed over time. In contrast to other compounds, no cleaning step was performed due to the single crystalline nature of the materials so that the origin could be "impurities" resulting in colloidal destabilisation. For 2D-Pol(1), flocculation and precipitation of the material occurred after size selection. A higher ionic conductivity and lower pH compared to the bare SC was observed in the aqueous dispersions of 2D-Pol(1) suggesting that components are present which affect the colloidal stability. In the case of this material, these are likely related to the template monomer or cyanopyridine intrinsically embedded in the crystal which are released on exfoliation. Importantly, the aggregates precipitated without centrifugation and could be redispersed with the aid of bath sonication in aqueous sodium cholate solution resulting in stable colloids.

In the case of the second compound, 2D-Pol(2), the charged character of the material was suspected for colloidal instability as the surfactant used for the exfoliation is also charged. Indeed, selected-area electron diffraction showed a loss of crystallinity in nanosheets of 2D-Pol(2) obtained from exfoliation in aqueous SC opposed to solvent exfoliation or micromechanical cleavage.²³ It was therefore anticipated that it is required to transform the charged pyrylium into a charge neutral building block. It was possible to convert the pyrylium entities to uncharged pyridine species by reaction in gaseous ammonia atmosphere (a detailed description and characterisation is given in ²³) in the single crystal. This complex post-polymerization reaction converts 1'400'000 pyrylium ions per

sheet μm^2 furnishing a material with tuneable protonation degree at the regular nano-sized pores (Figure 3.6-3). The chemical post polymerization modification of 2D-Pol(2) allows to create a novel 2D-Pol(2*) from the existing one, which saves having to go through the entire skeleton synthesis again. The synthesis can readily be performed in gram quantities and can be easily scaled up. For clarity, the pyrylium 2D-polymer is thus referred to as 2D-Pol(2O^+) and the transformed, pyridine-based polymer as 2D-Pol(2N). After the chemical modification of 2D-Pol(2O^+) into 2D-Pol(2N), exfoliation was performed on the uncharged 2D-polymer system, ultimately resulting in stable nanosheet dispersions in aqueous sodium cholate.

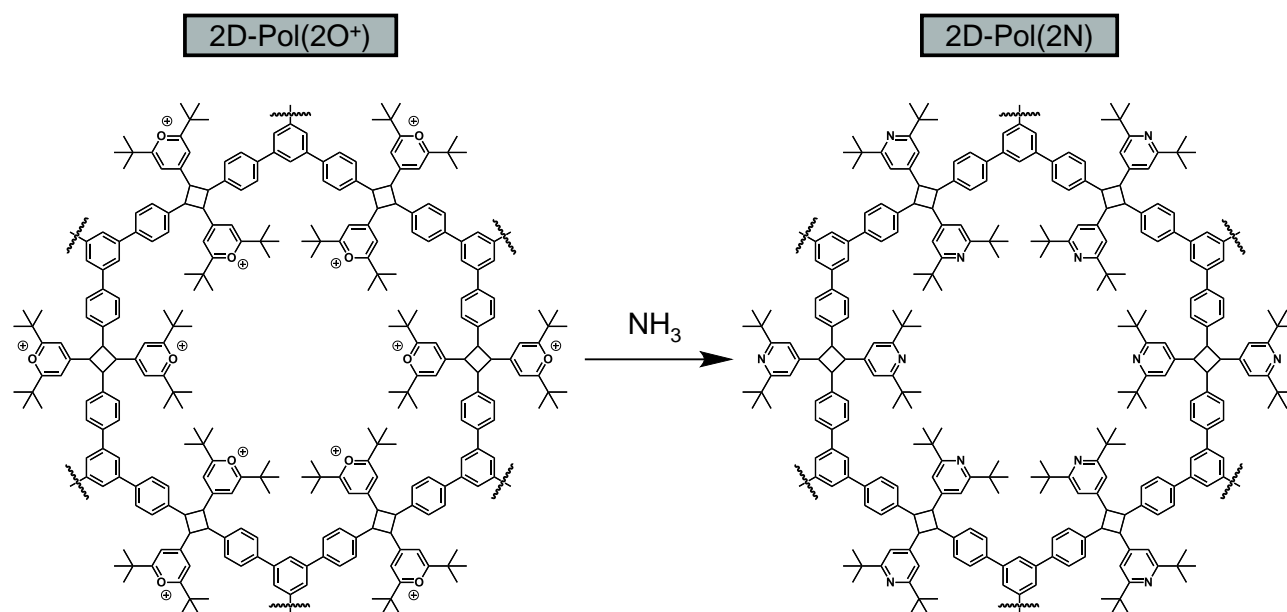


Figure 3.6-3: Post polymerisation reaction of 2D-Pol (2). Schematic presentation of the post polymerisation modification of the charged 2D-Pol(2O^+) into an uncharged 2D-Pol(2N) by exposure to gaseous ammonia.²³

It was thus possible to perform size selection by LCC on both 2D-Pol(1) and 2D-Pol(2N). To this end, the stock dispersions were subjected to consecutive centrifugation steps of increasing speeds. This allows to isolate nanomaterial of decreasing size in each step. To do this, the sediment of each fraction was redispersed in fresh solvent of reduced volume for analysis, while the supernatant was used for the subsequent step (for experimental details see Chapter 7.2). The respective size selection steps for 2D-Pol(1) were 400 g, 1000 g, 10000 g, 30000 g and 70000 g, respectively (for 2D-Pol(2N): 400 g, 1000 g, 3000 g, 6000 g, 30000 g, 70000 g and 300000 g). To determine the nanosheet size and thickness distributions of the different fractions, statistic AFM was performed on each fraction. As with the other materials described above, corrections of the measured height and lateral dimensions were applied. In this regard, similar TEM corrections as shown in Chapter 3.1 can be used. Additionally, step height analysis was conducted on both materials individually (Figure 3.6-4 A-B) to account for contributions from measurement parameters and surfactant leftovers on the material surface. For 2D-Pol(1), steps in multiples of 2.05 nm are observed (1.3 nm for 2D-Pol(2N)), which is the apparent AFM height of a monolayer. Thus, to convert into layer number,

Chapter 3 - Exfoliability

the measured height is divided by 2.05 or by 1.3 nm, respectively. After such corrections, the increased spectroscopic contribution from thicker structures compared to thinner material can be considered for evaluation of spectroscopic data (Figure 3.6-4 C). As well as for the other material systems discussed, a correlation between arithmetic and volume fraction-weighted mean layer number is found which can serve as a measure for the quality of the statistical evaluation. The scaling between the two quantities shown in Figure 3.5-2 C is similar to TMDs which are shown as reference in case of 2D-Pol(2N), thus further confirming that this is indeed a universal scaling. It is unclear why 2D-Pol(1) deviates from the behaviour. However, the overall trends will be discussed in comparison to all materials in Chapter 3.8.

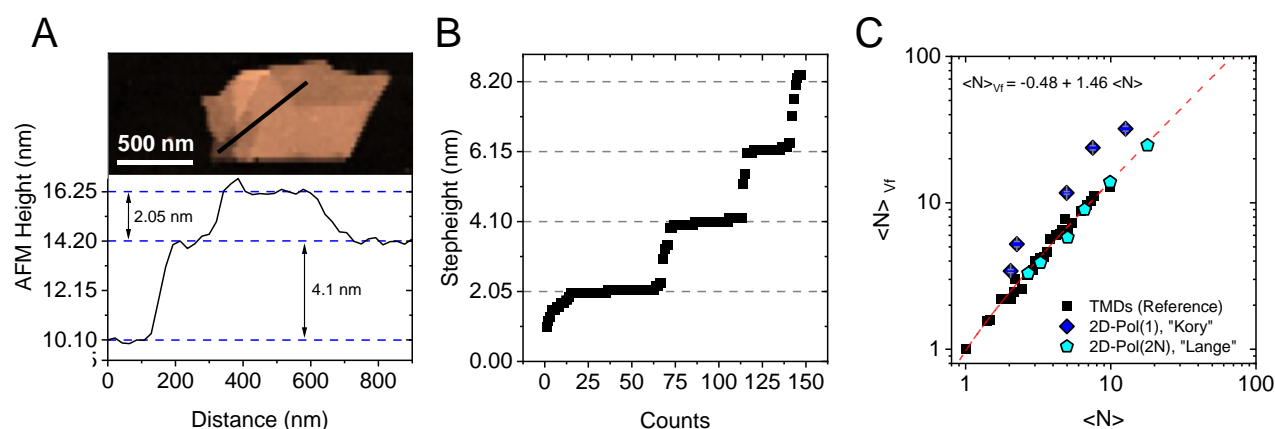


Figure 3.6-4: Corrections required for statistic evaluation of 2D-polymer nanosheet dimensions. (A) Height profile of an incompletely exfoliated 2D-Pol(1) nanosheet. The black line indicates where the profile is measured. Terraces of incompletely exfoliated material are resolved and analysed to determine the apparent AFM thickness of a single layer. (B) Statistic distribution of step heights such as the ones extracted from the nanosheet in (A) plotted in ascending order. The step height is found to be a multiple of 2.05 nm for 2D-Pol(1) and 1.3 nm for 2D-Pol(2N), which is the apparent height of a single layer for each compound individually and can be used to convert the measured height to the nanosheet layer number.⁷¹ (C) Correlation between volume fraction weighed layer number and arithmetic mean layer number of nanosheets for both polymers in comparison to TMDs.

After such corrections, statistical evaluation of the nanosheet dimensions in each size fraction can be carried out. Figure 3.6-5 A-B shows typical nanosheets of a large and a small fraction of the size selection of 2D-Pol (1). The corresponding histograms of the nanosheet layer number and lateral dimension distributions are shown in Figure 3.6-5 C-D, respectively (the complete dataset is shown in Appendix 3.6-1). For further quantitative analysis, the arithmetic mean nanosheet dimensions are plotted as function of the midpoint centrifugal acceleration applied between two consecutive centrifugation steps, where nanomaterial is isolated (Figure 3.6-5 E-F). Both extracted quantities, $\langle N \rangle_{Vf}$ and $\langle L \rangle$ follow a power law dependence with the centrifugation speed for both compounds. A similar trend is observed for $\langle N \rangle_{Vf}$ for both polymers, resulting in exponents (b) of -0.40 for 2D-Pol(1) and -0.41 for 2D-Pol(2-N) for the quantitative relation $\langle N \rangle_{Vf} \propto \overline{RCF}^b$. In case of the lateral dimensions, deviations between the two compounds are observed. Both materials show a power law decrease of the lateral dimensions with increasing centrifugal field applied but exhibit different exponents (c) in

the relation $\langle L \rangle \propto \overline{RCF}^c$. For 2D-Pol(1), $c = -0.28$ and for 2D-Pol(2N), $c = -0.38$. These are again lower than the ones extracted for TMDs exfoliated and size-selected using similar conditions (tip sonication in aqueous sodium cholate). It should be noted though that the nanosheets isolated at low centrifugal acceleration are relatively large which makes an accurate assessment of the fraction-averaged $\langle L \rangle$ through AFM challenging due to the limited field of view. Furthermore, the length calibration established for TMDs were not established in this size-range, as TMDs are typically significantly smaller than the 2D-polymer nanosheets. It is thus possible that $\langle L \rangle$ is underestimated in the fraction of larger sheets. In principle, TEM would be more suitable to determine $\langle L \rangle$, but poses its own challenges (low contrast for carbon-based materials and degradation under the electron beam).

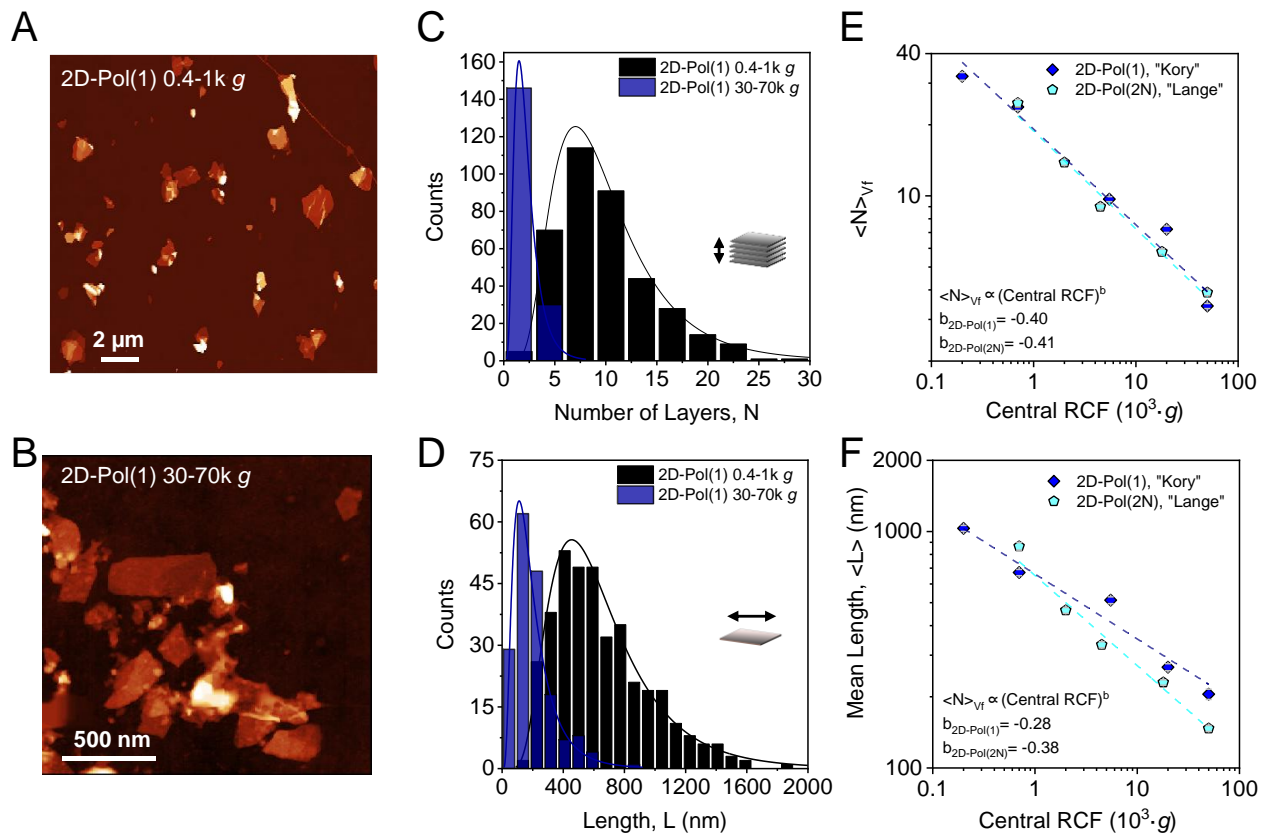


Figure 3.6-5: Statistic evaluation of 2D-Pol(1) nanosheet dimensions for different fractions of the size selection. (A-B) AFM images of drop-cast nanosheets for two fractions containing relatively large, RCF = 0.4-1k g (A) and small nanosheets, RCF = 30-70k g (B). (C-D) Histograms of the nanosheet layer number (C) and lateral sheet size (D) distribution for the two fractions shown in (A-B). (E) Mean volume fraction weighed layer number, $\langle N \rangle_{vf}$ for both 2D-polymer nanosheets across all fractions on a logarithmic scale. (F) Mean nanosheet length, $\langle L \rangle$ of the same nanosheet fractions on a logarithmic scale. Both, $\langle N \rangle_{vf}$ and $\langle L \rangle$ show a power law decrease with increasing centrifugation speed as indicated by the dashed lines.

While the size distribution isolated in the different fractions of the centrifugation cascade give valuable insights into material properties changing with size averaged over an ensemble of nanosheets, fundamentals of material exfoliability should be analysed differently, as indicated in previous Chapters. To address the size-range, which can be prepared by sonication-assisted LPE of the 2D-polymers, the nanosheet area of all fractions combined are shown as scatter plot as function of

Chapter 3 - Exfoliability

their layer number (Figure 3.6-6 A for 2D-Pol(1), see Chapter 3.8 for 2D-Pol(2N)). For a quantitative analysis, the dimensions of nanosheet of comparable thickness are averaged and shown as function on their layer number in a logarithmic plot (Figure 3.6-6 B). Similar to all other materials discussed, the dimensions of the organic compounds follow a power law dependence on the area *versus* layer number plot, exhibiting exponents of 1.3 for 2D-Pol(1) and 1.2 for 2D-Pol(2N). This clearly demonstrates, that the exfoliation of organic sheet stacks can occur similar to other van der Waals crystals. Note, that in addition to that, the nanosheet area of 2D-Pol(2N) is identical to graphite at comparable thicknesses, *i.e.* exfoliation down to the monolayer is readily feasible. Furthermore, 2D-Pol(1) has a higher lateral size to thickness aspect ratio than graphite as benchmark material for the material exfoliability, which makes the two compounds not only the first example for quantitative organic 2D-material delamination, but also the first layered crystal exhibiting a better exfoliability than graphite in LPE. Extrapolation of the data allows to estimate the average monolayer size, as discussed in previous Chapters and suggests a monolayer size of 182.7 nm for 2D-Pol(1), which is significantly larger than for graphite (*i.e.* 97.2 nm). For 2D-Pol(2N), the determined monolayer size is 94.7 nm. The reason for this observation is yet unclear but strong covalent bonds in plane and a decreased interlayer attraction due to the lack of π - π stacking between the sheets are the most likely origin. In addition, for 2D-Pol(1), this could be attributed to the template molecule inside the pores of 2D-Pol(1), which are displaced with respect to the mean plane by 1.10, 0.18 and -1.2 Å along the crystallographic c-axis.¹⁵⁴ Apart from the nanosheet area, additional insights into the sedimentation or exfoliation behaviour are expected to be contained in the nanosheet length/width aspect. Among other influences on the material aspect ratio, changes with material size can indicate, binding strength anisotropy along different directions of the 2D-plane. While this is observed for graphite and for 2D-Pol(1), no changes with material thickness are observed for 2D-Pol(2N). However, a systematic study of potential influences on the nanosheet aspect ratio is required for a conclusive discussion. As yet, reasons for changes with material thickness can only be presumed and discussed qualitatively. A comparison to different other material systems is given in Chapter 3.8.

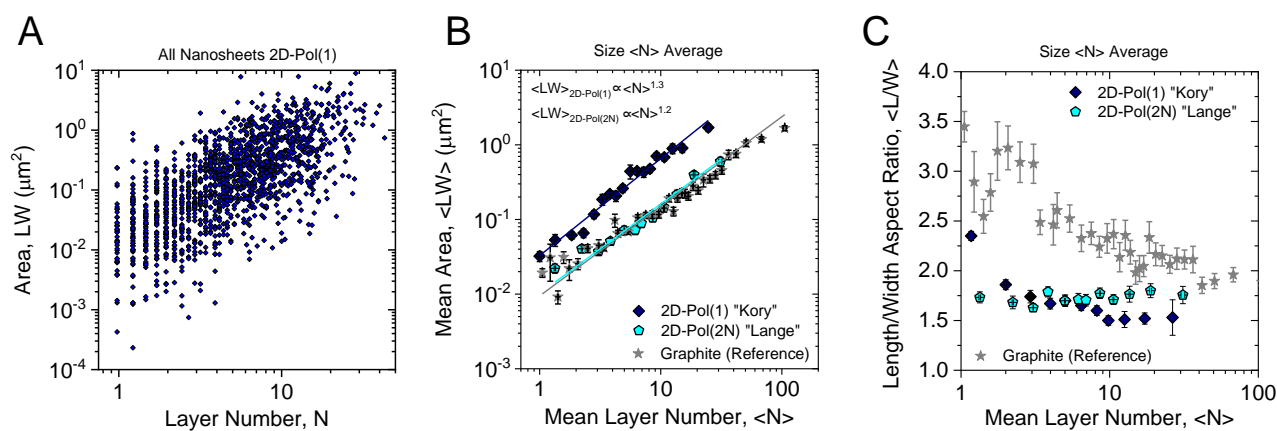


Figure 3.6-6: Accessible nanosheet dimensions for LPE 2D-Pol(1) and 2D-Pol(2N). (A) Scatter plot of measured 2D-Pol(1) nanosheet area *versus* layer number. Nanosheets from all fractions of the size selection are combined. (B-C) 2D-polymer nanosheet area as function of mean layer number (B) and nanosheet length/width aspect ratio (C) averaged for nanosheets exhibiting a similar thickness plotted for both 2D-polymers, respectively.

As the proposed applications of the 2D-polymer systems as membranes ideally require monolayers, size selection protocols have to be improved due to the low concentrations of mono-layered nanosheets achievable by standard LCC even for centrifugation at high accelerations (*e.g.* 300k *g*). The monolayer number fraction (ML_{Nf}) for different centrifugation speeds are shown as function of the midpoint centrifugal acceleration between two consecutive centrifugation steps applied for material size selection (Figure 3.6-7 A). For both polymers, ~30% of monolayers could be achieved by LCC for the last step of the size selection. In addition, the absolute amount of exfoliated material in the different size fractions could be determined for 2D-Pol(2N) by gravimetric filtering, which allows to calculate the yield of monolayers produced in the respective fractions from the layer number distribution (Figure 3.6-7 B). Note that this experiment could not be performed on 2D-Pol(1), as a lower quantity of the bulk material was available due to the more demanding synthesis.

While the monolayer content is higher than for most other materials under study, still ~70% of the nanosheets are thicker than required. To further increase the fraction of monolayers, additional centrifugation steps, so called secondary cascades have been performed on different fractions of the initial size selection. In this approach, the dispersion is centrifuged for prolonged times at low centrifugation speeds to remove thicker material from the dispersion by mild sedimentation. After centrifugation, the supernatant and the sediment of the second centrifugation sequence are subjected to statistic size and thickness analysis by AFM. The concept of secondary cascades is described in more detail in reference ²³.

The concept of secondary cascade centrifugation was at first tested on 2D-Pol(2N).²³ A slight increase of the monolayer content associated with a decrease of the overall layer number could be achieved in the supernatant fraction after centrifugation of preselected samples for 14 hours at centrifugal accelerations at 20% of the initial lower boundary of the primary cascade. The result is shown in Figure 3.6-7 C, where the monolayer number fraction is plotted as function of the mean layer number. The blue arrow indicates the changes of the monolayer content in different fractions upon secondary centrifugation. Using this technique, an increase of the total monolayer content by ~10% was achieved for different fractions. Note that the average lateral dimensions only slightly decreased. The results prove the applicability of the principle of secondary cascades and the knowledge gained can readily be transferred to other material systems.

Chapter 3 - Exfoliability

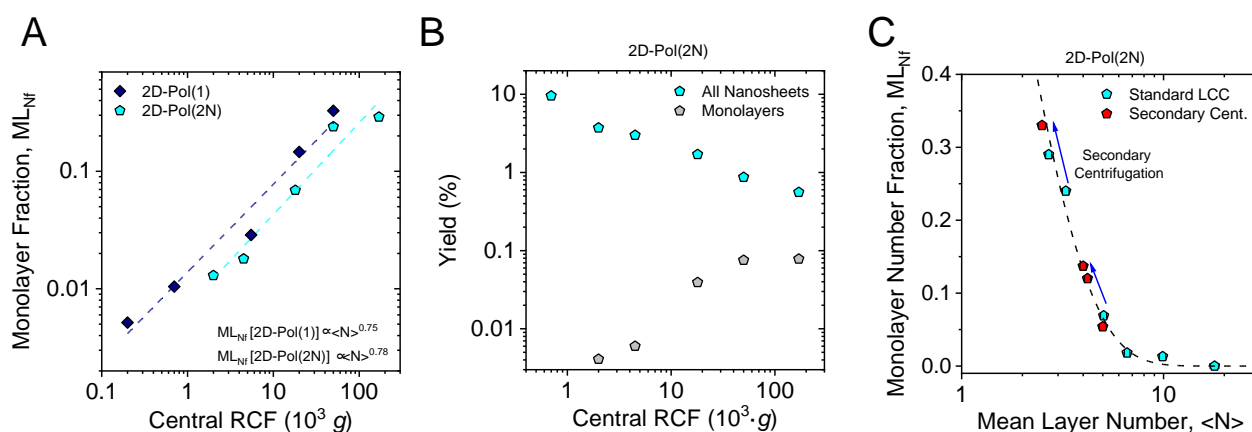


Figure 3.6-7: Monolayer content and further enrichment for 2D-polymers. (A) Monolayer number fraction for both 2D-polymers as achieved by standard size selection. (B) Yield of the nanomaterial in each size fraction. Knowledge over the mass of the dispersed nanomaterial and monolayer content in each fraction allows to determine the monolayer yield of each size fraction. (C) Monolayer number fraction as function of the average nanosheet layer number. Secondary centrifugation of preselected nanosheet dispersions can increase the monolayer content. Reproduced and adapted with permission from ²³.

The progress with respect to monolayer enrichment of exfoliated nanomaterial by secondary cascades is limited. In contrast, selective enrichment of single-layered structures from polydisperse mixtures of different 2D-nanomaterial sizes has readily been accomplished by density gradient ultracentrifugation, as described in more detail in Chapter 2.3.3.^{81, 82, 85} However, using this approach requires, among other restrictions, a gradient medium, which typically is hard to remove from the nanomaterial after size selection. To avoid this and other problems associated with DGU, a different protocol was tested to perform layer-dependent enrichment of the porous 2D-nanostructures: if the buoyant density of the nanomaterial is lower than the density of the medium, the material will float instead of sedimentation upon centrifugation. The buoyant density of the nanomaterial strongly depends on the chemical structure and the packing density of the surfactant molecules, as this defines the solvation shell of the nanoparticle. Because of this, it also changes with the layer number of the 2D-material, as this changes the volume to surface ratio and thus the contribution of the inherent material density to the buoyant density. Considering these aspects, it should be possible to sort 2D-materials by layer number if the buoyant density of the 2D-material is adjusted carefully in a way, that mono- and few-layered species float, while thicker material sediments (Figure 3.6-8 A). Note that, regardless of the surfactant/water environment, it will not be possible to lower the density of inorganic sheet stacks sufficiently. However, the porous organic sheet stacks have a significantly lower intrinsic density, which is in fact the reason why monolayer enrichment in LCC is much harder to achieve than for TMDs for example, where this method was initially demonstrated.⁷¹

As a larger amount of bulk 2D-Pol(2N) was available, initial experiments to test the technique were started on this system (experimental details are given in Chapter 7.2). Floating of the material could be achieved using D₂O with a concentration of 0.5 g/L sodium cholate (SC) as surfactant. The

nanomaterial moves to the water/air interface, while impurities (*e.g.* from tip wearing during exfoliation) sediment (Figure 3.6-8 B). For layer number selective material sedimentation, H₂O (0.5 g/L SC) was added stepwise to the dispersion to adjust the density of the medium. After each step, the dispersion was subjected to ultracentrifugation for 20 hours to separate the fractions as complete as possible. Material started to sediment at a H₂O/D₂O ratio of 40/60 (*i.e.* 60 vol% D₂O, Figure 3.6-8 C). With an additional increase of the water concentration, more material sediments while the fraction of floating material decreases (Figure 3.6-8 D-E). At 30 vol% D₂O, no material is observed at the water-air interface by the naked eye.

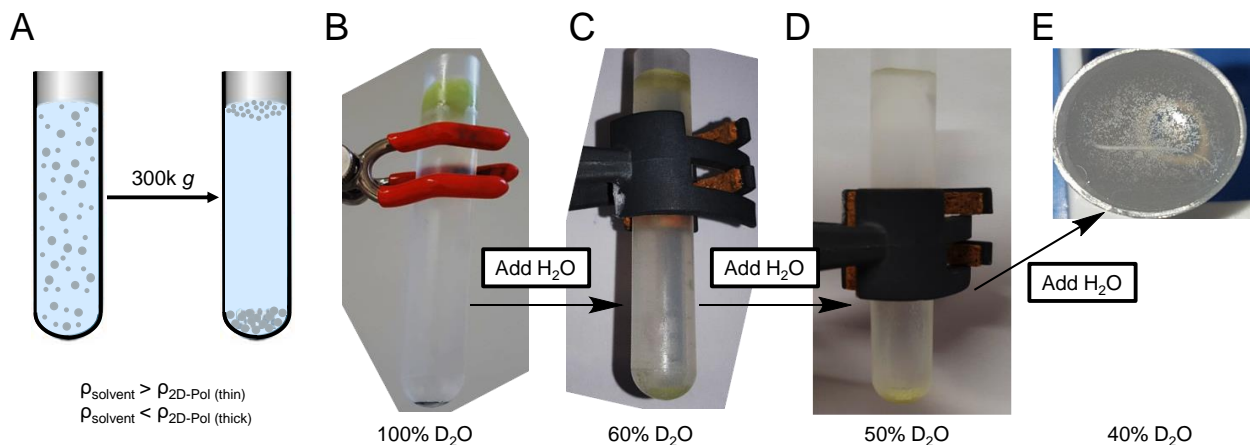


Figure 3.6-8: Layer selective floating (LSF) of 2D-materials. (A) Working principle of the method, which makes use of differences of the buoyant densities of 2D-materials with layer number. (B-E) Ultracentrifuged 2D-Pol (2-N) dispersions using different amounts of D₂O. For ~100% D₂O, all nanosheets float, while inorganic impurities from exfoliation are sedimented (B). Stepwise titration of the medium with H₂O (C→E) leads to splitting into two material fractions: one floating on the medium and one dwindling down.

These results qualitatively show, that a size selection without a gradient medium can be achieved for the porous 2D-polymer system. However, a quantitative analysis of the fractions at the top of the vial is necessary to adjust the medium density to selective monolayer enrichment in the floating fraction. A combined analysis of the decanted dispersion at the water/air interface by AFM and UV-Vis measurements revealed two causes for impurities being introduced to the system for this type of size selection that poses great challenges for quantitative analysis: The D₂O contains non negligible salt concentrations, which can cause colloidal destabilisation and lead to impurities on the substrate for AFM analysis. Thus, the D₂O was distilled prior to use. In addition, ultracentrifugation requires to apply lubricant and grease on the seal of the swinging bucket, which holds the centrifuge tube and keeps atmospheric conditions inside the bucket while the rotor room is under vacuum. Some of the grease or of the lubricant can contaminate the dispersion in the (open top) centrifuge tube upon centrifugation. It will preferentially remain at the most lipophilic environment, which is the nanosheets' surface. This can be prevented by using minimal amounts of grease and lubricant for sealing but with increasing number of steps of the size selection, more and more impurities remain on the nanosheet surface, which makes statistic evaluation impossible. Hence, the size selection was

Chapter 3 - Exfoliability

adjusted in a way, that material is enriched in one step of ultracentrifugation instead of stepwise titration and subsequent ultracentrifugation of collected supernatant fractions. To do this, a defined volume of a stock dispersion of the nanomaterial was filled up with different volumes of H₂O and D₂O to adjust the medium density and the dispersions were subjected to ultracentrifugation overnight. The supernatant fractions of the different H₂O/D₂O ratios were collected and statistic AFM evaluation of each fraction was performed (histograms for the size and thickness distribution of the floating material are shown in Appendix 3.6-2).

The AFM measurements reveal, that nanosheets are observed in the decanted fraction at the top of the vial even after ultracentrifugation in pure H₂O. The nanosheet size and thickness distribution decreases systematically with increasing H₂O content, until 70 vol% H₂O is reached. From this point on, the size and thickness distributions unexpectedly remain constant. While this is a puzzling result which will be addressed further below, it was possible to extract the number fraction of monolayers of 2D-Pol(2N) in the floating fraction from the statistics for all H₂O/D₂O ratios (Figure 3.6-9 A). A similar protocol was successfully applied to 2D-Pol(1), using 0.1 g/L SC as preliminary UV-Vis studies on the surfactant concentration in 100% D₂O showed an increased material concentration in the floating fraction for reduced SC concentrations. The monolayer number fraction of both compounds is shown as function of the volume fraction of D₂O in Figure 3.6-9 A-B, respectively. The results are similar for both components: the monolayer fraction peaks at a certain D₂O concentration, which decreases and plateaus for lower amounts D₂O (*i.e.* lower densities). To get additional insights, the mean nanosheet area versus layer number of the floating fractions is compiled in comparison to the material prepared by LCC, which serves as reference (Figure 3.6-9 C). For better visualisation, the $\langle N \rangle$ -averaged LCC datapoints are depicted transparent. For layer-dependent size selection, it would be expected, that the datapoints for the floating fraction fall on the same curve as the $\langle N \rangle$ -averaged nanosheets. Note that the fractions with a lower D₂O concentration tend to be further off the reference than material floating at high D₂O concentrations.

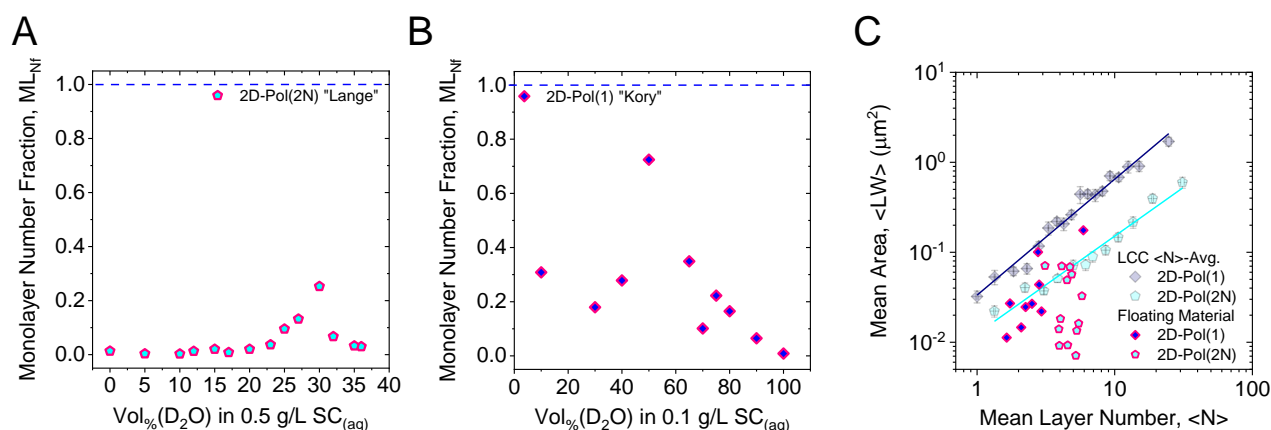


Figure 3.6-9: Characterisation of floating fractions using LSF. (A-B) Monolayer number fractions of 2D-Pol(2N) (A) and 2D-Pol(1) (B) as function of D₂O content in the centrifugation medium. A peak is observed for both components. (C) The average nanosheet area as function of the layer number for the floating fractions in comparison to the $\langle N \rangle$ -averaged nanosheet sizes. The material dimensions in the floating fractions are mostly off the trend observed for the $\langle N \rangle$ -average data shown (transparent).

Since the length/thickness aspect ratio is an indicator of the material binding strength, this behaviour may be attributed to defective nanosheets, which exhibit a decreased buoyant density and thus float at any H₂O/D₂O ratio. To test this hypothesis, new stock dispersions of both 2D-polymer were prepared and subjected to a short size selection sequence prior to the ultracentrifugation. In this approach, large and thick material was removed from the dispersion at 400 g and defective material was removed by sedimentation of the intact nanomaterial at 74k g. The sedimented nanomaterial was redispersed in two different H₂O/D₂O ratios, respectively (30 and 35 vol% D₂O for 2D-Pol(2N) and 50 and 60 vol% for 2D-Pol(1)). The results are indicated by a star in the Figure below (Figure 3.6-10 A-C). For both materials, a higher monolayer fraction is observed as before, being 35% and 85% of monolayers, respectively (Figure 3.6-10 A-B). Furthermore, the average length/thickness aspect ratios of the fractions isolated at the top of the vial after ultracentrifugation in this case (indicated by a star) agree with the $\langle N \rangle$ -averaged nanosheet area of the LCC reference (Figure 3.6-10 C) strongly supporting a size selection by layer number.

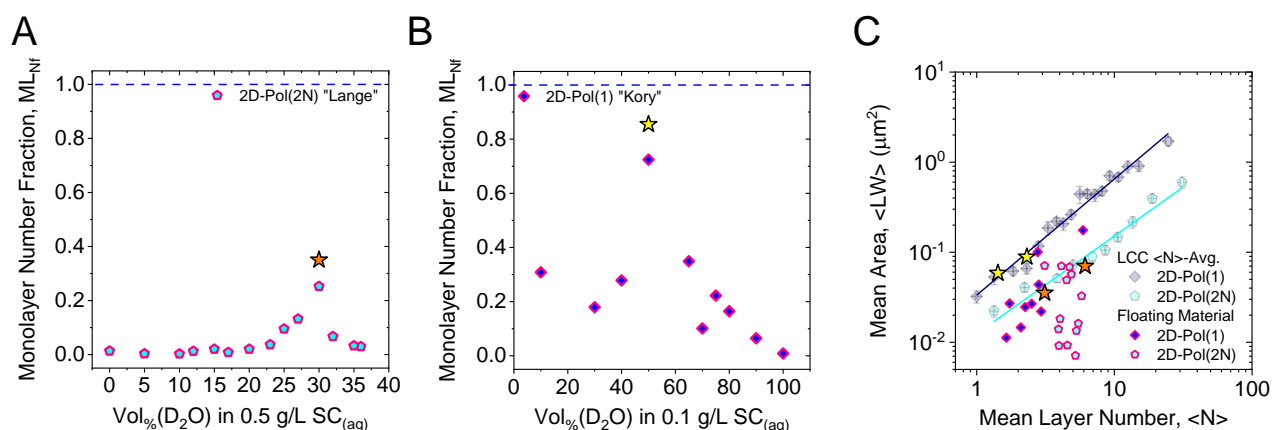


Figure 3.6-10: Characterisation of floating fractions using LSF for precleaned starting material. (A-B) Monolayer number fractions of 2D-Pol (2-N) (A) and 2D-Pol (1) (B) as function of D₂O content in the centrifugation medium. An improvement of the monolayer content is observed for the precleaned starting material. (C) The average nanosheet area as function of the layer number for the floating fractions in comparison to the $\langle N \rangle$ -averaged nanosheet sizes. The material dimensions extracted for the precleaned starting material fit to the expected trend.

In summary, knowledge on exfoliation and size selection gathered for inorganic van der Waals crystals could successfully be transferred to two different 2D-polymers prepared by rational organic synthesis. The material exfoliability could be improved by a post-polymerisation modification, converting charged pyrylium-functionalities into uncharged pyridines. This is the first example for such a reaction and for LPE combined with size selection of a layered crystal prepared by organic synthesis. Overall, similar trends for size-selected samples are observed as for other material systems, following a power law dependence of the material dimensions with increasing centrifugal acceleration. The nanosheet area shows the same layer power law dependence with layer number as observed for all other materials. In addition, the nanosheets are similarly large for 2D-Pol(2N) and even larger for

Chapter 3 - Exfoliability

2D-Pol(1) than exfoliated graphite, which is the current benchmark material in this regard. Importantly, no signs of material decomposition are observed over time in aqueous surfactant, which suggests long material durability for the outlined application as membrane for gas or ion separation.

Additionally, two routes for monolayer enrichment have been introduced: secondary cascades and layer selective floating. Secondary cascades prove that the size distributions can be adjusted by centrifugation of already size-selected fractions. This narrows the size distribution in both the resulting supernatant and sediment resulting in ~30% monolayers. However, due to the low buoyant density of the 2D-polymers, it is difficult to achieve a result comparable to for example WS₂ where a monolayer enrichment up to 75 vol% was previously demonstrated using this technique.²³ This led to the development of a new technique that benefits from these low buoyant densities. The results on layer selective floating show, that a layer number-based size selection without a gradient medium can be achieved and give valuable insights in aspects of particle movement in a strong centrifugal field. Monolayer contents of 35% for 2D-Pol(2N) and 85% (2D-Pol(1)) have been enriched in a floating fraction, using the new method. It is unclear, why 2D-Pol(2N) shows lower monolayer contents. A possible explanation could be, that not all defective material was removed in the cleaning step or that the H₂O/D₂O ratio (and hence density of the medium) requires re-adjustment. However, as the technique can be applied to both 2D-polymers under study with only little fine-tuning, it is likely that the knowledge gathered for the 2D-polymers can be transferred to other porous material systems. In consideration of the parameter space available to adjust the buoyant density of the nanomaterial through the surfactant, graphene selection from exfoliated graphite might even be possible. However, different aspects still need to be studied in more detail: The impact of the chemical structure of the surfactant, its concentration and adsorption ability (depending on counterion, pH and ionic strength) but also the temperature used for the centrifugation have to be considered to optimise the new size selection approach.

3.7 Metal Organic Frameworks

2D-materials prepared by organic synthesis do not have to be strictly organic. In addition to 2D-polymers and 2D-COFs consisting of covalently connected organic linkers, composite structures of inorganic and organic compounds can be made by wet-chemical synthesis. So-called metal organic frameworks (MOFs) are porous coordination networks that can exhibit a porous and layered character. MOFs are assembled from inorganic nodes, also called inorganic building units (IBUs), which are interconnected by organic linker molecules.^{24, 156, 157} Various 2D-MOFs have been reported in recent years. Yet, only little is known about the exfoliability of these structures. This can partly be attributed to synthetic challenges achieving long range order for MOFs, which typically exhibit grain boundaries in the nanometre size.¹⁵⁸ In addition, leftovers from incomplete products formed upon material synthesis impede the characterisation of exfoliation products. These side products have to

be removed before material characterisation. At last, whether the material can be exfoliated by sonication assisted liquid phase exfoliation or not strongly depends on the binding strength of the coordinative 2D-lattice. If the binding strength is too low the ratio of scission to material exfoliation is increased, which would lead to material decomposition rather than to layer separation.

To test the exfoliability of layered 2D-MOFs, six different structures have been subjected to LPE by bath sonication in aqueous SC (for experimental details see Chapter 7.1). The crystal structures and corresponding morphology of the bulk material are shown in Figure 3.7-1 in the upper and middle row, respectively. The structures from A-F are mostly reported in literature and consist of metal oxide clusters interconnected by organic linker molecules.^{24, 159-162} The structures are referred to as in the respective reports. However, to simplify the comparison, a colour code is used as indicated by the different colours of the crystal structures in Figure 3.7-1. After exfoliation, a short centrifugation sequence was applied: unexfoliated material was removed from the dispersion by sedimentation at 400 g. The resulting supernatant was then centrifuged at 30k g to precipitate the nanomaterial, while soluble impurities or defective nanosheets remain in the dispersion. The resulting dispersions were not subjected to size selection as in this experiment the exfoliability of the different materials was first assessed. These are thus referred to as stock-like dispersions. Note, that size selection of the compounds is in principle possible in analogy to other materials, as exemplarily shown for CAU-45 ("Green").²⁴ The stock-like dispersions of the six different compounds were characterised by statistic AFM. Representative nanosheets for all materials are shown in the lower row of Figure 3.7-1.

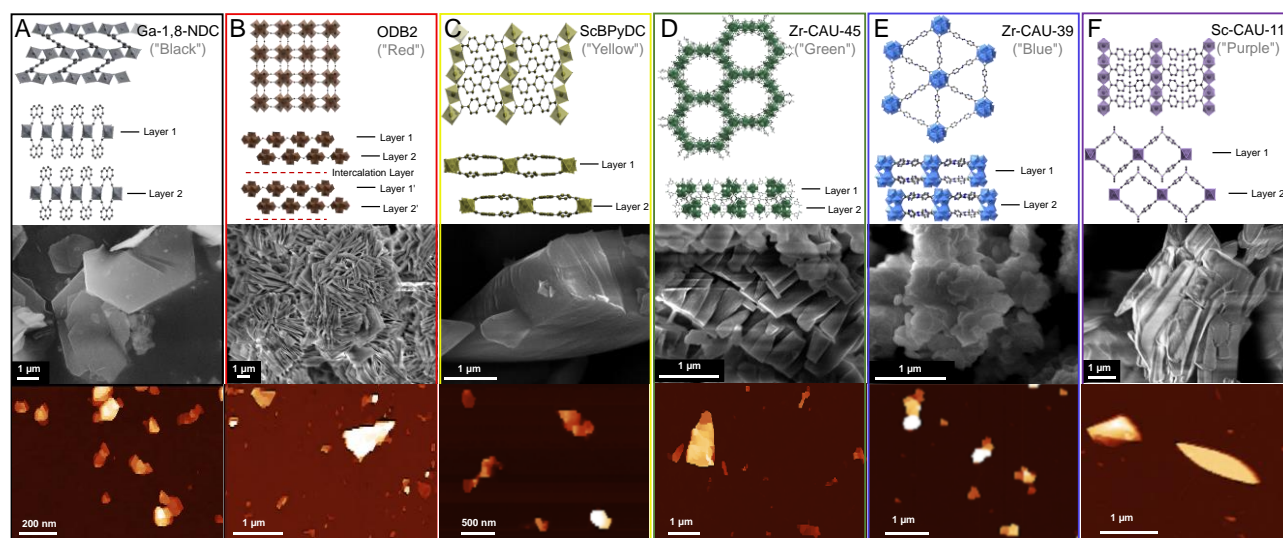


Figure 3.7-1: Character of the different 2D-MOFs under study. Upper row: crystal structures of the respective compounds. Centre row: low magnification SEM images of the starting materials. Different morphologies are observed for each MOF. The layered character is poorly resolved due to charging effects. Lower row: AFM images of exfoliated MOFs from drop-cast stock-like nanomaterial dispersions. Results are shown for (A) Ga-1,8-NDC ("Black"),¹⁶¹ (B) ODB2 ("Red"), (C) ScBPyDC ("Yellow"),¹⁶² (D) Zr-CAU-45 ("Green"),²⁴ (E) Zr-CAU-39 ("Blue")¹⁵⁹ and (F) Sc-CAU-11 ("Purple").¹⁶⁰

Chapter 3 - Exfoliability

As it is unclear whether the MOFs retain their structure upon exfoliation, powder diffraction, Raman and infrared transmission measurements have been performed on the bulk and on the exfoliated material. Figure 3.7-2 shows the resulting spectra exemplarily for "Black" (Ga-1,8-NDC, spectra for the other compounds are shown in Appendix 3.7-1). No changes between the spectra of the bulk and the exfoliated species are observed except for ODB2, which exhibits an intercalation layer of noncovalently bound 4,4-oxybis(benzoic acid). The intercalation compound is likely to be washed out upon material delamination, which leads to changes of the spectroscopic response of the nano-material with respect to measurements performed on bulk samples.

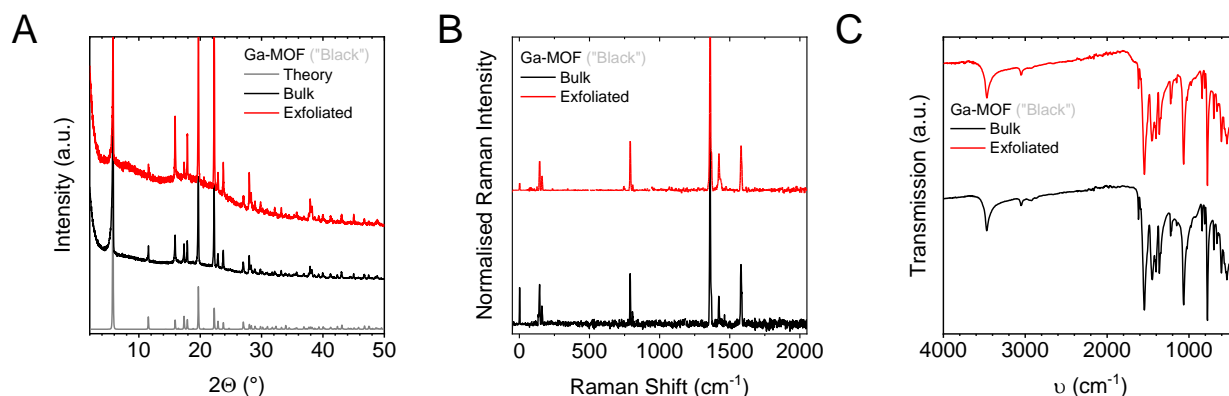


Figure 3.7-2: Structural and spectroscopic properties of exfoliated Ga-1,8-NDC ("Black"). Acquired diffraction pattern and spectra on dried nanosheet stock dispersions are shown in comparison to the bulk sample. (A) Powder XRD (B) Raman and (C) IR-transmission measurements show no other than the expected signals. The results imply no changes of the material composition and crystallinity upon exfoliation.

The nanosheet area *versus* thickness distributions for all materials are shown in Figure 3.7-2 A-B. A different spread of the data points is observed for the respective compounds. While the dimensions of the "Black" MOF (Ga-1,8-NDC) are clustered and are comparably small, nanosheet dimensions for "Red" (ODB2), "Yellow" (ScBPYDC) and "Green" (Zr-CAU-45) tend to be larger at the same thickness. For "Blue" (Zr-CAU-39) and "Purple" (Sc-CAU-11), nanosheets show a great spread in nanosheet dimensions. A possible explanation for this observation could be that the centrifugation parameters are not adjusted to the respective material. Thus, different material sizes are removed from the dispersion using only two steps, as described above. Note, that for the thickness analysis of the MOFs, no step height analysis was performed and that the graphs show the apparent AFM thickness without applying corrections for the nanosheet height. To address this and nonetheless derive an assessment of the layer number, the empiric nanosheet step height (h_{AFM}) of other materials is plotted as function of their crystallographic thickness (h_0). A roughly linear trend is observed, suggesting that the step height can be estimated from the crystallographic thickness as $h_{AFM} = 2.24 \cdot h_0$ (Figure 3.7-2 C). The datapoints are scattered within 25% deviation from the fitted line with one exception: 2D-Pol(2N), highlighted in red. This implies, that the empiric step height determined for 2D-Pol(2N) might be underestimated. If this is the case, the monolayer contents dis-

cussed in the previous Chapter would be higher for the second 2D-polymer. Nonetheless, the described relation between the crystallographic layer thickness and the AFM step height provides an important proxy for fast layer number estimation without tedious statistical analysis.

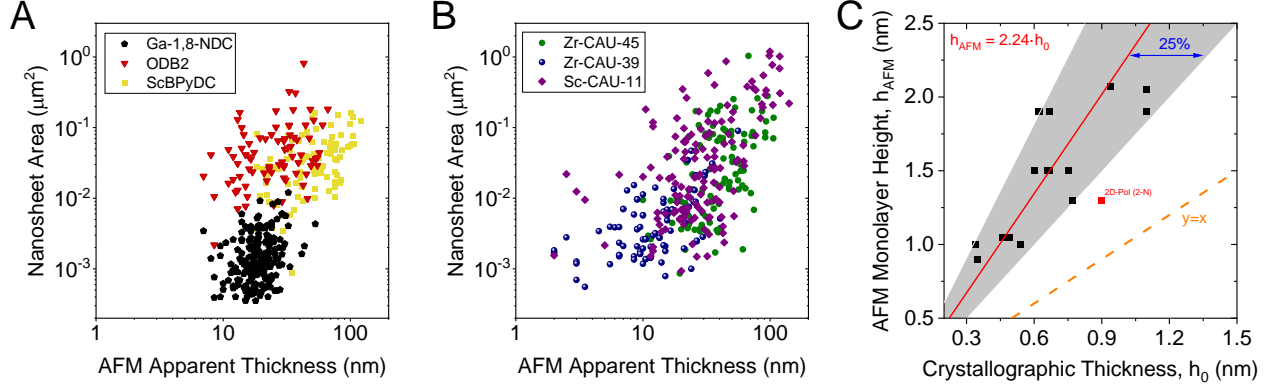


Figure 3.7-3: Minimal dataset evaluation of the six 2D-MOFs. (A-B) Scatter plots of the measured nanosheet area as function of their measured AFM thickness. The graph is split into two individual plots to reduce clutter. (C) Empiric correlation between statistic AFM monolayer height and the crystallographic layer thickness. The observed trend can be used as proxy to avoid step height analysis for layer number estimation.

For a quantitative comparison of the exfoliability, the arithmetic mean apparent nanosheet height, $\langle T \rangle$ is determined for each MOF (Figure 3.7-4 A). Using the correlation between the crystallographic thickness and the measured AFM step height, the relation between the mean nanosheet dimensions and the energy ratio for nanomaterial delamination and tearing, equation 1 (as described in Chapter 2.2.2) can be rearranged into the following form:

$$\frac{\sqrt{\langle LW \rangle}}{\langle T / (2.24 \cdot h_0) \rangle} = 2h_0 \frac{E_E}{E_S} \quad (\text{Eq. 21})$$

with $\langle N \rangle = \langle T / (2.24 \cdot h_0) \rangle$, which allows to simplify the expression as

$$\langle T / (2.24 \cdot h_0) \rangle = \frac{1}{n} \sum_i^n T_i / (2.24 \cdot h_0) = \frac{1}{2.24 \cdot n \cdot h_0} \sum_i^n T_i = \langle T \rangle / 2.24 \cdot h_0 \quad (\text{Eq. 22})$$

to the following form:

$$\frac{\sqrt{\langle LW \rangle}}{0.893 \cdot \langle T \rangle} = \frac{E_E}{E_S} \quad (\text{Eq. 23})$$

Note that h_0 is cancelled out from the equation. The evaluation allows a better comparison between the different structures and furthermore to estimate the edge to surface energy ratio which determines material tearing and delamination. To do this, the square root of the mean nanosheet area per nanosheet thickness is calculated (Figure 3.7-4 B) and divided by 0.893 to determine the edge to surface energy ratio, E_E/E_S , where E_E is the energy required to create edges (*i.e.* tearing) and E_S the

Chapter 3 - Exfoliability

energy required for peeling off a sheet per unit area (*i.e.* delamination, Figure 3.7-4 C). For comparison, results on exfoliated graphite and MoS₂ evaluated using the same method are included in the same graph (patterned bars in Figure 3.7-4 B-C). According to the energy ratio, the MOFs are less exfoliable than both reference compounds. However, it should be noted that also other layered materials can have lower area/thickness aspect ratios than TMDs (*e.g.* CrTe₃ described in this thesis or layered hydroxides reported in literature).⁴⁷

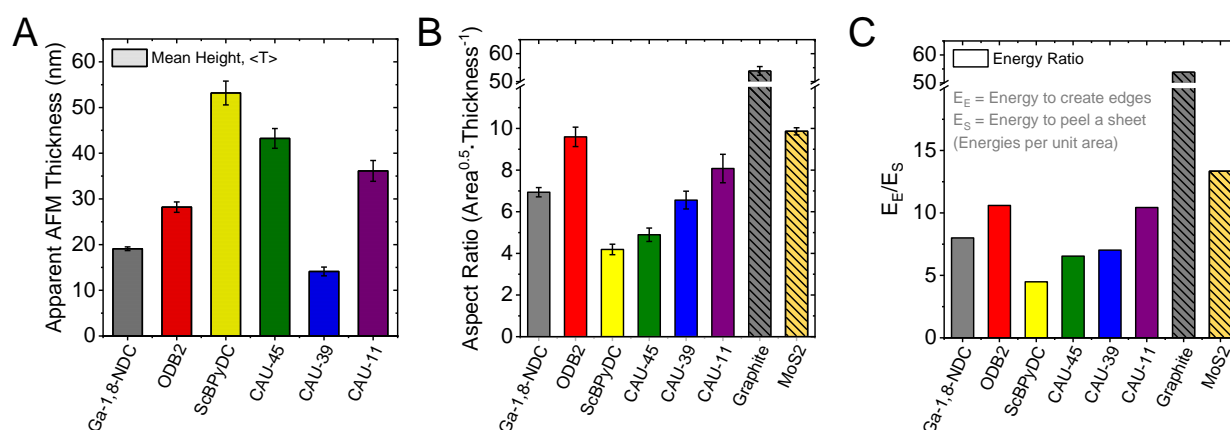


Figure 3.7-4: Bar charts of MOF nanosheet dimensions. (A) Arithmetic mean apparent AFM thickness as determined from statistic evaluation. (B-C) Square root of the average nanosheet area divided by the average thickness (B). This aspect ratio allows to estimate the in-plane to out-of-plane binding strength ratio (C), as derived in Eq 23. Data on exfoliated graphite and MoS₂ is shown for comparison.

In summary, six different mesoporous 2D-MOFs have successfully been exfoliated in aqueous solution. The resulting nanosheets have been characterised, using different spectroscopic methods and show no obvious signs of decomposition. Statistic evaluation of the nanosheet dimensions revealed that different nanosheet sizes are prepared for the respective compounds, which implies that the energy required for the exfoliation differ for each material. For a semi-quantitative analysis, an approximation has been made from data acquired for other material systems. This proxy allows to estimate the ratio between the covalent binding strength and the interlayer attraction, which defines the ratio of events of scission and events of delamination. The results show, that this ratio indeed significantly varies across the MOFs and is lower than for graphite and TMDs for all MOFs under study, but still higher than some other layered inorganic compounds.

3.8 Material Exfoliability in Comprehensive Comparison

In summary of Chapter 3, twelve different van der Waals crystals have been exfoliated by sonication-assisted liquid phase exfoliation. The exfoliation conditions and chemical environment have been customised for the individual components to achieve stable dispersions of the corresponding nanomaterials. Methods for inert gas exfoliation have been developed and successfully applied to materials prone to oxidation. For all materials, the exfoliation has been quantified which demonstrates

that the nanomaterial dimensions systematically change as a function of the centrifugal field applied during size selection. Independent of the material structure or chemical composition, a power law decrease of material dimensions is observed (Figure 3.8-1 A-B). While exponents determined for the decrease of the volume fraction weighted layer number are close to either ~ 0.4 or to ~ 0.25 , no clear trend is observed with the exfoliation method or the solvent used (Figure 3.8-1 A). A similar result is observed for the exponents describing the decrease of the average nanosheet length (Figure 3.8-1 B), where all exponents are in a similar range as for the decrease observed for $\langle N \rangle_{vf}$. For the sheet length, all exponents for tip-sonicated samples are higher than for bath sonication. Note that the current understanding of centrifugation theory suggests that the "cut-size", *i.e.* the largest diameter of a particle remaining in the supernatant after centrifugation is proportional to the inverse rotation rate.¹³⁴ Due to the relationship of centrifugation rate and relative centrifugal acceleration, one would expect exponents close to -0.5 which were indeed observed in literature.⁷¹ The reason for this deviation remains elusive at the current stage.

In addition to the power law relationship between average dimensions of nanosheets in size-selected fractions with centrifugal acceleration, a universal correlation between the arithmetic mean layer number and the volume fraction weighted layer number was empirically found to be $\langle N \rangle_{vf} = 1.46 \langle N \rangle - 0.48$ for all materials under study (Figure 3.8-1 C). This demonstrates that the scaling is indeed material independent as discussed above and can serve as an indicator for the reliability of the overall statistical analysis.

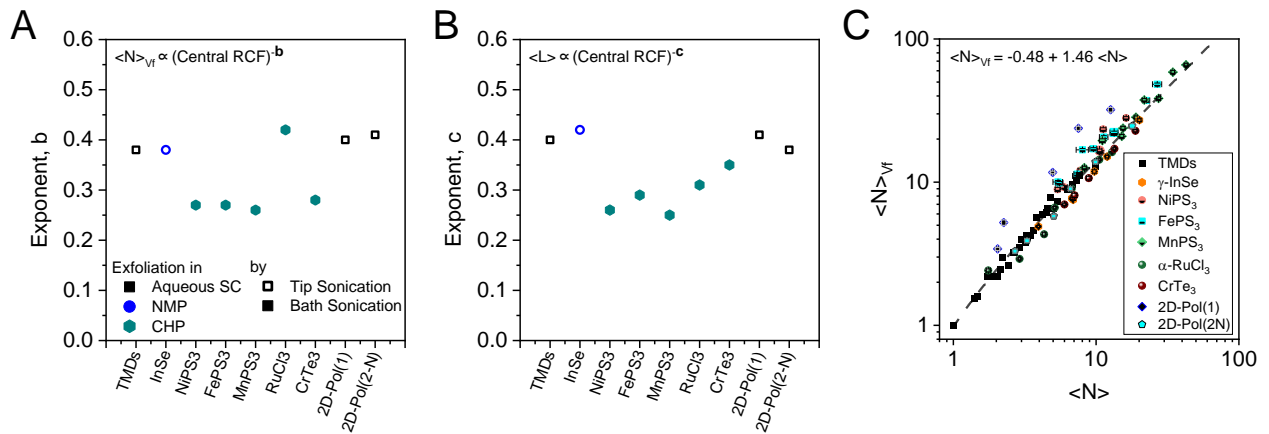


Figure 3.8-1: Exponents for power law dependence observed for different material systems in comparison. (A-B) Exponents for the power law decays of the nanosheet volume fraction weighted layer number (A) and for the arithmetic mean nanosheet length (B) with central centrifugal acceleration. No clear trend is observed for the exponents with exfoliation method or solvent used. (C) Correlation between volume fraction weighted layer number and arithmetic mean layer number of nanosheets to account for increased spectroscopic weight for thicker structures. Data for different materials falls on the same curve.

Scatter plots of the nanosheet area are shown in Figure 3.8-2 as function of the nanosheet layer number for each individual 2D-material under study. For better comparability the data clouds in Figure 3.8-2 A-M are shown with the same scaling. It is evident, that for some materials, the individual

Chapter 3 - Exfoliability

datapoints are more scattered (*e.g.* for TMDs) than for others (*e.g.* RuCl_3). We attribute this observation to varying defect densities in the starting material but also to differences of the energy intake using different sources of ultrasonic energy and exfoliation media. Similar observations have been made for the overall size and thickness distribution of graphite using different conditions for the exfoliation.⁴⁷

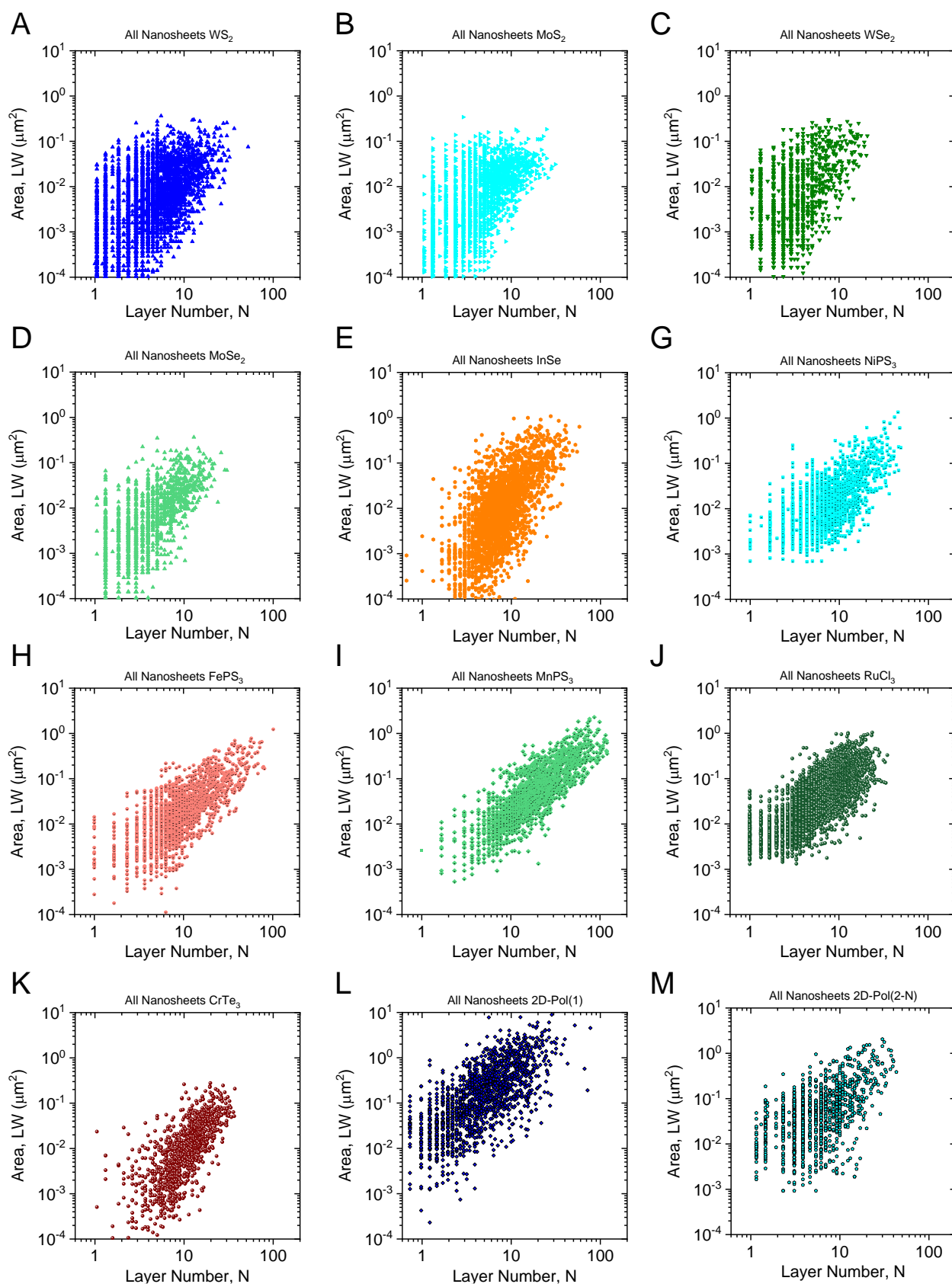


Figure 3.8-2: Scatter plots for the nanosheet area as function of their layer number for all materials under study. Individual plots for the MOFs are shown in Appendix 3.7-2.

The average nanomaterial dimensions follow a model, which predicts nanosheet dimensions to be predetermined by the in-plane to out-of-plane binding strength ratio, as reported previously.⁴⁷

Chapter 3 - Exfoliability

Re-evaluation of the AFM data by averaging nanosheet dimensions of sheets exhibiting a similar thickness rather than averaging the size distribution of sheets contained in fractions of the size selection significantly improves the data quality of this scaling. For all materials under study, a clear power law decrease of the average sheet area is observed with decreasing layer number. As suggested by the model, which is described in more detail elsewhere,⁴⁷ all materials show identical exponents for the power law dependence (Figure 3.8-3 A) with values between 1.2 and 1.3. Note that these are lower than the exponents in fraction-averaged data, where the exponent is ~ 2 , but influenced by the applied centrifugation.

Nonetheless, the identical exponents show, that the materials undergo similar mechanisms upon sonication-assisted LPE. While the slope of the linear trends on the logarithmic plot is fixed between 1.2-1.3 (inset Figure 3.8-3 A), the intercept of each fit contains information about the material exfoliability. A higher intercept translates to larger nanosheet sizes at similar thicknesses and thus easier exfoliation and *vice versa* (Figure 3.8-3 A). Extrapolation of the linear trends to the monolayer limit allows to determine the characteristic size of a monolayer, D_{ML} for different material systems even if no monolayers are available in the accessible size-range. These are summarised in the table below:

Table 3.8-1: Characteristic monolayer size extrapolated from trends in Figure 3.8-3 A.

Material	D_{ML} (nm)
Graphite	97.2
WS ₂	39.8
MoS ₂	41.5
WSe ₂	61.1
MoSe ₂	44.9
γ -InSe	41.4
MnPS ₃	37.6
NiPS ₃	40.6
FePS ₃	37.6
RuCl ₃	77.3
CrTe ₃	28.4
2D-Pol(1)	182.7
2D-Pol(2N)	94.8

In addition to the nanosheet area, changes of the length/width aspect ratio with nanosheet layer number are observed for some material systems (Figure 3.8-3 B). To date, it is not fully understood which material property defines the aspect ratio of the nanomaterial. A possible explanation for the observed trends could be a binding strength anisotropy along different directions of the 2D-plane which would mean that the length/width aspect ratio underlies a similar relation as described for the relation between area and layer number, where the binding strength ratio defines the resulting aspect ratio. However, apart from these conceptual considerations, experimental or theoretical proof for this claim is still required.

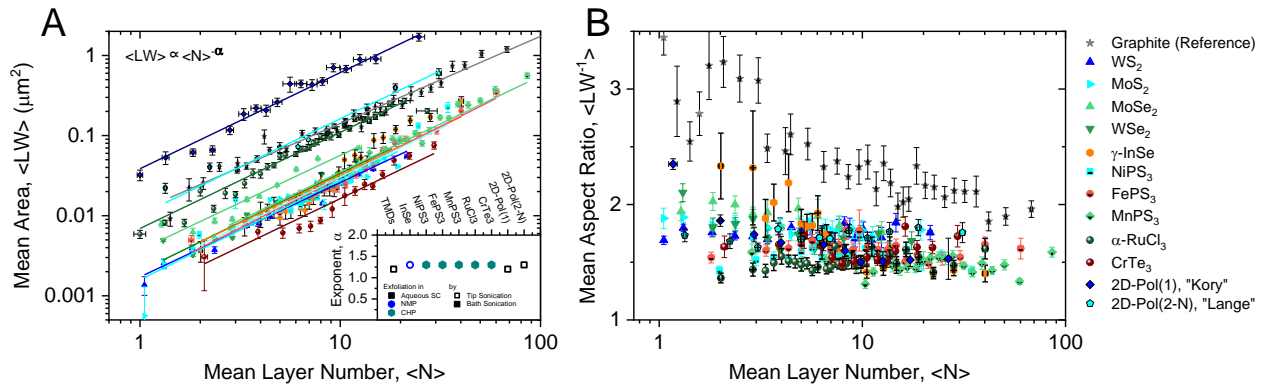


Figure 3.8-3: Trends of nanosheet dimensions with layer number. (A-B) Mean nanosheet area (A) and nanosheet length/width aspect ratio (B) for averaging nanosheets of similar thickness instead of nanosheets contained in a size fraction of the centrifugation cascade. Clear improvements of the data quality are observed compared to reported trends with size fractions.⁴⁷

In addition to the results summarised above, additional six layered compounds, 2D-MOFs have been exfoliated in aqueous solution. While a minimal dataset is provided for the nanomaterial dimensions, a correlation between crystallographic thickness and the step height determined for different 2D-material systems provides a proxy for the material exfoliability of the MOFs without comprehensive statistic measures. The presented results require additional experimental efforts to further improve the understanding of impacts on the exfoliation and size selection of van der Waals crystals but give valuable insights by comparison of different material systems.

Finally, a new method for thickness-dependent material size selection, based on differences of the buoyant densities with layer number has been presented and successfully implemented for two different 2D-polymers. In future perspective, a precise monolayer separation also for other 2D-structures might be possible.

Chapter 3 - Exfoliability

4. Size-Dependent Nanomaterial Properties

The following Chapter reports on trends of the spectroscopic response with nanomaterial size of different layered crystals. Apart from results reported previously, additional unpublished data is discussed. Parts of the data shown in this Chapter is published in *Chem. Mat.* (2019), 24; *Chem. Mat.* (2019), 31 and in *Angew. Chem.* (2020), 59. Reprints are shown in combination with a citation in the caption text and are reproduced or modified with permission from the respective publishers.

In addition to the chemical composition, the dimensionality of a material defines its properties. The dimensions of a solid can be reduced in one, two or all three dimensions to nanometre size, forming a two-, one- or zero-dimensional nanomaterial, respectively. The changes with material size are not limited to inherently spherical, tubular or layered materials which is the case for carbon allotropes (*i.e.* fullerenes, carbon nanotubes or graphite) and can also be observed for reducing the dimensions of a bulk material that exhibits covalent bonds in all three dimensions, such as silicon.¹⁻³ These changes of material properties occur progressively with decreasing particle size, when going from bulk solid to a nanomaterial of any dimensionality. Consequently, 2D-materials of different sizes exhibit different properties as well. This is because of three reasons: firstly, the material surface to volume ratio changes with particle size and thus the relative contribution of the chemically different material edges. In addition, this leads to different exposure to the environment resulting in solvatochromic effects for LPE materials (*i.e.* dielectric screening). Second, the decrease of material dimensions restricts the movement of charge carriers and quasiparticles which is reflected in changes of the band structure and thus also the spectroscopic response (*i.e.* quantum confinement effects). Third, in optical absorbance spectroscopy contributions from light scattering systematically change with particle size. Each of these different effects influences the spectra in a different, but characteristic way. In the following discussion, the impact of the material dimensions on optical extinction and absorbance spectra is addressed. Note that other effects might be observed for different types of spectroscopy.

Optical extinction spectra are a result of the attenuation of light intensity as function of wavelength when a light beam passes through a sample in transmission mode. Both absorbance and light scattering can result in this attenuation. To deconvolute these effects, measurements in the centre of an integrating sphere can be carried out, where the scattered light is collected and thus absorbance spectra are recorded. Prior to the work carried out within this thesis, size-dependent extinction and absorbance had been investigated for a few semiconducting 2D-materials, *e.g.* MoS₂,⁴⁸ WS₂,^{63, 71} black phosphorus⁷⁵ and GaS.¹² In general, the following conclusions were drawn that ultimately resulted in quantitative spectroscopic metrics for these materials that allow to determine the nanosheet lateral size and shape from absorbance/extinction spectra:

- 1) Changing the edge to plane ratio leads to changes of the spectral shape (*e.g.* peak intensity ratios) due to different wavelength-dependent absorption coefficients of both contributions.

Chapter 4 – Size-Dependent Properties

2) Dielectric screening can induce shifts within the spectra as the impact of the solvent (*i.e.* dielectric environment) is more pronounced for thinner nanosheets that exhibit a higher surface to volume ratio. The effect can be observed best in peak regions typically corresponding to excitonic transitions.

3) Confinement effects lead to restriction of the electronic wavefunction in two dimensions with decreasing layer number. Thus, the reduced degrees of freedom result in a blueshift of the band gap.^{10, 94} The quantitative impact of the confinement effects depends on the band structure and is not fully understood as yet.

4) Scattering effects strongly depend on the particle size: large and thick particles exhibit more intense light scattering compared to small and thin particles. The scattering contribution follows the shape of the absorbance in the resonant regime of the spectrum, but usually is slightly red-shifted which leads to peak broadening in optical extinction compared to absorbance spectra. This is especially the case for spectra with larger particles (*e.g.* high scattering contribution). In addition, the scattering masks the optical band-edge, as non-resonant contributions from scattered light (*i.e.* where no inherent light absorption of the material occurs) decrease in intensity following a power law with increasing wavelength.

To date, effects of particle sizes on these optical properties are understood on a qualitative level. To obtain a deeper understanding on a quantitative level, more empirical experimental studies are required in combination with a theoretical modelling. In addition, quantitative spectroscopic metrics for lateral size and layer number are of great practical use for subsequent in-depth studies of novel 2D-materials both in fundamental and applied science. To address these aspects, dispersions of the size-selected 2D-materials described in the previous Chapter are studied by means of UV-Vis, PL and Raman spectroscopy for their size-dependent optical response. Focus is laid on UV-Vis spectroscopy. Here, trends are quantified by correlation to mean sizes, determined by statistical AFM measurements as discussed in Chapter 3. Extinction and absorption coefficients are extracted by gravimetric filtering of the dispersions in the case of the materials, where sufficient quantities were available for reliable mass determination. For all materials, spectroscopic metrics for nanomaterial dimensions are presented.

Optical extinction and absorption spectra of nanosheet dispersions were acquired in transmission mode, where $T = 10^{-Ext}$ with $Ext = \varepsilon \cdot c \cdot d$ (ε = extinction coefficient, c = concentration of the nanosheets and d = depth of the light path). Note that the measured extinction (Ext) is the combination of the wavelength-dependent absorption (Abs) and scattering ($Scat$) contributions of the material where $Ext(\lambda) = Abs(\lambda) + Scat(\lambda)$. In addition, the dispersions were measured in the centre of an integrating sphere for the absorption measurements, where scattered light is collected as well (see Chapter 7.3 for details).

Size Effects on

4.1 Transition Metal Dichalcogenides

Direct band gap semiconductors, such as group-VI TMD monolayers¹¹⁵ which exhibit inter-band transitions in the visible and nIR range of the electromagnetic spectrum are promising for optoelectronic device applications due to potentially efficient light emission.^{116, 117} The optical response of the mono-layered materials is strongly determined by tightly bound excitonic transitions with binding energies in the range of hundreds of millielectron volts, significantly larger than for bulk solid TMDs.¹⁶³ Consequently, strong 2D-confinement of electronic transitions and decreased dielectric screening leads to small exciton radii compared to conventional, bulk inorganic semiconductors.

The effect of WS₂ and MoS₂ nanosheet dimensions on the optical extinction and absorption spectra was reported previously.⁴⁸ In short, systematic shifts of excitonic transitions with layer number and defined changes of peak intensity ratios are observed and allow to formulate spectroscopic metrics for the average material dimensions. In addition, changes of the wavelength-dependent extinction and absorption coefficients with material size are reported.^{8, 48} The electronic structure of TMDs has been studied intensively in recent years. Nonetheless, some rudimentary material characteristics are not understood on a quantitative level yet. The lowest energy absorption transition (*i.e.* the optical band gap) of TMDs exhibits an excitonic nature. This lowest energy excited state is referred to as A-exciton. Its excitation energy (E_A) is significantly lower compared to the free particle band gap (E_g). The difference between these two magnitudes represents the exciton binding energy (E_b): $E_g = E_A + E_b$. While this qualitative correlation is well understood, absolute values are not reported for different TMD thicknesses or even for monolayers of all TMDs. This can be attributed to different external contributions, such as environmental, doping or strain inhomogeneities, but also to insufficient statistical analysis for measurements on ME nanosheets. While E_A can be determined by linear absorption or reflection spectroscopy, as well as from photoluminescence for mono-layered species, knowledge over the layer number dependence of E_A is related to fundamental contributions.¹⁶³ The evolution of E_A is influenced by the hybridization of electron states (*i.e.* conventional quantum confinement) and by the effective Coulomb interaction strength. Changes of the Coulomb interaction leads to a renormalisation of E_g and E_b which accounts for shifts to E_A of roughly equal magnitude, but opposite direction. Resolving absolute changes of these magnitudes is thus difficult *i.a.* by virtue of inherent broadening of the required optical transitions. However, interest in deeper knowledge over size-dependent changes of fundamental material properties demands an accurate description of thickness-dependent changes of E_A . Various reports on mechanically-exfoliated TMD nanosheets describe thickness-dependent trends of E_A by linear spectroscopy.^{48, 78, 115, 118-120} However, the reported values are quite scattered, which may be attributed to the lack of large-number statistic averaging and due to inhomogeneities of the dielectric environment, as well as influences from the substrate as mentioned above. It seems thus useful to study thickness-dependent changes of E_A for

Chapter 4 – Size-Dependent Properties

large-number ensembles of nanosheets in a defined dielectric environment for the different semiconducting TMDs. With the capabilities mentioned in Chapter 3, fractionated dispersions containing different sizes of nanosheets can be prepared where both, the lateral size and the nanosheet thickness can be systematically varied.^{6, 23, 78} This allows to probe ensembles of nanosheets in controlled size-ranges and in a defined dielectric environment for reliable and reproducible measurements of the required magnitudes.¹⁶⁴

To address this, dispersions of different sizes of group-VI TMDs nanosheets (*i.e.* MoS₂, WS₂, MoSe₂ and WSe₂) were prepared by LPE coupled with LCC in aqueous surfactant solution (see Chapter 7.1 and 7.2 for details). After statistic evaluation of the nanosheet dimensions in each fraction, measurements of the extinction, absorption, scattering and photoluminescence were performed in dispersion on each size-selected fraction. Systematic changes of the extinction spectral shape with nanosheet lateral size are observed which may be attributed to edge effects. Additional, well defined variations of the peak position associated with the A-exciton transition are observed. The changes in peak position are correlated with changes of the nanosheet layer number. The data allows to consistently study the correlation between the layer number and the scaling of electronic band structure as well as the energies of excitonic transitions across a set of the most prominent semiconducting TMDs within a constant experimental framework. In addition, solid quantitative metrics are provided from the results presented below which enable quick determination of nanosheet size and thickness from absorption and extinction spectroscopy.

Extinction spectra were acquired for all sizes of each TMD dispersion and converted into extinction coefficient (ϵ) spectra. The results are exemplary shown for MoSe₂ (Figure 4.1-1 A, for other materials see Appendix 4.1-1). Both, the exciton binding energy and the free-particle bandgap are expected to show a thickness dependence due to changing interlayer electronic hybridisation and screening of the dielectric environment with the nanosheet layer number. Indeed, systematic shifts of the A-exciton peak positions are observed, as shown in the inset of Figure 4.1-1 A (for all TMDs see Appendix 4.1-1) as also reported for LPE WS₂ and MoS₂ before.^{48, 78} Shifts may be attributed to confinement effects, but a precise description of the origin is not reported as yet. Thus, a comprehensive discussion on the impact of the layer number on exciton energies for all four TMDs (WS₂, MoS₂, WSe₂ and MoSe₂) is still required. To do this, additional contributions, such as light scattering effects have to be addressed. Those have to be considered especially for large/thick nanomaterial. In transmission, and so extinction measurements, absorbance and scattering of light is observed, which allows to describe the extinction coefficient as sum of the scattering and the absorbance coefficients.⁴⁸ At energies below the onset of the optical absorption (*i.e.* non-resonant regime), only contributions from scattering are observed which typically follow a power law decrease with increasing wavelength.⁷³ This is observed in the extinction spectra of all four TMDs with reduced intensity for decreasing layer numbers (Appendix 4.1-1) for wavelengths above the A-exciton. For the spectral region, where light absorbance occurs (*i.e.* resonant regime) the scattering contribution is red-shifted to the absorbance and leads to peak broadening. Thus, the apparent positions of electronic transitions in the spectra are influenced by the scattering strength of the nanoparticles.⁴⁸ In order to determine the

isolated light absorbance (Abs), scattered light has to be collected. To do this, optical spectra have to be acquired in the centre of an integrating sphere. The difference of the extinction, absorbance and scattering coefficient spectra is illustrated best for a fraction exhibiting strong light scattering (*i.e.* large nanoparticles), as shown in Figure 4.1-1 B for the largest nanosheet fraction of LPE MoSe₂ (0.1-0.4k g, $\langle L \rangle = 272$ nm, $\langle N \rangle_{Vf} = 12.9$), where the scattering contributions exceed the actual absorbance. While measurements of excitonic transitions, such as the A-exciton, for nanosheet ensembles appear as single resonances, information about the thickness distribution within the sample can sometimes be extracted and the overall signal is a mass-weighted average of all nanosheets in the dispersion.⁷⁸ For a reliable analysis of the peak position, the second derivative of the spectra is taken. This leads to significant narrowing of many component peaks and allows to separate individual contributions in case the contributions are sufficiently shifted to one another. This is the case for mono- and few-layer contributions of WS₂ which show a logarithmic dependence of peak positions with layer number and thus a clear splitting of the response of monolayers and the sum of all fewlayers.⁷⁸ However, a high monolayer content is required for such an analysis. Another advantage of the second derivative is that background from scattering or partial overlap with the B-exciton is eliminated. Such analysis is exemplarily shown for the A-exciton peak in Figure 4.1-1 C for the same, large/thick fraction of MoSe₂ nanosheets as shown in Figure 4.1-1 B. No peak separation between mono- and few-layered species is observed due to the low monolayer content in the sample. However, the impact of scattering on the peak position is illustrated: the A-exciton peak position is observed at 1.542 eV in the absorbance measurement while the same peak is red-shifted to 1.502 eV in the scattering spectrum. The extinction measurement represents the superposition of both spectra. Hence, the peak position is located in between the position observed for the scattering and the absorption measurement.

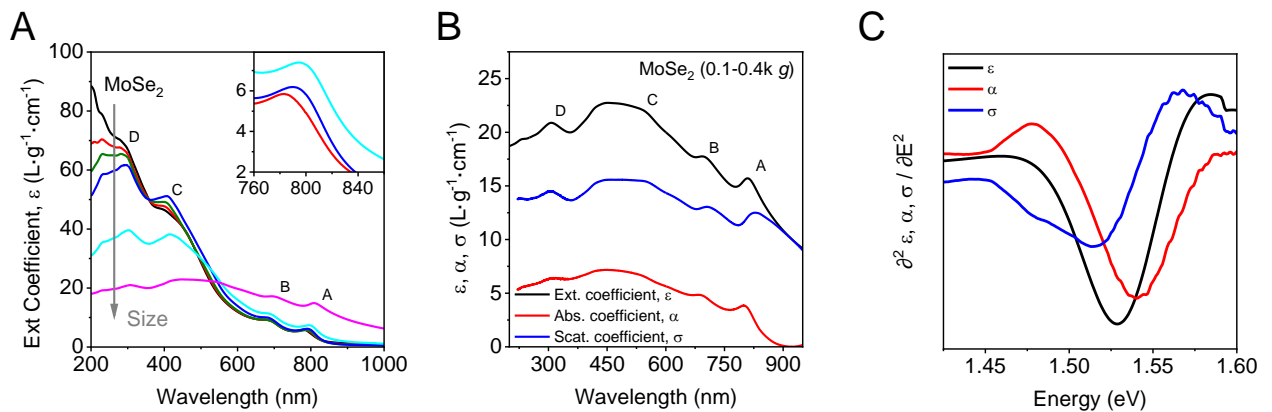


Figure 4.1-1: Impact of MoSe₂ nanosheet sizes on the optical spectra. (A) Extinction coefficient spectra of MoSe₂ dispersions with varying size- and thickness distributions from the ultraviolet to nIR range of the electromagnetic spectrum. The arrow indicates where length changes influence the extinction coefficient significantly. Inset: A-exciton (B) Extinction, absorbance and scattering coefficient spectra of a fraction containing relatively large nanosheets of MoSe₂. The scattering contribution is non-negligible and is even larger than the absorbance in this example. (C) Second derivative of the A-exciton region from the same spectra as shown in (B). Scattering in the non-resonant regime is red-shifted. Extinction peak positions are thus red-shifted compared to absorbance. Reproduced and adapted with permission from ¹⁰.

Chapter 4 – Size-Dependent Properties

As the scattering contribution varies with nanosheet dimensions, peak positions are extracted from absorbance measurements for the following discussion. However, peak positions and changing intensity ratios with nanosheet size from extinction measurements can still be used to derive spectroscopic metrics for average nanosheet dimensions.

Light scattering is particularly significant for large/thick nanosheets in the low energy region, close to the optical band-edge.⁴⁸ This is obvious for the fraction containing the large nanosheets, especially in comparison to smaller nanosheets (Figure 4.1-1 A-B). This is further illustrated in Figure 4.1-2 A, where the extinction coefficient at the A-exciton of the four TMDs is shown over the average nanosheet length of the different nanosheet size-fractions. While the extinction coefficient remains mostly constant for $\langle L \rangle < 150$ nm, an increase, following a power law dependence with nanosheet size attributed to stronger scattering contributions is observed for $\langle L \rangle > 150$ nm.

However, it was shown before that the scattering spectra of LPE TMDs follows the absorbance spectra in shape in the resonant regime⁴⁸ which enables to extract size-dependent information contained in the absorbance spectra also from the extinction spectra with some limitations, as discussed above. It is evident from the data shown in Figure 4.1-1 that the extinction coefficients systematically change with nanomaterial dimensions, as also reported elsewhere for WS₂ and MoS₂.^{48, 78} Extinction coefficients decrease with increasing nanosheet size at high energy (*i.e.* low wavelength), which is allocated to different electronic contributions from nanosheet edges and basal planes. In combination with size-dependent scattering effects,⁷³ extinction intensity ratios can be considered as metric for the average largest nanosheet dimensions (*i.e.* length). In Figure 4.1-2 B, the ratio of the extinction measured at two different wavelengths is shown as function of the nanosheet size for all four TMDs. Such a size dependence of the spectra is of great practical use, as it allows to extract the average nanosheet length of a TMD dispersion from extinction spectra. To do this, the data is fitted to a model that suggests two different electronic contributions in the spectra, as presented in Chapter 2.4 (Eq. 18). For data fitting, equation 18 can be simplified to the following form (Eq. 24):

$$R = \frac{Ext(\lambda_1)}{Ext(\lambda_2)} = \frac{A_1 \cdot \langle L \rangle + B_1}{A_2 \cdot \langle L \rangle + B_2} \quad (\text{Eq. 24})$$

The parameters A and B are obtained from fitting and are shown in Table 4.1-1 for all TMDs. To reduce the degrees of freedom, B₂ was fixed to 1 in all cases. Note, that using intensity ratios additionally bears the advantage that spectra can conveniently be measured in arbitrary units on the abscissa.

Chapter 4 – Size-Dependent Properties

Table 4.1-1: Fit parameters for the extinction ratio, R , over the mean nanosheet length (Figure 4.1-2 B, Eq. 24) for each of the four TMDs under study. Rearranging Eq. 24 allows to describe $\langle L \rangle$ as a function of R .

	λ_1 (nm)	λ_2 (nm)	A_1 (nm ⁻¹)	B_1	A_2 (nm ⁻¹)	B_2
MoS ₂	270	345	0.0144	1.97	0.0160	1
MoSe ₂	280	390	0.0117	1.83	0.0154	1
WS ₂	235	295	0.0159	2.20	0.0166	1
WSe ₂	235	347	0.0143	2.20	0.0200	1

To address the layer number dependence of the spectra, only absorbance spectra are discussed in the following, as a reliable determination of the peak positions is required for understanding the nature of excitonic shifts. Note that data from the extinction spectra can be used to formulate metrics for the layer number, which is practically more useful than from absorbance (see Table 4.7-1). To illustrate shifts in the A-exciton energy with layer number, the second derivative of the absorbance spectra in the region of the A-exciton is shown for a fraction containing relatively thick (0.4-1k g) and thin (10-22k g) nanosheets in Figure 4.1-2 C, for all TMDs under study, respectively. In every case, a significant redshift can be observed for the dispersions containing thick nanosheets (lighter lines), compared to the thinner counterparts (darker lines) as indicated by the arrows. In case of WS₂, a peak splitting for contributions from mono- and few-layered nanosheets is resolved,⁷⁸ which is not the case for the other TMDs. This is because the other TMDs intrinsically show broader linewidths, which is discussed in more detail below. The peak positions extracted from the second derivative are shown in Table 4.1-2. Furthermore, PL measurements are provided for the dispersions containing the highest monolayer contents (Figure 4.1-2 D, the average volume fraction weighted layer number and monolayer volume fraction of each sample is shown Table 4.1-2, additional PL-data is shown in Appendix 4.1-2). For all samples, the emission can be fit reasonably well to a single Lorentz function which implies, that predominantly excitonic emission is observed and additional contributions (*e.g.* from trions) can be neglected. This is consistent with small doping of LPE samples in aqueous sodium cholate.¹⁶⁵ The peak positions of the full width at half maximum (FWHM) of the PL emission is summarised in Table 4.1-2. The peak positions from absorbance (Figure 4.1-2 C) and PL emission (Figure 4.1-2 D) are shown on the same scale and can directly be compared.

As also reported for ME TMD nanosheets, the room temperature line-width of the LPE TMDs is narrowest for WS₂.¹⁶⁶ This is in agreement with theoretical findings that suggest the linewidth to be dominated by exciton/phonon-scattering for samples with sufficiently small inhomogeneous broadening at elevated temperatures (*e.g.* room temperature).¹⁶⁷ A number of possible exciton/phonon interactions can contribute to this effect. However, the coupling of A-excitons to low energy acoustic phonons is weaker in WS₂ which is, among other reasons, attributed to a combination of decreased effective mass of the quasiparticle¹⁶⁸ and smaller deformation potential matrix elements.¹⁶⁹ As a result, significantly lower (absorbance and PL) linewidths for excitonic transitions are observed for WS₂, compared to other TMDs. In case of the monolayer-rich WS₂ sample, where $\langle N \rangle_{Vf} = 1.6$, the

Chapter 4 – Size-Dependent Properties

PL peak position (2.032 eV) coincides with the monolayer peak in the second derivative of the absorbance spectra (2.034 eV) which is blue-shifted compared to the few-layer peak. This suggests a marginal Stokes-shift of 2 meV for WS₂ which is significantly larger for the other TMDs, especially the selenides. The 10-22k g WSe₂ dispersion shows a monolayer volume fraction of ~30% with $\langle N \rangle_{Vf}=2.3$ and exhibits an A-exciton absorbance at 1.664 eV with the PL emission being centered at 1.657 eV. Hence, a Stokes shift of 7 meV is observed which is an overestimate given that the absorbance measurement considers ~70% few-layered nanosheets, whereas only the monolayers show a radiative decay which is detected in PL measurements. For MoSe₂, the highest monolayer content exhibits a monolayer volume below 30%. The PL emission is red-shifted with respect to the absorbance peak position by 4 meV. This implies a much larger Stokes shift for the selenides compared to WS₂ as the absorbance peaks are averaged over all nanosheet sizes and WS₂ exhibits a by a factor ~2 higher monolayer contribution to the spectra compared to the selenides. The MoS₂ PL position shows a blueshift compared to the absorbance resonance which suggests, that the Stokes shift is small. Overall, no quantitative discussion on the monolayer absorbance is possible except for WS₂ where the monolayer optical absorbance resonance is well-separated from few-layered transitions.

Table 4.1-2: Arithmetic mean nanosheet layer number, monolayer volume fraction, centre of A-exciton peak from the second derivative of monolayer-enriched absorbance spectrum and centre as well as FWHM of PL spectra as found by Lorentzian fitting. * = from monolayer contribution.

	$\langle N_{Vf} \rangle$	Vf_{ML}	Abs, E_0 (eV)	PL, E_0 (eV)	$PL, \Delta E$ (meV)
MoS ₂	1.6	60%	1.877	1.891	48
MoSe ₂	2.5	27%	1.577	1.573	45
WS ₂	1.6	60%	*2.034	2.032	33
WSe ₂	2.3	31%	1.664	1.657	51

In addition to producing monolayer-enriched samples suitable to investigate photoluminescence, LCC enables the preparation of fractions with varying thickness distributions. This allows a consistent and statistically meaningful analysis of the A-exciton resonances for nanosheet ensembles of different average layer numbers from absorbance spectra. The resulting data is shown as a function of the volume fraction weighted mean layer number of the respective materials and fractions (Figure 4.1-2 E-H). For all four TMDs, the A-exciton transition energy follows an exponential shift with nanosheet layer number. The peak position blueshifts with increasing layer number with changes in the order of 32-65 meV in every case, consistent with previous data.^{48, 78, 118} Literature data on reflectance spectroscopy of individual nanosheets from micromechanically-cleaved TMDs is included for each material (E_A -Lit).^{115, 119, 120} The data extracted from literature is more scattered than the LPE data, which may be attributed to inhomogeneities and sheet-to-sheet variations, as discussed above. However, the data still agrees reasonably well with the observations made in large ensembles, as prepared by LPE combined with LCC. Here, we further emphasize that the liquid approach suppresses

individual sampling error due to the inherent averaging. Note, that some literature data obtained from microreflectance spectra on ME nanosheets deviates from the LPE data. This may be attributed to the different sample types (*e.g.* partial intercalation, inhomogeneous strain) and the different type of the measurement which is discussed in more detail elsewhere.¹⁰ The empiric decrease of the A-exciton position with increasing layer number is consistent with an exponential decay, as described by equation 25:

$$E_A = E_{A,Bulk} + (E_{A,ML} - E_{A,Bulk})e^{-\left(\frac{\langle N \rangle_{vf}-1}{N_0}\right)} \quad (\text{Eq. 25})$$

Here, E_A represents the measured A-exciton energy, $E_{A,Bulk}$ and $E_{A,ML}$ are the respective A-exciton energies of the bulk layered crystal and a monolayer and N_0 describes the rate at which the exciton energy approaches the value for the bulk (*i.e.* $E_{A,Bulk}$). Hence, N_0 is a characteristic, phenomenological decay constant empirically determined for each of the four TMDs.

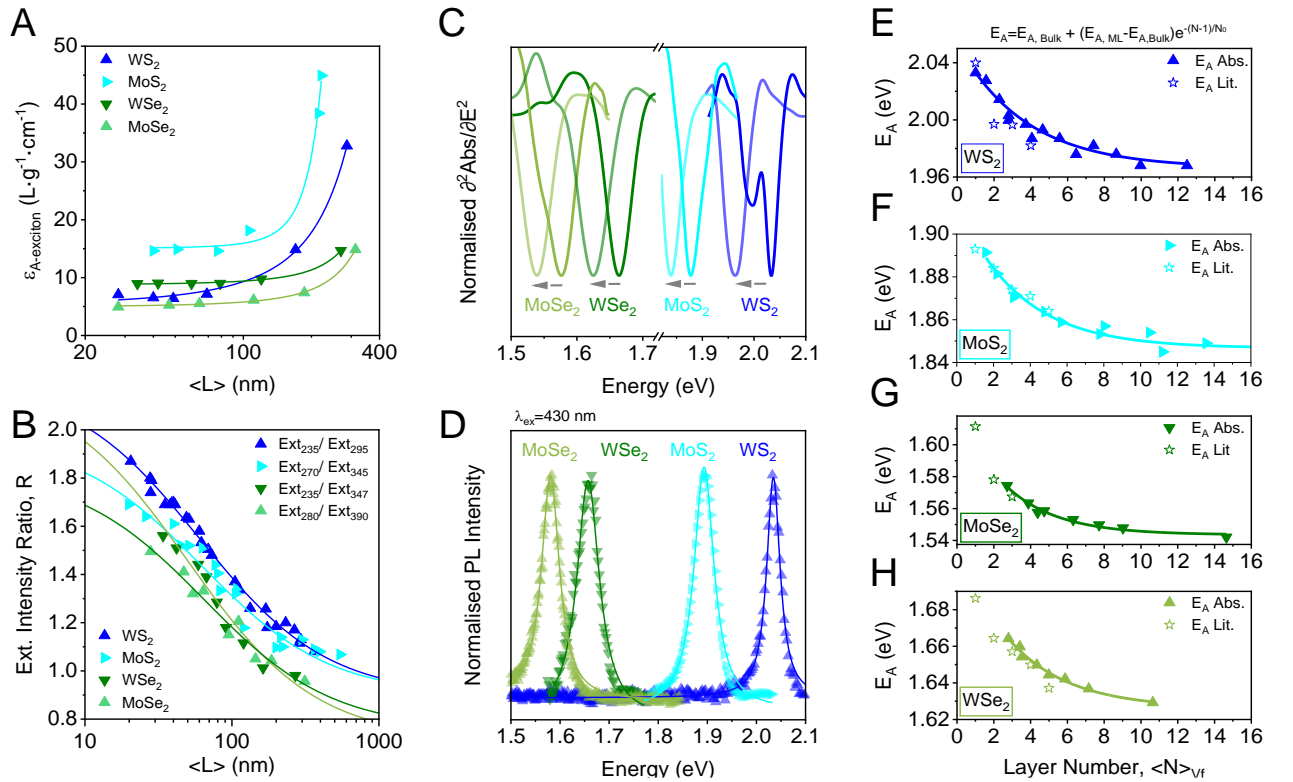


Figure 4.1-2: Changes of observed optical transitions with nanomaterial size. (A) Extinction coefficient at the A-exciton resonance as function of material lateral size. (B) Extinction intensity ratios over nanosheet length for different liquid-exfoliated TMDs. Previously reported data for MoS₂ and WS₂ is included.^{48, 70} (C) Second derivative of the TMD A-exciton region. Data for dispersions, containing thin (darker line) and thick (lighter line) is shown for each material. The arrows indicate the thickness-dependent shift. (D) PL emission spectra of monolayer-enriched samples. The excitation wavelength was 430 nm. (E-H) Energetic position of the A-exciton resonance as determined from absorbance spectra in comparison to literature data. The data from the literature is shifted by a constant offset in each case: WS₂ (E): 20 meV, MoS₂ (F): 12 meV, WSe₂ (G): 20 meV and MoSe₂ (H): 19 meV. Previously reported data on WS₂ and MoS₂ is included to the fits.^{48, 70} The lines are exponential fits in accordance with Eq. 25. Reproduced and adapted with permission from ¹⁰.

Chapter 4 – Size-Dependent Properties

The resulting parameters from fitting the data to equation 25 (Figure 4.1-2 E-H) is shown in Table 4.1-3. Note that this empiric fitting function is not restricted to TMDs, and can be potentially applied to any exfoliated 2D-materials where excitonic shifts with layer number are observed.

Table 4.1-3: Fit parameters for the A-exciton energy as function of layer number (Figure 4.1-2 E-H, Eq. 25) for each of the four TMDs under study. Rearranging Eq. 25 allows to describe $\langle N \rangle_{Vf}$ as a function of E_A .

	$E_{A,ML}$ (eV)	$E_{A,Bulk}$ (eV)	N_0
MoS ₂	1.895	1.846	3.37
MoSe ₂	1.599	1.544	2.80
WS ₂	2.033	1.966	3.72
WSe ₂	1.692	1.626	3.29

The data extracted from the fits (Figure 4.1-2 E-H) for $E_{A,Bulk}$ match well to the corresponding data reported in literature (Figure 4.1-3 A).^{166, 170, 171} However, comparison of monolayer resonances to literature values is challenging due to their significantly increased sensitivity to changes of the dielectric environment. Hence, values of $E_{A,ML}$ which are usually reported for nanosheets on a substrate cannot be compared to dispersed nanosheets coated with a surfactant. In addition, except for WS₂, no peak splitting between mono- and few-layered nanosheets is observed in the second derivative of the absorbance spectra. Consequently, no monolayer resonance can be measured directly, but inferred from the fit data. This scales well with the PL emission peaks (Figure 4.1-3 B) except for the selenides, which exhibit a comparatively larger Stokes shift than the sulfides as described above. These findings imply, that the data fitting is valid. However, for fitting limited data sets, fits may be more reliable if the parameters $E_{A,Bulk}$ and/or $E_{A,ML}$ are fixed to literature values. For each TMD, the difference between $E_{A,ML}$ and $E_{A,Bulk}$ is shown in Figure 4.1-3 C and represents the range over which the exciton position can vary for different material thicknesses. Interestingly, materials with the same transition metal atom show a similar range in this regard. For the two tungsten-based TMDs a range of 67 meV (WS₂) and 65 meV (WSe₂) is found while the molybdenum-based TMDs show ranges of 49 meV (MoS₂) and 56 meV (MoSe₂), respectively (Figure 4.1-3 C). In addition to that, a roughly linear scaling of N_0 with $E_{A,Bulk}$ (from LPE fits) is empirically observed (Figure 4.1-3 D).

To better understand this finding, factors influencing the energetic position of the A-exciton have to be considered. In general terms, the exciton energy is the energy of the free-particle band gap (E_g), which is the onset of unbound electrons and holes, minus the exciton binding energy (E_b).¹⁶³ As the dielectric screening is substantially larger in the bulk material, E_b tends to be comparatively large for the nanomaterial. For example, bulk MoS₂ shows an exciton binding energy of ~50 meV (Figure 4.1-3 E),¹⁷² while it is several hundred meV in confined systems, such as 2D nanosheets.¹⁶³ Especially in 2D-systems, quantum confinement effects on excitonic transitions in a single layer would contribute four times more strongly to the binding energy compared to a 3D-hydrogenic model

Chapter 4 – Size-Dependent Properties

although excitonic transitions are localized within the covalent nanosheet plane.¹⁷³ Additional contributions arise from changes of the effective Coulomb interaction strength between the charge carriers which is reduced for stronger dielectric screening (*i.e.* increasing layer number). A lower effective Coulomb interaction leads to two effects: a decrease of E_b , and to shifts of the free particle band gap of similar magnitude as the thickness changes from mono-layered to bulk material.¹⁶³

While the absolute energetic position of the excitonic resonance (E_A) can directly be measured in simple experiments, absolute values for E_g and E_b are much harder to determine and require either independent knowledge over the free-particle bandgap which can be determined *via* tunneling spectroscopy¹⁷⁴ or can be derived from probing into higher excited states.¹⁷⁵ The major problem with such experiments is that reported data for TMDs is scattered as the interpretation of such experiments is delicate. However, the same sheet-to-sheet variations as generally observed for single nanosheet measurements, particularly changes with respect to static dielectric screening or doping may apply.¹⁶³ Exciton binding energies in the range of 500-600 meV seem reasonable values for free-standing (*i.e.* suspended) nanosheets,¹⁷⁶ but can be significantly lower when deposited on a substrate or in presence of a solvent/stabiliser.^{121,177} In few-layered nanosheets, both E_g and E_b scale with the nanosheet layer number, but the absolute changes of these optical transitions result from a non-trivial combination of different contributions. First, E_g depends on the inter-layer hybridisation of electronic states, which is essentially identical to quantum confinement effects observed in III-V and in II-VI quantum wells.¹⁷⁸ Such effects can indeed be comparatively strong in case of semiconducting TMDs (*e.g.* for Γ and $\Lambda/Q/\Sigma$ valleys) due to strong contributions of the chalcogen orbitals to the respective electronic wavefunctions and lead to substantial overlap integrals from states in neighboring layers. However, the wavefunctions that determine the onset of the optical absorbance (*i.e.* K-points of the Brillouin zone) are mostly localized at the transition metal and thus show a lower coupling to proximate layers.^{115,179} However, even small coupling contributes shifts of the band gap. Second, the effective Coulomb interaction strength varies with layer number due to changes of the dielectric screening as discussed above. While the degree of the screening effect depends on the dielectric permittivity of the nanomaterial and its environment, it strongly depends on the distance to the surroundings. Thus, the screening efficiency increases with material thickness as the outer layers increase the distance of the surrounding dielectric environment to the inside layers. Hence, E_g is shifted towards lower energy which is partially cancelled out by a simultaneous decrease of E_b .

Nonetheless, shifts can be observed due to a remaining absolute transition energy and the thickness dependence of E_g and E_b leads to a similar correlation of E_A with the thickness, as described by equation 26 and shown in Figure 4.1-2 E-H:

$$E_A(N) = E_g(N) - E_b(N) \quad (\text{Eq. 26})$$

Particularly interesting in this regard is the magnitude of the changes for each parameter with material thickness. A schematic illustration of this dependence is shown in Figure 4.1-3 F for MoS₂. E_g and

Chapter 4 – Size-Dependent Properties

E_b vary in range of 300-400 meV when going from bulk material to a single layer while E_A shows a comparatively small change by 30-40 meV. Note that it was possible to quantify this small shift by the use of ensemble measurements of nanosheets with well-defined average size and layer number in a homogeneous dielectric environment enabled through LPE and LCC.

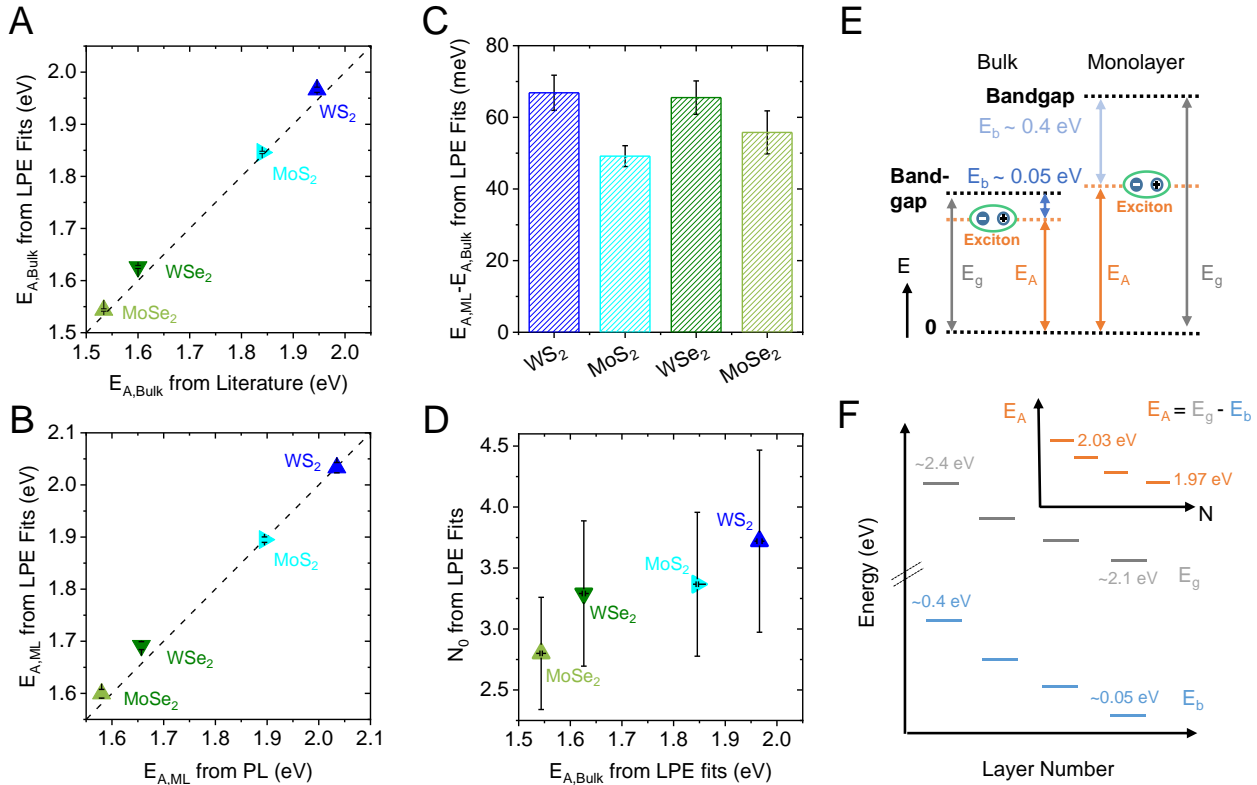


Figure 4.1-3: Results of fitting the exponential A-exciton – layer number dependence. (A) Plot of the bulk exciton energy extracted from the fit of the LPE samples *versus* literature data.¹⁶⁶ The line represents $y=x$. (B) Plot of bulk monolayer energy extracted from the fit of the LPE samples versus the position of the PL lines presented in Figure 4.1-2 D. (C) Plot of the difference in monolayer and bulk exciton energies for the different TMDs. (D) Decay constant representing rate at which the monolayer A-exciton approaches the bulk value as function of bulk exciton energy. (E-F) Schematic representation of changes in the band gap at the K-point and A-exciton binding energies as function of layer number. The indicated values are taken from the literature.^{163, 172} Both the band gap at the K-point and the A-exciton binding energies decrease by 0.3-0.35 eV as the layer number is increased from monolayer to bulk. As a result, the optical gap (*i.e.* the measured A-exciton binding energy) only weakly depends on layer number, but in a well-defined way (see Figure 4.1-2). Reproduced and adapted with permission from ¹⁰.

These results should be considered in the general framework of changes in the electron hybridization and Coulomb effects. Especially contributions of the latter on the relation between N_0 and $E_{A,Bulk}$ (Figure 4.1-3 D) can be explained with the Moss relation which suggests that a higher band gap leads to a decreased inherent material permittivity. This would result in a smaller contribution of the materials permittivity to the dielectric screening (*i.e.* smaller contribution of Coulomb effects to the thickness dependence) for an increase of the band gap. This, in turn suggests an increased phenomenological decay constant (N_0) as observed in Figure 4.1-3 D. A microscopic origin of this effect is discussed quantitatively and in more detail elsewhere, using a theoretical quantum electrostatic

Chapter 4 – Size-Dependent Properties

heterostructure (QEH) approach.¹⁰ However, apart from quantitative discrepancies between the calculations and the experiment, the proposed mechanism of a thickness-dependence for both the band gap and the binding of a van der Waal crystal is confirmed by theory. Moreover, the progression of the free particle band gap and the exciton binding energy with material thickness can be unified by the change of the dielectric screening providing a useful new approach for studying Coulomb interaction effects in other van der Waals crystals.

To summarise the results presented in this Chapter, four group-VI TMDs (WS₂, MoS₂, WSe₂ and MoSe₂) were studied with regard to size-dependent changes of the extinction, absorbance, scattering and photoluminescence response using ensembles of nanosheets to provide a large-number statistic averaging in each measurement in a homogenous dielectric environment. This enables to correlate even subtle changes of the optical response for few-layered nanosheets to nanosheet dimensions, such as the layer number. For each TMD, at least six fractions containing different sizes of nanosheets were prepared and material dimensions were quantified by statistical AFM measurements, as discussed in detail in Chapter 3.1. This information was correlated to the optical response of each fraction which enables to derive quantitative metrics for the lateral material size and layer number, by rearranging equation 24 and 25 as shown below (Eq. 27 and Eq. 28):

$$\langle L \rangle = \frac{B_1 - B_2 \cdot R}{A_2 \cdot R - A_1} \quad (\text{Eq. 27})$$

$$\langle N \rangle = 1 - \ln \left(\frac{E_A - E_{A,Bulk}}{E_{A,ML} - E_{A,Bulk}} \right) \cdot N_0 \quad (\text{Eq. 28})$$

The fit parameters for both metrics are summarised in Table 4.1-1 (for $\langle L \rangle$) and Table 4.1-3 (for $\langle N \rangle$), respectively. This allows to accurately determine these quantities from simple optical measurements of unknown samples without tedious microscopy statistics. In addition, size-dependent extinction, absorbance and scattering coefficients are provided by size correlation to gravimetric nanomaterial masses.

The probably most interesting observation is a minor, but systematic blueshift of the lowest energy excitonic transition with decreasing material thickness for all four TMDs. The shifts originate from two effects of almost similar magnitude, but opposite signs: changes of the exciton binding energy and of the electronic band gap. The presented experimental data is supported by first principles and shows, that the shift of the A-exciton resonance is larger for the tungsten-based TMDs compared to the molybdenum-based compounds under study, which suggests a dependence of the absolute energetic shift on the mass of the metal atom. In contrast, the change-rate, at which the shift is observed when going from bulk to monolayers depends on the materials' band gap at the K-point of the Brillouin zone.

The overall data analysis shines light on fundamental properties of excitonic transitions in TMDs as function of their layer number. This is particularly interesting in the regime of few-layered nanosheets which are more difficult to study in ME samples. This way of analysis may also be applied

Chapter 4 – Size-Dependent Properties

to other 2D-materials which might enable to identify unifying principles across different layered crystals.

4.2 Indium Selenide

To test the applicability of models that describe changing optical properties with material size as described in detail for TMDs, a comparison to other 2D-materials is required. To this end, optical properties of six different size-fractions of γ -InSe nanosheets with material dimensions, were studied by extinction, absorbance and Raman/PL measurements. Size-dependent trends in the optical spectra are correlated to average material dimensions, determined by statistical AFM measurements as discussed in Chapter 3.2. In addition, the nanomaterial concentration of all fractions was determined by gravimetric filtering which enables to determine wavelength and size-dependent extinction, absorbance and scattering coefficients for the γ -InSe nanosheets as exemplarily shown for a fraction containing relatively large nanosheets (Figure 4.2-1 A). The spectra show four broad excitonic features at 920, 500, 370 and 285 nm (1.35, 2.48, 3.35 and 4.35 eV, respectively), in accordance with literature, which we label as P1-4.¹⁸⁰ While the excitonic transition close to the band edge is associated with the nIR-PL emission of the material,^{180, 181} a reasonable peak analysis is not feasible for the LPE γ -InSe nanosheets due to the low oscillator strength of the transition. Furthermore, contributions from scattering in the extinction spectra mask the exciton resonance and the low signal-to-noise ratio in absorbance spectra of smaller nanosheet sizes does not allow a reliable evaluation. However, other excitonic transitions are expected to show similar shifts with material layer number as the lowest energy resonance. In addition, the same effects from dielectric screening, quantum confinement, material edges and light scattering, as discussed in more detail for TMDs in Chapter 4.1, are expected to hold for γ -InSe nanosheets. Systematic changes of the optical spectra with material dimensions are indeed observed for the γ -InSe, as exemplarily shown for the extinction coefficient (Figure 4.2-1 B). The combination of edge effects and contributions from scattering lead to changes of extinction peak intensity ratios, as indicated by the grey arrow. In addition, systematic changes of energetic exciton resonances can be observed as exemplarily shown for P3 which is attributed to confinement and dielectric screening effects, as described in Chapter 4.1. Figure 4.2-1 C shows the second derivative of the spectra in the region of P3 which allows a more reliable determination of the peak positions, as discussed in the previous Chapter. The same observations can be made in absorbance measurements, where contributions from scattering are excluded (Appendix 4.2).

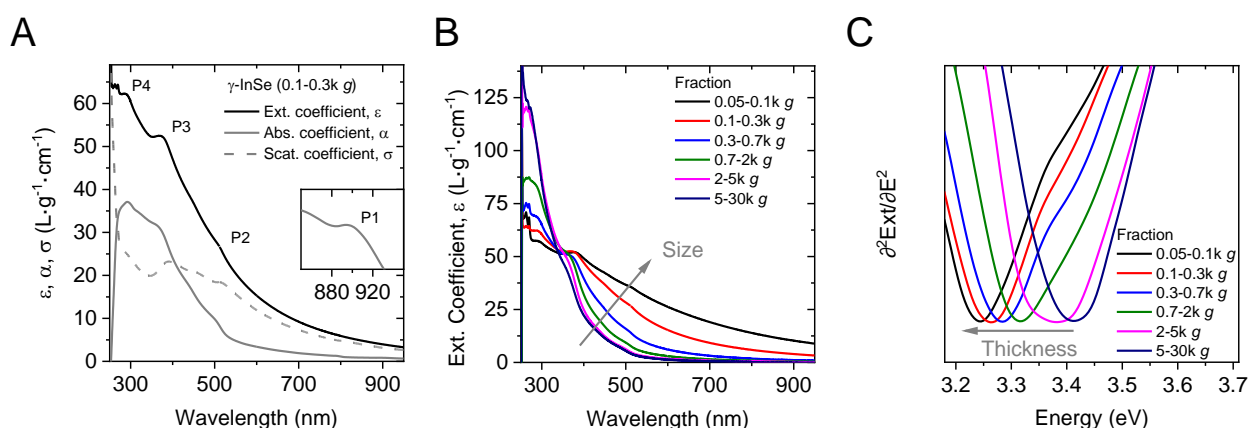


Figure 4.2-1: Impact of γ -InSe nanosheet sizes on the optical spectra. (A) Extinction, absorbance and scattering coefficient spectra of a fraction containing relatively large nanosheets of γ -InSe. The scattering contribution is non-negligible but for the given nanosheet size comparatively small in this example. (B) Extinction coefficient spectra of γ -InSe dispersions with varying size- and thickness distributions from the ultraviolet to nIR range of the electromagnetic spectrum. A systematic change is observed for the extinction coefficient with material dimensions. (C) Second derivative of the P3-exciton region from the same spectra as shown in (B). Note that extinction peak positions are red-shifted compared to absorbance (Appendix 4.2) which is attributed to contributions from scattering.

As changing material dimensions are associated with different edge to basal plane ratios and thus with contributions to the optical spectra, changes of the wavelength-dependent extinction and absorbance spectra are expected with the lateral size of the nanosheets. Extinction coefficients for different wavelengths are plotted as a function of average nanosheet length (Figure 4.2-2 A) to quantify the impact of material edges and the scattering contribution to the extinction spectra. The coefficients at 285, 341 and 700 nm show a different trend with size, respectively. The extinction coefficient at 285 nm shows a systematic decrease, following equation 24 and is thus attributed to the increasing impact of chemically different material edges. The extinction coefficient at 700 nm shows roughly a power law decrease with decreasing material sizes which can be ascribed to scattering contributions that exceed the light absorbance for a given material size in this wavelength range. The coefficient at 341 nm is size invariant. This is most likely because the two effects are cancelled out within the accessible nanomaterial size-range. Empirically, this wavelength thus enables a reliable determination of the nanomaterial concentration independent of the material size.

The changing edge contribution with material size can be used to derive metrics for the nanosheet lateral dimensions. This is achieved by fitting the most significant change of the absorbance and extinction intensity ratios with material size to equation 24 (Figure 4.2-2 B). The fits for both curves seem reasonable and allow a reliable determination of the nanomaterial length from extinction or absorbance spectra, respectively. Furthermore, changes of the excitonic resonance energy are expected with varying layer number. However, a reliable evaluation of peak positions requires ideally narrow transitions which applies best to resonance P3 at ~ 370 nm. For the analysis, centre of mass peak positions from the second derivative of the extinction and absorbance spectra are plotted as function of the nanosheet layer number. An exponential trend, resembling observations made for the TMDs is found and can be fitted in good agreement with equation 25, as suggested in Chapter 4.1.

Chapter 4 – Size-Dependent Properties

As a result, the fitted data as shown in Figure 4.2-2 B-C can be rearranged to derive metrics for the mean nanosheet length and thickness from simple extinction or absorbance measurements (see Eq. 27 and 28).

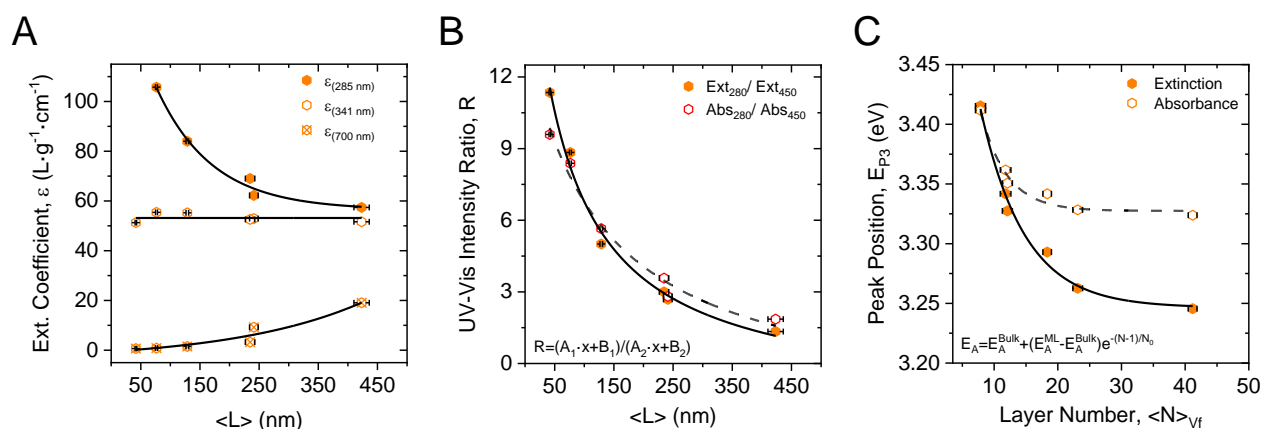


Figure 4.1-2: Quantified changes optical spectra with material dimensions for γ -InSe. (A) Size-dependent changes of the extinction coefficients of γ -InSe at different wavelengths. (B) Intensity ratio at 280 nm over 450 nm serves as metric for the lateral nanosheet size. (C) Plot of the centre of mass peak positions as function of mean layer number extracted from extinction and absorbance spectra. The fit represents a metric for the nanosheet layer number and allows to extract the phenomenological decay constant (N_0) for excitonic resonances in γ -InSe.

The fit parameters of the scaling in extinction and absorbance measurements to equation 27 and 28 are summarised Table 4.2-1, respectively.

γ -InSe is a direct band gap semiconductor independent of the material thickness, as mentioned in Chapter 3.2 exhibiting nIR photoluminescence. However, as confirmed by shifts of the excitonic resonances with the nanosheet layer number in absorbance spectra, the PL energy is expected to change with layer number due to confinement and dielectric screening effects. This has indeed been observed on micromechanically-exfoliated InSe in literature.^{124, 125}

In the solvent system NMP used for the exfoliation, no PL could be observed. It is possible that this is due to some charge or energy transfer that results in PL quenching, as also observed for other materials such as carbon nanotubes¹⁸² and TMDs.^{183, 184} To recover pristine material properties, nanosheet dispersions of different sizes were filtered and washed until no residual solvent was detected *via* Raman spectroscopy (Figure 4.2-2 A). In each case, PL emission from the filtered material could be observed for measurements in the Raman spectrometer with an excitation wavelength of 785 nm. The spectra in Figure 4.2-2 A are normalised to the $A_{1g}^{(1)}$ Raman mode of γ -InSe so that different PL intensities can be regarded as measure of variations in PL quantum yields across the fractions. The variations in PL intensity are not systematic with size. It is possible that reabsorption and inner filter effects occur to a varying extent across the films- depending on film thickness which could not be controlled through filtration. Note, that a discussion of the absolute quantum efficiency is also not possible as this would require PL measurements performed in an integrating sphere on dispersions

Chapter 4 – Size-Dependent Properties

or films exhibiting identical optical densities at the excitation wavelength combined with careful calibration to an optical standard. This was not feasible for these samples.

In addition to qualitative changes in PL quantum yield, a systematic redshift of the PL emission is observed with decreasing material thickness (Figure 4.2-2 B), in accordance with literature¹⁸⁵ and with observations made for TMDs. As the lowest energy transition (P1) could not be resolved in absorbance measurements on LPE γ -InSe nanosheets, no direct correlation between the absorbance and the PL emission is possible, but the phenomenological decay constant (N_0) is expected to be somewhat related to the material band gap and should thus be similar for the different excitonic resonances. However, the PL emission is broad and asymmetric which makes a reliable determination of the peak position challenging. In addition, the samples were transferred onto a substrate (filter) which leads to changes of the dielectric environment and results in random restacking, *i.e.* effective changes to the average layer number. This renders a direct comparison to the dispersions inappropriate. The fitting parameters for the PL data presented in Table 4.2-1 do therefore not match the absorbance data.

To additionally characterise the PL emission and excitation behaviour of the filtered nanosheets, PLE maps of filtered nanomaterial were acquired using excitation wavelengths from 300-600 nm, recording the PL emission between 800 and 1250 nm (exemplarily shown in Figure 4.2-2 C for the 0.1-0.3k g fraction). This resolves a broad single emission peak at ~950 nm (1.3 eV). While the position is broadly in agreement with observations from Raman/PL measurements, it should be noted that the feature is significantly less asymmetric pointing towards issues of reabsorption in the Raman measurement. The excitation spectrum (vertical line in the PLE contour plot) resembles the optical absorbance of the nanomaterial confirming that the absorbance and emission stem from the same species. However, due to the issues of comparing the PL response of filtered films discussed above, no further experiments were carried out at the current stage. In the future, these should focus on more well-defined thin films achievable for example by deposition at the liquid-liquid interface.

Chapter 4 – Size-Dependent Properties

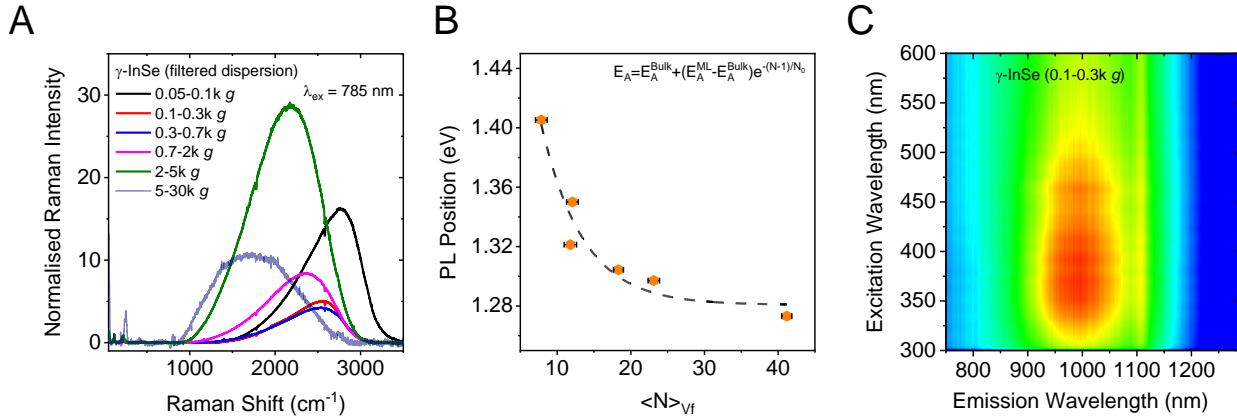


Figure 4.2-3: Radiative decay of excited states in deposited γ -InSe nanosheets. (A) Raman/PL measurements on filtered and washed γ -InSe nanomaterial from dispersions containing different nanosheet sizes. (B) PL peak positions as determined from centre of mass peak positions from Raman measurements. Note, that broad and asymmetric emission features complicate accurate determination of peak positions. (C) PL excitation and emission map of filtered nanosheets of a fraction containing relatively large nanosheets.

Table 4.2-1: Fitting Parameters for physically meaningful description of observed changes with material dimensions.

	$\langle L \rangle = \frac{B_1 - B_2 \cdot R}{A_2 \cdot R - A_1}$					$\langle N \rangle_{vf} = 1 - \ln \left(\frac{E_A - E_{A,Bulk}}{E_{A,ML} - E_{A,Bulk}} \right) \cdot N_0$		
	R	A_1 (nm ⁻¹)	B_1	A_2 (nm ⁻¹)	B_2	E_A^{ML} (eV)	E_A^{Bulk} (eV)	N_0
γ -InSe (Ext)	280 nm	-0.0269	20.53	0.0163	1	3.695	3.246	6.91
γ -InSe (Abs)	450 nm	0.0163	13.86	0.0081	1	3.516	3.318	5.60
γ -InSe (PL)	n.a.	n.a.	n.a.	n.a.	n.a.	1.769	1.281	5.64

In review of the results presented above, six fractions of exfoliated γ -InSe nanosheets have been studied for size-dependent changes of optical transitions. Similar trends as discussed in the previous Chapter could be identified and quantified by correlating optical extinction and absorbance measurements to nanosheet sizes as determined by statistical evaluation of nanosheet dimensions from AFM measurements as detailed in Chapter 3.2. The same models that describe size-dependent trends for TMDs can be applied to γ -InSe (Eq. 24 and 25). Metrics for the nanomaterial concentration, as well as for average material lateral size and thickness for extinction and absorbance measurements are presented, respectively.

Photoluminescence of the nanomaterial was recovered after deposition and extensive washing of the material to remove solvent molecules from the nanosheet surface. Changes of the emission energy are observed for different material sizes in qualitative resemblance of trends extracted from extinction and absorbance measurements. Absolute changes of the PL emission energy cannot directly be compared to the absorbance measurements likely due to changes of the dielectric environ-

ment and restacking upon nanomaterial deposition. However, the recovery of the PL emission implies, that pristine material properties can be restored after removal of leftover solvent or stabiliser so that more comprehensive studies will be accessible in films with improved quality.

4.3 Transition Metal Hexathiohypo Diphosphates

Successful exfoliation of MPS_3 crystals in liquid phase was reported before (*e.g.* for NiPS_3) by Dangol *et al.*¹⁸⁶ However, in this earlier work, no size selection or statistic evaluation of nanosheet dimensions is addressed. Thus, no size-dependent optical properties have been reported as yet. In particular for LPE nanosheets, these have shown to be powerful as they can be used to assess nanosheet dimensions spectroscopically.^{12, 48, 71} Such aspects are summarised in the following discussion for three different examples of MPS_3 nanosheets (NiPS_3 , FePS_3 and MnPS_3 , respectively). For each material, two different sets of samples, using different size selection sequences have been prepared and nanomaterial dimensions were quantified by statistical AFM evaluation of each material fraction, respectively (see Chapter 3.3). This knowledge allows to quantify qualitative changes of the optical spectra as shown in Figure 4.3-1. The spectra presented in Figure 4.3-1 A show the wavelength-dependent extinction, absorbance and scattering coefficients of NiPS_3 for a fraction containing relatively large nanosheets, isolated in the first centrifugation cascade (0.1-0.4k g). Note, that similar spectra are shown in Appendix 4.3-1 for each material. The following discussion is limited to changes of the NiPS_3 spectra to obviate redundant data presentation as analogous trends can be observed for the three material systems.

In case of NiPS_3 , three broad excitonic transitions can be observed centred at 600, 390 and 270 nm (2.07, 3.18 and 4.59 eV), respectively. The peaks are referred to as P1, P2 and P3 for the following discussion as indicated in Figure 4.3-1 A. The spectra shown in Figure 4.3-1 B display the dependence of the extinction coefficients as a function of wavelength, calculated from gravimetric mass determination. The optical spectra show a clear change with varying material dimensions, as indicated by the grey arrow. Similar changes have been demonstrated for other 2D-material systems discussed in the previous Chapters and suggest that both lateral size and layer number have an impact on the spectral shape and thus the extinction/absorbance coefficient, as also reported elsewhere.^{12, 48, 71, 72, 75} Hence, the same effects as discussed in detail in Chapter 4.1 influence the optical response of the nanomaterial. To obtain a deeper understanding of the spectral changes, a detailed analysis is required.

As shown by the set of extinction/absorbance/scattering spectra in Figure 4.3-1 A, the absorbance approaches zero at small energies (*i.e.* long wavelengths). This is observed for all fractions (Appendix 4.3-1) and implies an optical band gap at ~875 nm (1.42 eV) which shifts towards ~825 nm (*i.e.* larger optical gap of 1.50 eV) for increasing centrifugal force and thus smaller nanoparticles. In agreement with the TMDs and γ -InSe discussed above, the extinction spectra of the size-selected

Chapter 4 – Size-Dependent Properties

fractions vary systematically with size, as indicated by the arrow in Figure 4.3-1 B. Similar changes, but with smaller magnitude can be observed in the absorbance spectra (Appendix 4.3-1) so that these can be attributed to size-dependent contributions from material edges. The fact, that the observed changes in the absorbance spectra are smaller than in the extinction spectra arises from additional contributions due to light scattering.

As mentioned above, the spectra show three broad excitonic features. Small shifts of the peak positions can already be observed in Figure 4.3-1 B. As these transitions are broad and superimposed on a background, the second derivative of the spectra is calculated for a more reliable determination of the peak position. The second derivative of the spectral region of 300-450 nm is shown for cascade 1 (Figure 4.3-1 C). The centre of mass peak position of the extinction and the absorbance peaks, respectively, is determined. In both cases, a systematic redshift is observed with decreasing material dimensions, in agreement with comparable data of other 2D-materials, such as TMDs^{48, 71, 118} (Chapter 4.1) or GaS¹² and γ -InSe (Chapter 4.2).

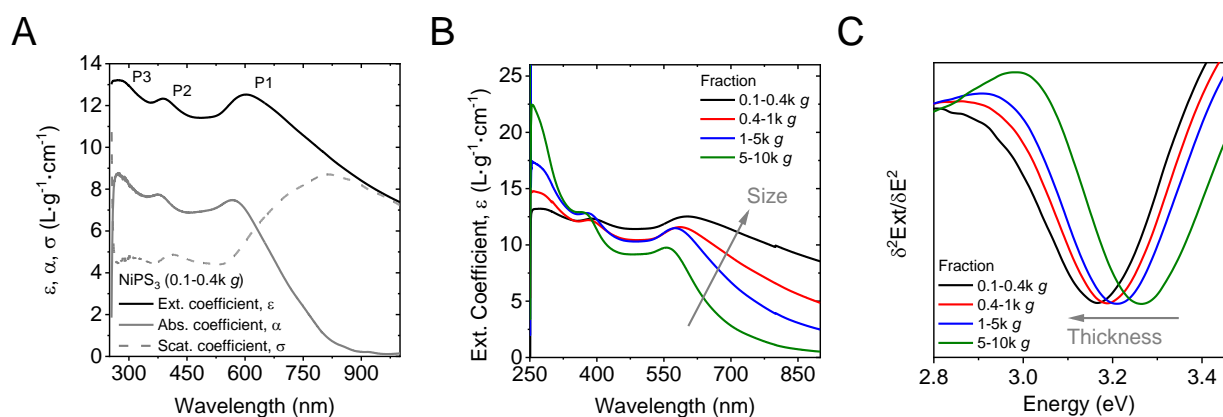


Figure 4.3-1: Impact of NiPS₃ nanosheet sizes on the optical spectra. (A) Extinction, absorbance and scattering coefficient spectra of a fraction containing relatively large nanosheets of NiPS₃. The scattering contribution is non-negligible, but for the given nanosheet size comparatively small in this example. (B) Extinction coefficient spectra of NiPS₃ dispersions with varying size- and thickness distributions from the ultraviolet to nIR range of the electromagnetic spectrum. A systematic trend is observed for the extinction coefficient with changing material dimensions. (C) Second derivative of the P2-exciton region from the same spectra as shown in (B). Extinction peak positions are red-shifted compared to absorbance (Appendix 4.3-1) which is attributed to contributions from scattering.

For a quantitative analysis of the trends discussed above, changes of the spectra are plotted as a function of nanomaterial dimensions (Figure 4.3-2). The evolution of the extinction coefficient of NiPS₃ is shown in Figure 4.3-2 A for three different wavelengths as function of lateral nanosheet size. While the extinction coefficient at 383 nm remains mostly constant, a roughly linear increase of the coefficient and a power law increase with nanomaterial size is observed for the extinction coefficients at 480 nm and 900 nm, respectively. The power law dependence of the extinction coefficient at 900 nm can be ascribed to the intensifying scattering contribution with increasing material sizes.⁷³

In addition, intensity ratios of the optical spectra scale with $\langle L \rangle$ as discussed above due to different electronic contributions from basal planes and edges to the average extinction/absorbance

coefficient. This relation can be used to construct quantitative metrics for the material lateral size by fitting the intensity ratios (*e.g.* $\frac{Ext_{370\text{ nm}}}{Ext_{460\text{ nm}}}$) as function of the arithmetic mean nanosheet length using equation 24 (Figure 4.3-2 B). The fit parameters are shown in Table 4.3-1. While the data fits well to the model described in Chapter 4.1, an empirically linear trend is observed for the discussed intensity ratio within the accessible size-range. For simplifying matters and to reduce the degrees of freedom of the fitting function, an alternative fit of the data to a linear function is presented as a second metric that describes the relation between the average lateral NiPS₃ nanosheet size according to equation 29:

$$\langle L \rangle = -\frac{480.8 \cdot Ext_{370\text{ nm}}}{Ext_{460\text{ nm}}} - 815.7 \quad (\text{Eq. 29})$$

Another empirical metric can be derived using the scattering contribution in the non-resonant regime of the extinction spectra. According to Mie theory,^{73, 187} the non-resonant scattering follows a power law with wavelength. In agreement with this, the extinction coefficient at >900 nm shows a power law scaling, as indicated in Figure 4.3-1 A. Unfortunately, Mie theory and related approximations do not strictly hold for platelets, and no approximations have been derived for the particle size-range under study here. To this end, a comprehensive study on 2D-nanosheets has recently been carried out which showed that the scattering coefficient is determined predominantly by the longest dimension of an anisotropically, platelet-like nanoparticle (*i.e.* L), while the scattering exponent scales with the characteristic nanosheet area.⁷³ Thus, it is in principle possible to determine $\langle L \rangle$ from the non-resonant scattering. The major limitation of this approach described by Harvey *et al.* is that a size determination from the scattering contribution requires independent knowledge over the nanomaterial concentration. In contrast to that, peak intensity ratios are generally accessible from a single measurement. It is suggested that the scattering coefficient scales with a peak intensity ratio at a non-resonant (900 nm) to resonant (460 nm) wavelength. It is found that this results a power law scaling (Appendix 4.3-2) that allows to fit the extinction ratio resulting in a second alternative equation (Eq. 30) for the determination of $\langle L \rangle$:

$$\langle L \rangle = 75.02 \left(\ln \left(\frac{Ext_{900\text{ nm}}}{Ext_{460\text{ nm}}} + 0.03388 \right) + 4.204 \right) \quad (\text{Eq. 30})$$

As discussed above, a fundamental understanding of contributions to optical spectra enables to derive quantitative metrics for a reliable determination of the nanomaterial concentration and the nanosheet dimensions. While metrics for lateral sizes are useful, it is of equal interest to determine the nanosheet thickness from standard spectroscopy. The layer number is reflected in changes of excitonic resonance energies, as discussed in more detail in Chapter 4.1. Analysis of excitonic transition energies (*i.e.* peak positions of P1-3) with the average nanosheet layer number should thus enable to extract quantitative relations by applying an appropriate fitting function (Eq. 25). The result is shown in Figure 4.3-2 C and allows to rearrange equation 25 to a metric for the NiPS₃ layer number for both, extinction and absorbance spectra, respectively (Eq. 28).

Chapter 4 – Size-Dependent Properties

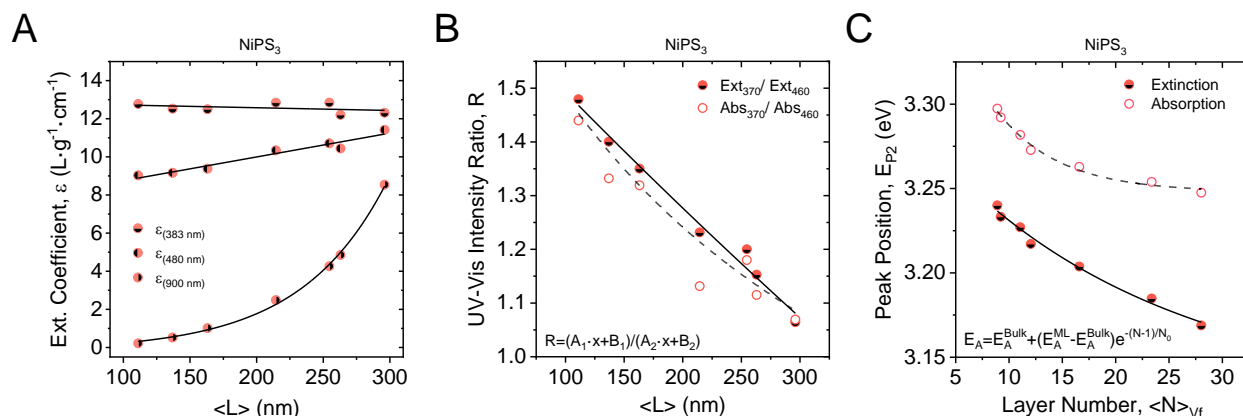


Figure 4.3-2: Quantified changes optical spectra with material dimensions for NiPS₃. (A) Size-dependent changes of the extinction coefficients of NiPS₃ at different wavelengths. (B) Intensity ratio at 370 nm over 460 nm serves as metric for the lateral nanosheet size. (C) Plot of the centre of mass peak positions as function of mean layer number extracted from extinction and absorbance spectra. The fit represents a metric for the nanosheet layer number and allows to extract the phenomenological decay constant (N_0) for excitonic resonances in MPS₃-species

Similar plots can be prepared for FePS₃ and MnPS₃ as well, while MnPS₃ is limited to a metric for the nanosheet length as no excitonic transitions are observed for the material (Appendix 4.3-2). The fitting parameters for the scaling of the intensity ratios with lateral size according to equation 24 and the shift of the excitonic resonances with nanosheet thickness according to equation 25 are summarised in Table 4.3-1. Equivalent data for FePS₃ and MnPS₃ nanosheets is included. Note that analysis of excitonic transitions was not possible for MnPS₃ as no excitonic resonances were resolved in the extinction and absorbance spectra for the LPE nanosheets within the accessible wavelength range.

Table 4.3-1: Fitting Parameters for physically meaningful description of observed changes with material dimensions.

		$\langle L \rangle = \frac{B_1 - B_2 \cdot R}{A_2 \cdot R - A_1}$				$\langle N \rangle_{vf} = 1 - \ln \left(\frac{E_A - E_{A,Bulk}}{E_{A,ML} - E_{A,Bulk}} \right) \cdot N_0$		
	R	A_1 (nm ⁻¹)	B_1	A_2 (nm ⁻¹)	B_2	E_A^{ML} (eV)	E_A^{Bulk} (eV)	N_0
NiPS ₃ (Ext) ¹¹	370 nm	-0.0185	1.72	0.0003	1	3.456	3.139	5.80
NiPS ₃ (Abs)	460 nm	-0.0009	1.69	0.0011	1	3.414	3.243	5.93
FePS ₃ (Ext)	350 nm	-0.0065	6.92	0.0053	1	3.199	3.041	6.31
FePS ₃ (Abs)	500 nm	-0.0054	5.88	0.0020	1	3.231	3.043	5.37
MnPS ₃ (Ext)	310 nm	-0.5212	999.14	1.3468	1	n.a.	n.a.	n.a.
MnPS ₃ (Abs)	400 nm	-0.0140	18.05	0.0063	1	n.a.	n.a.	n.a.

To summarise the results presented in this Chapter, three different metal hexathiohypo diphosphates (NiPS₃, FePS₃ and MnPS₃) were prepared by means of LPE and LCC and studied for their extinction, absorbance, scattering behaviour with changing material dimensions. To verify the robustness of the size selection *via* LCC, two cascades with slightly different centrifugation boundaries have been tested for their size-dependent optical response. The data of both cascades fall on the same curves, which allows to provide quantitative metrics for nanomaterial concentration, lateral size and

layer number by fitting changes of the optical spectra of the combined datasets for each material to theoretical models as discussed in Chapter 4.1. In addition, two alternative metrics for the nanosheet lateral size were presented using an empirical linear fit with less degrees of freedom than the model considering two electronic contribution (Eq. 29) and a power law dependence of an extinction intensity ratio in the non-resonant to resonant regime (Eq. 30).

4.4 Ruthenium Chloride

Size-dependent material properties of α -RuCl₃ nanosheets, prepared by inert gas exfoliation using standard Schlenk techniques and subsequent LCC were studied by extinction and absorbance measurements. Size-dependent trends in the optical spectra of seven fractions prepared are correlated to average nanosheet dimensions as determined by AFM statistics, as well as gravimetrically determined nanomaterial masses. Spectroscopic metrics for the material thickness and concentration are presented in the following discussion which conveniently allows to determine average material dimensions by standard spectroscopy.

For material characterisation, similar effects as discussed in detail for TMDs in Chapter 4.1 are considered. Changes of the optical spectra with material dimensions are thus attributed to contributions from size-dependent light scattering as well as edge and confinement effects and due to layer-dependent dielectric screening. Figure 4.4-1 A shows the wavelength-dependence of the extinction, absorbance and scattering coefficients for a dispersion containing relatively large α -RuCl₃ nanosheets. Compared to TMDs, a relatively low scattering contribution is observed for α -RuCl₃ in spite of similar dimensions pointing towards a high oscillator strength. The extinction coefficient spectra of all extracted nanosheet sizes are shown in direct comparison in Figure 4.4-1 B. For absorbance coefficients, see Appendix 4.4. All nanosheet sizes show two broad resonant features at \sim 370 and \sim 555 nm. It is conspicuous, that the change of the spectra with nanosheet size is very subtle compared to the other 2D-materials thus not enabling a reliable determination of the lateral size. However, as demonstrated for other materials, in addition to the nanosheet lateral size, also the nanosheet thickness has a characteristic impact on the spectra, manifested by systematic shifts of excitonic resonances with nanosheet thickness. Such a behaviour is indeed observed for the α -RuCl₃ nanosheets as well. For a precise determination of the peak position, the second derivative of the spectra was calculated (Figure 4.4-1 C). A redshift of the exciton energy with increasing nanosheet thickness is observed for both, extinction and absorbance spectra (absorbance is shown in Appendix 4.4) as indicated by the grey arrow. This agrees with reported data on excitonic transitions of other 2D-materials.^{10, 11, 48}

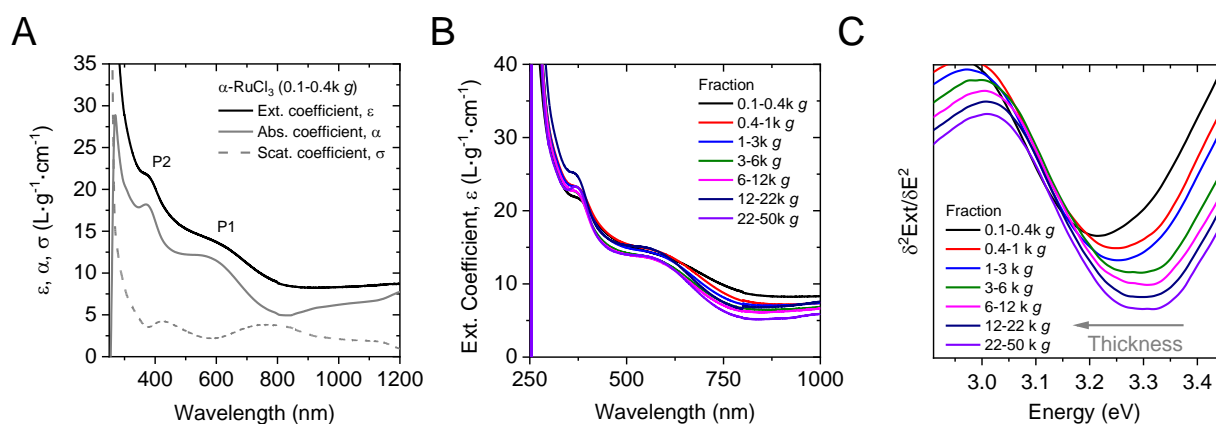


Figure 4.4-1: Impact of nanosheet sizes on the optical spectra. (A) Extinction, absorbance and scattering coefficient spectra of a fraction containing relatively large nanosheets of α -RuCl₃. The scattering contribution is non-negligible, but for the given nanosheet size comparatively small for this material. (B) Extinction coefficient spectra of α -RuCl₃ dispersions with varying size- and thickness distributions from the ultraviolet to nIR range of the electromagnetic spectrum. No systematic trend is observed for the extinction coefficient with changing material dimensions. (C) Second derivative of the P2-exciton region from the same spectra as shown in (B). Extinction peak positions are red-shifted compared to absorbance (Appendix 4.4) which is attributed to contributions from scattering.

The extinction coefficients at different fixed wavelengths (400, 500 and 600 nm), as determined by gravimetric filtering of the nanomaterial, show no systematic change with nanosheet sizes (Figure 4.4-2 A). While this behaviour is not usually observed for 2D-material systems, it enables to reliably determine the α -RuCl₃ nanosheet concentration at any wavelength, using the Beer-Lambert law. This is useful, as the narrow band gap material absorbs light even in the nIR region and concentrations can potentially be determined even in a mixture with other materials. However, due to the experimental error associated with gravimetric nanosheet mass determination, especially for material systems which might decompose during extensive washing steps to remove residual CHP from the nanosheet surface, an alternative method to extract the subtle changes in the optical spectra with material size is required. In this regard, normalisation of the spectra is beneficial. Indeed, after normalising the spectra (Appendix 4.4), subtle systematic changes of the optical extinction and absorbance spectra with material size are revealed. This allows to identify the most significant changes to fit intensity ratios to the average nanosheet dimensions as shown in Figure 4.4-2 B. In agreement with the data presented in previous Chapters, variations of the intensity ratio can be fitted to equation 24. The observed trend may thus be attributed to changes of the nanosheet edge to plane ratio, which are electronically dissimilar and thus contribute to the spectra in a different way. However, considering the small changes observed for α -RuCl₃ intensity ratios, the electronic edge contribution to the spectra seems to be negligible within the accessible wavelength range and does not allow for a reliable nanosheet length determination from the absorbance or extinction spectroscopy.

In addition to the changes of extinction or absorbance intensity ratios, the shift of excitonic resonances with material size (Figure 4.4-1 C) can be analysed in more detail. Transition energies were determined from the centre of mass peak positions from the second derivative of the spectra and

correlated to the average nanosheet layer numbers in the respective fractions as suggested by equation 28 (Figure 4.4-2 C). Fitting the data provides a metric for α -RuCl₃ nanosheet layer number from both, extinction and absorbance spectroscopy.

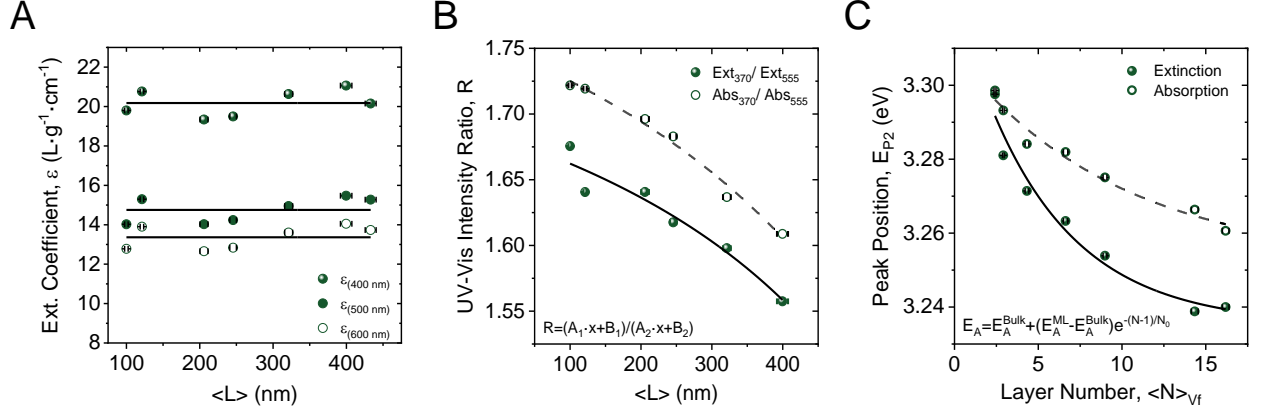


Figure 4.4-2: Quantified changes optical spectra with material dimensions for α -RuCl₃. (A) Extinction coefficients of α -RuCl₃ at different wavelengths remain approximately constant across all fractions. (B) Intensity ratio at 370 nm over 555 nm scale weakly with the lateral size. Note, that the changes in the spectra are very subtle in case of α -RuCl₃ compared to other materials. (C) Plot of the centre of mass peak positions as function of mean layer number extracted from extinction and absorbance spectra. The fit represents a metric for the nanosheet layer number and allows to extract the phenomenological decay constant (N_0) for excitonic resonances in α -RuCl₃.

The fit parameters for changes in intensity ratio with $\langle L \rangle$ and peak position with $\langle N \rangle$ for both extinction and absorbance are summarised in Table 4.4-1.

Table 4.4-1: Fitting Parameters for physically meaningful description of observed changes with material dimensions. Note that changes of intensity ratio are systematic but comparatively subtle and do not allow for a reliable nanosheet length determination from the absorbance or extinction spectra.

	$\langle L \rangle = \frac{B_1 - B_2 \cdot R}{A_2 \cdot R - A_1}$					$\langle N \rangle_{vf} = 1 - \ln \left(\frac{E_A - E_{A,Bulk}}{E_{A,ML} - E_{A,Bulk}} \right) \cdot N_0$		
	R	A_1 (nm ⁻¹)	B_1	A_2 (nm ⁻¹)	B_2	E_A^{ML} (eV)	E_A^{Bulk} (eV)	N_0
RuCl ₃ (Ext)	$\frac{370\text{ nm}}{555\text{ nm}}$	-0.0019	1.68	-0.0010	1	3.309	3.235	5.30
RuCl ₃ (Abs)		-0.0018	1.75	-0.0009	1	3.305	3.262	6.47

To summarise size-dependent changes of the optical response of α -RuCl₃ nanosheets, seven fractions containing different dimensions of nanomaterial were studied for systematic changes of their optical response by extinction and absorbance spectroscopy. Similar systematic trends as reported for other 2D-material systems were identified. However, changes of relative peak intensities due to edge and scattering effects are insignificant and do not allow for an accurate lateral size determination from the extinction of the absorbance spectra. Overall, the magnitude of the changes is small so that extinction, absorbance and scattering coefficients from gravimetric nanomaterial filtering can be considered size-independent over the entire spectral region. The reasons for this behaviour are unclear. In contrast, variations of the excitonic resonances show systematic shifts in accordance with equation

Chapter 4 – Size-Dependent Properties

28, as discussed in more detail for TMDs in Chapter 4.1. This allows to reliably determine the nanosheet average layer number from extinction or absorbance measurements.

4.5 Chromium Telluride

In the following Chapter, size effects of CrTe₃ nanosheets on their optical properties are discussed. To this end, five different sizes of CrTe₃ nanosheet ensembles prepared by a combination of LPE and LCC in an inert gas atmosphere were subjected to extinction and Raman measurements. Average nanosheet sizes were correlated to changes of the optical response in agreement with results presented in previous Chapters. Figure 4.4-1 A shows the systematic change of the extinction spectra with material size. No meaningful results could be achieved from gravimetric filtering of the CrTe₃ particles, as the nanomaterial is highly sensitive to ambient conditions which complicates quantitative analysis. Soluble products from material decomposition may be washed off and additional contributions from degradation products might falsify the resulting weight of the nanomaterial. Hence, trends of the extinction were extracted from normalised spectra. The knowledge over material size and thickness from the statistical AFM evaluation of each sample (Chapter 3.5) allows to quantify the observed changes in the extinction spectra. However, the analysis is limited by the absence of excitonic transitions in the spectra. Hence, the focus is laid on the evaluation of the extinction spectra of CrTe₃ nanosheet with lateral size which is best described by intensity ratios, as indicated by the arrows in Figure 4.4-1 A. A well-defined trend with the material lateral size is observed for the extinction intensity ratio at 400/1000 nm which can be fitted to equation 24 Figure 4.4-1 B. This agrees with the presented model for different electronic contributions for nanosheet edges and planes changing with sheet size and allows to derive a metric for the material lateral size in accordance with equation 24. The fitting parameters for the trends of the CrTe₃ extinction are $A_1 = -0.0121$, $B_1 = 11.659$, $A_2 = 0.017$ and $B_2 = 1$.

In addition to extinction measurements, Raman experiments were carried out on different sizes of exfoliated nanosheets. The material was drop-cast into a drill hole on a gold-coated aluminium substrate and encapsulated in a nitrogen atmosphere before the measurements (Chapter 7.3). As observed for the bulk material, three distinct peaks are found for all sizes of the exfoliated nanosheets, but red-shifted with respect to the bulk reference (Figure 4.4-1 C-D). To understand this behaviour in more detail, a density functional perturbation theory (DFPT) approach was applied on both, monolayered and bulk CrTe₃ to calculate phonon resonances (Figure 4.4-1 C-D) by the group of Janina Maultzsch (for details see Chapter 7.4). Discrepancies between measured and calculated modes are observed. However, shifts of transition frequencies and changes of the absolute intensity are suggested by the theoretical approach, as experimentally observed. However, it should be noted that changes in the Raman spectra on all size selected fractions were not systematic in the applicable size-range independent of the excitation wavelength (see Chapter 5.5).

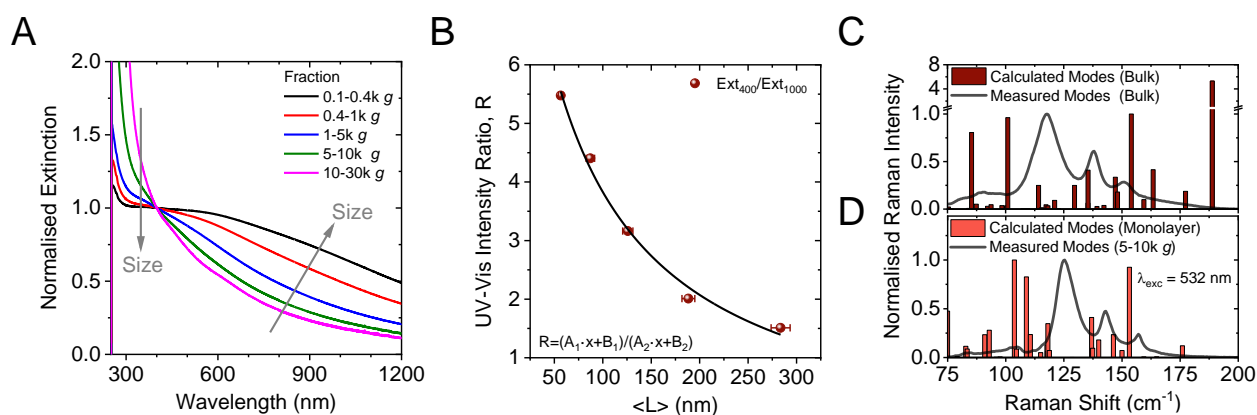


Figure 4.5-1: Size-dependent optical response of CrTe₃. (A) Extinction coefficient spectra of CrTe₃ dispersions with varying size- and thickness distributions from the ultraviolet to nIR range of the electromagnetic spectrum. A systematic trend is observed for the extinction coefficient with changing material dimensions. (B) Intensity ratio at 400 nm over 1000 nm serves as metric for the lateral size. (C-D) Raman measurements and DFPT calculations for Bulk solid (C) and delaminated (D) CrTe₃. Both, theory and experiment show changes of the phonon modes with material thickness.

In addition, large discrepancies between measurements acquired at different spots of the same sample are observed as exemplarily shown in Figure 4.4-2 A-B for measurements of small (5-10k g) and large (0.1-0.4k g) nanosheets at two different spots, respectively. Slight shifts, as well as differences in intensity ratios can be observed for measurements in the centre compared to measurements at the edge of the drill hole where the nanosheets are deposited in. The effect is more pronounced for the 5-10k g fraction, which may be due to a different alignment of the small nanosheets (*i.e.* random orientation) compared to the larger sheets. A custom-built sample holder was used to further study the angle dependence between the incident light beam used for the excitation of vibrational modes and the CrTe₃ crystals. To achieve this, the surface of a comparatively large bulk crystallite was cleaned by applying and removing adhesive tape. The cleaned sample was then tilted and measured applying 5° steps in a total range of 50° (Figure 4.4-2 C). A systematic change of the Raman intensity ratios at 113 cm⁻¹ and 157 cm⁻¹ with the excitation angle is observed with progressing sample rotation (Figure 4.4-2 D). A roughly linear scaling of the intensity ratio within the studied tilting range is observed. While this is an unexpected result, it is important to note that the experimental setup used for the sample tilting is prone to experimental errors and observed trends might not be fully quantitative. In addition, no information can be provided about the crystallographic orientation of the crystallite. Absolute changes of the sample tilting is thus not accessible, but the measurements show, that the spatial orientation of the crystal has an impact on the observed phonon excitation.

A direct comparison of the peak intensity ratios of the two different positions measured for the small exfoliated nanosheets (Figure 4.4-2 A) to the results presented in Figure 4.4-2 D, suggests tilting angles of about 10 and 30° for the exfoliated small nanosheets, respectively which fits roughly to the geometry of the conical drill hole where the material was deposited in (see Chapter 7.3). This is an interesting observation, as it implies that the nanosheets align on the substrate surface even for confined deposition from dispersion at high concentrations. In addition, it emphasizes that care needs

Chapter 4 – Size-Dependent Properties

to be taken to evaluate spectroscopic changes across samples even in the case of nanosheet ensembles produced from LPE.

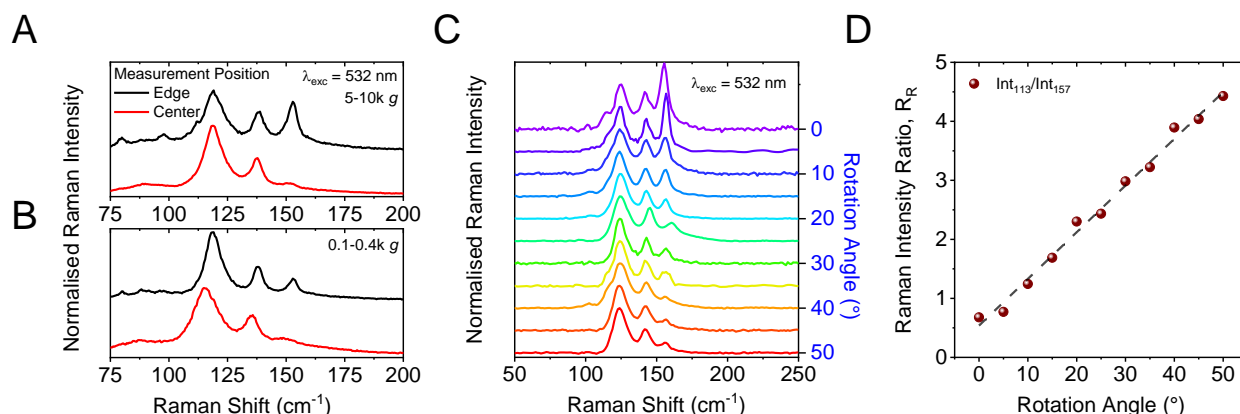


Figure 4.5-1: Angle dependence of CrTe₃ phonon modes. (A-B) Raman measurements (excitation wavelength 532 nm) for different sizes of LPE nanosheets acquired at different positions of the substrate (*i.e.* drill hole, see Chapter 7.3). Both, relatively small (A) and relatively large (B) nanosheets show distinct signals for measurements at the edges and for measurements at the centre of the hole. (C) Raman spectra of a CrTe₃ crystal for different tilting angles. (D) Intensity ratio for the phonon modes at 113 and 157 cm⁻¹. The roughly linear trend is strictly empirical and is not correlated to crystallographic data, but serves the purpose to demonstrate the angle dependence of the phonon resonances with the angle of the incident light for excitation.

Similar changes with lateral nanosheet size as observed for other 2D-materials were found for CrTe₃ and allow to extract spectroscopic metrics in good agreement with equation 24 which considers two different electronic contributions (*i.e.* edges and basal planes) to the extinction spectra. No excitonic transitions can be observed in the extinction and absorbance spectra of CrTe₃ nanosheet dispersions. These are also not reported in literature. In addition to extinction, Raman measurements were carried out on encapsulated nanomaterial which was deposited inside a drill hole on an aluminium substrate in an inert gas atmosphere to protect the nanosheets from changing environmental influences. A dependence of the tilting angle (*i.e.* measurement position in the drill hole) could be identified by measuring a bulk reference in differently tilted positions. Systematic changes of phonon resonances were found, following a roughly linear trend with the tilting angle of the crystal. No correlation with crystal parameters was possible using this setup, but a comparison to observed changes for exfoliated nanomaterial fits to the geometry of the conical drill hole in which the material was deposited. This implies, that the nanomaterial aligns flat on the substrate surface even at high concentrations which are used for the material deposition in a confined space.

4.6 Organic 2D-Polymers

As extensively discussed in literature and also in previous Chapters, a number of inorganic 2D-materials^{12, 48, 71, 75, 188} and graphene⁷⁰ all exhibit size-dependent optical properties. In particular, extinction and absorbance spectra show well-defined changes with nanosheet lateral size and layer

number due to edge and confinement effects, as well as contributions from non-resonant light scattering.⁴⁸ To assess the limits of the developed models, similar experiments have to be considered for the organic compounds under study. The impact of material dimensions on the optical response of two different 2D-polymer systems, prepared by means of LPE and LCC is therefore discussed within the following Chapter. For both material systems, five fractions containing different size- and thickness-distributions of nanosheets are considered. The discussion is split into two parts, individually addressing observed changes for both 2D-polymers.

2D-Pol(1) as per Kory *et al.*¹⁵⁴

Extinction spectra corresponding to different sizes of tip-exfoliated 2D-Pol(1) in aqueous sodium cholate, size-selected by LCC are shown in Figure 4.6-1. As exemplarily deconvoluted for the fraction isolated between 0.1 and 0.4k g, the absorbance is superimposed on a scattering background which follows a power law in the non-resonant regime and is red-shifted to the absorbance in the resonant regime (Figure 4.6-1A) in analogy other material systems. The spectra show characteristic peaks in the ultraviolet region between 300-400 nm which can be attributed to the anthracene core (Figure 4.6-1 A, P1-4) in the polymer subunits. The vibronic fine-structure of the lowest energy resonance is clearly resolved in both, extinction and absorbance spectra which resembles the structural homogeneity of the 2D-polymer and is unchanged for different nanosheet sizes (Figure 4.6-1 B).

The absorbance spectra imply an optical band edge at ~400 nm (3.10 eV), which is almost identical to unsubstituted anthracene in ethanol.¹⁸⁹ The strong resemblance of the optical transitions observed for the two 2D-polymer and anthracene is additionally confirmed by measuring extinction spectra of unsubstituted anthracene, as well as the monomer molecule of 2D-Pol(1) dispersed in aqueous sodium cholate and in various other solvents for comparison (Appendix 4.6-1). No change of transition energies is observed for P1-4 with nanosheet dimensions, which may be attributed to strong localisation of excited states within individual anthracene units as the covalent 2D-plane does not possess a delocalised π -system. This also explains why no systematic shifts with nanosheet size are observed in contrast to excitonic transitions in materials where the excitons are delocalised over the sheets.

However, the two additional features are observed in the extinction and absorbance spectra (P5 and P6). While P5 was identified to correspond to contributions from cyanopyridine, which was used for the pre-oriented crystallisation of the monomer before polymerisation,¹⁵⁴ the exact origin of P6 remains unclear. Contributions from P5 and P6 are larger with respect to the vibronic fine structure of the anthracene core for measurements of the floating fraction in LSF experiments compared to LCC sediments. These observations imply that both features originate from soluble impurities or solvent leftovers from synthesis which are removed from the material during the size selection as only the sedimented nanomaterial is redispersed and subjected to analysis. This is further supported by comparison to bath-exfoliated samples, where the exfoliation energy was insufficient for material delamination. Hence, large crystallites are dispersed which clearly show leftovers of cyanopyridine as well as contributions from the template monomer which results in a doubling of the anthracene peaks (see Appendix 4.6-2).¹⁵⁴ The sig-

Chapter 4 – Size-Dependent Properties

nificant narrowing of the finger-structure which is observed for tip-exfoliated samples compared to measurements of larger crystallites (Figure 4.6-1 and Appendix 4.6-2) may be attributed to almost complete removal of the template monomer also in the case of few-layer sheets.

In addition to the changes discussed above, fundamental phenomena such as contributions from particle size-dependent light scattering can be observed in the extinction spectra, as indicated by the grey arrow in Figure 4.6-1 B. A systematic trend with particle size is observed after normalisation to the first vibronic transition of the spectra. The evolution of the intensity ratio between the first vibronic transition and the scattering background is shown in Figure 4.6-1 C and can be fitted to a power law function in agreement with recent reports on non-resonant scattering contributions for 2D-materials (dashed black line).⁷³ A metric for the nanosheet lateral size based on this fit can be derived, as shown in equation 31.

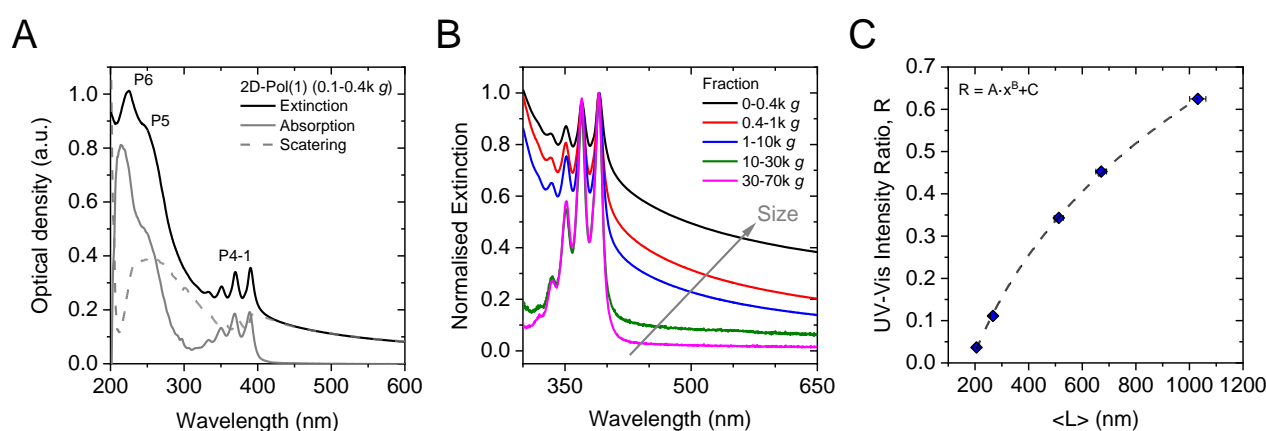


Figure 4.6-1: Impact of 2D-Pol(1) nanosheet sizes on the optical spectra. (A) Extinction, absorbance and scattering spectra of a fraction containing relatively large nanosheets of 2D-Pol(1). The scattering contribution is non-negligible, but for the given nanosheet size comparatively small for the organic compound. (B) Normalised Extinction spectra of 2D-Pol(1) dispersions with varying size- and thickness distributions from the ultraviolet to the visible range of the electromagnetic spectrum. A systematic trend is observed for the extinction coefficient with changing material dimensions. (C) Intensity ratio at 450 nm over 390 nm may serve as metric for the lateral size. A power law fit can be applied, as indicated in the plot.

$$\langle L \rangle = \left(\frac{\text{Ext}_{450}}{\text{Ext}_{390}} + 1.52 \right)^5 \quad (\text{Eq. 31})$$

In addition to extinction and absorbance measurements, PL measurements on 2D-Pol(1) nanosheets were performed for the different sizes of the nanomaterial. PLE maps of the exfoliated species were recorded to study the excitation and emission behaviour of the material, as representatively shown for a fraction containing relatively large nanosheets (0.4-1k g) in Figure 4.6-2 A (for other sizes see Appendix 4.6-3). The contour plot resembles the vibronic fine-structure for the PL-excitation as observed for the extinction and absorbance measurements in Figure 4.6-1 A. For a better comparison, individual emission and excitation spectra were acquired and plotted together with the corresponding absorbance spectra, as exemplarily shown for the 0.4-1k g fraction (Figure 4.6-1 B). For PL excitation, 333 nm was used to avoid contributions from Raman modes of water as indicated

by the dashed black line in the PLE-map (here: small peak at 375 nm). The absorbance and the PL-excitation spectra show the same fine structure which results from different allowed electronic transitions from the lowest vibrational level in the ground state to the higher vibrational energy levels in the excited state. The emission spectra also contain multiple peaks, as already shown in the PLE-map. The most favourable transitions from excited state to the ground state are the ones where the rotational and vibrational electron density between the stages maximally overlap. The vibrational energy level spacing of 2D-Pol(1) seems similar for the ground and excited state, which is a common observation for fluorophores and results in the mirror image of the absorption spectrum for the PL emission. This means that the states displayed in the absorbance measurements are involved in the radiative relaxation process. Hence, the exfoliated 2D-Pol(1) nanosheets follow the Kasha's and Vavilov's rules¹⁹⁰ which is an untypical observation for a macromolecule and may be attributed to a combination of a well-defined long range order of the 2D-lattice with highly localised excited states in a homogenous dielectric environment.

Structural integrity of the 2D-polymer is therefore expected as this is the case for all size fractions of the nanomaterial (Appendix 4.6-3). Furthermore, no changes of the emission features are observed across the different sizes (Figure 4.6-1 C) as expected from a localised system. Note that the increasing contribution of the peak at 375 nm which is attributed to the decreasing nanomaterial concentration (*i.e.* higher contribution from the Raman mode of the solvent) in fractions isolated at higher centrifugal accelerations.

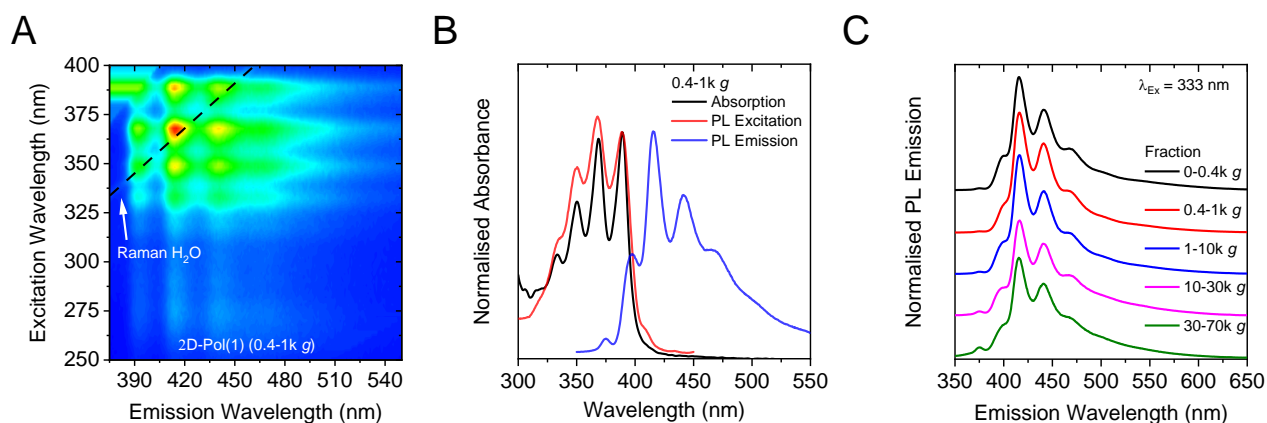


Figure 4.6-2: PL characteristics of 2D-Pol(1) nanosheets. (A) PLE map of dispersed nanomaterial containing relatively large nanosheets. The dashed line shows where Raman modes of the solvent (*i.e.* water) contribute to the spectra. (B) Normalised absorbance, PL excitation and PL emission spectra of the same 2D-Pol(1) dispersion as shown in (A). The PL excitation spectra were acquired for the emission at 475 nm. The emission was recorded with an excitation wavelength of 333 nm. (C) PL emission spectra for different sizes of 2D-Pol(1) measured using similar conditions as in (B). The spectra were normalised and are shown with a horizontal offset for clarity.

In summary, measurements of the optical extinction and absorbance of 2D-Pol(1) reveal a typical acene finger-structure, representing the vibronic fine structure of energetically allowed states. No shifts can be observed with material size which may be attributed to localisation of excited states in the anthracene units in combination with a homogenous dielectric environment of the material.

Chapter 4 – Size-Dependent Properties

Signatures from template monomer in the optical response are only observed for bath-exfoliated samples, where the energy input was not sufficient for efficient exfoliation.

Changes of the non-resonant light scattering can be used to derive a metric for the lateral nanosheet sizes, using the power law dependence of the scattering contribution with particle size (Eq. 31), as discussed elsewhere.⁷³ The optical PL excitation and emission behaviour resembles molecular acene patterns following Kasha's and Vavilov's rules, untypical for a macromolecule. The same behaviour is observed for all nanosheet sizes with minor differences between the spectra. This may be attributed to high long-range order of the 2D-Polymer which provides a homogenous dielectric environment for each emitting anthracene subunit, combined with highly localised excited states caused by the chemical structure of the polymer.

2D-Pol(2N) as per Lange *et al.*²³

In case of the second 2D-polymer, a single broad excitonic transition can be observed at 275 nm (4.51 eV) which is referred to as P1, as indicated in Figure 4.6-3 A. The extinction, absorbance and scattering coefficient spectra have been determined by gravimetric filtering of the nanomaterial and are exemplarily shown for a fraction containing relatively large nanosheets (0.4-1k g). The extinction coefficient spectra of different sizes of 2D-Pol(2N) show a systematic change with the nanosheet lateral size (Figure 4.6-3 B). By eliminating contributions from light scattering by measurement in an integrating sphere, it is clear that not only scattering is responsible for the size-dependent changes of the extinction, but that similar edge and confinement effects previously observed for inorganic 2D-materials^{12, 48, 71, 72, 75} are at place (Appendix 4.6-4). This is of great practical use, as it allows to establish quantitative size and thickness metrics based on optical spectra for rapid size assessment, as discussed below. More importantly, it shows that the optical properties of exfoliated 2D-Pol(2N) exhibit a similar thickness dependence known for inorganic 2D-materials, *i.e.* the properties are governed by the nanosheet layer number in contrast to 2D-Pol(1).

Systematic variations in the spectral profile are observed in the case of the extinction coefficient spectra. For example, above 400 nm the extinction follows a power law decay. This background is more pronounced for larger/thicker nanosheets strongly suggesting that this is due to light scattering which is confirmed by the absorbance coefficient spectra (Appendix 4.6-4) which show no signal in this spectral region. Nonetheless, these absorbance spectra also exhibit sample-dependent changes which we attribute to edge and confinement effects. According to these absorbance coefficient spectra, the exfoliated 2D-Pol(2N) can be classified as wide bandgap semiconductor with an optical gap of ~3.55 eV with a slight dependence of the band edge on nanosheet thickness.

To analyse peak positions in addition to the overall shape, it has been proven useful to plot the second derivative of peaks to reveal fine-structure that is not otherwise accessible (Figure 4.6-3 C).⁷¹ The second derivative in the region of the resonant peak reveals a hidden fine structure resembling vibrational structure of molecules and will be investigated in more detail below.

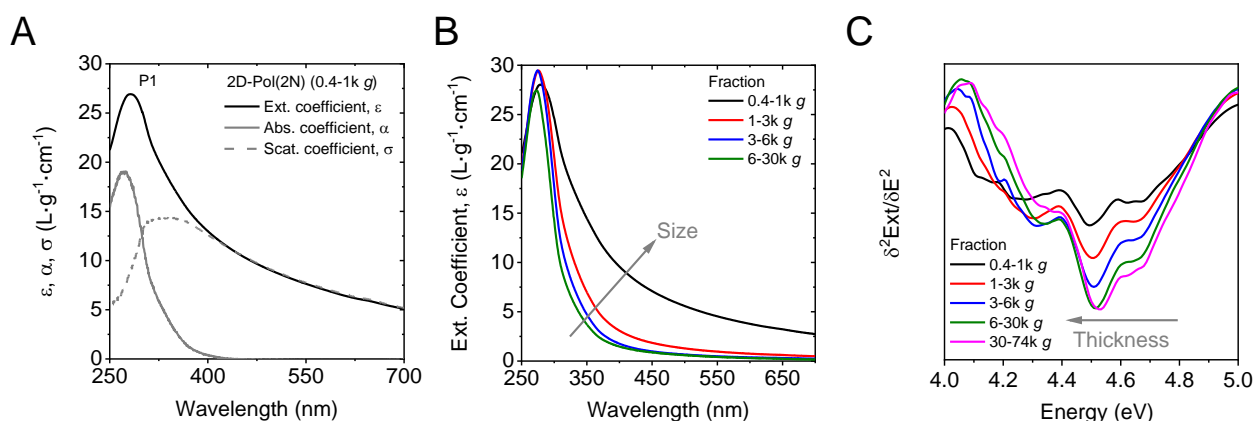


Figure 4.6-3: Impact of 2D-Pol(2N) nanosheet sizes on the optical spectra. (A) Extinction, absorbance and scattering spectra of a fraction containing relatively large nanosheets of 2D-Pol(2N). The scattering contribution is non-negligible for the second organic van der Waals crystal. (B) Normalised extinction spectra of 2D-Pol(2N) dispersions with varying size- and thickness distributions from the ultraviolet to the visible red range of the electromagnetic spectrum. A systematic change is observed for the extinction coefficient with changing material dimensions. (C) Second derivative spectra in the spectra region of P1. Reproduced and adapted with permission from ²³.

To analyse these coefficient spectra in more detail, we plot the extinction coefficient as function of nanosheet length for three different wavelengths in Figure 4.6-4 A (for absorbance see Appendix 4.6-4). The extinction coefficient at 258 nm is size-independent so that this wavelength can be used for a determination of the nanosheet concentration. In the non-resonant regime (*i.e.* at 400 nm), it increases following a power law with nanosheet size. The absorbance coefficient (Appendix 4.6-4) is in turn zero so that the extinction coefficient at this wavelength is essentially a measure of the scattering strength which scales in a well-defined way with nanosheet dimensions.⁷³ This is in contrast to wavelengths in the resonant regime (*e.g.* 210 nm). In this wavelength region, both extinction and absorbance coefficient decrease with nanosheet size which can be attributed to varying contributions from nanosheet edges and basal plane to the absorbance. Also, in absorbance coefficient spectra, a point, where the coefficient is invariant with nanosheet size can be found. In this case, this is observed at the local minimum at 237 nm *i.e.*, slightly blue-shifted compared to the wavelength of the size-independent extinction coefficient. This is because scattering spectra in the resonant regime follow absorbance spectra in shape, albeit red-shifted due the dependence of the resonant scattering with refractive index of the dispersed material.¹⁹¹

Importantly, since the absorbance and extinction coefficient spectra are comparable in shape in the resonant regime, extinction spectra rather than absorbance spectra can be analysed to extract further information. The size-dependent optical response described above gives scope for quantitative metrics to relate the nanosheet lateral size and/or thickness to the spectral profile. This is extremely useful for future optimisation of both exfoliation and size selection, as tedious and time-consuming AFM statistics can be minimized. It has previously been suggested that edge effects are manifested by different absorbance coefficients at edge and central region, respectively.⁴⁸ As a result, peak intensity ratios in the resonant regime are expected to scale with the nanosheet lateral size in a well-defined way according to equation 24 (Chapter 4.1)

Chapter 4 – Size-Dependent Properties

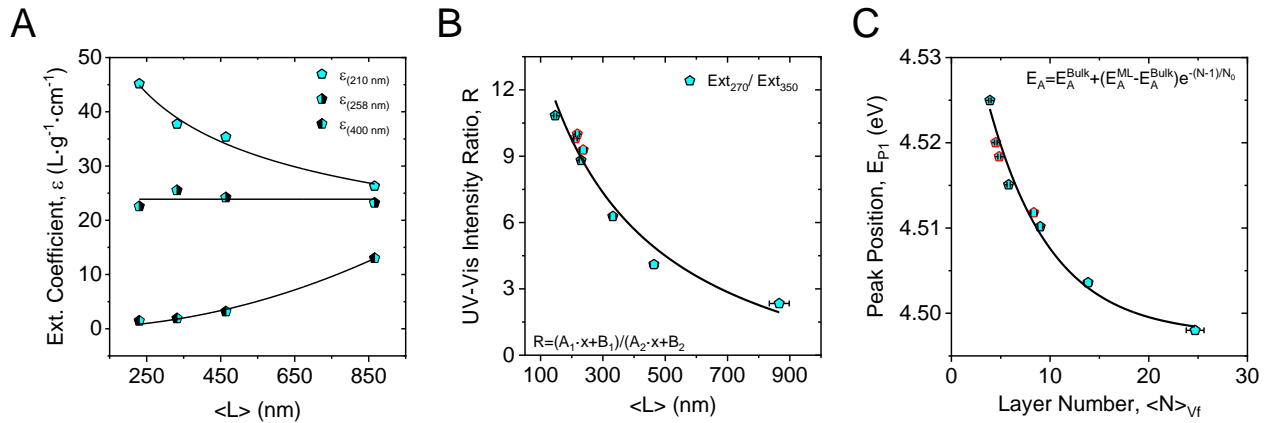
In Figure 4.6-4 B, an extinction peak intensity ratio in the resonant regime (*i.e.* $\frac{Ext_{270}}{Ext_{350}}$) is plotted as a function of mean nanosheet length. Data from the standard cascade (black) and the secondary cascade (red) is included and falls on the same curve (Chapter 3.6). The solid line is a fit to equation 24 and describes the data reasonably well confirming that similar edge effects contribute to the size-dependent optical properties as previously observed for TMDs.^{48, 71} This allows to derive a quantitative relation of the extinction peak intensity ratio to the mean nanosheet length. The fitting parameters are shown in Table 4.6-1. Alternatively, a peak intensity ratio in the non-resonant regime and a wavelength in the resonant regime can be used to express the contribution from scattering to the extinction spectra. As an example, the ratio $\frac{Ext_{500}}{Ext_{240}}$ is plotted as function of nanosheet length (Appendix 4.6-4). Again, the data from the standard cascade and the secondary cascade, respectively, falls on the same curve. The dashed line is an empirical exponential fit which can be rearranged to establish a second length metric according to equation 32:

$$\langle L \rangle = 1053 \ln \left(\frac{\frac{Ext_{500}}{Ext_{240}} + 0.187}{0.167} \right) \quad (\text{Eq. 32})$$

Note that this metric will only be accurate as long as the scattering contribution is not negligible, (*i.e.* for nanosheets >200 nm), as the ratio drops to almost 0 for nanosheets <150 nm.

Perhaps of more interest than metrics for nanosheet length are metrics for nanosheet layer number. In the case of TMDs^{48, 71} and for other 2D-materials discussed in previous Chapters, it was empirically found that the peak energies of the excitonic transitions scale exponentially with layer number due to confinement and dielectric screening effects. To test this for the 2D-Pol(2N), the second derivative of the extinction spectra (Figure 4.6-3 C) are used to determine the peak positions. These are plotted as function of layer number in Figure 4.6-4 C. An exponential decrease with increasing layer number can be observed. Importantly the data from the secondary cascade, where $\langle N \rangle$ and $\langle L \rangle$ are decoupled, fall on the same curve confirming that the peak positions are indeed related to nanosheet thickness rather than length. The fitting parameters are shown in Table 4.6-1.

These metrics are not only powerful for further sample optimization, but are also interesting in its own right, as they suggest that 2D-materials show a generic size-dependent behaviour irrespective of their chemical composition also for organic sheet stacks if excitons are not localised in subunits as was the case for 2D-Pol(1) .



Quantified changes optical spectra with material dimensions for 2D-Pol(2N). (A) Plot of extinction coefficients of 2D-Pol(2N) at three wavelengths as function of nanosheet mean length. (B) Intensity ratio at 270 nm over 350 nm serves as metric for the lateral nanosheet size. (C) Plot of the centre of mass peak positions as function of mean layer number extracted from the extinction spectra. The fit represents a metric for the nanosheet layer number and allows to extract the phenomenological decay constant (N_0) for the P1 resonance of 2D-Pol(2N). The red-rimmed datapoints represent data from secondary cascades. Reproduced and adapted with permission from ²³.

Table 4.6-1: Fitting Parameters for physically meaningful description of observed changes of the optical response of 2D-Pol(2N) with material dimensions.

	$\langle L \rangle = \frac{B_1 - B_2 \cdot R}{A_2 \cdot R - A_1}$					$\langle N \rangle_{vf} = 1 - \ln \left(\frac{E_A - E_{A,Bulk}}{E_{A,ML} - E_{A,Bulk}} \right) \cdot N_0$		
	R	A_1 (nm ⁻¹)	B_1	A_2 (nm ⁻¹)	B_2	E_A^{ML} (eV)	E_A^{Bulk} (eV)	N_0
2D-Pol(2N) (Ext) ²³	$\frac{270 \text{ nm}}{350 \text{ nm}}$	-0.0134	20.47	0.0041	1	4.539	4.497	6.35

Note that in addition to the measurements presented above, further structural characterisation of the 2D-Pol(2N) nanosheets was performed (*i.a.* infrared reflection-absorption spectroscopy, Raman and TEM) which confirms the structural integrity of the nanomaterial as presented elsewhere.²³

To summarise size-dependent trends identified for 2D-Pol(2N), changes of the optical extinction and absorbance resemble observations made for inorganic 2D-materials. Metrics for the material concentration, size and thickness are presented, using models presented in Chapter 4.1, as well as an alternative metric for the lateral size in consideration of the size-dependent scattering contribution of nanoparticles.

Chapter 4 – Size-Dependent Properties

4.7 Unifying Principles for Size-Dependent Phenomena in 2D-Materials

In review of Chapter 4, new insights on excitonic transitions in 2D-materials have been provided using standard optical measurements, such as extinction, absorbance and photoluminescence spectroscopy. Most reports on excited states of layered crystals that can be found in literature consider few-number statistic averaging over single micromechanically-cleaved nanosheets. In contrast to single sheet measurements, nanosheet dispersions prepared by LPE in the concentration range used for the discussed experiments contain a sheet ensemble in the range of $\sim 10^{10}$ nanosheets.¹⁰ In addition, while micromechanically-cleaved nanosheets characteristically exhibit a defined and laterally large surface structure, strain and dielectric inhomogeneities as well as a varying defect contents can hardly be avoided. Therefore, large sheet to sheet variations can be observed even for using similar substrates and for different spots probed on the same sheet.¹²¹ Such environmental impacts are mostly eliminated for LPE nanosheet dispersions as the surrounding liquid environment is quite homogenous and inhomogeneities (*e.g.* from varying defect density) are inherently averaged out. This enables to measure even minor changes of the size-dependent optical properties for such nanosheets. However, a drawback of measurements on LPE nanosheets is that solid size and thickness statistics have to be performed for a meaningful correlation of observed differences in the optical response of nanosheet ensembles.

For all materials under study, at least 5 fractions obtained from size selection *via* LCC were subjected to statistical AFM and optical measurements. which allows to correlate changing properties to average lateral dimensions or layer number.⁴⁷ For TMDs, both layer number and nanosheet length are reflected in a well-defined change of the optical spectra. Practically speaking, this enables to establish quantitative spectroscopic metrics for concentration, $\langle L \rangle$ and $\langle N \rangle$ for the four group-VI TMDs as discussed in Chapter 4.1, which can be used to determine these quantities accurately from optical spectra of unknown samples to avoid tedious statistic measurements of nanosheet dimensions.

For TMDs, probably the most interesting change in the optical spectra is a slight, but systematic blueshift of the A-exciton resonance with decreasing layer number which arises from changes of the electronic band gap and the exciton binding energy. The data reveals that the shift is larger for higher mass of the centred metal atoms which can be associated to the fact that the wavefunctions determining the onset of the absorbance are mostly localized at the metal atoms. In contrast, the rate at which the A-exciton energy shifts from the monolayer to bulk value is widely dependent on the materials' bandgap at the associated point in the Brillouin zone. The overall data evaluation gives new insights into fundamental physical properties of excitonic transitions in 2D-materials.

Similar contributions to the optical spectra as discussed extensively for TMDs *i.e.* effects from layer-dependent dielectric screening and quantum confinement as well as scattering and edge contributions are expected for other 2D-materials. This was shown for various other liquid-exfoliated material systems, including a wide band gap organic 2D-polymer. Developed models to describe trends

Chapter 4 – Size-Dependent Properties

with changing nanomaterial dimensions were successfully applied to develop a library of spectroscopic metrics for the lateral size and for the nanosheet layer number for all materials under study, including a 2D-Zr-MOF ("Green") which is discussed elsewhere,²⁴ as shown in Table 4.7-1.

Table 4.7-1: Fitting Parameters for physically meaningful description of observed changes in the optical response of different 2D-materials with material dimensions.

	$\langle L \rangle = \frac{B_1 - B_2 \cdot R}{A_2 \cdot R - A_1}$					$\langle N \rangle_{Vf} = 1 - \ln \left(\frac{E_A - E_{A,Bulk}}{E_{A,ML} - E_{A,Bulk}} \right) \cdot N_0$		
	R	$A_1(\text{nm}^{-1})$	B_1	$A_2(\text{nm}^{-1})$	B_2	E_A^{ML} (eV)	E_A^{Bulk} (eV)	N_0
WS ₂ (Ext) ¹⁰	235 nm	0.0159	2.20	0.0166	1	2.034	1.957	3.69
WS ₂ (Abs)	295 nm	0.0252	2.66	0.0270	1	2.033	1.966	3.72
MoS ₂ (Ext) ¹⁰	270 nm	0.0144	1.97	0.0160	1	1.896	1.828	5.72
MoS ₂ (Abs)	345 nm	0.0044	2.04	0.0083	1	1.895	1.846	3.37
WSe ₂ (Ext) ¹⁰	235 nm	0.0143	2.20	0.0200	1	1.686	1.610	5.15
WSe ₂ (Abs)	347 nm	0.0219	2.64	0.0308	1	1.692	1.626	3.29
MoSe ₂ (Ext) ¹⁰	280 nm	0.0117	1.83	0.0154	1	1.581	1.516	8.59
MoSe ₂ (Abs)	390 nm	0.0064	1.79	0.0103	1	1.599	1.544	2.80
γ-InSe (Ext)	280 nm	-0.0269	20.53	0.0163	1	3.695	3.246	6.91
γ-InSe (Abs)	450 nm	0.0163	13.86	0.0081	1	3.516	3.318	5.61
NiPS ₃ (Ext) ¹¹	370 nm	-0.0185	1.72	0.0003	1	3.456	3.139	5.80
NiPS ₃ (Abs)	460 nm	-0.0009	1.69	0.0011	1	3.414	3.243	5.92
FePS ₃ (Ext)	350 nm	-0.0065	6.92	0.0053	1	3.199	3.041	6.31
FePS ₃ (Abs)	500 nm	-0.0054	5.88	0.0020	1	3.231	3.043	5.37
MnPS ₃ (Ext)	310 nm	-0.5212	999.14	1.3468	1	n.a.	n.a.	n.a.
MnPS ₃ (Abs)	400 nm	-0.0140	18.05	0.0063	1	n.a.	n.a.	n.a.
RuCl ₃ (Ext)	370 nm	-0.0019	1.68	-0.0010	1	3.309	3.235	5.30
RuCl ₃ (Abs)	555 nm	-0.0018	1.75	-0.0009	1	3.305	3.262	6.47
CrTe ₃ (Ext)	370 nm 555 nm	0.0121	11.65	0.0173	1	n.a.	n.a.	n.a.
2D-Pol(2N) (Ext) ²³	270 nm 350 nm	-0.0134	20.47	0.0041	1	4.539	4.497	6.35
Zr-CAU-45 (Abs) ²⁴	310 nm 230 nm	0.9069	-275.69	0.9000	1	n.a.	n.a.	n.a.

In addition to the metrics shown above, other 2D-materials were reported to show similar trends with nanosheet dimensions throughout literature. Systematic size-dependent changes of the optical response are reported for GaS,¹² GeS,¹³ MoO₂,⁷⁴ PtSe₂,¹⁹² *h*-BN,⁷² black phosphorus⁷⁵ and graphite.⁷⁰ However, most of these reports use different empiric fit functions which makes a direct comparison difficult. The observed spectroscopic changes for these other materials qualitatively fit to trends observed with the materials discussed within the scope of this work and should thus fit to equation 24 and 25. For a solid discussion, the raw data is required which was not accessible in every case. However, the data on *h*-BN,⁷² PtSe₂,¹⁹² GaS,¹² TiS₂¹⁹³ and BP¹²⁷ was provided from the respective authors or collaborators and were refitted to Eq. 24 and Eq. 25, respectively (Appendix 4.7). The results are shown in Table 4.7-2.

Chapter 4 – Size-Dependent Properties

Table 4.7-2: Refitted data extracted from literature in accordance to Eq. 24 and Eq. 25.

	$\langle L \rangle = \frac{B_1 - B_2 \cdot R}{A_2 \cdot R - A_1}$					$\langle N \rangle_{Vf} = 1 - \ln \left(\frac{E_A - E_{A,Bulk}}{E_{A,ML} - E_{A,Bulk}} \right) \cdot N_0$		
	R	$A_1(\text{nm}^{-1})$	B_1	$A_2(\text{nm}^{-1})$	B_2	E_A^{ML} (eV)	E_A^{Bulk} (eV)	N_0
<i>h</i> -BN (Abs)	n.a.	n.a.	n.a.	n.a.	n.a.	6.143	6.117	11.50
PtSe ₂ (Ext)	800 nm	0.0134	-0.06	0.0035	1	3.194	3.639	3.42
PtSe ₂ (Abs)	255 nm	0.0141	-0.11	0.0042	1	3.508	3.206	5.08
GaS (Abs)	420 nm 290 nm	0.0002	-0.02	-0.0013	1	4.031	4.204	7.92
TiS ₂ (Abs)	n.a.	n.a.	n.a.	n.a.	n.a.	1.965	2.084	4.48
BP (Ext)	600 nm 340 nm	1.61·10 ⁶	1.63·10 ⁶	-1.38·10 ⁸	1	n.a.	n.a.	n.a.

Similar changes are observed for all materials independent of their chemical composition or the solvent used as medium which allows to compare and correlate fitting parameters for the different material systems. To do this, the change of the phenomenological decay constant (from absorbance if accessible) is shown as a function of the empiric bulk and monolayer exciton resonance on a logarithmic scale, respectively (Figure 4.7-1 A-B). Note that for materials with multiple excitonic transitions, all resonances were analysed and included in the plot. Additional datapoints originating from different excitonic transitions other than the one summarised in the table above are shown as open symbols. The data of all materials, including literature data (depicted as red spheres) roughly follows a linear trend which suggests that N_0 is directly proportional to $2E_{Bulk}$ or $2E_{ML}$ as indicated by the red lines in Figure 4.7-1 A and B, respectively. In addition, a similar plot correlating N_0 to the energetic difference between the bulk and the monolayer resonance ($E_{ML} - E_{Bulk}$) is shown in Figure 4.7-1 C, where no clear trend is observed.

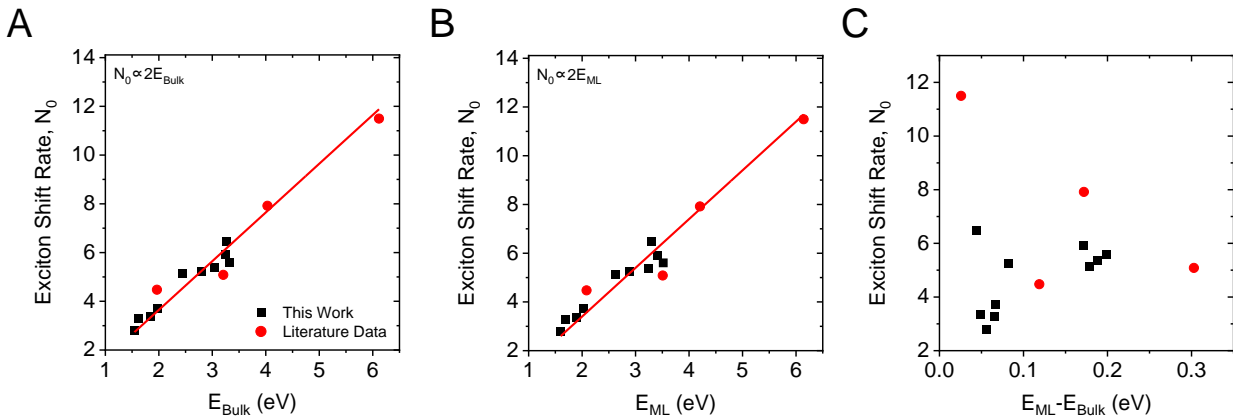


Figure 4.7-1: Fit parameters for changing excitonic resonances with layer number. Note that a systematic exponential blueshift of the exciton energy with decreasing layer number is observed for all materials which can be fit to extract the phenomenological decay constant N_0 . (A-B) Roughly linear change of the phenomenological exciton decay constant with bulk (A) and monolayer (B) exciton energy. (C) Scaling of the phenomenological decay constant with the energetic difference between monolayer and bulk exciton resonance. The blueshift of excitons with decreasing layer number is manifested as $\Delta E > 0$.

Chapter 4 – Size-Dependent Properties

While N_0 does not scale with the energetic difference between E_{ML} and E_{Bulk} , the positive values of ΔE are a manifestation of the underlying blueshift of the exciton energy with decreasing layer number. This shift is associated to different effects with approximately similar impact but opposite sign (*i.e.* changing exciton binding energy and electronic band gap) in case of TMDs, as discussed in Chapter 4.1. First principles suggest that the absolute energetic shift depends on the mass of the metal atom in TMDs, which cannot be transferred to other materials due to structural differences and also due to the absence of a metal in the material stoichiometry in some cases. Theory additionally predicts a direct correlation of the change rate of the blueshift with decreasing material thickness to the materials' band gap at the K-point of the Brillouin zone for TMDs which seems to hold for other materials as well since a linear correlation of N_0 is observed with E_{ML} and E_{Bulk} . However, to understand such trends in more detail, additional theoretic considerations are inevitable. Nonetheless, the data discussed in this Chapter provides an important basis for further experimental and theoretical studies and clearly shows that simple models can be applied to describe spectroscopic changes with material size in a whole host of 2D-material systems. The resultant data on spectroscopic metrics does not only provide a convenient method to determine average material dimensions of a nanosheet ensemble by standard spectroscopy, but also shows that unifying principles can be identified which allow a deeper understanding of fundamental material properties.

Chapter 4 – Size-Dependent Properties

5 Environmental Stability of LPE Nanosheets

The following Chapter focuses on the environmental stability of the nanosheets. With the understanding of the optical absorbance and extinction spectra as function of size and thickness discussed in the previous Chapter, it is possible to track the nanomaterial decomposition as function of time using for example absorbance spectra. Through this methodology, a dependence on the storage temperature and the water content of the solvent is conveniently accessible for different material dimensions. In addition to results already reported in *Chem. Mat.* (2019), 31, additional unpublished data is discussed. Reprints are shown in combination with a citation in the caption text and are reproduced or modified with permission from the respective publishers.

Sonication-assisted liquid phase exfoliation of van der Waals crystals is particularly promising in view of large-scale processing of nanomaterials. Nevertheless, it is important to study the stability of such materials before a liquid processing can be considered, as upon device fabrication and during operation, the nanomaterial may be exposed to relatively harsh conditions, depending on the intended application. Therefore, the material may have to endure warm aqueous environments (*e.g.* in biomedical applications¹⁹⁴), elevated temperatures during material deposition (*e.g.* printing¹⁹⁵ or casting), and light irradiation in perspective of photocatalytic¹⁹⁶ or optoelectronic applications (*e.g.* photodetectors,¹⁹⁷ lasers,¹⁹⁸ *etc.*). Hence, it is important to study the durability of the nanomaterial with respect to expected environmental impacts such as oxygen, water or the solvent itself depending on the light dose and/or at different temperatures which are expected upon further processing or device operation. To obtain deeper insights into material decomposition, different 2D-materials were investigated for their decomposition depending on their storage conditions. The chemical reactivity is expected to be significantly increased for the nanomaterial compared to the corresponding bulk crystal due to the increased effective surface exposed to the liquid environment. A different degradation behaviour is thus expected for varying material sizes *i.a.* due to variations in the ratio of chemically different material edge and basal plane atoms. Trends with material size therefore may give additional insights into preferred decomposition mechanisms.

Stability of

5.1 Transition Metal Dichalcogenide Nanosheets

TMDs have been widely considered as stable materials due to their high temperature tolerance in current industrial applications as lubricants.⁹⁶ However, awareness about decreased stability of the nanomaterials compared to their bulk counterparts is increasing as outlined in Chapter 2.5. Especially for TMDs, various theoretical and experimental studies are reported to date. However, most reports consider the 2D-material deposited on a substrate, such as *h*-BN, gold or silicon/silicon oxide which

Chapter 5 – Nanomaterial Stability

has an additional impact on the degradation behaviour of the nanomaterial as reported recently.¹¹⁰ Hence, to study the inherent oxidation behaviour of the 2D-material, nanosheets would ideally be suspended in a controlled (and inert) environment. Such studies however, are only feasible in theoretical approaches. While this may give new insights into the fundamental chemical properties arising from material surface effects (*e.g.* from defects), the chemical behaviour will differ from industrially relevant processing conditions.

In a study by Tapasztó *et al.*, the degradation of micromechanically-exfoliated MoS₂ nanosheets on a gold (111) surface was followed over time by scanning tunnelling microscopy (STM) in atomic resolution.⁹⁸ They demonstrate that the initial nanosheet surface of a MoS₂ monolayer shows progressively increasing defect densities over time after exposure to ambient oxygen. Considering the electronic band structure of TMDs, this would drastically decrease the application potential of pristine nanosheets with regard to optoelectronic applications as point defects on the material surface lead to non-radiative inter-band transitions which can in turn quench the photoluminescence.¹⁹⁹

In this regard, it is also important to consider that nanosheets prepared by means of micromechanical cleavage or grown by chemical vapor deposition (CVD) may show a different chemical behaviour as the ratio between the material plane and edges is significantly different compared to sonication-assisted liquid-exfoliated nanosheets due to the significant difference in nanosheet sizes that can be prepared by the different methods. For decreased nanosheet sizes, it is important to consider the impact of chemically different material edges which are often considered as defects that exhibit a distinct chemical reactivity than the material planes as shown by various studies.^{200, 201} In addition to such considerations, contributions from various types of defects have to be studied in detail as well. While theoretical approaches again suggest different reactivity of defects close to material edges and on the material basal planes,²⁰²⁻²⁰⁴ experimental proof of such a behaviour remains challenging especially as different types of defects (*e.g.* sulfur vacancies or adatoms) are expected to show a different chemical behaviour as well.

Prior to the work conducted in the framework of this thesis, studies on decomposition of liquid-exfoliated nanosheets are limited to reports on black phosphorus¹²⁷ and on chemically-exfoliated MoS₂,²⁰⁵ where a significant conversion of the initially semiconducting 2H-crystalphase to the metallic 1T-phase is observed which in turn leads to significant changes of the material properties.²⁰⁶ Hence, sonication-assisted LPE dispersions of group-VI TMDs (*i.e.* WS₂ and MoS₂) were studied for their degradation behaviour in the framework of this thesis. To this end, the optical response of different sizes of TMD dispersions was followed as a function of time and temperature. The following discussion focuses on changes of the material photoluminescence as only minor changes can be observed in the extinction spectra (Appendix 5.1-1). The PL emission is more sensitive to structural changes as even small concentrations of introduced defects can efficiently quench the radiative emission. This bears the inimitable possibility of studying changes of the optical response of monolayer ensembles with different average lateral sizes. To do this, the photoluminescence behaviour of three different nanomaterial sizes (*i.e.* 1-5k g, 5-10k g and 10-30k g) of WS₂ and MoS₂ in aqueous sodium

cholate was studied. A PLE map of a WS₂ dispersion containing comparatively small nanosheets (*i.e.* 10-30k g) is exemplarily shown in Figure 5.1-1 A (for additional data see Appendix 5.1-1). The broad emission feature at ~560 nm can be attributed to minor impurities in the natural bile salt sodium cholate which is used as surfactant for colloidal stabilisation. Based on the excitation profiles, the excitation wavelength was fixed to 440 nm for the following experiments, as a reasonable PL emission is observed for both WS₂ and MoS₂ and simultaneously no additional contributions from the stabiliser are observed.

In order to obtain a better understanding on effects on the PL emission arising from changing the temperature, single emission spectra of the different nanosheet dispersions were acquired at stepwise increased temperatures, starting from 5°C with increments of 5 C up to 80°C. The temperature is then decreased in steps of 5 C until the initial temperature of 5°C is reached. For both, increasing and decreasing temperature, PL measurements are acquired after each temperature step and a short equilibration time (max. 5 min, see methods section for additional details). The resultant spectra show a systematic decrease of the emission intensity in combination with a redshift with increasing temperature (Figure 5.1-1 B). The observed trend is reversible to some extent for the subsequent decrease to 5°C (Figure 5.1-1 C). For a comprehensive analysis, the spectra were fitted to a Lorentzian function (solid lines in Figure 5.1-1 B-C). While the shift of the peak position is completely restored after decreasing the temperature back to the initial value, the PL intensity is irreversibly decreased by a factor of ~2/3 after the exposure to elevated temperatures, as shown by the PL intensity evolution with the changing temperatures in Figure 5.1-1 D. The drop of the PL intensity is associated to material decomposition.

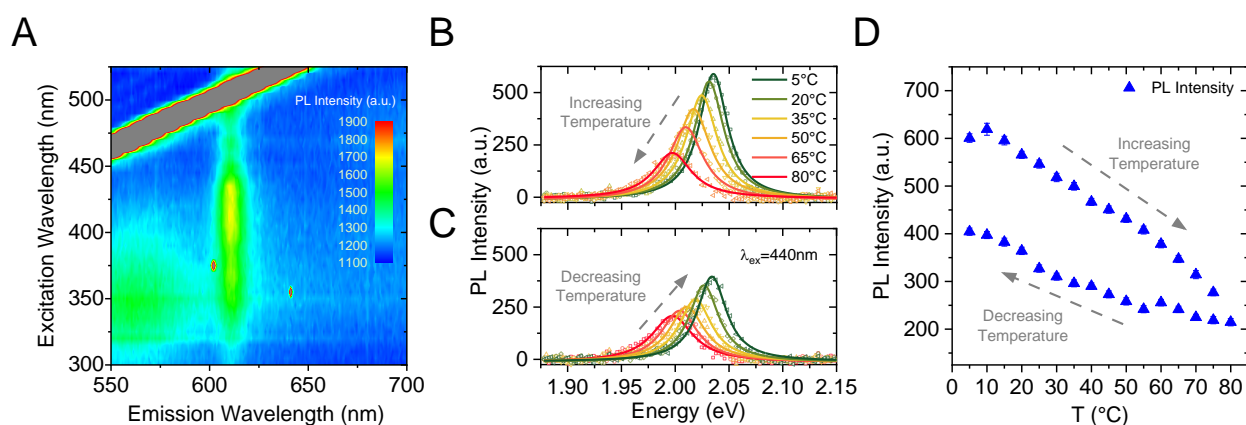


Figure 5.1-1: Impact of temperature on the TMD PL. (A) PLE map of a WS₂ dispersion containing relatively small nanosheets (10-30k g). The emission at ~610 nm is attributed to radiative decay of excitonic transitions in TMD monolayers. The signal at 560 nm can be ascribed to luminescent impurities from SC. (B-C) PL emission spectra excited at 440 nm recorded at different sample temperatures. (B) Evolution of the PL emission with stepwise increase of the sample temperature. The PL intensity declines with increasing temperature associated with a redshift (C) Evolution of the PL emission with stepwise decrease of the sample temperature. Shifts of the spectra are reversible while the drop of the PL intensity is not completely restored. (D) Quantitative analysis of the PL emission change with temperature by peak fitting to a Lorentzian. The PL emission remains at ~2/3 of its initial intensity after the temperature treatment.

Chapter 5 – Nanomaterial Stability

For further analysis, systematic temperature experiments were designed to study the material decomposition. In the approach presented below, samples are alternately exposed to two different temperatures for defined times: at first the sample is equilibrated to 20°C and an initial PL spectrum is measured, which serves as reference. Afterwards the temperature is increased for 30 min (*e.g.* to 50°C) while PL spectra are acquired five minute increments. This procedure is repeated over 400 min, as indicated by the pulse-diagram (Figure 5.1-2 A). This results in two complementary datasets for evaluation of time-dependent changes of the spectra: one of increased time-resolution acquired at a defined elevated temperature and one at a constant reference temperature which allows to compare changes and shifts of the PL emission for different elevated temperatures, as discussed below. The evolution of the emission spectra over time at 50°C is exemplarily shown for measurements of the small WS₂ sample acquired at 20°C in Figure 5.1-2 B. The spectra clearly show a significant decrease of the PL emission intensity accompanied with a slight redshift over time. Both observations can be explained by additional inter-band transitions originating from defect states and imply significant material decomposition at 50°C.²⁰⁷ To quantify the change of the emission spectra, both datasets (*i.e.* spectra recorded at 20°C and at the elevated temperature) were fitted to a Lorentzian envelope to extract position, area and height. The change of the PL emission peak area and height normalised to the initial measurement are plotted as a function of time Figure 5.1-2 B. In every case, an exponential decay is observed over time. Figure 5.1-2 C shows all parameters normalised to the first spectrum recorded at the respective temperature. The normalisation leads to a collapse of all datapoints on the same curve. As this is the case for all samples under study, the normalised peak area recorded at 20°C is discussed in more detail as representative parameter to describe the material decomposition.

Similar experiments and analysis was performed on the three different sizes of WS₂ and MoS₂ for varying elevated temperatures in the range of 40-80°C. Decays of the PL response with time of the small size of WS₂ nanosheets is again shown representative for all samples in Figure 5.1-2 D (additional data is shown in Appendix 5.1-2). For all temperatures, the decays of WS₂ can be fit to a single exponential function which clearly results in different amplitudes and half-lives depending on the exposed temperature. Note that the decay of MoS₂ is slightly more complicated resulting in uncertainties in fitting the data to a single exponential. A discussion is beyond the scope of this thesis and was addressed within the master thesis of Leonhard Karger, submitted in December 2020 at Heidelberg University. Due to these uncertainties, only the data of WS₂ is summarised below.

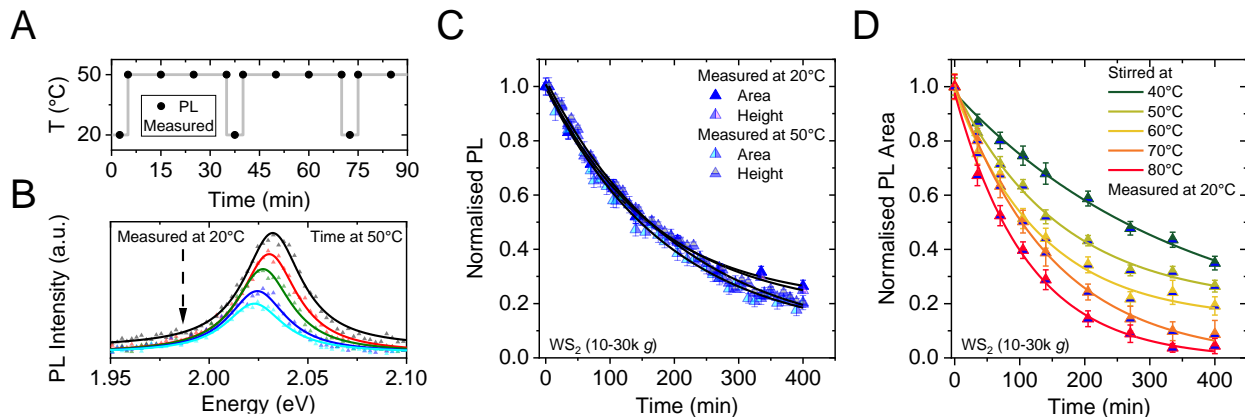


Figure 5.1-2: Evolution of the 10-30k g WS₂ PL emission for exposure to constant temperatures. (A) Illustration of the experimental procedure in a pulse-diagram. Samples were first measured at 20°C as reference and then held and repeatedly measured at a constant elevated temperature for 30 minutes. After that, the samples were measured at 20°C again and for another 30 minutes at the elevated temperature. This procedure is looped until the samples were exposed to the elevated temperature for 400 minutes. (B) Evolution of the PL spectra recorded over time at 20°C after repeated exposure to 50°C. Significant changes of the emission intensity and position can be observed. (C) Normalised peak area and height for measurements acquired at 20°C and at 50°C. The relative change of all parameters falls on the same curve. (D) Normalised PL area as representative parameter for material decomposition for different temperatures. Similar spectra for different sizes of WS₂ are shown in Appendix 5.1-2.

The exponential fits allow to extract temperature-dependent macroscopic nanomaterial half-lives for different monolayer sizes of both material systems as outlined above. The change of the half-life linearises if plotted as function of the inverse absolute temperature (Figure 5.1-3 A) which allows to extrapolate the activation energy for the nanomaterial decomposition according to Arrhenius (Eq 33-34),²⁰⁸

$$\ln(t_{1/2}) = -\frac{E_A^{Dec.}}{R} T^{-1} + \ln(t_0) \quad (\text{Eq. 33})$$

$$E_A^{Dec.} = -R \cdot \frac{\partial \ln(t_{1/2})}{\partial T^{-1}} \quad (\text{Eq. 34})$$

where $E_A^{Dec.}$ is the macroscopic activation energy for the degradation, R is the gas constant, T is the absolute temperature, $t_{1/2}$ is the macroscopic half-life of the TMD monolayer PL and $\ln(t_0)$ is the intercept in the Arrhenius-type plot (Figure 5.1-3 A) which is cancelled out in the derivative and has thus no relevant contribution to $E_A^{Dec.}$. Note that the ordinate in Figure 5.1-3 A is scaled logarithmic. The solid lines in the plot are linear fits and allow evaluation of the data according to equation 34 which suggests different activation energies for the decomposition of different sizes of WS₂ nanosheets as determined from metrics presented in Chapter 4.1. The results are summarised in Table 5.1-1.

Chapter 5 – Nanomaterial Stability

Table 5.1-1: Macroscopic size-dependent activation energies for WS₂ monolayer decomposition.

WS ₂	
$\langle L \rangle$ (nm)	$E_A^{Dec.}$ (kJ/mol)
36	28.15±1.2
43	31.81±13.4
73	20.75±5.2

In addition to approximate macroscopic activation energies that can be determined from the temperature-dependent half-lives extracted from the exponential decrease of the PL area over time, the portion of reacted material can be approximated from the amplitude of the exponential fit for the different storage temperatures, as previously demonstrated for LPE black phosphorus.¹²⁷ A plot of the portion of reacted material as function of temperature is exemplarily shown for comparatively small WS₂ nanosheets (10-30k g) in Figure 5.1-3 B. Furthermore, Hanlon *et al.*, suggested that a plot of half-life as function of portion of reacted material can be used to compare the result of the degradation using different storage conditions. In strong resemblance to the results reported by Hanlon *et al.*, which were provided from the authors as reference, a defined scaling between the macroscopic monolayer TMD half-life and the portion of reacted material is observed, following an empirical power law function, as indicated in Figure 5.1-3 C. The solid lines are fits to the empirical function shown in the lower right corner of the graph where x is the portion of reacted material from extrapolation of the exponential decay to infinite times while A and η are fit parameters. A physically meaningful description of the empirical correlation could not be provided within this work, but the plot conveniently gives important insights into material decomposition kinetics directly encoded in the exponential fits and allows to estimate how complete and how fast the material decomposition occurs for different environmental conditions, which is discussed in more detail in Chapter 5.6.

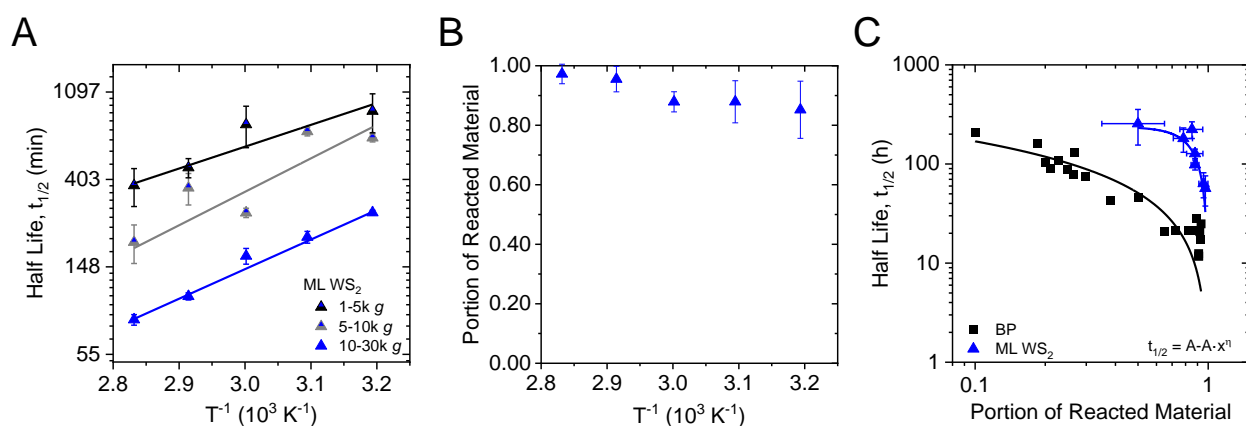


Figure 5.1-3: Thermodynamic and kinetic aspects of mono-layered WS₂ decomposition. (A) Dependence of the macroscopic material half-life as function of the inverse temperature on a semi-ln scale. The Arrhenius-type plot enables to approximate the activation energy for the nanomaterial decomposition. (B) Dependence of the activation energy of WS₂ monolayers with the average nanosheet length. An edge centred mechanism can be inferred from the increasing activation energy with size for WS₂. (C) Plot of the half-life as function of the portion of reacted material of WS₂ in comparison to LPE BP at different storage conditions. Modified and reproduced with permission from ¹²⁷.

In summary of this Chapter, novel approaches for studying nanomaterial decomposition have been presented applying basic principles of physical chemistry. The decomposition WS₂ could be quantified by evaluation of the temperature-dependent optical response as function of time. In contrast to BP, measurements of extinction and absorbance show only minor changes over time, which suggests a decent stability of few-layer nanosheets (Appendix 5.1-1). However, if the PL emission is studied instead under similar environmental conditions, a significant decrease of the emission intensity is observed. As only mono-layered nanosheets are detected in PL measurements, which are additionally more sensitive to structural changes of the nanosheets due to PL quenching by point defects, as discussed above, discrepancies between extinction and PL measurements may also be explained by passivation effects of surrounding nanosheet layers for thicker nanosheets which contribute to extinction, but not PL. The impact of environmental changes on few-layered TMD nanosheets are part of ongoing studies and could not be included in this work. However, the results on mono-layered WS₂ nanosheets provided in this work give valuable insights into nanomaterial stability in a realistic environment for further processing for potential device applications. In addition, they set the tone for further work on other materials that will be presented below. Activation energies for the material decomposition according to the Arrhenius equation could be extracted by fitting the first order decay kinetics to determine the half-lives of the reaction at different temperatures for different nanomaterial sizes. While this is a simple procedure, it is the first time that it was applied to LPE nanosheets. Due to the feasibility of the approach, the basic principle will be applied to other materials studied within this thesis.

For WS₂, it was found that activation energies are widely invariant with nanosheet size and in the range of 20-30 kJ/mol. Overall, smaller WS₂ monolayers decayed faster than larger ones implying a degradation from the edge inwards. It was also found that MoS₂ behaves differently to WS₂ even

Chapter 5 – Nanomaterial Stability

though this was not fully elaborated. Additional preliminary experiments (Appendix 5.1-3) show that photochemical decomposition cannot be neglected which has to be considered in future studies. Furthermore, the surfactant used for material stabilisation (SC) is known to interact more strongly with the material planes which might have an impact on the decomposition behaviour due to non-covalent surface passivation by the surfactant. Additional studies including other stabilisers will be required in order to understand the impact of the surfactant on the nanosheet stability. Moreover, the influence of temperature and of light on the nanosheet decomposition needs to be decoupled for a meaningful discussion.

5.2 Indium Selenide

While TMDs can be considered as common commercially available and extensively studied 2D-materials, only little is reported about the nanomaterial stability or their degradation. Consequently, even less is known about the stability of more exotic 2D-nanostructures. Indium selenide nanosheets display, in contrast to TMDs, PL emission independent of the material thickness which conceptually enables to directly correlate differences of the optical response from extinction or absorbance measurements over time to the PL emission. However, the PL emission is quenched in the solvent used for preparation of colloiddally stable γ -InSe nanosheet dispersions. While PL emission can be observed for aqueous SC stabilised nanosheet dispersions, significant oxidation of the nanosheets can be observed associated with colloidal destabilisation, as mentioned in Chapter 3.2. Such dispersions are not subjected to further analysis for two different reasons. Firstly, while strong oxidation may be considered as starting point to investigate the material decomposition, no reasonable material processing in such an environment is possible. Second, the simultaneous material and colloidal instability in aqueous SC may lead to size-dependent precipitation of nanomaterial as soluble decomposition products lead to changes of the dispersions' ionic strength. Such convoluted effects can hardly be decoupled from actual material decomposition and render results from PL and absorbance measurements on such samples difficult to interpret.

However, it is feasible to study the degradation in NMP, where no issues with colloidal instability were observed. Importantly, the PL of colloiddally stable γ -InSe dispersions in NMP could be partially restored after material deposition and extensive washing steps with isopropanol. While such films of deposited nanomaterial cannot be directly compared to dispersed nanosheets, the confirmation of structural integrity after the deposition and washing procedure is substantial. Hence, the deposited nanomaterial was studied by a combination of SEM energy-dispersive X-ray (EDX) and Raman spectroscopy (Figure 5.2-1). For better comparability, an EXD spectrum of a bulk γ -InSe crystal is shown in Figure 5.2-1 A. In addition to the signal at ~ 0.9 keV which can be attributed to the $L\alpha$ -line of copper in the brass sample holder, no other than the expected characteristic indium or selenium X-ray energies are observed in the spectrum. Similar spectra have been measured for all deposited nanosheet sizes (Figure 5.2-1 B) and display no other than the expected signals except for the sample

containing the smallest size of nanosheets (5-30k g) which shows a significantly decreased selenium content. The EDX measurements suggest a stoichiometry of $\text{InSe}_{0.29}$ in this sample, which is noticeably understoichiometric in contrast to the other nanosheet sizes. This may be attributed to preferential oxidation of selenide sites into soluble decomposition products that are removed from the substrate by the washing steps after deposition. The suggested stoichiometry from the EDX spectra is summarised in Table 5.2-1 for all nanosheet sizes which widely suggest structural integrity of the nanomaterial with the 5-30k g sample being the only exception. To gain further insights on the degradation of the nanomaterial, Raman spectroscopy was performed on the same samples as studied by EDX spectroscopy (Figure 5.2-1 C). The resultant spectra show a slight broad background for the exfoliated nanosheets centred at $\sim 240 \text{ cm}^{-1}$ which intensifies with decreasing nanomaterial size. The exact origin of the background remains unclear, but it points towards a structural change. Importantly, it is only significant for the smallest two nanosheet sizes, being 2-5k g and 5-30k g, respectively. In addition, a broadening of the Raman modes is observed in all LPE samples which may be attributed to structural deterioration with increasing surface to volume ratio or random orientation in the drop-cast film.

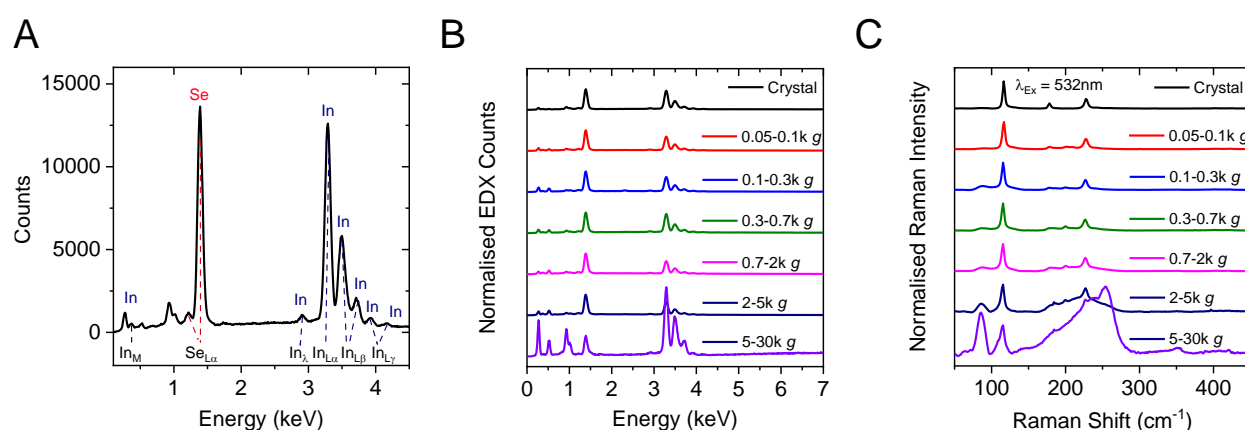


Figure 5.2-1: Spectroscopic response of deposited γ -InSe nanosheets for different nanomaterial sizes. (A) Reference EDX spectrum of the γ -InSe bulk crystal. (B-C) Normalised EDX (B) and Raman (C) spectra of different sizes of deposited γ -InSe nanosheets. The spectra are shown with horizontal offset for better comparison.

Table 5.2-1: Stoichiometry of deposited γ -InSe samples as suggested by EDX spectroscopy.

Fraction	0.05-0.1k g	0.1-0.3k g	0.3-0.7k g	0.7-2k g	2-5k g	5-30k g	Crystal
Stoichiometry	InSe	$\text{InSe}_{0.96}$	$\text{InSe}_{0.80}$	$\text{InSe}_{1.07}$	$\text{InSe}_{1.04}$	$\text{InSe}_{0.29}$	$\text{InSe}_{0.77}$

While the EDX and Raman spectra in Figure 5.2-1 imply a partial degradation of the γ -InSe nanosheets depending on the size of the deposited nanomaterial, it remains unclear whether the material decomposition is occurring in the dispersion or during or after deposition. In order to quantify the stabilising effect of NMP on the nanosheets, extinction spectra of γ -InSe dispersions containing relatively large (0.1-0.3k g) and relatively small (2-5k g) nanomaterial have been acquired as a function of time for different sample storage conditions. To this end, γ -InSe dispersions were stored in ambient

Chapter 5 – Nanomaterial Stability

conditions at 20, 40 and 60°C, and repeatedly measured after defined time intervals. Prior to the measurements, samples were refreshed by bath sonication to prevent additional contributions from potential nanosheet aggregation similar to previous reports.^{75, 193, 209, 210} The evolution of the spectra is exemplarily shown for the large nanosheets stored at 40°C for a total of 360 h (Figure 5.2-2 A, other sizes and storage conditions are shown in Appendix 5.2). All spectra are normalised to the extinction at 340 nm for better comparability. In every case, a systematic increase of the relative absorbance intensity in the UV-region is observed as indicated by the grey arrow in Figure 5.2-2 A which typically is a sign of material decomposition.¹¹ Furthermore, a dip at ~265 nm evolves over time for extended exposure of the nanomaterial to elevated temperatures. In order to track changes of the extinction spectra over time, the intensity ratio at 344 over 275 nm is followed as a function of time at the different storage temperatures for both nanosheet sizes, respectively (Figure 5.2-2 B-C). The change of the intensity ratio over time follows a single exponential decay with clearly decreasing macroscopic half-lives for increasing temperature, in resemblance to changes of the TMD PL emission for different temperatures as discussed in Chapter 5.1. The data is fitted to an exponential function for a quantitative evaluation of the changing γ -InSe extinction intensity ratio as indicated by the solid lines in the plots.

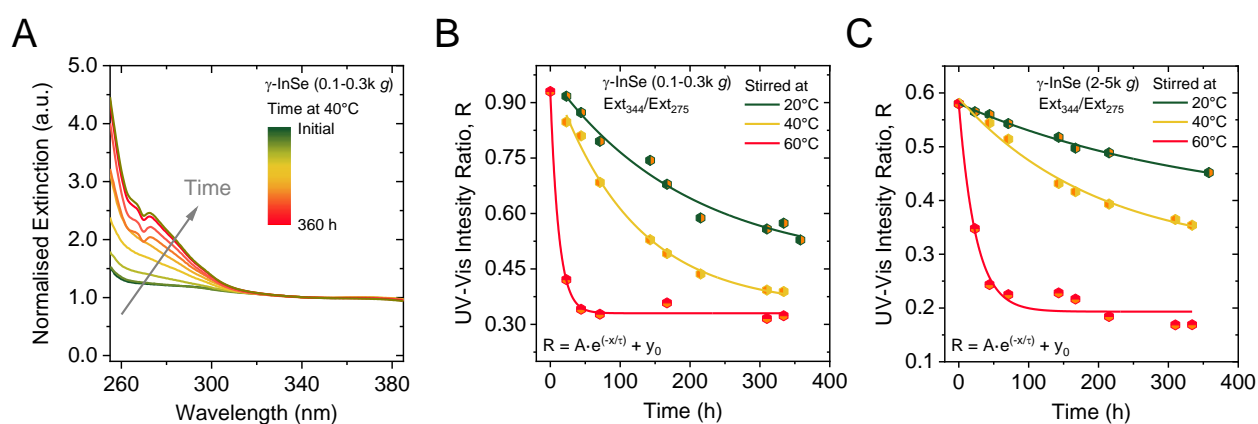


Figure 5.2-2: Trends of extinction spectra for γ -InSe nanosheets at different storage conditions. (A) Evolution of the extinction spectra over time exemplarily shown for large (0.1-0.3k g) nanosheets at 40°C (for other samples and conditions see Appendix 5.2). (B-C) Change of the extinction peak intensity ratio at 344 over 275 nm for relatively large (B) and relatively small (C) γ -InSe nanosheets at different storage temperatures. Solid lines are empirical exponential fits of the data.

The data fitting allows to extract the macroscopic half-life for the material degradation. This enables to study the temperature dependence of the half-lives in an Arrhenius-type plot, similar to the data discussed on TMD decomposition in Chapter 5.1, where the natural logarithm of the half-life is plotted as function of the inverse temperature (Figure 5.2-3 A). In contrast to the study on TMDs, no linearization of the data is observed for γ -InSe nanosheets in NMP. This is further illustrated by the dashed lines in the plot, which represent linear fits of the data as a guide for the eye. This lack of linearisation may be partially be due to the limited number of data points and scatter in the data.

Alternatively, it is possible that multiple reactions occur so that the degradation does not follow Arrhenius behaviour. While these fits do not allow for a determination of the activation energy for γ -InSe nanosheet decomposition, the information on the range of half-lives depending on temperature and nanosheet size is nonetheless an important piece of information. As observed for TMDs, a higher surface to volume ratio in the small nanosheets results in lower half-lives of the degradation.

In addition, information about the portion of reacted material is encoded in the exponential fits. Extrapolation of the data in Figure 5.2-2 B-C to infinite times (*i.e.* amplitude) allows to approximate the expected degree of material decomposition for the given storage conditions as shown in Figure 5.2-3 B, where the estimated portion of reacted material is plotted as a function of the storage temperature. Note, that these values are no intrinsic material property and that passivation will have an impact so that other solvents may give a different result. The data suggests that decomposition of relatively large/thick nanosheets (0.1-0.3k g) is more complete than for the comparatively small/thin sheets (2-5k g) which may be interpreted as preferential basal plane degradation in γ -InSe nanosheets due to the higher plane to edge ratio in larger nanomaterial. However, for a discussion on nanosheet decomposition mechanisms, additional studies are required, including inert gas experiments and controlled exposure to ambient oxygen and/or water. However, such experiments are tedious and beyond the scope of this work.

To facilitate a comparison with other materials, the two key parameters describing the degradation, *i.e.* portion of reacted material and half-life, are plotted *versus* each other in Figure 5.2-3 C. As discussed in the previous Chapter, such a plot can be considered as a measure of the decomposition efficiency for different storage conditions. The data of γ -InSe is shown in comparison to BP,⁷⁵ which shows significantly lower material half-lives. Interestingly, the data points extracted for γ -InSe in NMP follow the same power law dependence as BP (and TMD monolayers, see Chapter 5.1) as indicated by the solid lines which are fits of the data to the empirical function as shown in the graph.

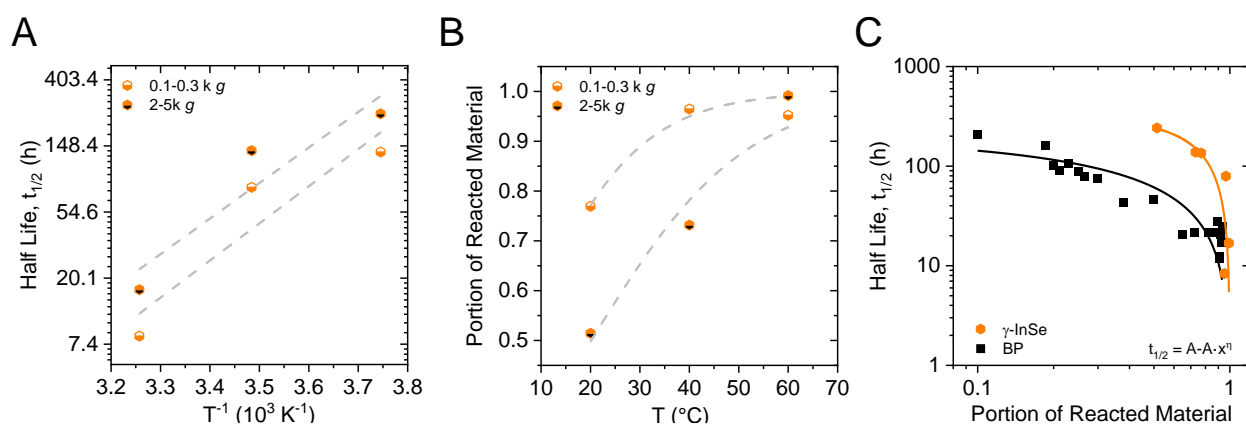


Figure 5.2-3: Thermodynamic and kinetic aspects of γ -InSe nanosheet decomposition in NMP. (A) Dependence of the macroscopic material half-life as function of the inverse temperature on a semi-ln scale. The Arrhenius-type plot shows no linear dependence of the data points which averts the determination of activation energy. (B) Estimated portion of reacted material from fitting the decay kinetics as function of the storage temperature (C) Plot of the half-life as function of the portion of reacted material of γ -InSe in comparison to LPE BP at different storage conditions. Modified and reproduced with permission from ¹²⁷.

Chapter 5 – Nanomaterial Stability

The data on γ -InSe nanosheets discussed in this Chapter shows that significant material decomposition occurs over time if the material is exposed to ambient oxygen or water, which is further increased at elevated temperatures. This limits the application potential of the material and will require additional studies in inert gas conditions and with respect to surface passivation.

The degradation was studied by standard extinction spectroscopy for different sample sizes and storage conditions and quantified by fitting the time-dependent changes of the spectra to first order decay kinetics. No linearisation of the half-lives is displayed in an Arrhenius-type plot, which may be either attributed to the limitation to three temperatures or point towards a more complex degradation. While this does not allow to determine activation energies for the material degradation, other parameters, such as the portion of reacted material and the macroscopic half-lives can be extracted from the fits. γ -InSe shows the same empirical power law correlation between the half-life and the portion of reacted material as observed for TMD monolayers and BP, which seems to be a general trend that is not understood as yet. However, the position of the data in this plot can be interpreted as decomposition efficiency of the material at the given environmental conditions and thus enables a material comparison.

5.3 Transition Metal Hexathiohypo Diphosphates

Exotic van der Waals structures, such as transition metal hexathiohypo diphosphates are receiving increasing attention due to their magnetic properties. While such materials promise new insights into fundamental physics of magnetic ordering in low dimensional structures, applications in various areas are also considered. Recent studies show promising results for electrochemical energy storage and conversion.¹⁴⁴ Comparative studies on different transition metals in the MPS_3 structure in their application potential show that $NiPS_3$ and $CoPS_3$ exhibit the highest activity in a hydrogen evolution reaction (HER), while $MnPS_3$ shows superior performance in an oxygen reduction reaction (ORR) and $CoPS_3$ in an oxygen evolution reaction (OER).¹⁰³ However, it is currently unclear whether exfoliated MPS_3 nanosheets are stable under ambient conditions or whether they oxidise similar to other materials such as black phosphorus,^{75, 211, 212} TiS_2 ¹⁹³ or MoO_2 .²⁰⁹ This information is absolutely crucial given the interest in using transition metal hexathiohypo diphosphates as catalysts for water splitting¹⁴⁴ or to exploit magnetic properties. Hence, a deeper understanding of the material decomposition is required.

To address the structural integrity of the nanosheets after exfoliation and size selection, fractions of different material sizes were drop-cast in an inert gas atmosphere and subjected to different characterisation techniques. Note that in this case, exfoliation was also performed in inert gas conditions. In the following discussion, results on exfoliated $NiPS_3$ are presented. Similar experiments have been performed for $FePS_3$ and $MnPS_3$ except of XPS and XRD measurements. The resultant data for $FePS_3$ and $MnPS_3$ is shown in Appendix 5.3. Raman measurements on drop-cast nanosheets from

fractions of the second size selection cascade acquired with a 532 nm laser for excitation are shown in Figure 5.3-1 A. The nanosheet spectra strongly resemble the Raman spectra acquired for the bulk material with only minor differences (*e.g.* peak broadening for exfoliated sheets). These insignificant deviations can be ascribed to random orientation of the nanomaterial and agree with literature data.²¹³ No signs of material decomposition are therefore observed in the Raman spectra. While this suggests that the structural integrity of the nanomaterial is retained after exfoliation, it is important to consider that potential products from material decomposition might not be Raman active or not resonant with the excitation wavelength. Hence, drop-cast nanosheets of different size-selected fractions were subjected to XPS measurements. The S 2p and P 2p core level spectra of a fraction containing relatively small nanosheets (*i.e.* 10-30k g) are shown for NiPS₃ nanosheets in Figure 5.3-1 B-C. This sample was chosen as representative, as compositional changes are expected to be most pronounced for nanosheets with a high effective surface area (additional XPS data is shown in Appendix 5.3-1). In particular for the small nanosheets, additional contributions can be observed at increased binding energy which is consistent with oxidised sulfur and phosphorus. Fitting of the peaks enables to estimate the degree of the oxidation for phosphorus and sulfur sites on the nanosheets individually. The contribution of oxides to the core level spectra make up ~26 % and ~4 % of the total peak area for phosphorus and sulfur spectra, respectively for the sample shown in Figure 5.3-1 B-C. The same peak analysis can be carried out for the other sizes. This allows to test whether the oxide content scales with the nanosheet dimensions (determined from AFM statistics). The degree of oxidation according to XPS scales best with the mean nanosheet volume (Figure 5.3-1 D) and not length or thickness, (see Appendix 5.3-1) suggesting a degradation occurring on both edge and basal plane. Interestingly, the oxidation is more pronounced at phosphorous sites (reaching up to ~26 %) than at sulfur sites (~5 %), which may be ascribed to the higher oxophilicity of phosphorous compared to sulfur. Similar measurements have additionally been performed on the initial nanosheet stock dispersion prior to LCC which shows a significantly higher contribution of oxide species than any of the fractions (up to 58 % on P-sites, Appendix 5.3-1). This result emphasises that the size selection is associated with a simultaneous sample purification as soluble impurities or highly defective nanomaterial remain in dispersion while the intact nanomaterial is collected as sediment.

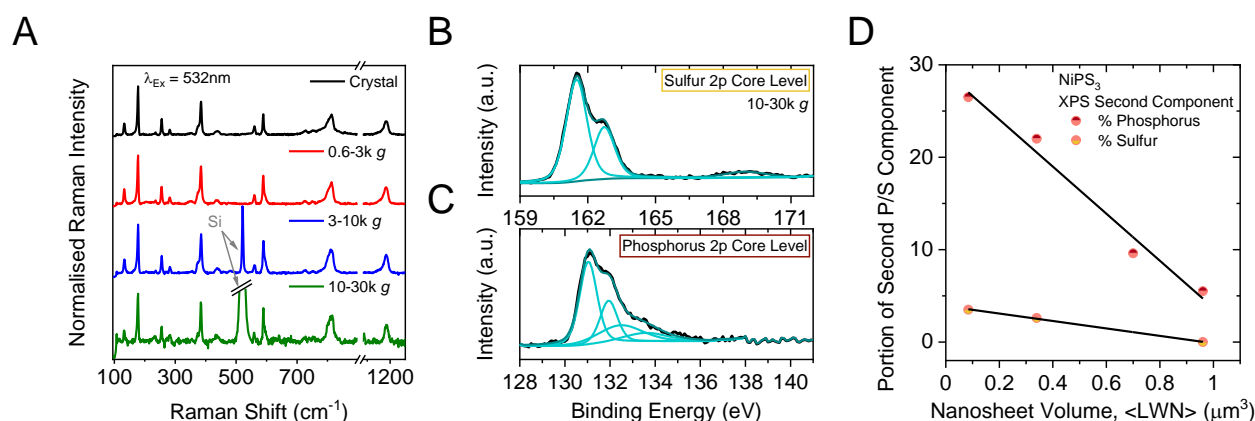


Figure 5.3-1: Structural characterisation of nanosheets by surface sensitive methods. (A) Raman spectra of all nanosheet sizes isolated in the second size selection cascade, including a measurement on a bulk crystal for comparison. No other than the expected signals are observed. (B-C) XPS core level spectra of a fraction containing comparatively small nanosheets (10-30k g). The sulfur 2p core level (B) shows a minor additional doublet at higher binding energy which contributes ~4 % to the overall signal. The phosphorus 2p core level spectrum (C) shows an additional doublet which constitutes ~26 % of the total signal. (D) Portion of the second component to the XPS spectra in the P and S 2p core level spectra of NiPS₃ as a function of material volume. Reproduced and adapted with permission from ¹¹.

As XPS is a surface sensitive characterisation method with a small penetration depth which might overestimate the material decomposition, further structural characterisation of the MPS₃ nanosheets is required to reliably discuss the integrity of the nanomaterial. In this regard, different fractions of size-selected nanosheets (*i.e.* 0.6-3k g, 3-10k g and 10-30k g) have been combined to probe a sufficient amount of material for analysis *via* XRD (dispersed in CHP). Prior to the diffraction measurement, the sample was refreshed by bath sonication to redisperse aggregated particles. The pattern is compared to a measurement on a bulk crystal in order to identify structural changes of the material upon delamination (Figure 5.3-2 A). Both measurements were performed in the group of Wolfgang Bensch (Kiel University). No structural disintegration of the nanomaterial is observed for the combined sample as the characteristic Bragg reflections of bulk NiPS₃ can also be observed in the exfoliated sample, which implies that the crystallinity of the nanosheets is retained. In further analysis, the (001) reflection is found to be less intense in the pattern of the exfoliated samples and the (002) reflection disappeared completely after the exfoliation process. This result is not surprising as these two reflections result from material stacking direction along [001]. Hence, for a decrease of the relative number of atoms in the [001] direction (*i.e.* material delamination), reflections with contributions in [001] direction are expected to decline as a result of the exfoliation.

One could argue that only crystalline material can be detected by diffraction measurements and that the detected reflexes originate from large and thick nanomaterial which is less prone to oxidation. Since it was not possible to prepare a sufficient nanomaterial mass for diffraction measurements of individual size fractions, transmission electron microscopy (TEM) was used to study the diffraction of individual nanosheets from different fractions of the first size selection cascade (*i.e.* 0.1-0.4k g, 1-5k g and 10-50k g) in the group of Sarah Haigh (Manchester University). Nanosheets

of similar morphology to AFM images are observed as exemplarily shown in Figure 5.3-2 B. Representative selected area electron diffraction patterns (SAED) of nanosheets found in the fraction isolated at low centrifugal acceleration (0.1-0.4k g) shows sharp and bright diffraction spots in good agreement with the expected pattern for single crystalline NiPS₃ (Figure 5.3-2 C). Similar patterns can be observed for other nanosheet sizes as well (Appendix 5.3-2). In some examples, diffraction patterns consistent with polycrystalline material are observed, which is attributed to randomly re-stacked or several rotated nanosheets within the ~100 nm diameter SAED field of view (Appendix 5.3-2).

High-resolution TEM (HRTEM) imaging of the NiPS₃ basal planes reveals the expected atomic lattice as exemplarily shown for the 0.1-0.4k g fraction in Appendix 5.3-2. The corresponding lattice spacing is found at 4.98 Å, 4.86 Å, 4.86 Å and 2.85 Å which fits to the expected (020), (110), ($\bar{1}$ 10) and ($\bar{1}$ 30) crystal planes. In addition, STEM-EDX maps were measured of freshly-prepared nanosheets from the small-sized fraction, revealing a uniform distribution of the different elements with a stoichiometry of NiPS_{2.8}.

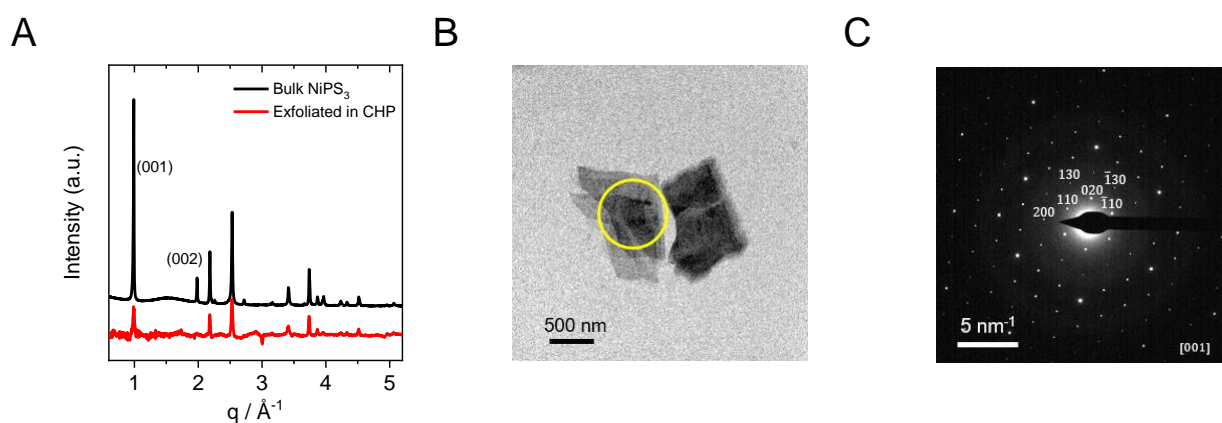


Figure 5.3-2: Ensemble and individual nanosheet diffraction measurements on exfoliated NiPS₃. (A) XRD measurements the bulk crystal (black) compared to combined fractions of exfoliated nanosheets in dispersion (CHP, red). As the XRD pattern of the exfoliated sample was collected at DESY, P02.1 and the pattern of the bulk sample in-house, both patterns are plotted in q-space for a better comparability. The background of the dispersion medium CHP was subtracted from the diffractogram of the exfoliated sample using a simple spline fit method. (B) Bright field TEM image of the large nanosheets. The yellow circle indicates the probed area for the electron diffraction measurement. (C) SAED pattern of the nanosheet in shown in (B). Reproduced and adapted with permission from ¹¹.

Overall, the structural characterisation of the nanosheets demonstrates that NiPS₃ nanosheets remain widely intact after LPE and size selection in CHP and show high crystallinity with only minor surface oxidation. The discussed results prove the initial structural integrity of the nanomaterial after exfoliation and size selection in inert gas conditions, which renders the nanosheet dispersions as ideal starting point for systematic studies of the material decomposition by variation of the environmental conditions. To this end, optical extinction and absorbance measurements on fractions containing nanosheets with different lateral sizes and thicknesses were measured over time for different storage

Chapter 5 – Nanomaterial Stability

conditions. A sample of each size was stored in the refrigerator (4°C) and stirred at 20, 40 and 60°C, respectively. Before each measurement, samples were refreshed by bath sonication to avoid potential impact from sedimentation similar to previous work.^{75, 193, 209, 210}

The evolution of the extinction spectra of a fraction containing relatively large NiPS₃ nanosheets, stirred at 40°C for up to 488 hours is shown in Figure 5.3-3 A. The extinction and absorbance spectra of the other materials, sizes and storage conditions are shown in Appendix 5.3-3. Both, extinction and absorbance spectra show a systematic decrease in intensity over time. Aggregation of the nanomaterial can be excluded, as the same trend is observed in both, extinction and absorbance and no increase of the non-resonant scattering contribution is found. The changes in the spectra can thus be ascribed to progressive material decomposition. While the decrease of the optical density in the spectra is more severe for elevated temperatures, additional signals are formed over time: a new peak at ~315 nm and a dip at ~290 nm can be observed for NiPS₃. In addition, an increase of the relative intensity at high energies is observed, which is a typical sign of oxidation as nickel and phosphorous oxides tend to absorb in the UV region.²¹⁴⁻²¹⁶

In order to follow the degradation-based changes systematically, the optical density at 460 nm, where the spectral shape remains unchanged in all cases, is plotted as a function of time for different NiPS₃ nanosheet sizes (*i.e.* 0.6-3k g and 3-10k g) in Figure 5.3-3 B-C. For all samples, an approximately exponential decrease of the optical density at 460 nm is found. Independent of the NiPS₃ nanosheet size, the optical density approaches 0 for storing temperatures above 40°C, which is consistent with complete decomposition of the nanomaterial.

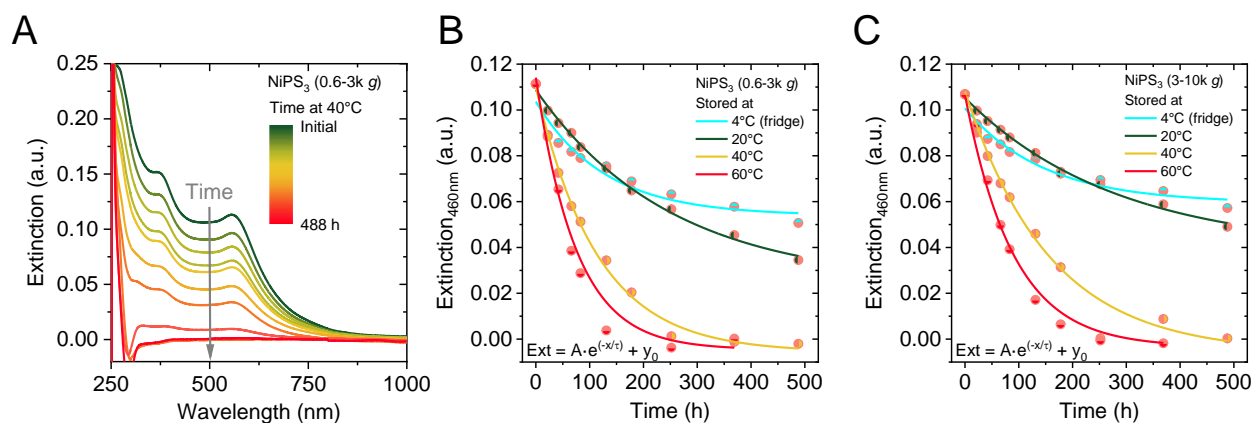


Figure 5.3-3: Change of the optical response of NiPS₃ nanosheets in CHP over time. (A) Evolution of the extinction spectra for comparatively large NiPS₃ nanosheets (0.6-3k g) at 40°C. (B-C) Change of the optical density of NiPS₃ extinction spectra at 460 nm for relatively large (B, 0.6-3k g) and relatively small (C, 3-10k g) nanosheets at different storage temperatures. Solid lines are empiric exponential fits of the data. Reproduced and adapted with permission from ¹¹.

For sample storage temperatures at 20, 40 and 60°C, a linearisation of the data can be observed if the natural logarithm of the optical density from both, extinction and absorbance measurements is plotted as a function of time as exemplarily shown for the relatively large NiPS₃ nanosheets (0.6-3k g)

in Figure 5.3-4 A. This is also the case for other sizes of NiPS₃ and FePS₃ nanosheets as shown in Appendix 5.3-4. This is consistent with first order degradation kinetics and allows to fit the data to a linear regression which has less degrees of freedom than the exponential fit function. This improves the reliability of extracted parameters for degradation kinetics, such as the macroscopic half-life.

The sample stored in the refrigerator deviates from this behaviour as clearly no linearisation is observed in the plot of the natural logarithm of the optical density as exemplarily shown for NiPS₃ nanosheets (0.6-3k g: Figure 5.3-4 B, 3-10k g: Appendix 5.3-4). While this result is not intuitive, it is important to consider that the vials were not sealed on storage. Ambient water can therefore condense into the sample, which is expected to be more pronounced for storage in the refrigerator as the environment is expected to be more humid than inside the laboratory. Thus, varying contributions from water and ambient oxygen to the sample decomposition can be expected. If this is the case, a second order degradation kinetic can be anticipated. To test this, the inverse optical density at 460 nm is plotted as a function of time (Figure 5.3-4 C). Indeed, for both absorbance and extinction, a linear behaviour is observed which suggests that the decay follows a second order rate law. Note that nanosheet aggregation can be induced by increasing the water content in the solvent which may also result in a deviation from first order decay kinetics in extinction spectra where scattering is expected to change the oscillator strength in aggregated nanosheets. However, no obvious change of the scattering background in the extinction spectra can be observed for the sample sets stored at 4°C (Figure 5.3-3 A and Appendix 5.3-3). Hence, aggregation is considered to play a minor role with respect to the discussed observations.

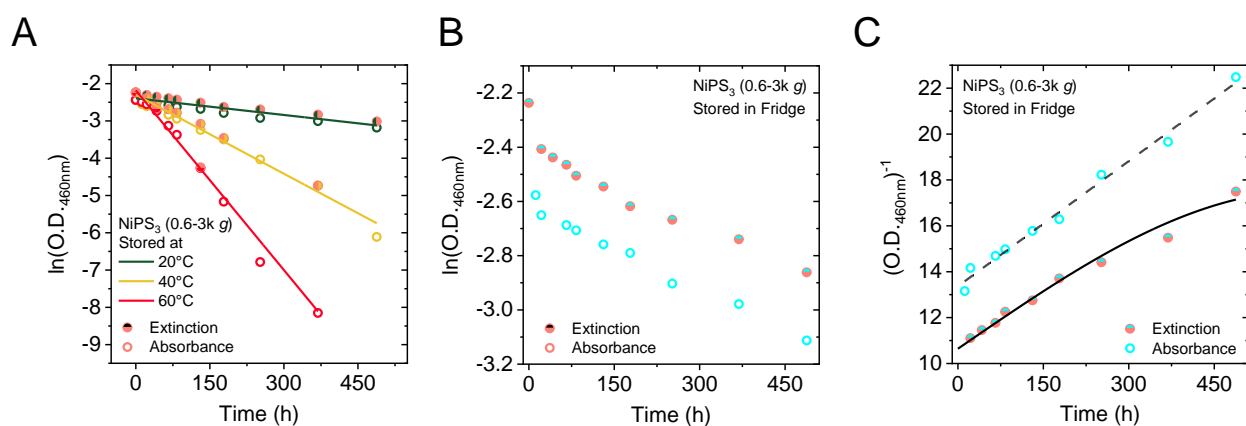


Figure 5.3-4: Kinetic aspects of the NiPS₃ nanosheet decomposition. (A) Plot of the natural logarithm of the optical density at 460 nm for both extinction (filled symbols) and absorbance (hollow symbols) measurements of comparatively large NiPS₃ nanosheets (0.6-3k g). For 20, 40 and 60°C a linearisation of the data is observed which implies a first order rate law for the decomposition. (B) Plot of extinction and absorption at 460 nm as function of time plotted on a semi-ln scale for the same sample as shown in (A), but stored in the refrigerator. No linearisation of the data is observed. (C) Same data as in (B) plotted as inverse optical density at 460 nm as function of time. The linear trend suggests second order kinetics due to additional contributions from water condensing into to the sample. Reproduced and adapted with permission from ¹¹.

Chapter 5 – Nanomaterial Stability

Plotting the natural logarithm of the macroscopic nanosheet half-life from the linear fits in Figure 5.3-4 A as a function of the inverse temperature (Figure 5.3-5 A) shows a linear dependence which enables to extract the activation energy for the nanosheet decomposition from the slope of linear fits according to the Arrhenius equation (Eq. 34). As both data from extinction and absorbance show the same trend, activation energy from both fits are averaged to improve the accuracy. The error bars in the plot represent the standard deviation of the fit in Figure 5.3-4 A (or Appendix 5.3-5 for FePS₃ and MnPS₃). For NiPS₃, the plots suggest an activation energy of 20-30 meV with only minor differences between the two size fractions (0.6-3k g: 23 kJ/mol 3-10k g: 27 kJ/mol) which confirms that the same macroscopic reactions occur independent of the nanosheet size. Note that the XPS measurements shown above (Figure 5.3-1 B-D) suggest that the nanosheet decomposition occurs on the edges and basal plane for NiPS₃. If that was the case, the half-lives should also be independent on nanosheet size. While Figure 5.3-4 A illustrates slightly smaller half-lives for small nanosheets, the sample-to-sample difference is much smaller than for TMDs or γ -InSe suggesting that degradation indeed occurs on both edge and basal plane. A similar analysis can be applied to the data extracted for FePS₃ and MnPS₃, as shown in Appendix 5.3-5. The results for all compounds are summarised in Table 5.3-1, where the activation energy is shown with respect to the average nanosheet size.

Table 5.3-1: Macroscopic size-dependent activation energies for NiPS₃, FePS₃ and MnPS₃ decomposition.

NiPS ₃		FePS ₃		MnPS ₃	
$\langle L \rangle$ (nm)	$E_A^{Dec.}$ (kJ/mol)	$\langle L \rangle$ (nm)	$E_A^{Dec.}$ (kJ/mol)	$\langle L \rangle$ (nm)	$E_A^{Dec.}$ (kJ/mol)
254.6	23.04±0.33	216.8	26.87±1.99	323.3	17.49±1.89
163.2	27.85±1.19	151.6	27.68±1.05	220.7	17.09±0.74
n.a.	n.a.	80.5	27.19±1.93	125.7	6.19±0.6

Different measurements imply a size-independent material decomposition for NiPS₃. However, to test this, the activation energy of all compounds is plotted as a function of the mean nanosheet volume (Figure 5.3-5 B), length, area and thickness (Appendix 5.3-5). While no clear trends are found for NiPS₃ and FePS₃, a size dependence is observed for MnPS₃ which suggests that various degradation pathways occur with a different weight depending on the nanosheet size. The results can be interpreted as preferential oxidation on the edges, as the activation energy for the degradation is significantly decreased for smaller nanosheets.

While such insights are useful in view of finding measures for passivation of the nanosheets to protect them from decomposition, no information about the expected portion of reacted material can be extracted from the linear fits thus not enabling a comparison to other materials. Hence, the material decomposition decay kinetics in Figure 5.3-3 are fitted to exponential functions. This enables to correlate the half-life for the material decomposition from the linear fits (*e.g.* Figure 5.3-4 A) to the portion of reacted material from the amplitude of the exponential fit (Figure 5.3-5 C). Similar to discussions above (Chapter 5.1 and 5.2) an empirical power law scaling for all transition metal hexathiohypo diphosphates under study is observed. As the number and spread of data points of the

individual materials does not allow for a reliable fitting of individual trends, a fit to the combined data is applied instead which is shown in comparison to black phosphorus.¹²⁷ Note that a different result can possibly be obtained, if additional data is generated for the individual materials. However, a larger spread of the data is required for such considerations which might be achievable for smaller doses of oxygen, larger nanosheets or decreased storage temperatures in a dry environment.

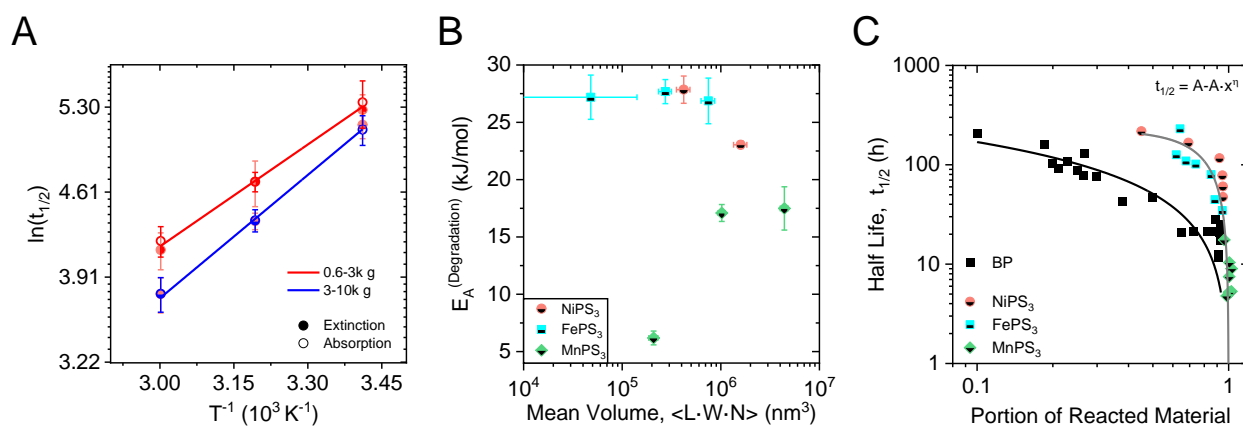


Figure 5.3-5: Thermodynamic and kinetic aspects of MPS₃ nanosheet decomposition in CHP. (A) Dependence of the macroscopic material half-life of NiPS₃ nanosheets as function of the inverse temperature on a semi-ln scale. A linearisation of the data points is observed which enables the determination of activation energies. (B) Dependence of the activation energy of NiPS₃, FePS₃ and MnPS₃ nanosheets with the average nanosheet volume. Different trends are observed for the individual materials, which imply different preferential decay mechanisms. An edge centred mechanism can be inferred from the increasing activation energy with size for MnPS₃. No trends with material dimensions are observed for NiPS₃ and FePS₃. Consequently, no preferential degradation of the basal plane or the edges can be postulated. (C) Plot of the half-life as function of the portion of reacted material of MPS₃ species in comparison to LPE BP at different storage conditions. Modified and reproduced with permission from ^{11, 127}.

To obtain deeper insights into the degradation behaviour, the local structure of single nanosheets was studied by scanning TEM-EDX measurements after stirring comparatively small-sized nanosheets (3-10k g) at 40°C for 500 hours in the group of Sarah Haigh (Manchester University). Elemental maps of nickel, phosphorus, sulfur and oxygen are shown in Figure 5.3-6 A for a pair of degraded nanosheets. Contrary to deposited nanosheets from a freshly prepared sample (Appendix 5.3-2), oxygen is not distributed homogeneously over the frame of measurement but shows contrast across the nanosheets which can be ascribed to surface oxidation. For further analysis of the nanosheet decomposition, atomic percent maps were generated (insets in Figure 5.3-6 A) by masking based on the Ni counts in order to account for spurious signals from the sample support. Using masks around the edge, the central region and an oxygen deficient region (highlighted by the red rectangle in the oxygen map in Figure 5.3-6 A) enables to determine a local stoichiometry for different regions on the flake. For the edge region of the sheets, a relatively high concentration of phosphorus with a stoichiometry of Ni_{0.8}P₁S₁ is observed, while the central mask suggests a stoichiometry of Ni_{0.8}P₁S_{1.8}. In the oxygen-depleted region towards the centre of the larger nanosheet, the local stoichiometry is Ni_{0.9}P₁S_{2.7}, *i.e.*, much closer to the expected composition measured for the freshly prepared nanosheet (NiPS_{2.8}, Appendix 5.3-2). The compositional deviation compared to the homogenous stoichiometry

Chapter 5 – Nanomaterial Stability

found for the freshly prepared nanosheet illustrates that particularly sulfur is dissolved and removed during oxidative degradation. It is evident from the images that the stoichiometry is different at the nanosheet edges compared to the planes. However, it is important to consider that the edge region is fully exposed to the environment, while the planes of inner layers of few-layered species are protected from the outward layers. Having this in mind, the overall STEM-EDX analysis confirms the proposed degradation on both edges and basal plane.

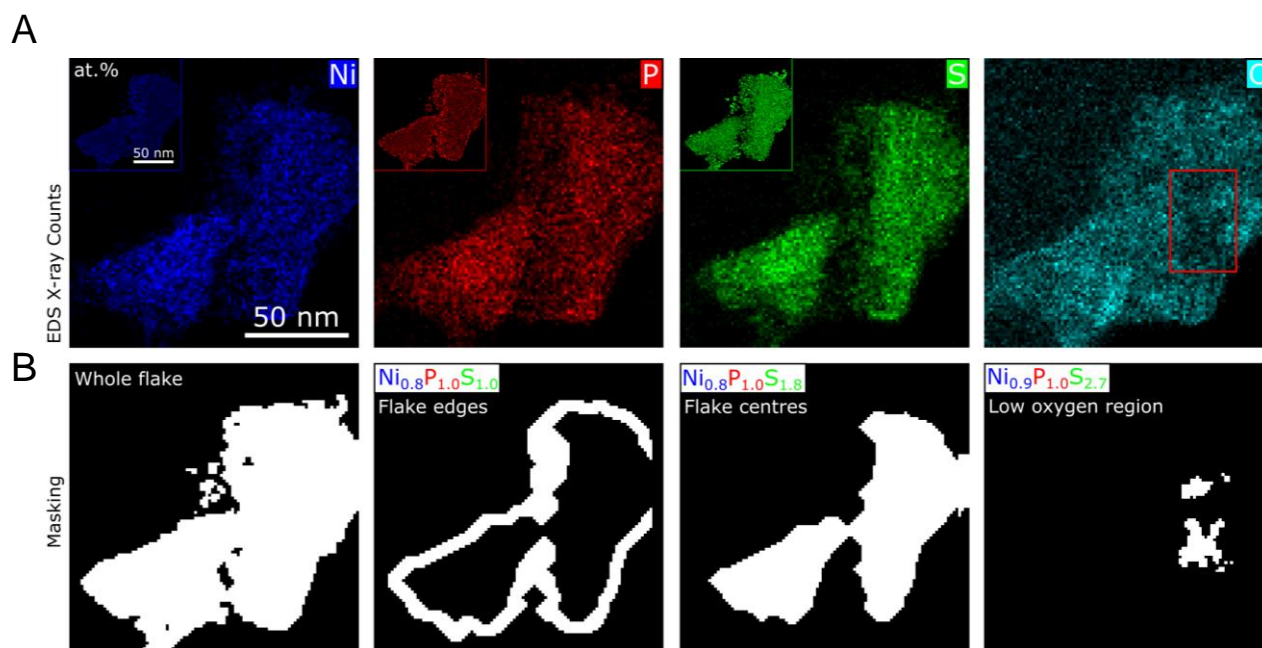


Figure 5.3-6: Measurement of the local oxidation of NiPS₃ nanosheets using STEM-EDX. (A) EDX maps of two flakes showing oxygen distributed within and on the surface as well as on the surrounding carbon support. Atomic percent maps of the Ni:P:S ratio (inset) show a relatively high concentration of P at the flake edges. Absolute quantification for the O signal is not possible due to the presence of oxygen in the carbon support. **(B)** Quantification of the Ni:P:S ratio in different regions of the flake was achieved by masking the raw spectrum image using the masks shown (where the signal from the white areas is included and black areas are excluded). The location of the flakes was determined based on the presence of Ni counts. The ‘flake edges’ mask yields a Ni_xP_yS_z ratio of 0.8:1:1 (x:y:z) and the ‘flake centres’ mask yields 0.8:1.0:1.8. A relatively pristine (‘low oxygen region’) towards the centre of the larger flake (region highlighted by the red rectangle on the O map) gives a ratio of 0.9:1.0:2.7. Reproduced and adapted with permission from ¹¹.

To summarise the results presented on transition metal hexathiohypo diphosphates, a novel approach on inert gas exfoliation in distilled, dried and degassed CHP enables to prepare nanomaterials that are structurally widely intact (as confirmed by various techniques) which are the ideal starting point to study environmental degradation. The results from XPS measurements additionally emphasise that the size selection by LCC cleans the material from oxides and impurities as soluble decomposition products and highly defective nanomaterial remains in the supernatant after centrifugation. The results provide an important guide for researchers interested in exploiting the electrochemical, magnetic or optical properties of transition metal hexathiohypo diphosphates. Various spectroscopic methods show that the material is mostly intact after exfoliation and shows only minor oxidation across all fractions.

Environmental impacts on the nanosheets from initially unimpaired nanomaterial were studied in depth. TEM-EDX shows that the oxidation occurs on nanosheet edges and basal planes with more pronounced oxidation at the nanosheet edges which are fully exposed to the environment. This is confirmed by XPS. Studies of the optical response by extinction and absorbance spectroscopy enables to follow the nanosheet decomposition as a function of time. Further analysis reveals that samples stored at different temperatures in ambient conditions follow first order degradation kinetics, while samples stored at increased humidity (*i.e.* in the refrigerator) deviate from this behaviour and show a second order kinetic which implies that both water and oxygen have an impact the decomposition of the material.

The samples following a first order rate-law are used to determine the macroscopic material half-life at different storage temperatures which allows to determine the activation energy for material decomposition. For NiPS₃ and FePS₃ no significant change of the activation energy is observed with material dimensions (*e.g.* volume). This implies similar activation energy for decomposition at the edges and the basal plane. This is not the case for MnPS₃, where an increase of the activation energy is observed with increasing material size which suggests a lower activation energy for edge degradation. The exponential decrease of the optical density in the extinction and absorbance spectra as function of time allows to approximate the expected portion of reacted material for infinite storage times at different temperatures. A full decomposition is observed at >40°C for all three materials. A correlation between the half-life and the portion of reacted material seems to follow the same power law behaviour as observed for BP,¹²⁷ monolayers of TMDs and γ -InSe. However, the complete decomposition leads to a clustering of most data points so that the information from all three materials had to be combined for fitting. While additional data might be required for meaningful analysis, it is evident from the data that a somewhat universal behaviour is observed. A deeper understanding of the empirical correlation will require theoretic considerations in future perspectives.

The overall data gives valuable insights into material decomposition mechanisms in a realistic environment for further processing in view of applications in energy storage. The results clearly show that the nanomaterial is prone to ambient oxygen and water which makes it extremely important to decouple catalytic activity from effects arising from material decomposition in view of widely studied applications of MPS₃ nanosheets for electro catalytic applications such as water splitting.^{103, 144, 148}

5.4 Ruthenium Chloride

Nanosheets of α -RuCl₃ are considered particularly interesting for fundamental studies of magnetic properties in low-dimensional structures.^{102, 217, 218} While reported studies focus predominantly on micromechanically-cleaved nanosheets, basically nothing is reported about magnetic properties of dispersed nanomaterials. To enable such studies, it is important to investigate the nanomaterial for structural changes after exfoliation and exposure to various environments. For this purpose, different

Chapter 5 – Nanomaterial Stability

sizes of LPE α - RuCl_3 were prepared in inert gas conditions and subjected to various spectroscopic methods to unravel potential structural changes of the material (Figure 5.4-1).

In order to assess the structural integrity of the nanomaterial after exfoliation and size selection, the material was drop-cast in a nitrogen atmosphere on a gold coated aluminium support for Raman and XPS measurements and on a quartz substrate for XRD (for details see Chapter 7.3). The Raman spectra (532 nm excitation) of three different sizes representative for large, intermediate and small nanosheets (*i.e.* 0.1-0.4k g, 6-12k g and 22-50k g) are shown in Figure 5.4-1 A. Measurements on a bulk crystal are shown for comparison for easier identification of changes in the spectra. While all modes from the bulk material can also be observed in the exfoliated nanosheets, a significant broadening of the modes is observed for the nanomaterial which may be ascribed to randomly distributed orientation of the drop-cast nanomaterial or structural deterioration, respectively. As no additional modes appear in the spectra of the nanosheets, no clear indications for material decomposition after LPE and LCC can be observed by Raman measurements. However, decomposition products may not be Raman active or resonant with the excitation wavelength. Hence, XPS measurements were additionally performed on the samples. The ruthenium 3d core level spectrum is shown in Figure 5.4-1 B for a sample containing small (22-50k g) nanosheets. In addition to the expected signals from RuCl_3 , additional contributions from carbon, elemental ruthenium, RuO_2 and $\text{Ru}(\text{OH})_3$ can be identified. The spectra suggest that $\sim 50\%$ of the initial RuCl_3 is retained on the surface. Fitting of the data to the response from the individual components implies that $\sim 10\%$ of the signal stems from elemental ruthenium, $\sim 21\%$ from RuO_2 and 16% from $\text{Ru}(\text{OH})_3$. The samples were measured in a collaboration with the Duesberg group in Munich and were exposed to ambient oxygen and water before the measurement. Furthermore, the actual sample decomposition may be intrinsically overestimated as XPS is surface sensitive.

In addition to Raman and XPS, PXRD measurements were acquired (Figure 5.4-1 C) in the group of Bettina Lotsch (MPI Stuttgart). The diffraction pattern of the large, medium and small nanosheets show different patterns than bulk α - RuCl_3 which is shown as comparison. In order to understand these differences, reflexes are additionally compared to the recently reported pattern of the restacked $[\text{RuCl}_3]^{x-}$ nanosheets¹⁰² which is shown in grey. The most intense Bragg reflexes of the exfoliated nanomaterial resembles the reflexes for the restacked material with slight differences of the peak positions. In addition, a signal broadening is observed which is assigned to structural distortion of restacked material upon drop-casting, similar to observations made for Raman measurements. A closer analysis reveals that a decreasing number of un-assignable reflexes is observed with increasing material size which indicates that crystalline degradation products are formed which are observed in the samples with higher surface to volume ratio. However, an alternative interpretation of the data could be that these are due to preferred orientation effects which are less prominent in the smaller sheets and therefore out-of-plane reflections show up more strongly as in the larger sheets, where mostly (001) reflections can be observed due to the reflection geometry. This would imply that the other reflections at higher angles are assignable to other RuCl_3 polymorphs. However, simulations

will be required for a deeper understanding of the observed reflexes, in particular because the data does not fit to expected species from XPS measurements.^{102, 219, 220}

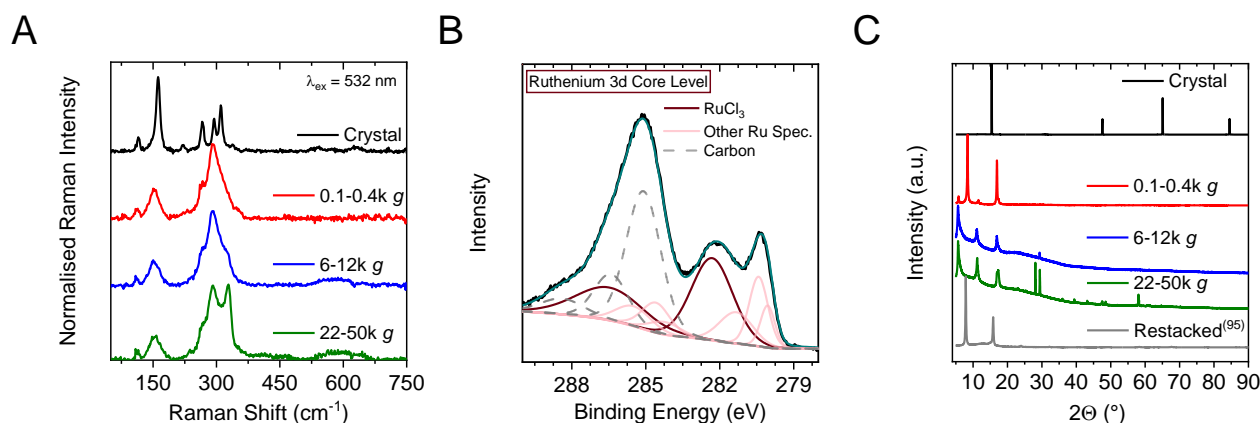


Figure 5.4-1: Structural characterisation of LPE α - RuCl_3 nanosheets. (A) Raman spectra of different nanosheet sizes including a measurement on a bulk crystal for comparison. Apart from signal broadening, no other than the expected signals are observed. (B) Ruthenium 3d core level spectrum of a fraction containing comparatively small nanosheets (22-50k g). Data fitting suggests that only $\sim 50\%$ of the material surface is composed of α RuCl_3 at the time of the measurement. (C) PXRD measurements of the bulk crystal (black) compared to different size-selected fractions of exfoliated nanosheets deposited on a quartz support. Reported data on restacked $[\text{RuCl}_3]^x$ nanosheets is shown for comparison. Modified and reproduced with permission from¹⁰².

To further study the decomposition of α - RuCl_3 , extinction and absorbance spectra were acquired after defined stirring times for samples of different sizes at different storage conditions. Specifically, samples containing relatively large (0.1-4k g), intermediate (6-12k g) and small (22-50k g) nanosheets were stirred at 20, 40 and 60°C, respectively. Prior to each measurement, samples were bath sonicated for ~ 1 minute to avoid potential impact from aggregation or sedimentation. Absorption spectra of large-sized nanosheets (0.1-0.4k g), acquired at different stirring times, up to 672 h (*i.e.* 28 days), at 40°C are exemplarily shown in Figure 5.4-2 A. Absorption spectra of other nanosheet sizes and storage conditions are shown in Appendix 5.4-1. In all cases, a systematic decrease of the overall intensity can be observed over time, which agrees well with similar experiments with layered NiPS_3 nanosheets (Chapter 5.3) and is an indication for material degradation. The drop of intensity is more drastic at elevated temperatures. In addition, broad absorption features arise over time in the UV-region for storage at 60°C, independent of the nanomaterial dimensions. The increased absorption at high energies is a typical sign for material oxidation, as observed for many other material systems. To follow the material degradation as a function of time and temperature, a wavelength was chosen, where no additional contributions from degradation products are observed. This is the case for the absorbance at 525 nm (and higher wavelengths). Thus, to track the degradation systematically, the absorption at 525 nm is extracted from the spectra and plotted as a function of time.

For all sizes and temperatures studied, the absorption at 525 nm follows an exponential decay (Figure 5.4-2 B-C, for all sizes see Appendix 5.4-2). As expected, degradation is both more complete and faster for storage at elevated temperatures. Plotting the natural logarithm of the absorption at

Chapter 5 – Nanomaterial Stability

525 nm as a function of stirring time reveals a clear linearization, consistent with a first order kinetics degradation mechanism. The linear fit on the semi-ln scale is used to extract the macroscopic half-lives for the material decomposition, as fewer degrees of freedom are required compared to an exponential fit which renders the result more reliable.

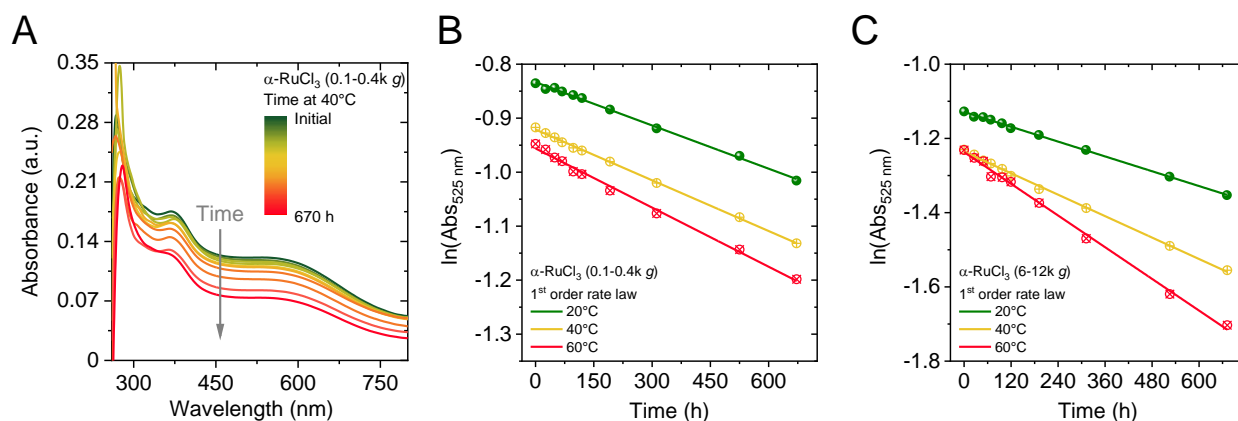


Figure 5.4-2: Change of the optical absorbance for different storage conditions as function of time. (A) Evolution of the extinction spectra for comparatively large α -RuCl₃ nanosheets (0.1-0.4k g) at 40°C. **(B-C)** Plot of the natural logarithm of the optical density at 525 nm for absorbance measurements of comparatively large **(B)** and intermediate sized nanosheets **(C)** of α -RuCl₃. For all temperatures (20, 40 and 60°C) a linearisation of the data is observed which implies a first order rate law for the decomposition.

The half-lives extracted from those fits for all nanosheet sizes and storage conditions can be used in an Arrhenius type analysis and are thus plotted as a function of the inverse storage temperature (Figure 5.4-3 A). In all cases, a linear scaling is observed, which allows to estimate the activation energy for the material decomposition from the slope of the linear fit according to the Arrhenius equation. The error bars are taken from the standard deviation of the fit in Figure 5.4-2 B-C. For α -RuCl₃, activation energies in the range of 6-20 kJ/mol are found, depending on the nanosheet size (Table 5.4-1). While this is significantly lower than for WS₂ and MPS₃, it should be noted that the half-lives are in the order of 300-700 min, *i.e.* larger than for the other materials under study. This is important, as it should still allow for further processing in application-oriented science.

Table 5.4-1: Macroscopic size-dependent activation energies for the α -RuCl₃ decomposition.

α -RuCl ₃	
$\langle L \rangle$ (nm)	$E_A^{Dec.}$ (kJ/mol)
100.0	6.35±0.15
205.8	15.40±0.82
433.1	18.87±0.90

The activation energy of α -RuCl₃ shows a similar size dependence as MnPS₃ which suggests a lower activation energy for the material decomposition at edges (Figure 5.4-3 B). While the linear

fitting of the natural logarithm of the absorbance results in improved reliability of the extracted activation energy compared to an exponential fit, no information of the portion of reacted material can be extracted. The initial absorbance data is therefore additionally fitted to an exponential function (Appendix 5.4-2). These fits imply that already at 20°C, more than 60% of the nanosheets decompose over time in the solvent used. The expected portion of reacted material approximated for infinite times is shown as a function of the macroscopic half-life in Figure 5.4-3 C. Reported data on black phosphorus is again shown for comparison.¹²⁷ The plot again illustrates that decomposition of α -RuCl₃ nanosheets in CHP is comparatively severe, but with longer half-lives which implies that sufficient processing time is available before significant decomposition occurs.

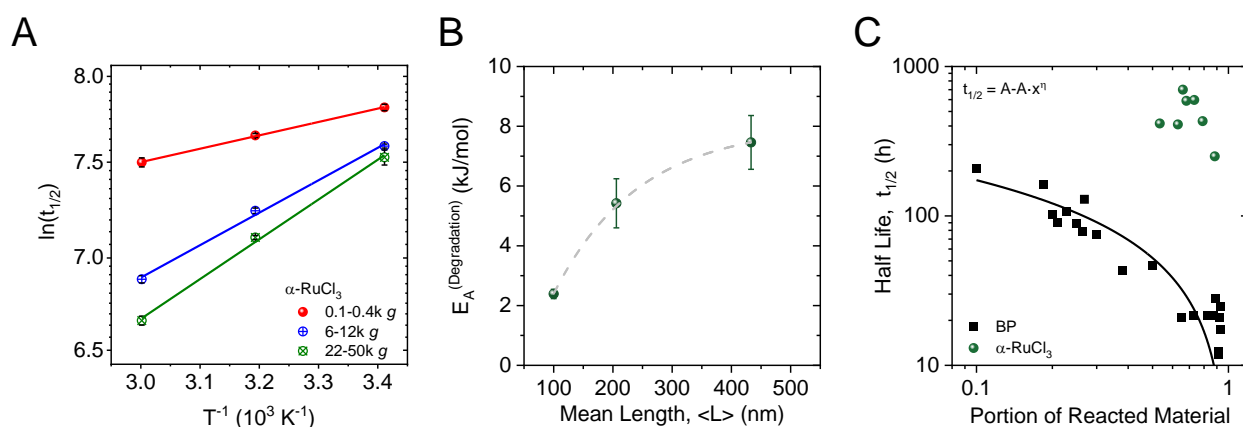


Figure 5.4-3: Thermodynamic and kinetic aspects of α -RuCl₃ nanosheet decomposition in CHP. (A) Dependence of the macroscopic material half-life of α -RuCl₃ nanosheets as function of the inverse temperature on a semi-In scale. The Arrhenius-type plot shows a linear dependence of the data points which enables to determine the activation energy for the material decomposition. (B) Dependence of the activation energy on the average nanosheet length. The trend infers a preferential edge centred degradation mechanism. (C) Plot of the half-life as function of the portion of reacted material of α -RuCl₃ species in comparison to LPE BP for different storage conditions. Modified and reproduced with permission from ¹²⁷.

The overall results on layered ruthenium chloride nanosheets show that a significant amount of the material undergoes structural changes over time. While the exact composition of potential products of material degradation remains unclear, mixed species of ruthenium oxides and hydroxides are suggested by XPS measurements. Similar to other material systems discussed in this work, material decomposition can be followed by absorbance spectroscopy. Here, the decomposition follows a first order rate law. Further evaluation of the data allows to extract activation energies for the degradation and reveals that a preferential edge decomposition can be expected for RuCl₃, as the activation energy is significantly decreased for comparatively smaller nanosheets. A similar behaviour is also observed for MnPS₃. While the decomposition of the nanomaterial is relatively complete even at room temperature, the available time frame for processing is orders of magnitudes larger than for black phosphorus and can potentially be increased further if the exposure to ambient oxygen or water is avoided. In addition, other solvent systems or stabilisers may help to prevent the degradation in future perspectives.

5.5 Chromium Telluride

Comparatively little is reported about layered chromium telluride which may be attributed to experimental challenges with regard to the synthesis of high quality, large crystals of the bulk material. However, challenges may also arise for nanomaterial preparation, as the nanosheets seem to be sensitive to ambient conditions which was shown in preliminary experiments, using aqueous surfactant as stabiliser in sonication-assisted LPE. Thus, it is important to address the stability of the exfoliated nanosheets in more detail from a fundamental point of view.

To test whether the structural integrity of the bulk material is retained for the nanomaterial, Raman spectroscopy was applied on drop-cast nanosheets of different sizes using different excitation wavelengths. Three different sizes of nanosheets (0.4-1k g, 1-5k g and 5-10k g) are shown in comparison to measurements on a bulk reference (Figure 5.5-1). This allows to identify resonance effects on the observed Raman modes and on potential decomposition products. As extinction spectra generally show light absorbance in the entire range of the accessible wavelength range for all sizes of the material (see Figure 4.5-1 A), three different lasers covering a large range of the visible spectrum (*i.e.* 475, 532 and 633 nm) are used for the measurements on both bulk- and nanomaterial. While changes of the relative intensity can be attributed to variations in the average nanosheet orientation as discussed in detail in Chapter 4.5, no other than the expected modes are observed in all spectra. This implies that the initial material lattice remains unchanged upon exfoliation and that insignificant oxidation occurs for the exfoliation in inert gas conditions.

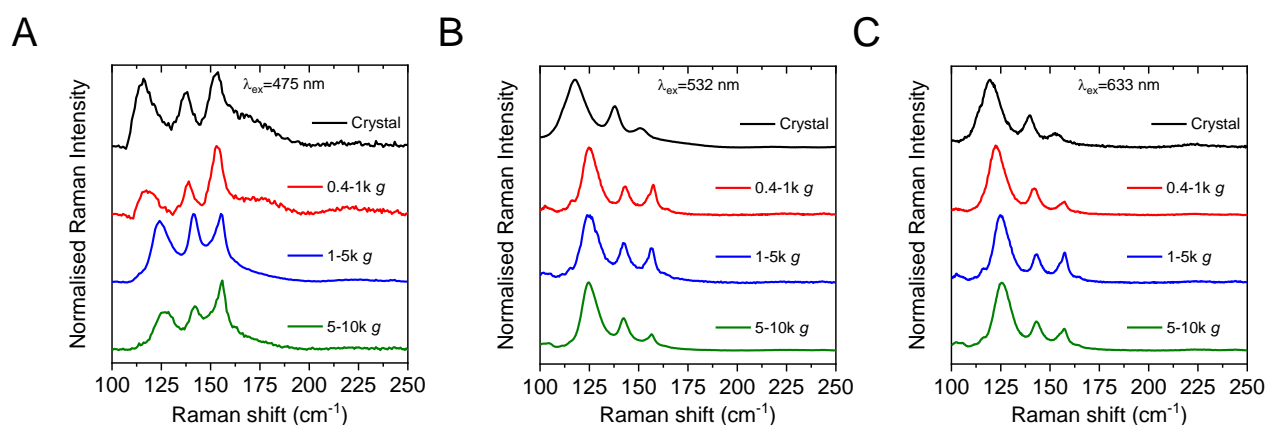


Figure 5.5-1: Resonance effects on Raman modes for different CrTe₃ nanosheet sizes. Vibrational modes of relatively small, intermediate and large nanosheets of drop-cast LPE CrTe₃ nanosheets in comparison to a bulk crystal, acquired with 475 nm (A), 532 nm (B), and 633 nm (C) laser wavelength for excitation. No other than the expected vibrational modes are observed in the Raman spectra.

While the Raman spectra suggest that the material structure is retained after exfoliation and size selection, potential products of the material decomposition may be Raman inactive. Hence, no unambiguous comments on the material compositions can be made from Raman spectra alone.

To further account for the stability, dispersions of size-selected nanosheets were freshly prepared in a nitrogen atmosphere and extinction spectra for samples stored in ambient conditions under light exclusion were acquired over time (Appendix 5.5-1). All sizes show similar changes within the first 24 h: a water peak arises at ~1430 nm, the intensity in the UV-region increases and the overall optical density decreases with respect to the initial spectrum. In addition, the formation of additional features, between 250 and 280 nm is observed. The change of the spectra seems to be mostly size invariant. Hence, a polydisperse stock dispersion was prepared for a systematic analysis. To avoid distortion of the results from bulk-like or oxidised starting material, a short centrifugation sequence was applied. Unexfoliated material was removed from the dispersion by sedimentation at 100 g. In addition, the material of interest was sedimented at 30k g, which enables to increase the material concentration upon redispersion in fresh solvent and goes hand in hand with removal of already defective or oxidised nanomaterial, as clearly demonstrated in Chapter 5.3. A dispersion was freshly diluted in the glovebox and stored at 20°C in ambient conditions, excluding light for subsequent extinction measurements of the initial sample and after 24, 44, 98 and 118 h (Figure 5.5-2 A). The trend described above is observed for the polydisperse sample and progresses over time. An additional peak is formed at 268 nm and a dip develops at 350 nm (Figure 5.5-2 A - inset). In addition, a water peak intensifies over time at ~1450 nm as indicated by the grey arrows in Figure 5.5-2 A. The changes in the UV-region may be attributed to the formation of non-stoichiometric tellurium and chromium oxides and the increasing water concentration can be ascribed to the hygroscopicity of the dried solvent. It is thus important to investigate the role of water in the reaction in more detail. To achieve this, samples containing defined initial concentrations of water (0, 3 and 10 vol%) were prepared in an identical way (nitrogen atmosphere, light exclusion) and extinction spectra were acquired over time at similar conditions. The spectra are shown in Appendix 5.5-2.

Different wavelength at specific positions of the spectra are followed over time to find the most suitable position for a quantification of the degradation (see Appendix 5.5-2). The extinction at 500 nm, where only contributions from the initial CrTe₃ are observed, shows the most systematic change of the spectral profile over time. A linearisation is achieved when plotting the optical densities at 500 nm on a semi-ln scale. Fitting allows to extract decay rates of the optical density at 500 nm of $1.2 \cdot 10^{-3}$, $1.0 \cdot 10^{-3}$ and $7.4 \cdot 10^{-4} \text{ h}^{-1}$ for the samples with 0, 3 and 10 vol% H₂O added, respectively. The fits are reasonable in all cases, albeit with some scatter (Figure 5.5-2 B). Interestingly, the decrease of the optical density over time is steepest in the sample with no water added. To illustrate this more clearly, the absolute value of the decay rates extracted as slopes from the linear fits are plotted as function of the initially added water concentration (Figure 5.5-2 C). A roughly linear decrease in the decay rate with increasing amount of water is observed. This is counterintuitive, as it would be expected that the time constants increase with increasing amount of water if water participates in the reaction as has previously been observed for liquid-exfoliated black phosphorus.¹²⁷ To understand this, the water peak in the extinction spectra is explicitly analysed in more detail.

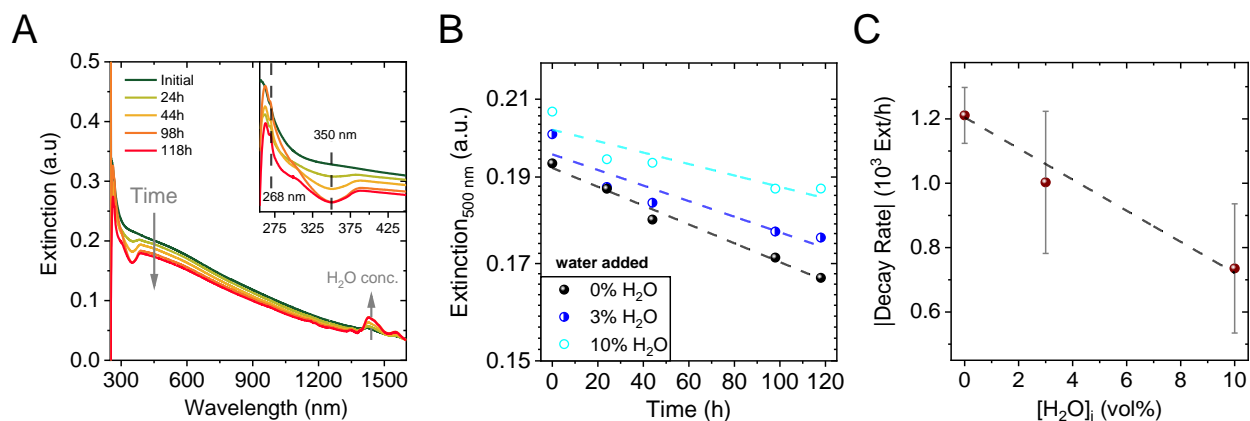


Figure 5.5-2: Tracking CrTe₃ degradation by extinction spectroscopy. (A) Extinction spectra of a polydisperse CrTe₃ nanosheet stock dispersion stored at 20°C in ambient conditions as function of time. The evolution of an additional feature at 268 nm and the formation of a dip at 350 nm is observed (inset). (B) Extinction intensity at 500 nm (on a semi ln-scale) as function of time for three sample sets with different amounts of water added after the exfoliation (0, 3 and 10 vol%). The dashed lines are fits to first order decay kinetics. (C) Absolute extinction decay rate extracted from the slopes in (B) as function of the initial water concentration. The decay is slower when more water is present suggesting the formation of a passivation layer.

The effective concentration of water is estimated, using the published extinction coefficient of water in CHP¹²⁷ at 1430 nm and the background of CrTe₃ at this wavelength is subtracted. Figure 5.5-3 A a plot of the water concentration as a function of time. The water concentration increases within the first 100 hours before saturating for the samples where no water was initially added. This applies to the sample where 3 vol% water was added as well. In contrast, the water concentration decreases as a function of time within the first 100 hours for the sample where initially 10 vol% of water was added. This is consistent with the 10 vol% CHP-H₂O mixture being less hygroscopic, so that the consumption of water upon reaction with CrTe₃ can be spectroscopically observed. This clearly demonstrates that water participates in the reaction. Another way to represent this data is to plot the change in the water concentration as function of the change in the CrTe₃ extinction intensity (Figure 5.5-3 B). As the concentration of CrTe₃ decreases, the water content increases in the case of the 0 vol% and 3 vol% sample, but decreases for the 10 vol% sample.

The decreasing time constant of the CrTe₃ degradation with increasing water content illustrated in Figure 5.5-2 C is puzzling. A possible rational explanation is the formation of a passivation layer that forms relatively quickly in the presence of excess water which then slows down further degradation which is consistent with previous reports on the oxidative passivation of antimony.²²¹ The methodology of adding water allows to see more clearly how the spectra evolve in the UV-Vis spectra. Thus, it was possible to determine various signals in the UV-area, which suggests that different oxidation products are created over time. Since the extinction values did not decay as significantly as for other materials over time, it is expected that the oxidation of the material only takes place at the surface area of the nanomaterial. This can lead to a passivation shell which protects the samples from further oxidation and agrees with the observation of decreasing time constants for the material degradation with increasing water content.

Since no significant further change of the spectra can be observed after 100 h, the portion of reacted material can be estimated in spite of some scatter in the decays. The result is shown in a plot of the half-life as function of the portion of reacted material in comparison to reproduced data on black phosphorus (Figure 5.5-2 C).¹²⁷ The data on CrTe₃ is limited to three data points which are comparatively scattered. Hence, no trend can be identified from the data. However, it should be noted that the data is located in regions of low portions of reacted material which supports an efficient passivation of the nanomaterial. This is further supported by AFM relocation of deposited nanosheets from a stock-like dispersion as described above which was measured right after preparation and after storage in ambient conditions for 2 days (Appendix 5.5-3). To test whether the sample changes over time, the same spot on a substrate was relocated and remeasured to identify changes of the nanosheet morphology. The images show no significant change of the nanosheets which allows to conclude that no severe degradation occurs on deposited nanosheets within the timeframe required for the analysis.

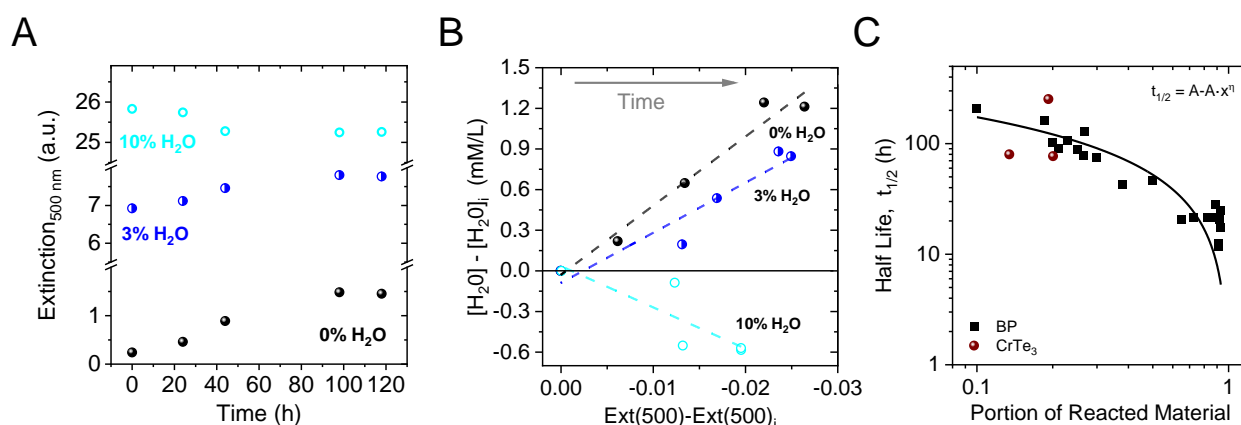


Figure 5.5-3: Quantification of the water-driven CrTe₃ nanosheet decomposition. (A) Change of the water concentration (extracted from the extinction at 1430 nm) for the three sample sets. The samples with an initial water concentration of 0 and 3 vol% show a systematic increase of the water content, while the sample with initially 10 vol% water shows a systematic decrease indicating the consumption of water on nanosheet decomposition. (B) Change of the water concentration *versus* change of the extinction at 500 nm. Only for the 10 vol% sample, both water and nanosheet concentration drop. For initially lower water contents, more water is attracted to the hygroscopic solvent than is consumed in the reaction with CrTe₃ resulting in a positive slope. (C) Plot of the half-life as function of the portion of reacted material of CrTe₃ species in comparison to LPE BP for different water concentrations stored in ambient conditions at 20°C. Modified and reproduced with permission from ¹²⁷.

In summary, Raman spectroscopy does not show any traces of decomposition of the nanomaterial and no significant changes with material dimensions apart from orientation-based effects as discussed in more detail in Chapter 4.5. While the Raman experiments suggest no severe material decomposition, extinction data on CrTe₃ acquired over time reveals systematic changes of the spectra for samples stored in ambient conditions. Titration experiments with water show that water contributes to the degradation which can be quantified by fitting the tracked changes of the extinction spectra over time. The systematic decrease of the optical density at 500 nm follows a first order rate law for the decomposition and allows to determine a water concentration-dependent decay rate of the material

Chapter 5 – Nanomaterial Stability

which is higher for lower water concentrations. The results imply that a passivation of the material occurs over time. Further analysis shows that water is consumed in the degradation process if the water concentration is high enough that the change rate of material decomposition exceeds the increase of the water concentration from ambient water by the hygroscopicity of the solvent.

Continuous measurements of the same samples for extended storing times in ambience shows a saturation of the observed changes in agreement with the postulated material passivation which simultaneously allows to estimate the portion of reacted material and the half-life for the oxidative passivation. While the data is minimal and scattered, no more than ~20% of the initial material is consumed according to the extinction measurements. This is further supported by relocalisation of initially fresh deposited nanosheets after 2 days which shows no significant change of the nanosheet morphology. Importantly, the techniques and overall results achieved for CrTe₃ nanosheets can readily be transferred to study the decomposition of other material systems by using standard spectroscopy.

5.5 Quantitative Assessment of the Environmental Stability for Van der Waals Nanoparticles

In perspective of the overall results presented in Chapter 5, methods to evaluate the environmental nanomaterial stability using standard spectroscopy have been presented. While Raman spectroscopy which is often applied for material characterisation seems to be insufficient, as decomposition products are expected to be of amorphous and undefined character and may additionally be Raman inactive, absorbance and extinction spectroscopy has proven to be powerful to track material decomposition as function of time. Measurements of nanosheet properties by a combination of XPS, XRD, TEM, and EDX measurements have demonstrated that materials prone to ambient conditions can be prepared by means of sonication-assisted LPE exhibiting inherent material properties in inert gas conditions using standard Schlenk techniques. It is important to consider that each method has its characteristic significance with respect to structural changes of the material. As such, for a meaningful analysis of the nanosheet properties and potential compositional changes, a set of different methods is always required.

While it is important to demonstrate that the materials do not undergo structural or compositional changes upon exfoliation, it is of equal interest to understand environmental impacts on the material. For many applications, certain solvents and temperatures are required for further processing. It is therefore substantial to investigate the material under such conditions. Hence, materials under study have been systematically exposed to a controlled environment in ambient conditions using varying temperatures or water concentrations in the solvent.

Extinction and absorbance measurements have proven to be powerful for identification of changes of the nanomaterial over time. The materials studied in the framework of this thesis typically

show single exponential decays consistent with (pseudo) first order decay kinetics which allows to determine the macroscopic half-life and the portion of reacted material by fitting of the relative changes of the spectra over time. A plot of these two parameters *versus* each other lends itself to compare the degradation for different materials. This is shown for stock-like dispersions of various materials studied in this thesis, as well as group internal results on other van der Waals crystals (LaSeTe₂ and TiS₂) and literature data (BP and GeS)^{13, 127} in Figure 5.6-1 A. Note that a low portion of reacted material is indicative of passivation, either induced by the solvent or through a passivating oxide layer. Such passivation effects are observed for TiS₂, BP, CrTe₃ and NiPS₃ (to a lesser extent). For TiS₂ and BP, this was shown to be a result of the pyrrolidone-based solvent,^{127, 193} as the portion of reacted material significantly increased by adding water or performing the exfoliation in aqueous surfactant. In contrast, for CrTe₃ investigated here, the portion of reacted material remained widely constant after addition of water suggesting that an inherent passivation layer from degradation products is formed in this case. It is also important to note that this solvent passivation documented in literature does not occur for many of the materials studied (*e.g.* RuCl₃, FePS₃). This suggests that the solvent shell is dependent on the structure of materials. While this is to be expected, it should be noted that this finding is not obvious from exfoliation experiments, where similar surface energies and Hansen solubility parameters were found for a broad range of van der Waals crystals, irrespective of their structure.^{58, 12, 20, 50, 75} The half-life and portion of reacted material seem to be somewhat correlated and follow a power law dependence for different sizes and storage conditions of the same material (Figure 5.6-1 B). While the exact position of the data in these plots can be influenced by varying the size, water content or storage temperature of the samples, a general trend line can be identified within different conditions applied for the same material. The relative position of the materials in this degradation space can thus be regarded as solid comparison of the material degradation irrespective of the conditions applied. The exact origin of this empirically observed behaviour is not understood to date and will require additional support from theory. However, it strongly suggests a unifying principle for the 2D-material decomposition that will be extremely useful to construct a degradation library, similar to the spectroscopic size and thickness metrics library suggested in Chapter 4.

In addition to these findings, it was possible to fit the changes in the spectra which could be ascribed to material degradation to first and second order rate laws depending on the storage conditions which implies different degradation pathways. As exemplarily shown for NiPS₃, contributions from water condensing into the sample has an impact on the material decomposition manifested by a second order rate law which can be observed for storage at decreased temperatures in a humid atmosphere (refrigerator at ~4°C). Apart from this, the thermodynamically favoured mechanism seems to follow a first order rate law for samples stored at elevated temperatures (20-60°C). The extracted half-lives can be plotted, in an Arrhenius-type plot to determine the macroscopic activation energy for certain materials. Such analysis allows to evaluate preferential sites for the material decomposition from trends with nanosheet size (Figure 5.6-1 C). While a decrease of the activation energy with nanosheet size implies a lower activation energy for edge-centred degradation - which is observed

Chapter 5 – Nanomaterial Stability

for MnPS_3 , RuCl_3 , no trend of the activation energy with material size suggests simultaneous degradation of edge and basal plane sites with similar activation energies. In addition, the activation energies for the degradation give useful insights to assess suitable processing temperatures for the different materials. Note that by virtue of the experiments, all materials included in this plot exhibit significant degradation already at 40°C .

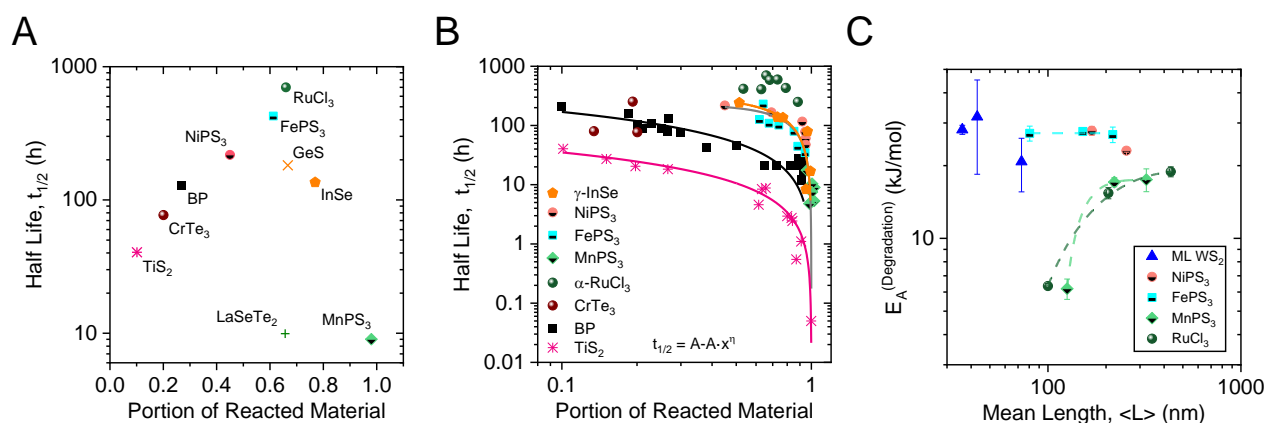


Figure 5.6-1: Assessment of the stability for different 2D-nanomaterial systems. (A) Material half-life as function of the portion of reacted from extrapolated exponential trends for stock-like material dispersions. The position of the data in the plot implies how fast and how complete the decomposition occurs. For materials with a low portion of reacted material, an efficient passivation of the material can be inferred either induced by a solvent passivation shell or a passivating oxide layer. (B) The same plot as presented in (A) for different sizes and storage conditions of the nanomaterials. A universal power law dependence can be observed. (C) Plot of the activation energy as a function of nanomaterial size (*i.e.* mean length). Trends with size allow to determine preferential decomposition on edge or basal plane sites. Modified and reproduced with permission from ^{127, 193}.

The presented results demonstrate the possibility of identifying potent materials for applications based on their environmental stability at realistic processing conditions and allow to quantify the decomposition at different storage conditions using standard spectroscopy. While this work focuses on low dimensional van der Waals crystals, it can be expected that the presented techniques and data analysis can readily be transferred to other material systems.

6 Conclusion and Future Perspectives

This Chapter summarises insights and conclusions drawn from the results presented within this work. The discussed findings are put in context with related work reported in literature. Ultimately, perspectives for future fundamental studies and promising applications are given.

Within the scope of this work, the intriguing change of material properties upon delamination of van der Waals crystals into sheet stacks of reduced dimensionality down to the monolayer limit were exploited to study fundamental and unifying principles. To this end, 17 different van der Waals crystals of seven different material classes have successfully been exfoliated into their respective nanosheets and sorted by size and thickness. These includes previously unstudied materials such as organic 2D-polymers and metal organic frameworks. Unlike other reports on individual nanosheets, where changes in the properties can arise due to inhomogeneities of the dielectric environment, the presented studies are carried out in a liquid environment. This enables not only to study nanosheets in homogenous dielectric conditions, but also to probe ensembles of typically $\sim 10^{10}$ nanosheets. A downside of the LPE approach is that samples are still polydisperse even after size selection. As such, these samples require delicate statistical analysis of the nanosheet size and thickness distribution for quantitative statements on properties arising with changing the material dimensions. To address this, a total of 23199 individual nanosheets were measured in length, width and thickness using atomic force microscopy. This kind of analysis may be tedious and time consuming, but enables to study rudimentary principles for nanomaterial preparation and to develop advanced models revealing fundamental limitations of the widely applied sonication-assisted exfoliation.

A model developed widely independently of this work suggests equipartition of energy between events of covalent bond tearing and of layer delamination.⁴⁷ As such, the size and thickness of the produced 2D-nanomaterials is correlated to the ratio of the in-plane and out-of-plane binding strength. Theoretical considerations propose a power law dependence between the nanosheet area and layer number,⁴⁷ which could be confirmed by experiments. The model holds for all materials studied in this thesis, but with a deviation of the expected scaling exponent ($\gamma_{Model} = 2$).⁴⁷ A refined data analysis revealed exponents centred at around 1.3, also for the published data, which disagrees with the model. The reason for the empirical deviation from the model are still to be explored in collaborations with theoreticians.

In addition, maybe more importantly, constraints with respect to sizes at a given thickness for nanomaterial produced by means of sonication-assisted LPE need to be tackled in future research. While theoretical considerations reveal intrinsic limitations of the process, strategies to overcome such obstacles need to be developed. As the energy ratio of the in-plane to out-of-plane bonding determines the accessible nanosheet dimensions, the out-of-plane binding strength needs to be lowered in order to access laterally larger nanomaterial at the same thickness. Techniques to achieve such

Chapter 6 – Conclusion

a decrease of the interlayer attraction are readily reported using osmotic swelling^{154, 222, 223} or intercalation chemistry.²²⁴⁻²²⁷ Elaboration of such techniques without changing the material characteristics (*e.g.* by charge transfer processes)²²⁸ will be an important topic in advanced approaches.

In spite of the identified constraints with respect to material dimensions, the statistic evaluation enables to correlate nanosheet dimensions to changes of their optical response. Systematic changes of the spectral profile of the optical extinction and absorbance spectra allow to derive quantitative spectroscopic metrics for the material size and thickness. The changes of the spectral profile essentially underlie four distinct principles based on effects arising from material edges, scattering, quantum confinement and dielectric screening. While each effect has a different, but defined impact on the spectra, two different models have been applied to correlate these changes to average material dimensions. A previously reported model⁴⁸ can be applied to all materials under study in order to determine the mean material lateral size of the nanomaterial based on intensity ratios arising from changing electronic contributions from material edges and planes depending on the nanosheet sizes.⁴⁸ Additionally, a thus far empirical exponential function can be used to quantify the change of peak positions associated with decreasing layer numbers. For all systems, a blueshift of the energies of the excitonic transitions is observed with decreasing layer number. It was possible to identify simultaneous changes of the exciton binding energy and the optical band gap to be responsible for this effect in TMDs. The experiments were supported by first principle calculations which suggest that the absolute shift of the resonance depends on the mass of the metal atom, while the change-rate is defined by the materials band gap. A similar behaviour is found for all materials studied, where excitonic transitions are observed, and an empirical direct proportionality between the change-rate of the shift and the materials' band gap is observed (including data extracted from literature). Overall, the presented changes in optical properties are qualitatively based on geometric effects and can be transferred and applied even to non-2D-materials, as demonstrated recently.²²⁹ The reported metrics do not only offer a fast and reliable determination of average material dimension and concentration which is useful to study the application potential of the materials in the future, but also give additional insights into unifying principles arising from geometric aspects.

While such universally applicable phenomena are fascinating from an experimentalists' point of view, it is important to consider the increased chemical reactivity arising with the increased effective surface area upon exfoliation. Consequently, a nanomaterial may be less stable with respect to environmental decomposition than the corresponding bulk material. Results presented in this work shed light on such aspects at realistic conditions expected for further material processing. As some materials showed characteristic signs of decomposition in microscopy experiments, dispersions were prepared in inert gas conditions using dry and degassed solvents. For all materials under study, only minor decomposition is observed for inert gas LPE and LCC according to multiple spectroscopic methods such as diffraction, EDX, XPS and Raman measurements. This enabled to assess and to quantify the observed decomposition in a controlled environment for initially "undamaged" nanomaterials using standard spectroscopy such as PL, extinction and absorbance measurements. Changes of the spectra can be followed as a function of time and give insights into the macroscopic material

half-life as well as the portion of reacted material from extrapolation fitted exponential decays to infinite timescales. Kinetic considerations have shown that the decomposition often follows a first order rate law, with exceptions of second order decay kinetics under certain storage conditions. For many examples, the half-life as function of inverse temperature follows an Arrhenius-type behaviour which allows to extract the activation energy for the material decomposition. Trends with material size can be used to postulate preferential mechanisms for the degradation. At last, a plot of the macroscopic half-life as function of the portion of reacted material is suggested to assess the material stability in a comparative way. While the spread of the data in this plot can be varied by adjusting the sample storage conditions, an empiric power law correlation of the two parameters is observed. The exact origin for this behaviour is unclear and requires theoretical considerations, but the relative position of each material can be considered as a metric for the nanomaterial stability.

Since for many materials a complete decomposition can be expected over time, it will be important in future research to identify stabilisers or passivating agents for these compounds which do not significantly influence the inherent material properties.

Final remarks. In conclusion, van der Waals crystals are fascinating materials promising for a range of applications. While some materials currently have to be prepared under harsh conditions, leading to structural imperfections which limit the application potential, novel approaches at milder conditions may help to overcome experimental challenges at ever growing structural precision. The experimental realisation and rudimentary understanding of aspects defining properties of 2D-nanomaterials have greatly been improving in the past years due to extensive research in the field. Beyond the discussions in this thesis, advances in material processing enabled all-printed devices based on 2D-materials²³⁰ or preparation of structurally precise 2D-heterostructures revealing synergistic effects.^{108, 231} Novel synthetic materials close to structural perfection were demonstrated exploiting manifold strategies offered by organic synthesis. Overall, exciting insights can be expected in the field improving the current understanding of fundamental prospects and properties of matter.

Chapter 6 – Conclusion

7 Methods

In this Chapter, a detailed description of experimental procedures and spectroscopic methods used for material characterisation is given. At last, an overview of materials used within this work is presented. Measurements performed by collaborators are included and highlighted in bold letters.

7.1 Liquid Phase Exfoliation

Exfoliation by tip sonication: TMD, 2D-Polymer and InSe dispersions were prepared by probe-sonicating the powder in two steps. The exact parameters for the exfoliation, as well as the initial concentration of the dispersions and solvent volumes are shown in Table 7.1-1. In every case, the powder was immersed in the solvent and sonicated at 4°C.

For volumes of 80 ml, a 100 mL metal beaker was used and subjected to probe sonication using a solid flathead tip (SonicsVXC-500, *i.e.* Probe 1) for 1 h at 60% amplitude with a typical pulse sequence of 6 s on and 4 s off. During the sonication, the sonic probe was placed 2 cm from the bottom of the beaker. The dispersion was centrifuged in 20 mL of aliquots using 50 mL vials in a Hettich Mikro 220R centrifuge equipped with a fixed-angle rotor 1016 at 2660 g for 1.5 h. The supernatant was discarded, and the sediment was collected in 80 mL of fresh solvent and subjected to a second sonication using a solid flathead tip (Sonics VX-500, Probe 1) using the parameters shown in the table below. From our experience, this two-step sonication procedure yields a higher concentration of exfoliated material and removes soluble impurities from the starting material.

For samples prepared in solvent volumes of 30 ml, a 50 mL centrifuge tube (VWR, order number 525-0402) was used and the sonication was performed in one step due to limited amounts of the available starting material. A tapered sonication microtip (Probe 2) was lowered to the bottom of the vial, then raised 2 cm above the vial bottom. The mixture was sonicated by probe sonication using parameters as shown in the table below. Resulting samples after exfoliation are referred to as stock dispersion

Table 7.1-1 Parameters used for exfoliation by Tip sonication

	Probe	Amplitude	Pulse (on/off)	Time	Volume	Concentration
WS ₂	1	60%	6 s / 4 s	5 h	80 mL	20 g/L
MoS ₂	1	60%	6 s / 4 s	5 h	80 mL	20 g/L
WSe ₂	1	60%	6 s / 4 s	5 h	80 mL	20 g/L
MoSe ₂	1	60%	6 s / 4 s	5 h	80 mL	20 g/L
γ -InSe	1	60%	6 s / 6 s	7 h	80 mL	20 g/L
2D-Pol(1)	2	40%	6 s / 4 s	7 h	30 mL	1 g/L
2D-Pol(2N)	2	40%	6 s / 6 s	5 h	30 mL	4 g/L

Chapter 7 – Methods

Exfoliation by bath sonication for the exfoliation of metal organic frameworks in aqueous surfactant solution. For each MOF, 5 mg of the starting material was exfoliated in 5 ml aqueous SC ($2 \text{ g}\cdot\text{L}^{-1}$) in a round bottom flask using a Branson ultrasonic bath (Bransonic CPX2800-E, 130 W). The dispersion was kept at $\sim 5^\circ\text{C}$ by exchanging the water in the bath after every 30 minutes of sonication to avoid heating effects. Ice-cooled water was used for this purpose. For MOFs, no size selection was performed, but the nanomaterial stock dispersion was purified after the sonication treatment by removal of unexfoliated material at low centrifugal accelerations in a Hettich Mikro 220R centrifuge equipped with a fixed-angle rotor 1016 at 100 g for 2 h. To concentrate the nanomaterial for further analysis and to account for potential soluble impurities, the supernatant after the centrifugation at 100 g was sedimented using a Beckman Coulter Avanti XP centrifuge with a fixed angle rotor (JA 25.50) at 74k g and redispersed in 1-2 ml of $0.1 \text{ g}\cdot\text{L}^{-1}$ aqueous SC. The sample preparation is schematically shown in Figure 7.1-1.

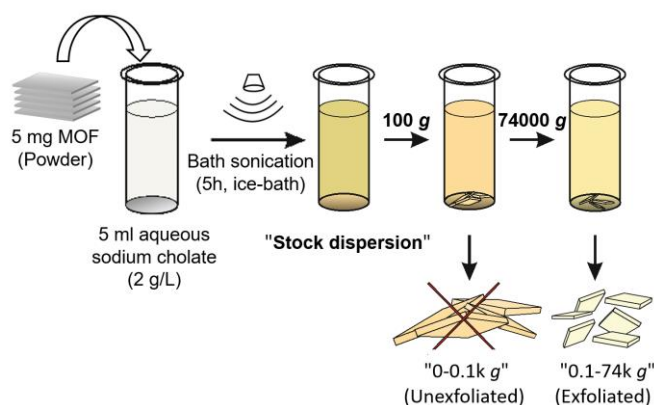


Figure 7.1-1: Schematic illustration of the MOF exfoliation and sample preparation for further analysis.

Exfoliation under inert gas conditions: Dispersions of NiPS_3 , FePS_3 , MnPS_3 , $\alpha\text{-RuCl}_3$ and CrTe_3 were prepared by sonication of the ground powder in an argon atmosphere over 7 h in dried, distilled and degassed CHP ($c = 2 \text{ g}\cdot\text{L}^{-1}$) in a round bottom flask using a Branson ultrasonic bath (Bransonic CPX2800-E, 130 W). The dispersion was kept at $\sim 5^\circ\text{C}$ by exchanging the water in the bath after every 30 minutes of sonication to avoid heating effects. Ice-cooled water was used for this purpose. Samples prepared according to this protocol are referred to as stock dispersion.

7.2 Size Selection

Liquid cascade centrifugation: Dispersions were size-selected by liquid cascade centrifugation in multiple steps of subsequently increasing centrifugation speeds. For speeds up to 30k g , a Hettich Mikro 220R centrifuge equipped with a fixed-angle rotor (1195A) was used. For centrifugation at speeds higher than 30k g , a Beckman Coulter Avanti XP centrifuge was used with a fixed angle rotor (JA25.15). Each centrifugation step was performed for 2 hours at 20°C . After each step,

the sediment was redispersed for analysis in a reduced solvent volume (~1 mL) and the supernatant was used for the subsequent step. The expression “0.1-0.4k g” describes consecutive centrifugation steps. In this example, the sample was obtained by sedimentation of nanosheets at 400 g from the supernatant obtained after centrifugation at 100 g. The central g -force used in different Figures in Chapter 3 is given by the mean centrifugal acceleration between two steps (in this example: 0.25k g).

Layer selective floating: Floating experiments on the 2D-Polymer systems have been performed at 300k g in a Beckman Coulter OPTIMA XPN-80 ultracentrifuge with a swinging bucket rotor (SW40Ti, 12.5 mL Beckman polypropylene tubes). Unexfoliated material of as-prepared stock dispersions were removed from the dispersion at low centrifugal accelerations in a Hettich Mikro 220R centrifuge equipped with a fixed-angle rotor 1016 at 100 g for 2 h. To concentrate the nanomaterial for further analysis and to account for potential soluble impurities or defective nanosheets, the supernatant after the centrifugation at 100 g was sedimented using a Beckman Coulter Avanti XP centrifuge with a fixed angle rotor (JA 25.50) at 74k g and redispersed in 1-2 ml of 0.1 $g \cdot L^{-1}$ aqueous SC.

7.3 Material Characterisation

Atomic force microscopy: AFM measurements were carried out on a Dimension ICON3 scanning probe microscope (Bruker AXS S.A.S.) in ScanAsyst mode in air under ambient conditions using aluminium coated silicon cantilevers (OLTESP-R3). The concentrated dispersions were diluted with solvent to optical densities <0.1 across the resonant spectral region. For samples sensitive to ambient conditions, a similar procedure was applied using dried and distilled isopropanol to dilute and deposit the samples. Drops of the dilute dispersions (20 μL) were deposited repeatedly on pre-heated (180°C) Si/SiO₂ wafers (0.5x0.5 cm²) with an oxide layer of 300 nm. After deposition, the wafers were rinsed with ~15 mL of water and ~15 mL of isopropanol and dried in a nitrogen flow. Typical image sizes were between 20x20 and 4x4 μm^2 (depending on the nanomaterial size) at scan rates of 0.5 Hz with 1024 lines per image. Step height analysis was used to convert the apparent AFM thickness to layer number as discussed in the main manuscript. Previously published length corrections were used to correct lateral dimensions from cantilever broadening.²³²

Extinction and absorbance spectroscopy: Optical extinction and absorbance measurements were carried out with an Agilent Cary 6000i spectrometer in quartz cuvettes. The spectrometer was equipped with an integrating sphere (external DRA-1800) for absorbance measurements. In this case, the cuvettes were placed in the centre of the sphere. For this measurement, the optical density of the dispersions was adjusted to 0.3-0.4 at the peak. The measurements of both, extinction and absorbance spectra allow for the calculation of the scattering spectra (Ext–Abs). All spectra were acquired with 0.5 nm increments and 0.1 s integration time.

Chapter 7 – Methods

Gravimetric filtering: The concentration of nanomaterial in different fraction was determined by filtering a known volume of dispersion through AlO_x membranes (pore size 20 nm) and washing with 1 L Isopropanol. Prior to weighing, membranes were dried overnight in vacuum at 60°C before and after deposition.

Photoluminescence: PL was measured using a Horiba Scientific Fluorlog-3 spectrometer equipped with a Xe lamp (450 W) and a PPD-900 photomultiplier tube detector. Measurements were taken under ambient conditions with double monochromators for excitation and emission. Prior to the measurement, the samples were diluted to an optical density at the excitation wavelength where no reabsorption or inner filter effects were observed according to dilution series (typically 0.4 or lower with respect to 1 cm path length). The quartz cuvettes with 0.4 x 1 cm dimensions were placed inside the spectrometer so that the excitation light passed through the 0.4 cm side of the cuvette. Emission was collected in a 90° angle, *i.e.* after having passed through the 1 cm side.

For single spectra measurements acquisition parameters were adjusted to the respective material. TMDs were typically measured at bandwidths of 5 nm with an acquisition time of 0.4 s using 430 nm for excitation. For 2D-Polymer(1) samples, measurements were acquired at bandwidths of 5 nm with an acquisition time of 1 s with 333 nm for excitation. Maps of the γ -InSe films were measured with 12 nm bandwidth at acquisition times of 60 s

To avoid artefacts from scattering of the nanomaterial dispersion, appropriate cut-off filters were placed on the emission side. The excitation was corrected for the light intensity.

Raman spectroscopy: Raman measurements were carried out on a Renishaw InVia-Reflex confocal Raman microscope equipped with a 532 nm, 633 nm and 785 nm laser for excitation in air under ambient conditions. The Raman emission was collected by a 50× long working distance objective lens in streamline mode and dispersed by a 2400 l/mm grating with a maximal laser power of 1% (<10 μ W). The spectrometer was calibrated to a silicon reference sample prior to the measurement to correct for the instrument response. Liquid dispersions were dropped (~20 μ L) onto an aluminium support and left to dry in vacuum at 60°C overnight before measuring. For each sample, several spectra were accumulated on at least 3 different positions and averaged. In the streamline mode, where a larger sample area is probed, no spot-to-spot variations were observed except for absolute intensities.

Raman spectra of exfoliated CrTe₃ samples were acquired with a micro-Raman spectrometer (Horiba LabRAM 800) in backscattering geometry in ambient conditions using a 457, 532 and 633 nm laser for excitation. The Raman emission was collected by a 100× magnification long-working distance objective (Olympus LMPlanFl 100x, NA 0.8) and dispersed by 1800 l/mm grating. The laser power was kept below 1.1 mW at all times. Typical integration times were 30 seconds, using 5

accumulations for each spot. Neon lines were used to calibrate the Raman spectra for the instrument response. Liquid dispersions were dropped ($\sim 5 \mu\text{L}$) into conical drill holes ($\text{Ø} = 1 \text{ mm}$, $\downarrow = 0.5 \text{ mm}$) on a gold coated ($t_{\text{Au}} = 150 \text{ nm}$) aluminium support and left to dry in a nitrogen atmosphere at 60°C overnight (see Figure 7.3-1). The samples were protected from ambience by encapsulation with a glass slide, which was glued on top of the holes before the measurements. **Raman measurements on exfoliated CrTe_3 samples were performed by the Maultzsch group in Erlangen.**



Figure 7.3-1: Au-coated aluminium support used for Raman measurements. Samples of nanosheet dispersions were drop-cast inside the holes. Dimensions of the support are 3x3 cm.

Scanning electron microscopy: SEM images were acquired with a JEOL JSM-7610F field emission scanning electron microscope (FE-SEM), using an In-lens Schottky field emission electron gun at 2.5×10^{-9} mbar. The images were measured with a dual (upper and lower) detector system consisting of collector-, scintillator-, light guide- and photomultiplier units for secondary electron imaging (SEI). EDX was performed at 15 kV, at 9 mm working distance, using a Thermo-Scientific 30mm²-UltraDry silicon drift detector for X-ray detection in 28.5° angle to the specimen.

Transmission electron spectroscopy: The samples for (S)TEM measurements were sonicated in a sonication bath for about 2 hours at room temperature in order to split the agglomerated nanosheets. After sonication, the NiPS_3 colloids were drop-cast onto carbon-coated copper TEM grids and dried at 100°C for 2 hours in a vacuum system ($\sim 2.7 \times 10^{-5}$ mbar). TEM imaging and diffraction measurements were performed in an FEI Tecnai G2 20 TEM at 200 kV at room temperature.

High angle annular dark field (HAADF)-STEM imaging was performed in an FEI Titan G2 80-200 ‘ChemiSTEM’ operated at 200 kV. STEM-EDX data was acquired with the Titan’s Super-X detector system, with all four detectors used for a total collection angle of ~ 0.7 srad. All STEM-EDX data was processed in Hyperspy and quantification was performed using the Cliff-Lorimer method with standardless k-factors. **TEM measurements were performed by the Haigh group in Manchester.**

Chapter 7 – Methods

X-ray photoelectron spectroscopy: For XPS, measurements of NiPS₃ samples, the bulk material was glued on Capton tape, the size-selected dispersions were filtered on alumina membranes. The stock was drop-cast on ITO to also capture the signal from very small nanosheets and potential oxidation products. XPS measurements were carried out with an ESCALAB 250Xi (Thermo Scientific) in ultrahigh vacuum, an XR6 monochromated Al K α source ($h\nu = 1486.6$ eV), and a pass energy of 20 eV. XPS of samples prepared on non-conducting substrates was measured with charge compensation employing a flood electron source. **XPS measurements on NiPS₃ were performed by the Vaynzof group in Dresden.**

XPS measurements of RuCl₃ samples were performed using an ESCAProbeP spectrometer (Omicron Nanotechnology Ltd, Germany) with a monochromatic Al K α X-ray radiation source ($h\nu = 1486.7$ eV). Wide-scan surveys of Ru species were performed, with subsequent high-resolution scans. The samples were drop-cast on aluminium support prior to the measurements. An electron gun was used to eliminate sample charging during measurement (1–5 V). **XPS measurements on RuCl₃ were performed by the Duesberg group in Munich.**

X-ray diffraction measurements: XRD patterns of the MPS₃ bulk samples were collected in Debye-Scherrer geometry using Cu K α_1 radiation ($\lambda = 1.54058$ Å) with a PANalytical Empyrean diffractometer equipped with a PIXcel1D detector. XRD patterns of the exfoliated dispersion of NiPS₃ were collected at beamline P02.1, Petra III, DESY, Hamburg at a wavelength $\lambda = 0.207$ Å (60 keV) and a sample detector distance of 1010 mm. The detector used was a PerkinElmer XRD1621 two-dimensional (2D) detector. The 2D data was processed using the software DAWN Science.²³³ To account instrumental contributions to XRD, a NIST 660a LaB₆ reference material was measured. **XRD measurements on NiPS₃ were performed by the Bensch group in Kiel, measurements on RuCl₃ were performed by the Lotsch group in Stuttgart.**

7.4 Computational Methods

Theoretical description of the TMD exciton shifts: Theoretical models of the band structure and exciton binding energies were performed based on the QEHE model²³⁴ using the *ab initio* package GPAW.²³⁵ Dielectric building blocks of monolayer MoS₂, MoSe₂, WS₂ and WSe₂ were retrieved from ref.²³⁴. Band structures of the 2D-material stacks studied were calculated using the G Δ W-QEH method.²³⁶ A detailed description of data modelling is given elsewhere.¹⁰ **Calculations on TMD exciton shifts were performed by the Santos group in Belfast.**

Simulation of vibrational modes for CrTe₃: For calculation of the vibrational modes of CrTe₃, a density functional theory (DFT) approach as implemented in Quantum Espresso²³⁷ is used

for all calculations. For the exchange-correlation a local density approximation (LDA) is applied. Norm-conserving pseudopotentials which are taken from the old FHI PP table on the Quantum Espresso website are used. 60 Ry (816.34 eV) are used for the energy cut off. A Monkhorst-Pack grid with $8 \times 8 \times 1$ and $6 \times 6 \times 6$ k points is used for monolayer and bulk calculation, respectively. The structural optimization is performed until the forces on every atom are less than $0.005 \text{ eV}/\text{\AA}$. To ensure that interlayer interactions for the Monolayer structure are negligible, a unit cell with a size of 25 \AA in the direction perpendicular to the stacking direction is used. A density functional perturbation theory (DFPT) approach is used for the phonon calculations. **Raman calculations on CrTe₃ were performed by the Maultzsch group in Erlangen.**

7.5 Index of Chemicals and Materials

Van der Waals Crystals:

Thungsten disulfide	WS ₂	Sigma-Aldrich (C1254)
Molybdenum disulfide	MoS ₂	Sigma-Aldrich (69860)
Thungsten disulfide	WSe ₂	VWR (13084.18)
Molybdenum diselenide	MoSe ₂	VWR (13112.14)
Indium selenide	γ -InSe	Sofer Group (Prague)
Nickel hexathiohypo diphosphate	NiPS ₃	Bensch Group (Kiel)
Iron hexathiohypo diphosphate	FePS ₃	Bensch Group (Kiel)
Manganese hexathiohypo diphosphate	MnPS ₃	Bensch Group (Kiel)
Ruthenium trichloride	α -RuCl ₃	Lotsch Group (Stuttgart)
Chromium telluride	CrTe ₃	Bensch Group (Kiel)
2D-Polymer(1)		Schlueter Group (Zurich)
2D-Polymer(2O ⁺)		Schlueter Group (Zurich)
2D-Polymer(2N)		Schlueter Group (Zurich)
Ga-1,8-NDC		Stock Group (Kiel)
ODB2		Stock Group (Kiel)
ScBPyDC		Stock Group (Kiel)
Zr-CAU-45		Stock Group (Kiel)
Zr-CAU-39		Stock Group (Kiel)

Chapter 7 – Methods

Sc-CAU-11

Stock Group (Kiel)

Solvents and surfactants:

N-Cyclohexyl-2-pyrrolidone, CHP	$C_{10}H_{17}NO$	Merck (232254-100G)
Deuterium oxide	D_2O	Merck (151882-500G)
Isopropanol, IPA	C_3H_8O	Merck (34863-1L)
N-Methyl-2-pyrrolidone, NMP	C_5H_9NO	Merck (270458-1L)
Sodium cholate hydrate, SC	$C_{24}H_{39}NaO_5 \cdot nH_2O$	Merck (C6445-100G)

8 Appendix

This Chapter provides supplementary data for the discussions in this work. Parts of the data shown in this Chapter are published in *ACS Nano* (2019), 13; *Chem. Mat.* (2019), 24; *Chem. Mat.* (2019), 31 and in *Angew. Chem.* (2020), 59. Presented reprints are marked by a citation in the caption text.

Appendix 3.1:

3.1-1 TEM measurements on exfoliated WSe₂ and MoSe₂:

As the size selection of WSe₂ and MoSe₂ was not presented before, additional characterisation of the materials by TEM was performed to validate the corrections applied for the AFM measurements. In all fractions nanosheets resembling the particles observed in AFM can be observed. For each size, the length of 100-200 nanosheets was measured. Figure A3.1-1.1 and A3.1-1.2 show representative images of electron transparent WSe₂ and MoSe₂ nanosheets with the length distribution histograms below for each fraction, respectively.

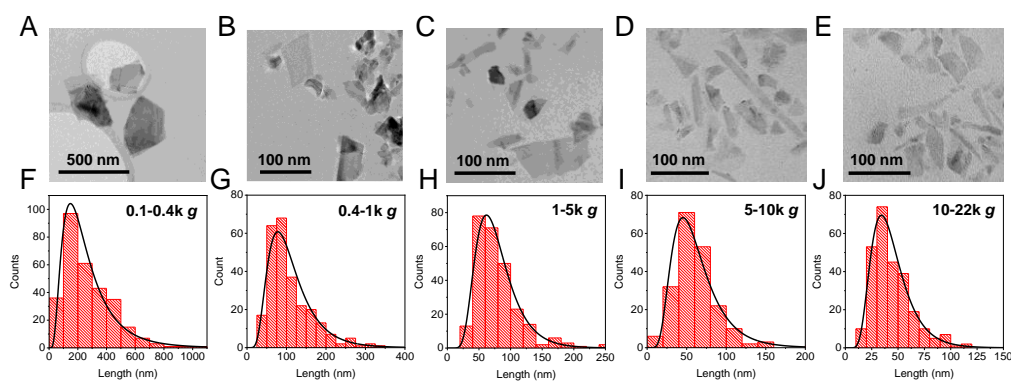


Figure A3.1-1.1: TEM analysis of the WSe₂ fractions obtained with the standard cascade. (A-E) Representative images of the different fractions isolated at the centrifugal acceleration indicated below. **(F-J)** Distribution histograms of the longest lateral dimension, L (in nm). See also in reference ¹⁰.

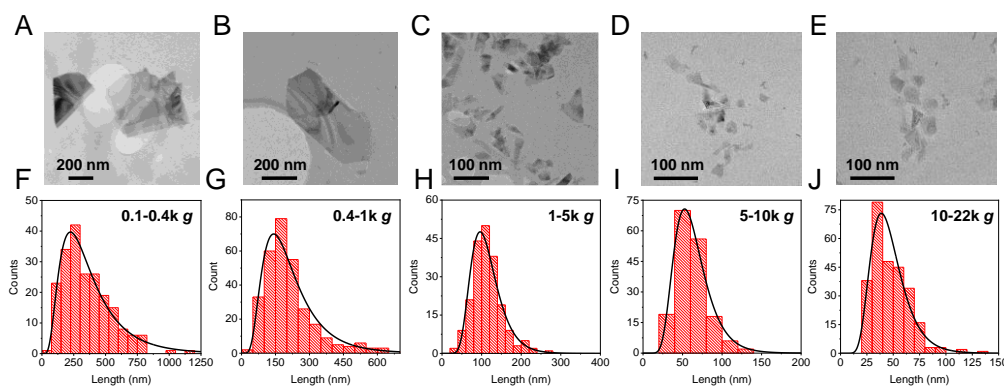


Figure A3.1-1.2: TEM analysis of the MoSe₂ fractions obtained with the standard cascade. (A-E) Representative images of the different fractions isolated at the centrifugal acceleration indicated below. (F-J) Distribution histograms of the longest lateral dimension, L (in nm). See also in reference ¹⁰.

AFM measurements

Statistical AFM analysis was carried out as described in Chapter 7.3. This includes measurements of the nanosheet thickness, length and width. Representative AFM images for the fractions isolated during the size selection cascade for the different materials discussed in Chapter 3 are shown in the Figures below. Histograms of the length and layer number distribution are shown in the first and second row below the nanosheet images, respectively. A decrease in size and thickness and a narrowing of the size distribution is observed with increasing centrifugal force for both cascades.

The AFM height measurements of the nanomaterial has to be calibrated by step height analysis to account for residual solvent to convert the, AFM apparent thickness to the nanosheet layer number. In addition to solvent residues, the measured AFM thickness of LPE nanosheets is influenced by chemical characteristics of the surface and the measuring parameters (*e.g.* measurement setpoint, free amplitude, *etc.*).^{238, 239} This means an apparent height, which is proportional, but not identical to the real height, is measured. Performing step height analysis allows to calibrate the AFM apparent thickness to the thickness of a single layer.^{48, 72, 75, 240} To do so, line profiles across the terraces of incompletely exfoliated nanosheets are extracted as discussed and shown for different Materials in Chapter 3. The extracted apparent height of a single layer is used to convert the measured AFM height data to layer number. Note that a significant reduction of solvent leftovers and thus improvement of the AFM image quality is achieved, if the nanosheet dispersions in NMP or CHP are diluted with freshly distilled isopropanol before deposition.

The dimensions of all nanosheets from all fractions are shown as a scatter plot in Figure A3.1-3 for TMDs, Figure A3.2-2 for graphite, in Figure A3.3-4 for the different MPS₃ species and in Figure A3.7-2 for 2D-MOFs. Scatter plots of the other materials are shown and discussed in more detail in Chapter 3. Note, that the length of a nanosheet is defined as its longest dimension and the width as dimension perpendicular to the length. The Nanosheet area (*i.e.* length x width) versus extracted layer number shows the spread of nanomaterial dimensions across all fractions.

3.1-2: AFM measurements on exfoliated TMDs

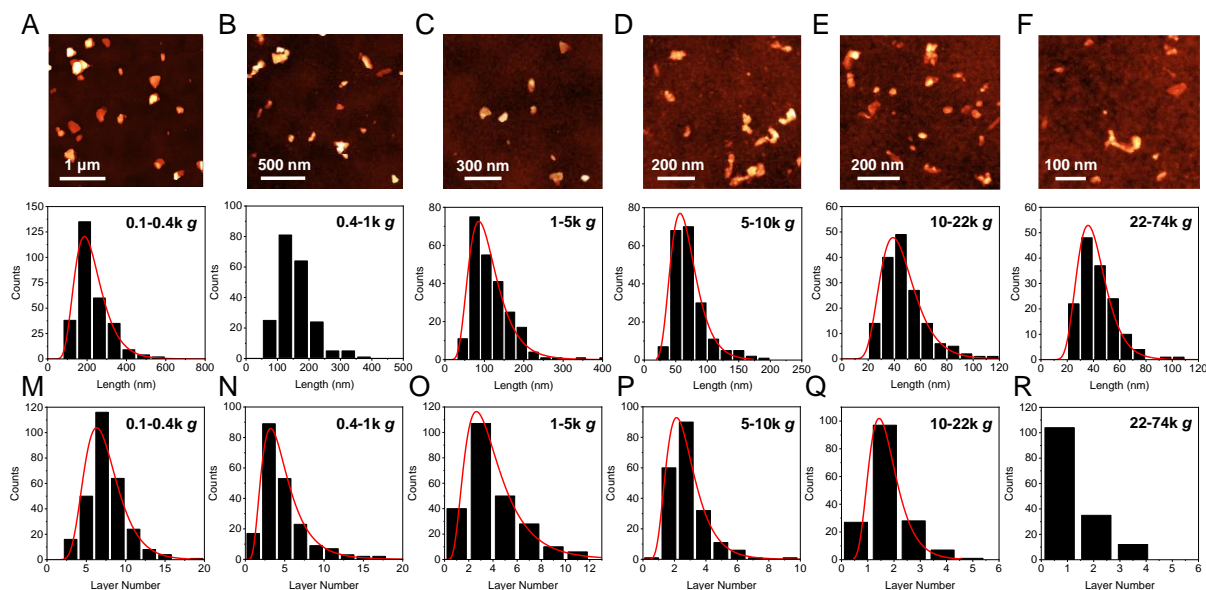
MoS₂:

Figure A3.1-2.1: AFM analysis of the MoS₂ fractions obtained with the standard cascade. (A-F) Representative images of the different fractions isolated at the centrifugal acceleration indicated below. (G-L) Distribution histograms of the longest lateral dimension, L (in nm). (M-R) Distribution histograms of the layer number, N . See also in reference ¹⁰.

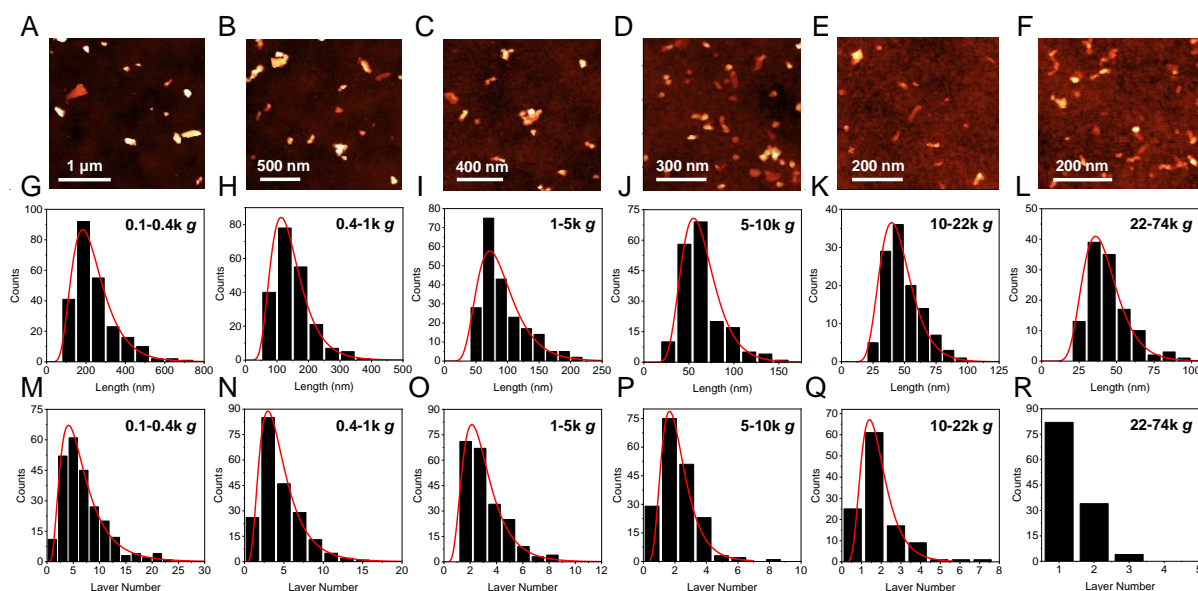
WS₂:

Figure A3.1-2.2: AFM analysis of the WS₂ fractions obtained with the standard cascade. (A-F) Representative images of the different fractions isolated at the centrifugal acceleration indicated below. (G-L) Distribution histograms of the longest lateral dimension, L (in nm). (M-R) Distribution histograms of the layer number, N . See also in reference ¹⁰.

Chapter 8 – Appendix

WSe₂:

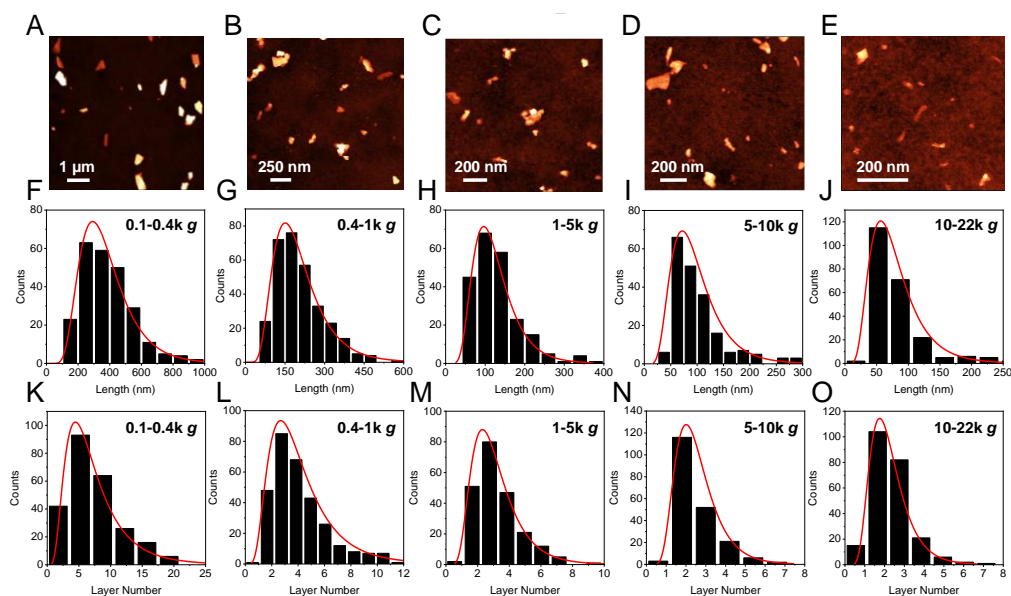


Figure A3.1-2.3: AFM analysis of the WSe₂ fractions obtained with the standard cascade. (A-E) Representative images of the different fractions isolated at the centrifugal acceleration indicated below. **(F-J)** Distribution histograms of the longest lateral dimension, L (in nm). **(K-O)** Distribution histograms of the layer number, N . See also in reference ¹⁰.

MoSe₂:

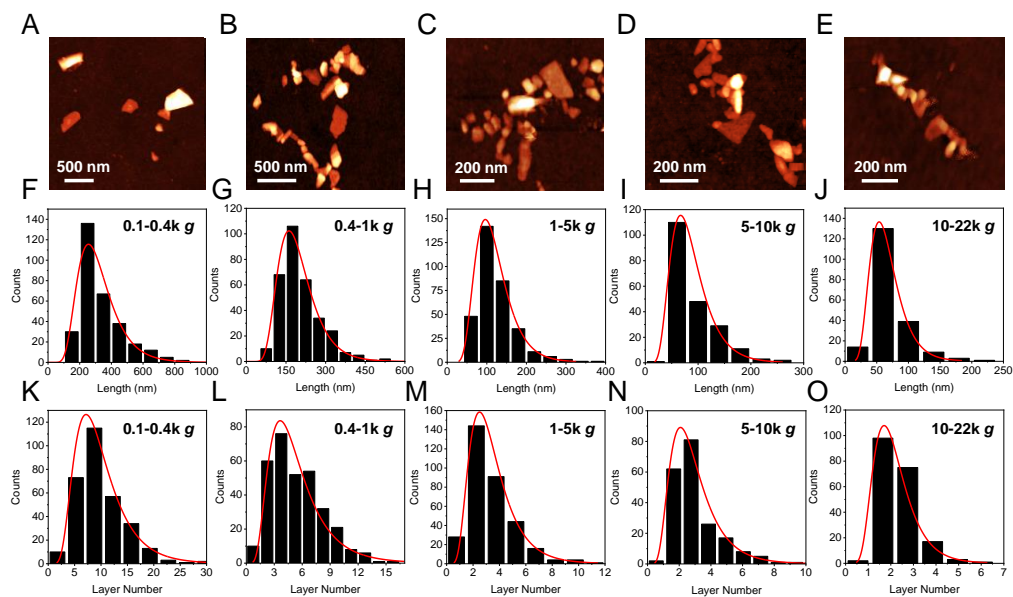


Figure A3.1-2.4: AFM analysis of the MoSe₂ fractions obtained with the standard cascade. (A-E) Representative images of the different fractions isolated at the centrifugal acceleration indicated below. **(F-J)** Distribution histograms of the longest lateral dimension, L (in nm). **(K-O)** Distribution histograms of the layer number, N . See also in reference ¹⁰.

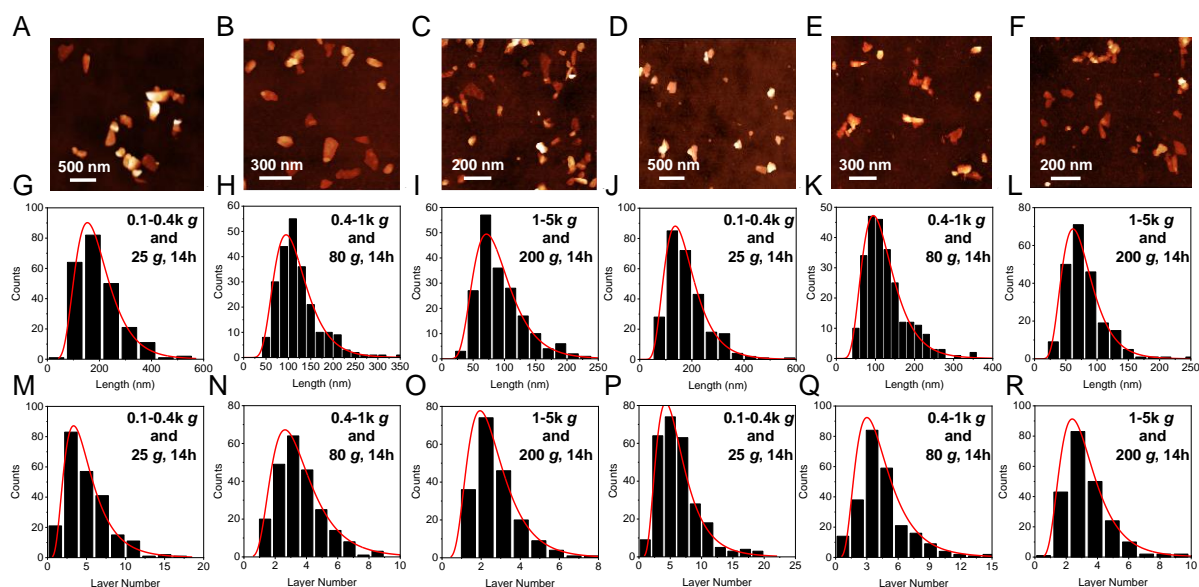
Secondary Centrifugation of WSe₂ and MoSe₂:

Figure A3.1-2.3: AFM analysis of the WSe₂ (left half) and MoSe₂ (right half) fractions obtained after overnight centrifugation. (A-F) Representative images of the different fractions isolated at the centrifugal acceleration indicated below. (A-C): for WSe₂, (D-F): for MoSe₂. (G-L) Distribution histograms of the longest lateral dimension, L (in nm). (G-I): for WSe₂, (J-L): for MoSe₂. (M-R) Distribution histograms of the layer number, N . (M-O): for WSe₂, (P-R): for MoSe₂. See also in reference ¹⁰.

3.1-3: Nanosheet area versus thickness scatter plots for TMDs

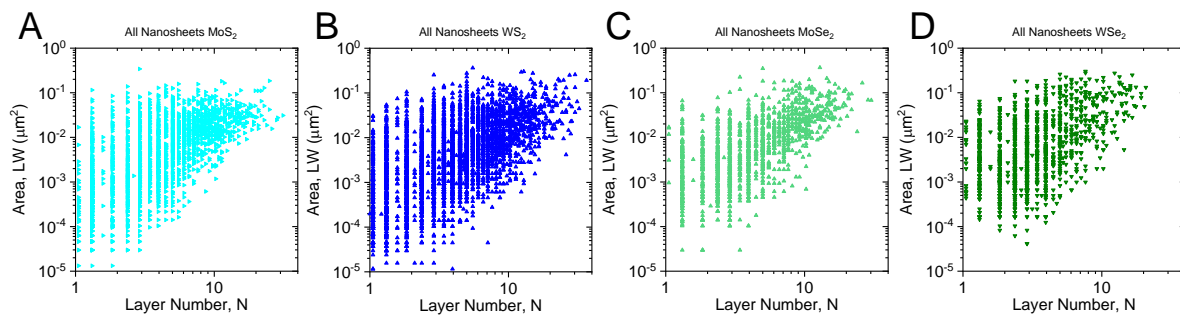


Figure A3.1-3: AFM scatter plot of measured nanosheet area versus layer number. (A-D) Dimensions of individual TMD nanosheets. (A) MoS₂, (B) WS₂, (C) MoSe₂ and (D) WSe₂.

Appendix 3.2:

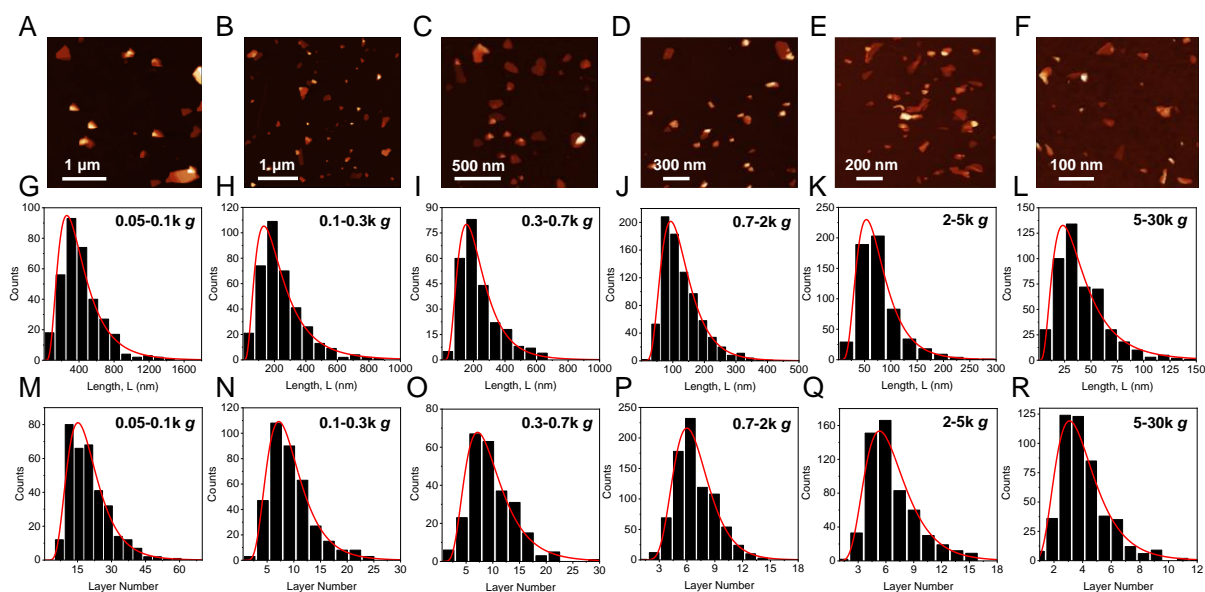
3.2-1: AFM measurements on exfoliated γ -InSe

Figure A3.2-1: AFM analysis of the γ -InSe fractions obtained with the standard cascade. (A-F) Representative images of the different fractions isolated at the centrifugal acceleration indicated below. **(G-L)** Distribution histograms of the longest lateral dimension, L (in nm). **(M-R)** Distribution histograms of the layer number, N .

3.2-2: AFM measurements on exfoliated graphite

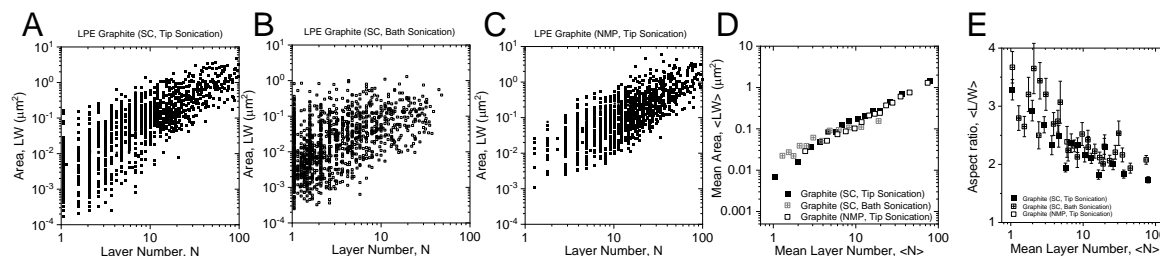


Figure A3.2-2: AFM analysis of graphite exfoliated using different conditions. (A-C) Scatter plots of the nanosheet area *versus* layer number for samples exfoliated in aqueous SC using tip sonication **(A)** and bath sonication **(B)** and in NMP using tip sonication **(C)**. **(D)** Mean γ -InSe nanosheet area as function of mean layer number. **(E)** Mean nanosheet length/width aspect ratio. Plots in **(C-D)** are averaged for nanosheets exhibiting a similar thickness. See also in reference ⁴⁷.

Appendix 3.3:

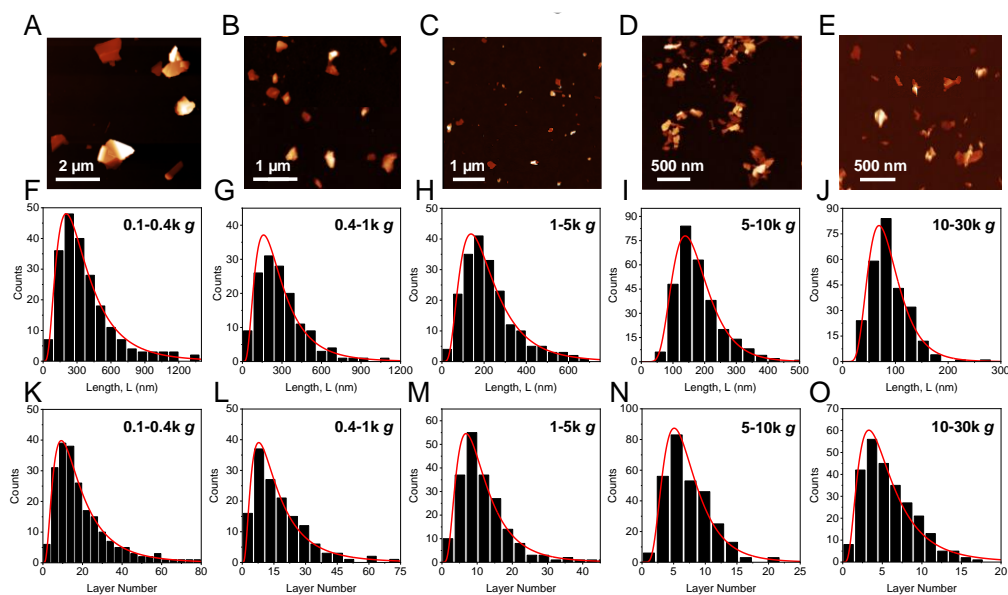
3.3-1: AFM measurements on NiPS₃

Figure A3.3-1.1: AFM analysis of the NiPS₃ fractions obtained by the first centrifugation cascade. (A-E) Representative images of the different fractions isolated at the centrifugal acceleration indicated below. **(F-J)** Distribution histograms of the longest lateral dimension, L (in nm). **(K-O)** Distribution histograms of the layer number, N . See also in reference ¹¹.

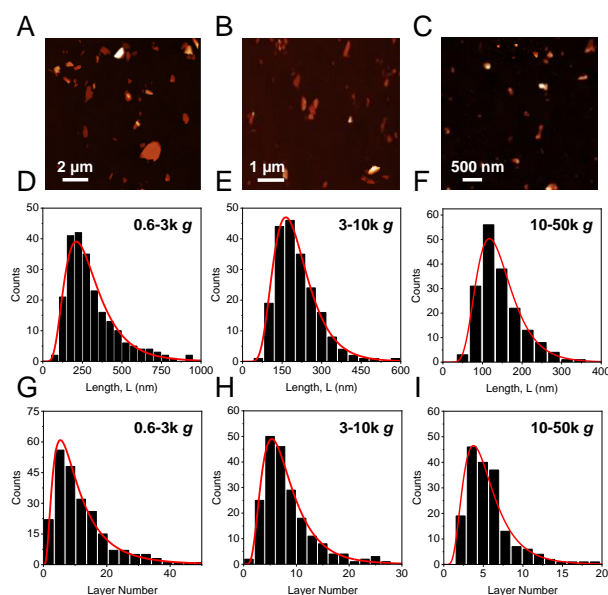


Figure A3.3-1.2: AFM analysis of the NiPS₃ fractions obtained by the second centrifugation cascade. (A-C) Representative images of the different fractions isolated at the centrifugal acceleration indicated below. **(D-F)** Distribution histograms of the longest lateral dimension, L (in nm). **(G-I)** Distribution histograms of the layer number, N . See also in reference ¹¹.

3.3-2: AFM measurements on FePS₃

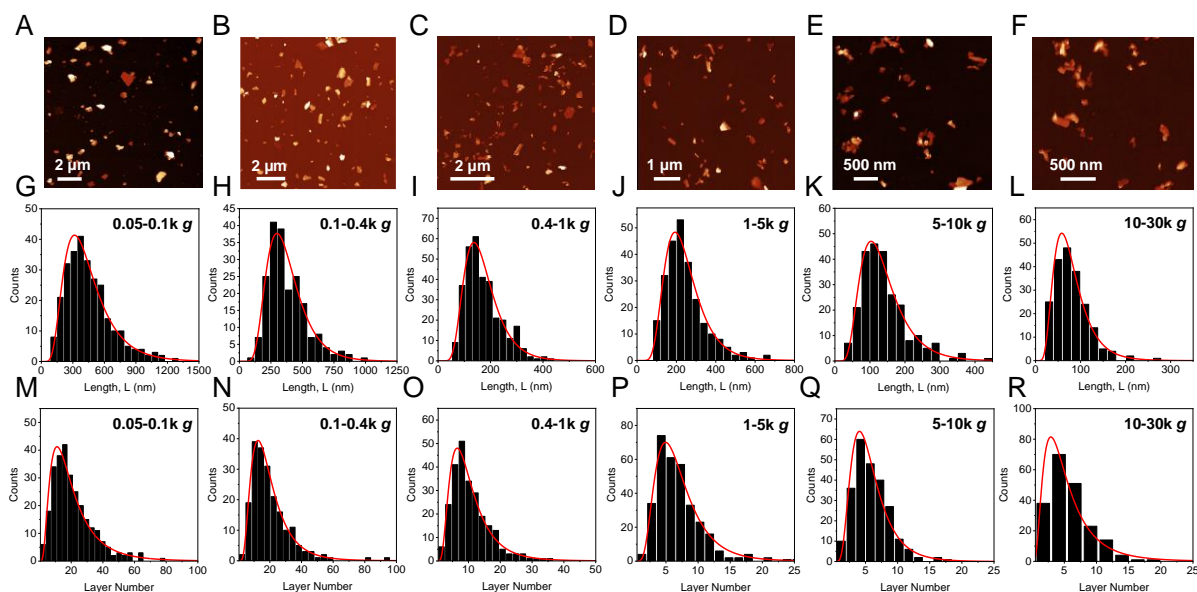


Figure A3.3-2.1: AFM analysis of the FePS₃ fractions obtained by the first centrifugation cascade. (A-E) Representative images of the different fractions isolated at the centrifugal acceleration indicated below. (F-J) Distribution histograms of the longest lateral dimension, L (in nm). (K-O) Distribution histograms of the layer number, N .

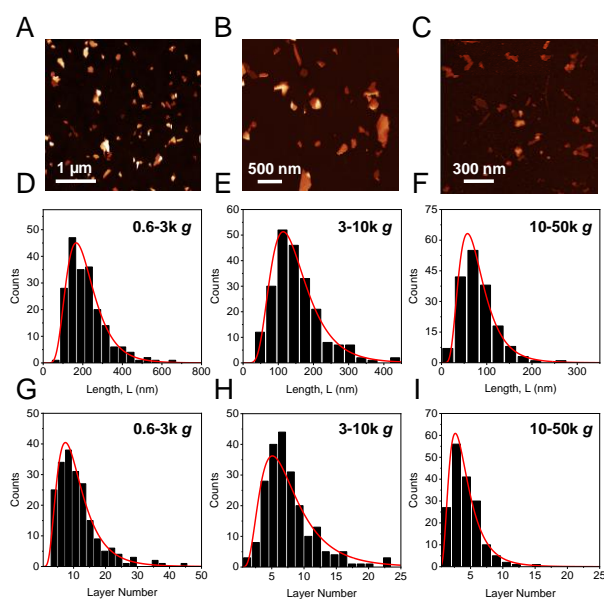


Figure A3.3-2.2: AFM analysis of the FePS₃ fractions obtained by the second centrifugation cascade. (A-C) Representative images of the different fractions isolated at the centrifugal acceleration indicated below. (D-F) Distribution histograms of the longest lateral dimension, L (in nm). (G-I) Distribution histograms of the layer number, N .

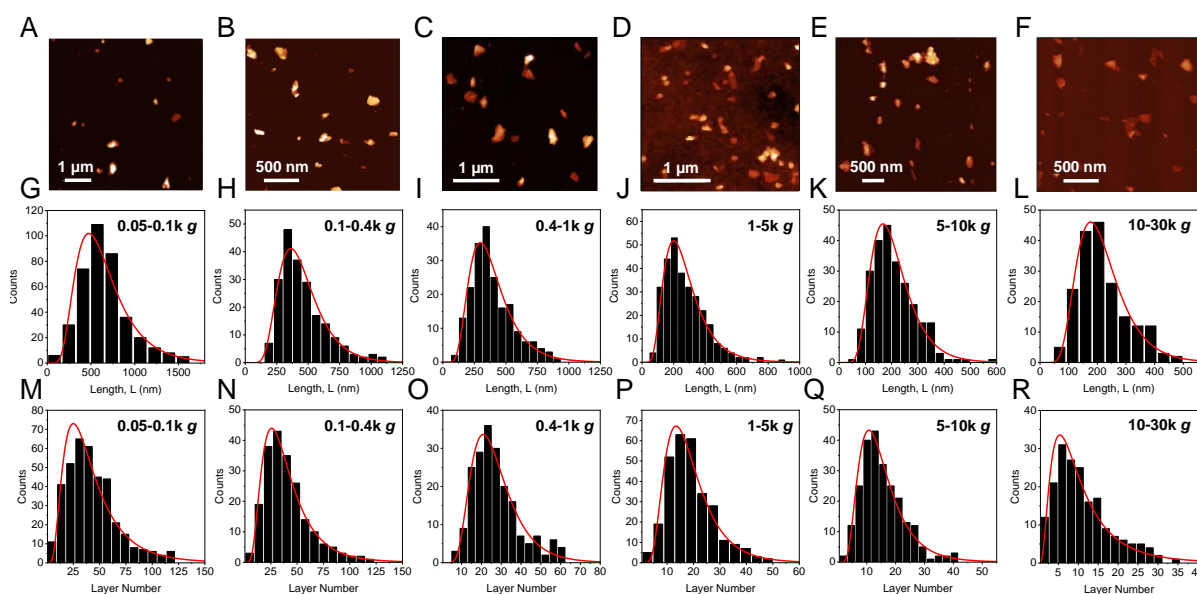
3.3-3: AFM measurements on MnPS₃

Figure A3.3-1: AFM analysis of the MnPS₃ fractions obtained by the first centrifugation cascade. (A-E) Representative images of the different fractions isolated at the centrifugal acceleration indicated below. **(F-J)** Distribution histograms of the longest lateral dimension, L (in nm). **(K-O)** Distribution histograms of the layer number, N .

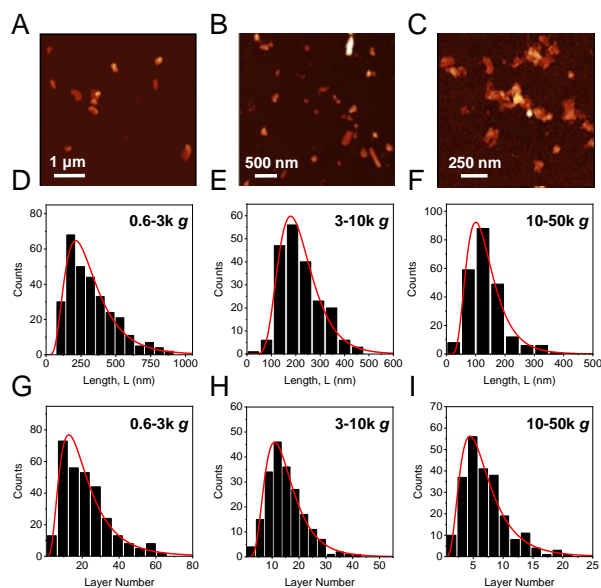


Figure A3.3-2: AFM analysis of the MnPS₃ fractions obtained by the second centrifugation cascade. (A-C) Representative images of the different fractions isolated at the centrifugal acceleration indicated below. **(D-F)** Distribution histograms of the longest lateral dimension, L (in nm). **(G-I)** Distribution histograms of the layer number, N .

3.3-3: Nanosheet area versus thickness scatter plots for different MPS₃ species

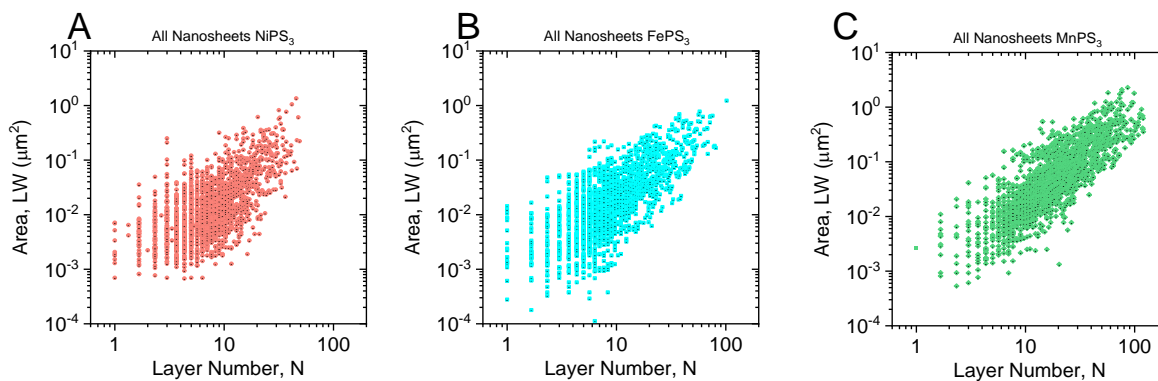


Figure A3.3-3: AFM scatter plot of measured nanosheet area *versus* layer number. (A-C) Dimensions of individual MPS₃ nanosheets. (A) NiPS₃, (B) FePS₃, (C) MnPS₃.

Appendix 3.4:

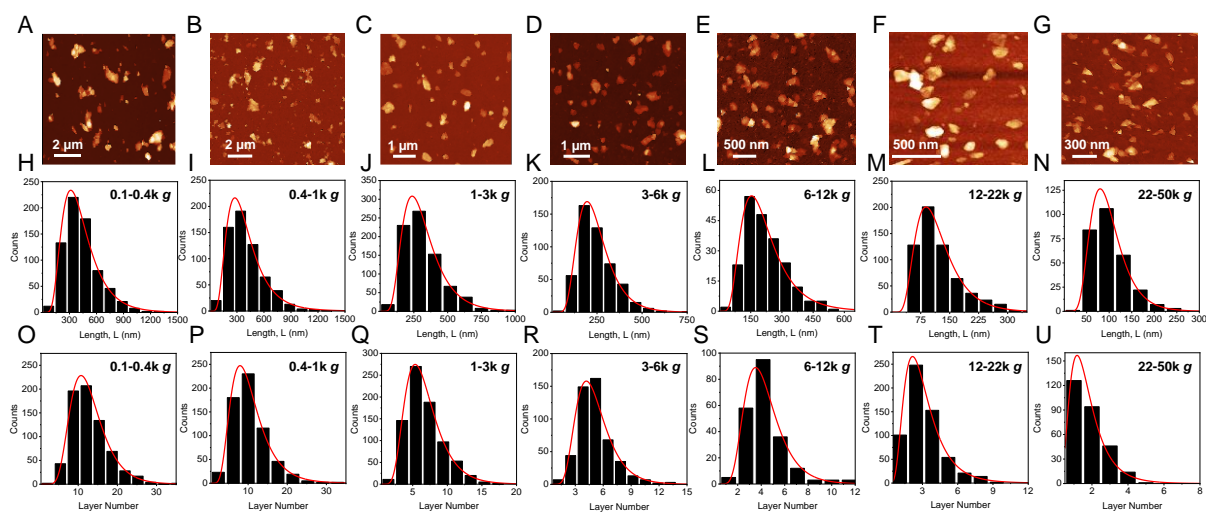
3.4-1: AFM measurements on exfoliated α -RuCl₃

Figure A3.4-1: AFM analysis of the RuCl₃ fractions obtained by a standard centrifugation cascade. (A-G) Representative images of the different fractions isolated at the centrifugal acceleration indicated below. **(H-N)** Distribution histograms of the longest lateral dimension, L (in nm). **(O-U)** Distribution histograms of the layer number, N .

Appendix 3.5:

3.5-1: AFM measurements on exfoliated CrTe₃

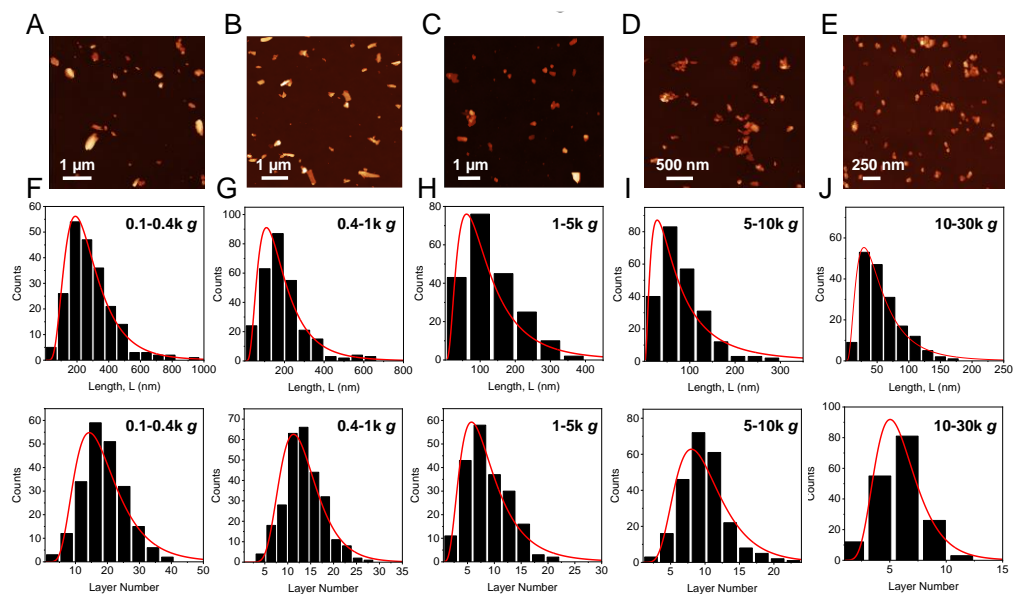


Figure A3.5-1: AFM analysis of the CrTe₃ fractions obtained by a standard centrifugation cascade. (A-G) Representative images of the different fractions isolated at the centrifugal acceleration indicated below. **(H-N)** Distribution histograms of the longest lateral dimension, *L* (in nm). **(O-U)** Distribution histograms of the layer number, *N*.

Appendix 3.6:

3.6-1: AFM measurements on exfoliated organic sheet stacks

2D-Pol(1):

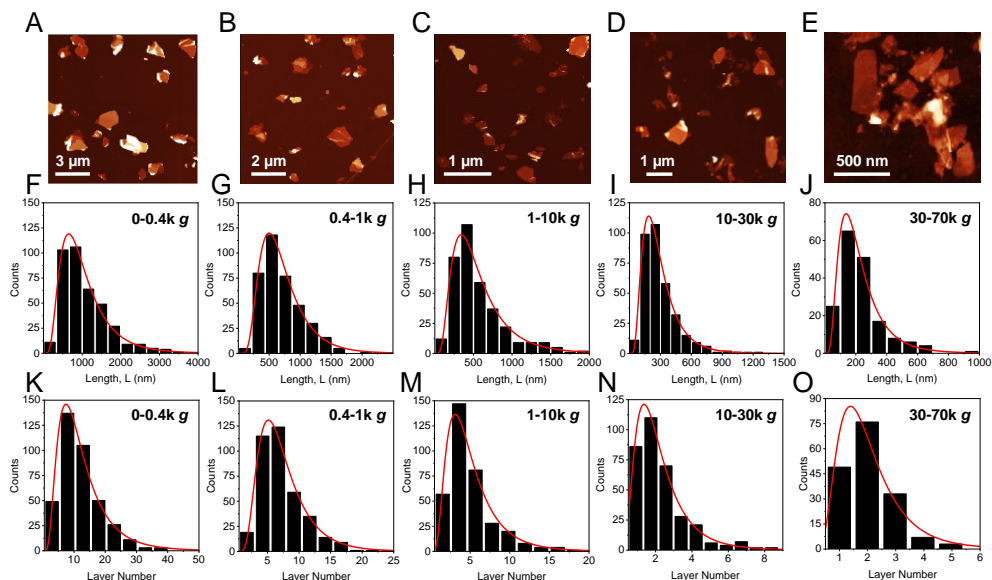


Figure A3.6-1.1: AFM analysis of the 2D-Pol(1) fractions obtained by a standard centrifugation cascade. (A-E) Representative images of the different fractions isolated at the centrifugal acceleration indicated below. **(F-J)** Distribution histograms of the longest lateral dimension, L (in nm). **(K-O)** Distribution histograms of the layer number, N .

2D-Pol(2N):

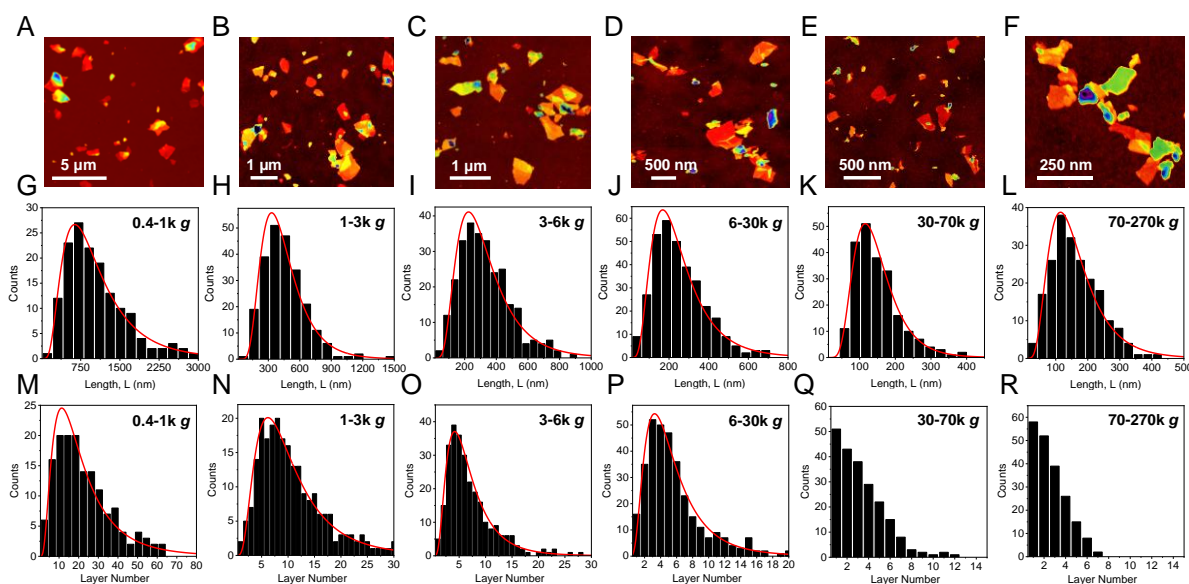


Figure A3.6-1.2: AFM analysis of the 2D-Pol(2N) fractions obtained by a standard centrifugation cascade. (A-F) Representative images of the different fractions isolated at the centrifugal acceleration indicated below. **(G-L)** Distribution histograms of the longest lateral dimension, L (in nm). **(M-R)** Distribution histograms of the layer number, N . See also in reference ²³.

Chapter 8 – Appendix

Secondary centrifugation of 2D-Pol(2N):

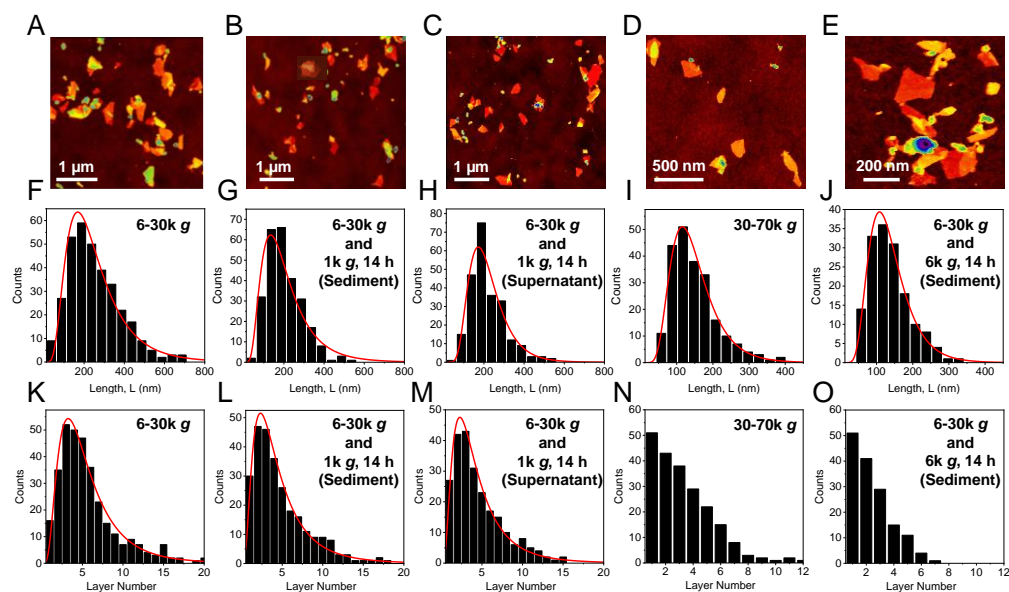


Figure A3.6-1.3: AFM analysis of the 2D-Pol(2N) fractions obtained after overnight centrifugation. (A-E) Representative images of the different fractions isolated at the centrifugal acceleration indicated below. **(F-J)** Distribution histograms of the longest lateral dimension, L (in nm). **(K-O)** Distribution histograms of the layer number, N . See also in reference²³.

3.6-2: AFM measurements on floating nanosheet fractions

Layer selective floating of 2D-Pol(1):

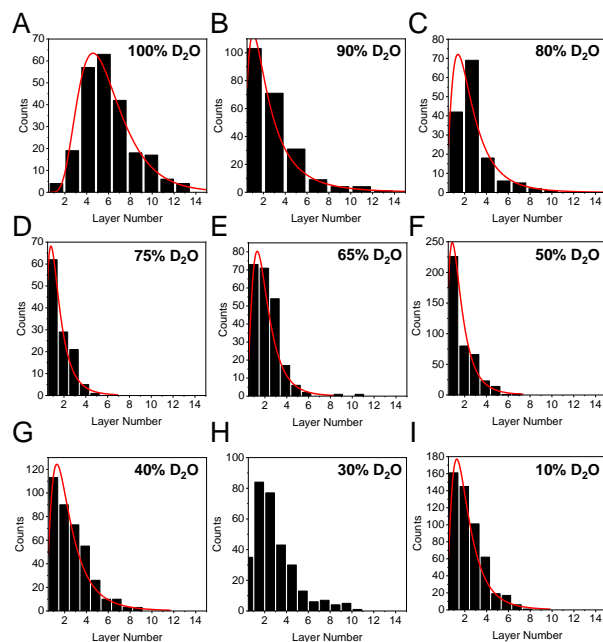


Figure A3.6-2.1: AFM analysis of the floating 2D-Pol(1) fractions obtained after LSF experiments. (A-I) Distribution histograms of the nanosheet layer number after centrifugation for 24 h at 300k g at different D_2O concentrations as indicated in the individual plots.

Layer selective floating of 2D-Pol(2N):

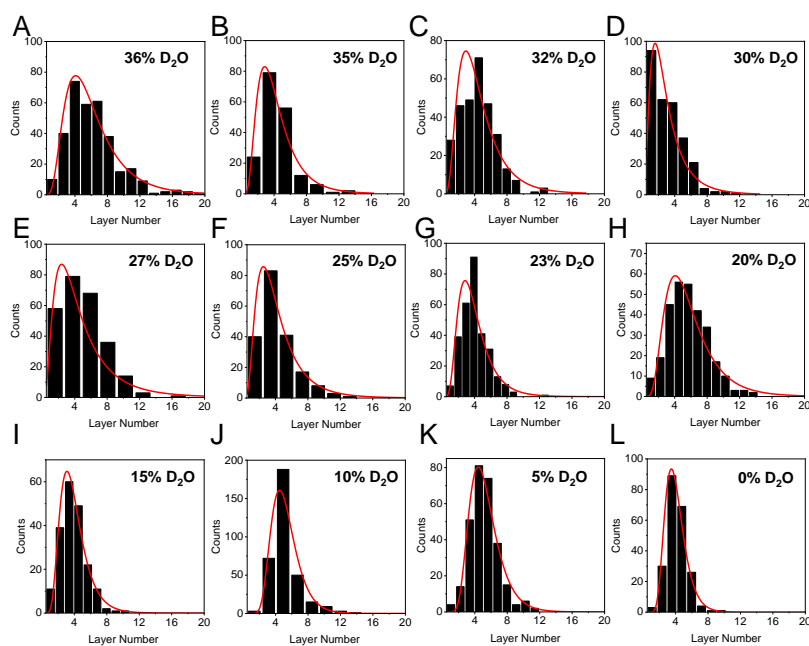


Figure A3.6-2.2: AFM analysis of the floating 2D-Pol(2N) fractions obtained after LSF experiments. (A-L) Distribution histograms of the nanosheet layer number after centrifugation for 24 h at 300k g at different D₂O concentrations as indicated in the individual plots.

Appendix 3.7:

Similar to the characterisation of the nanosheets obtained for Ga-1,8-NDC ("Black"), a combination of diffraction measurements with Raman and IR spectroscopy was used to demonstrate the structural integrity of the nanomaterial. Measurements on exfoliated nanomaterial are shown in red colour. For better comparability, measurements on the bulk material are depicted in black.

3.7-2: Characterisation of exfoliated 2D-MOFs

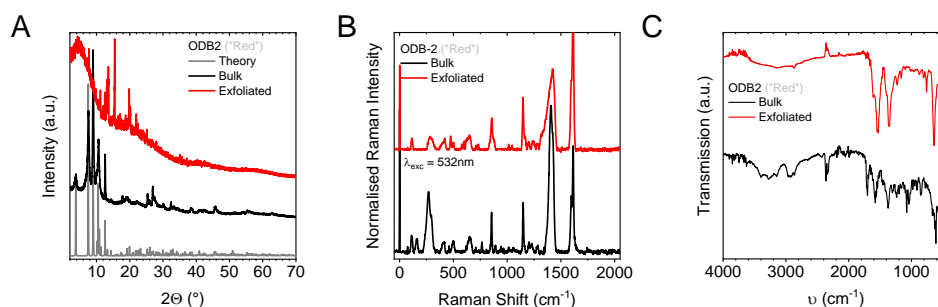


Figure A3.6-1: Structural and spectroscopical properties of exfoliated ODB2 ("Red"). (A-C) Acquired spectra on dried nanosheet stock dispersions are shown in comparison to a bulk crystal. Significant differences between the powder diffraction patterns (A) as well as some missing signals in the Raman- (B) and IR-spectra (C) indicate structural and compositional changes of the sample. This might be caused by the removal of the intercalated species upon exfoliation.

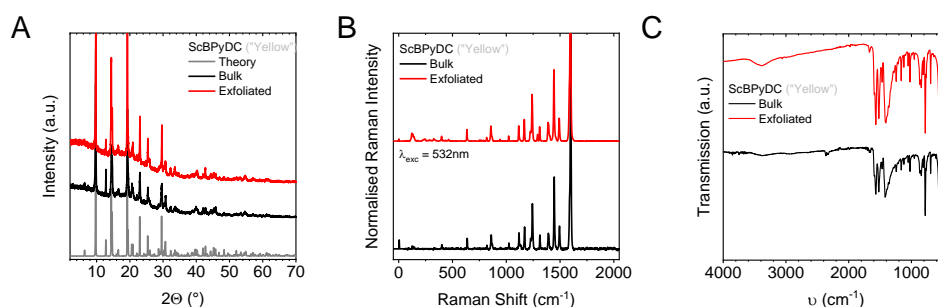


Figure A3.6-1.2: Structural and spectroscopical properties of exfoliated ScBPYDC ("Yellow"). (A-C) Acquired spectra on dried nanosheet stock dispersions are shown in comparison to a bulk crystal. (A) Powder XRD (B) Raman and (C) IR-transmission measurements show no other than the expected signals. The results imply no changes of the material composition and crystallinity upon exfoliation.

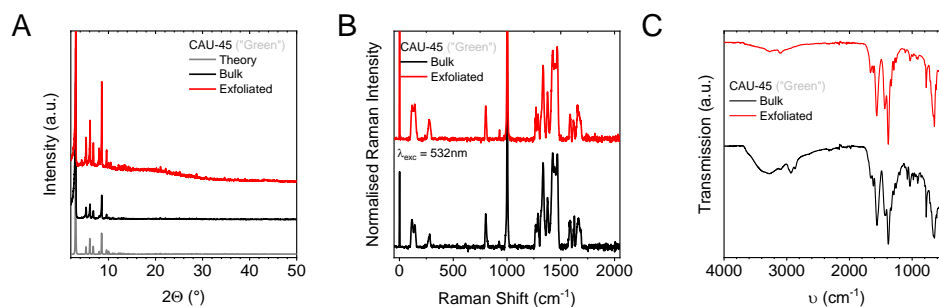


Figure A3.6-1.3: Structural and spectroscopical properties of exfoliated CAU-45 ("Green"). (A-C) Acquired spectra on dried nanosheet stock dispersions are shown in comparison to a bulk crystal. (A) Powder XRD (B) Raman and (C) IR-transmission measurements show no other than the expected signals. The results imply no changes of the material composition and crystallinity upon exfoliation.

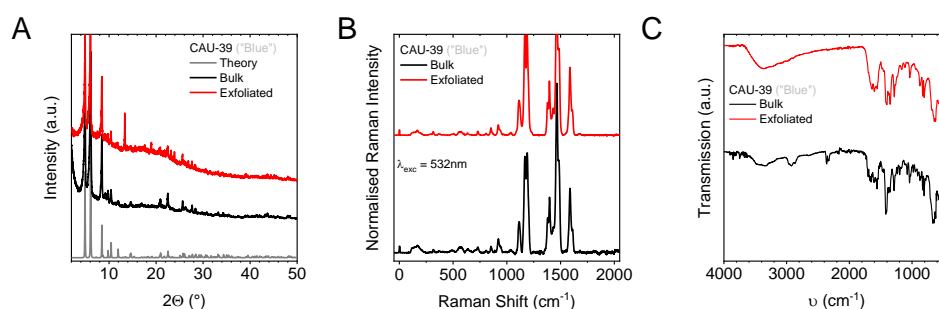


Figure A3.6-1.4: Structural and spectroscopical properties of exfoliated CAU39 ("Blue"). (A-C) Acquired spectra on dried nanosheet stock dispersions are shown in comparison to a bulk crystal. (A) Powder XRD (B) Raman and (C) IR-transmission measurements show no other than the expected signals. The results imply no changes of the material composition and crystallinity upon exfoliation.

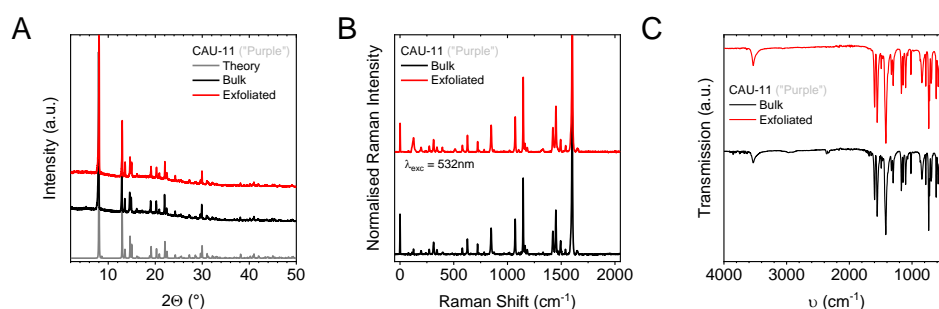


Figure A3.6-1.5: Structural and spectroscopical properties of exfoliated CAU11 ("Purple"). (A-C) Acquired spectra on dried nanosheet stock dispersions are shown in comparison to a bulk crystal. (A) Powder XRD (B) Raman and (C) IR-transmission measurements show no other than the expected signals. The results imply no changes of the material composition and crystallinity upon exfoliation.

3.7-2: AFM measurements on exfoliated 2D-MOFs

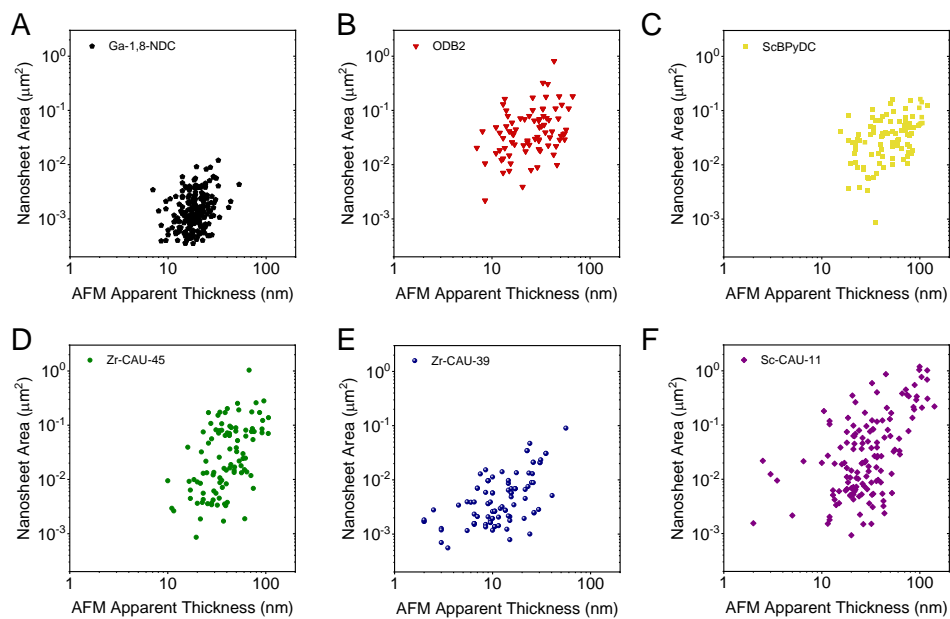


Figure A3.6-2: AFM scatter plot of measured nanosheet area *versus* layer number. (A-F) Dimensions of individual MPS₃ nanosheets. (A) Ga-1,8-NDC ("Black"), (B) ODB2 ("Red"), (C) ScBPYDC ("Yellow"), (D) Zr-CAU-45 ("Green"), (E) Zr-CAU-39 ("Blue") and (F) Sc-CAU-11 ("Purple").

Appendix 4.1:

Optical spectra of all nanomaterials show systematic changes with material size. The peak intensity ratios change with material sizes and the position of optical transitions shift systematically with decreasing layer number, which can better be seen if the second derivative of the spectra is taken. This allows for deriving spectroscopic metrics for the average nanosheet size ($\langle L \rangle$) and the mean layer number ($\langle N \rangle$) for both, extinction and absorbance peak positions based on the AFM statistics as discussed in more detail in Chapter 4 for various material systems. Additional spectra which could not be shown in the discussions in Chapter 4 are shown below.

4.1-1 Extinction and absorbance measurements of exfoliated TMDs

MoS₂:

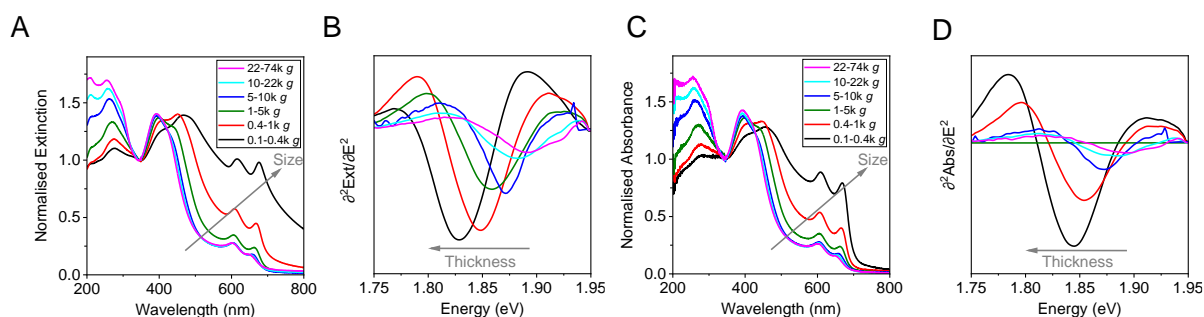


Figure A4.1-1.1: UV-Vis measurements of dispersions containing different sizes of MoS₂ nanosheets. (A) Extinction measurements of different nanosheet sizes. (B) Second derivative of the extinction measurements shown in (A). (C) Absorbance measurements on different nanosheet sizes. (D) Second derivative of the extinction measurements shown in (C). See also in reference ¹⁰.

WS₂:

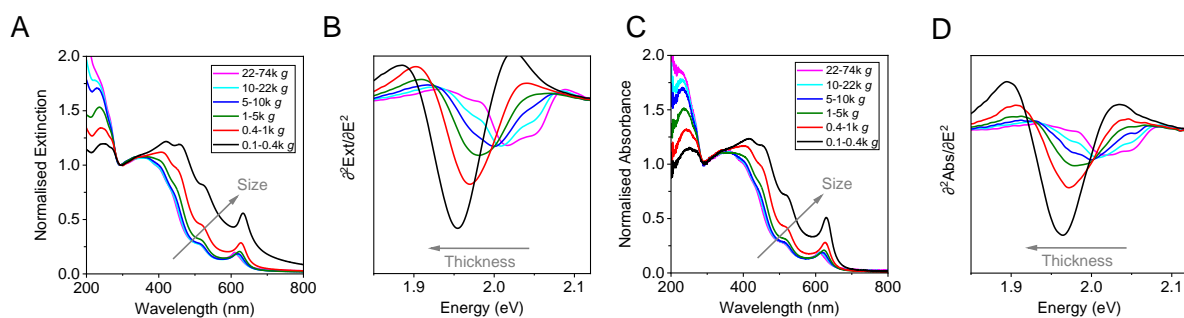


Figure A4.1-1.2: UV-Vis measurements of dispersions containing different sizes of WS₂ nanosheets. (A) Extinction measurements of different nanosheet sizes. (B) Second derivative of the extinction measurements shown in (A). (C) Absorbance measurements on different nanosheet sizes. (D) Second derivative of the extinction measurements shown in (C). See also in reference ¹⁰.

Chapter 8 – Appendix

WSe₂:

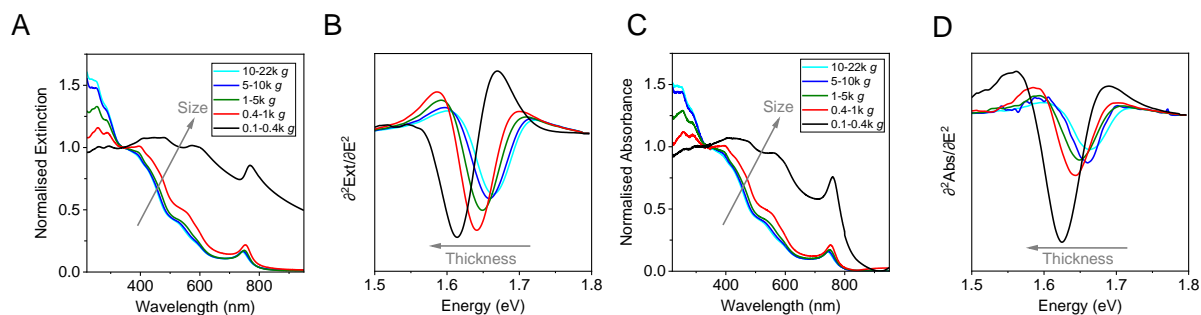


Figure A4.1-1.3: UV-Vis measurements of dispersions containing different sizes of WSe₂ nanosheets. (A) Extinction measurements of different nanosheet sizes. **(B)** Second derivative of the extinction measurements shown in **(A)**. **(C)** Absorbance measurements on different nanosheet sizes. **(D)** Second derivative of the extinction measurements shown in **(C)**. See also in reference ¹⁰.

MoSe₂:

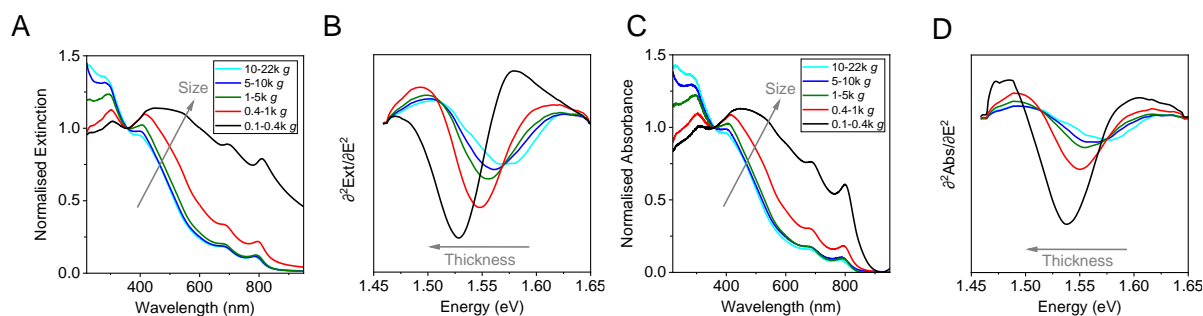


Figure A4.1-1.4: UV-Vis measurements of dispersions containing different sizes of MoSe₂ nanosheets. (A) Extinction measurements of different nanosheet sizes. **(B)** Second derivative of the extinction measurements shown in **(A)**. **(C)** Absorbance measurements on different nanosheet sizes. **(D)** Second derivative of the extinction measurements shown in **(C)**. See also in reference ¹⁰.

4.1-2 Extinction and absorbance measurements of exfoliated TMDs

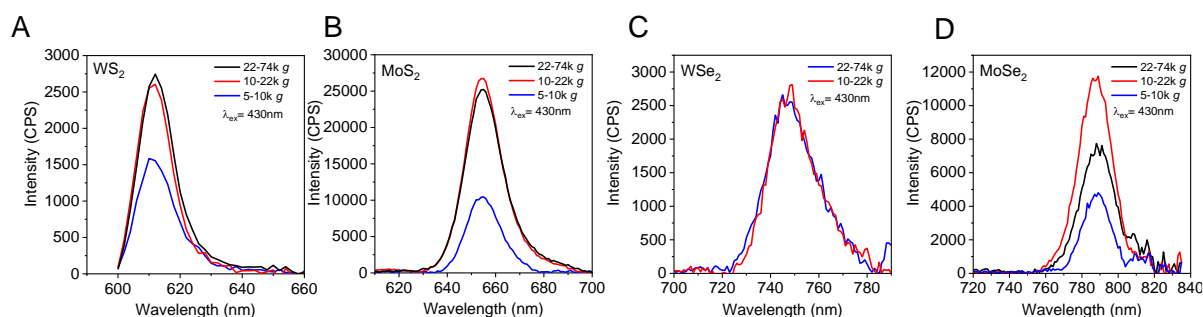


Figure A4.1-2: Photoluminescence measurements of dispersions containing different sizes of TMD nanosheets. (A) For WS₂, **(B)** for MoS₂, **(C)** for WSe₂ and **(D)** for MoSe₂. See also in reference ¹⁰.

Appendix 4.2:

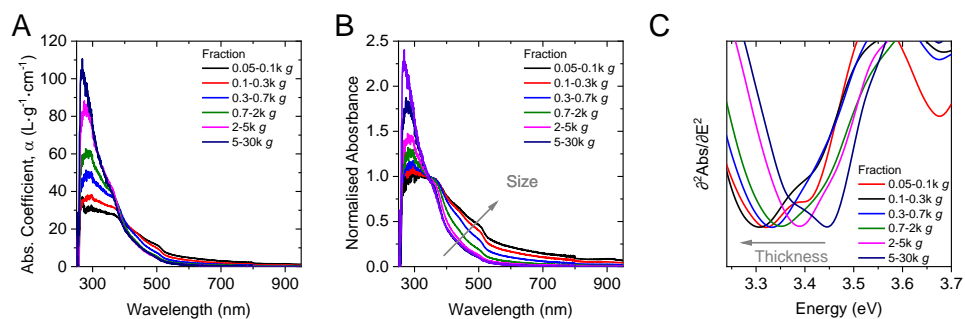
4.2-1 Absorbance measurements of exfoliated γ -InSe

Figure A4.2-1: Absorbance measurements of dispersions containing different sizes of γ -InSe nanosheets. (A) Absorbance coefficient spectra for different nanosheet sizes. **(B)** Normalised absorbance spectra of different nanosheet sizes. The grey arrow indicates systematic changes with nanosheet lateral size. **(C)** Second derivative of the absorbance measurements shown in **(A-B)**. The centre of mass peak position is used to identify changes of the resonance energy of optical transitions. The grey arrow indicates changes of the peak position with nanosheet layer number.

Appendix 4.3:

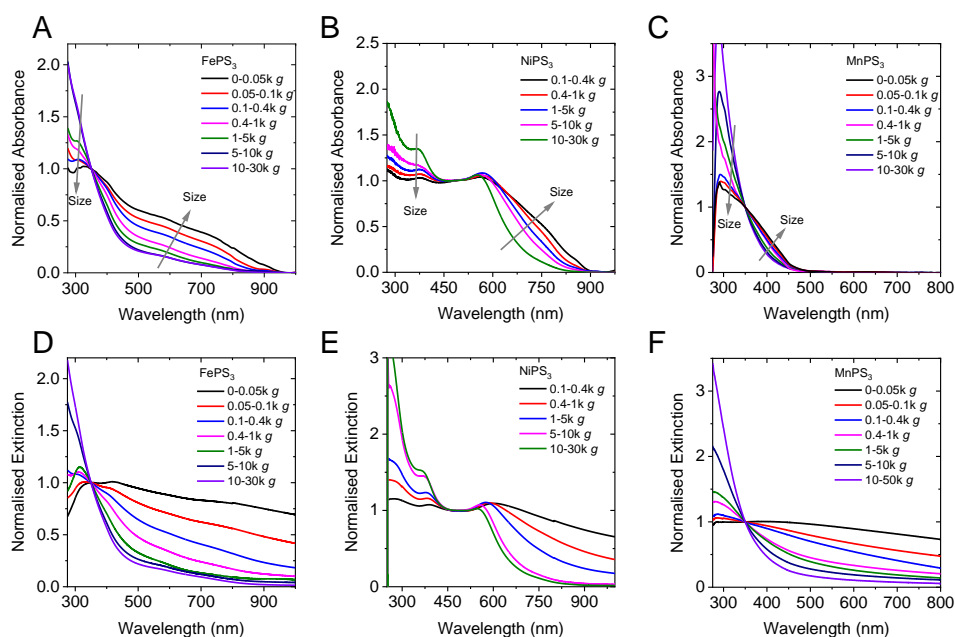
4.3-1 Extinction and absorbance measurements of exfoliated MPS₃ species

Figure A4.3-1: UV-Vis measurements of dispersions containing different sizes of MPS₃ nanosheets obtained from the first centrifugation cascade. (A-C) Normalised extinction spectra of NiPS₃ (A), FePS₃ (B) and MnPS₃ (C), respectively. The grey arrow indicates systematic changes with nanomaterial size. (D-F) Normalised absorbance spectra of NiPS₃ (D), FePS₃ (E) and MnPS₃ (F), respectively. See also in reference ¹¹ (NiPS₃).

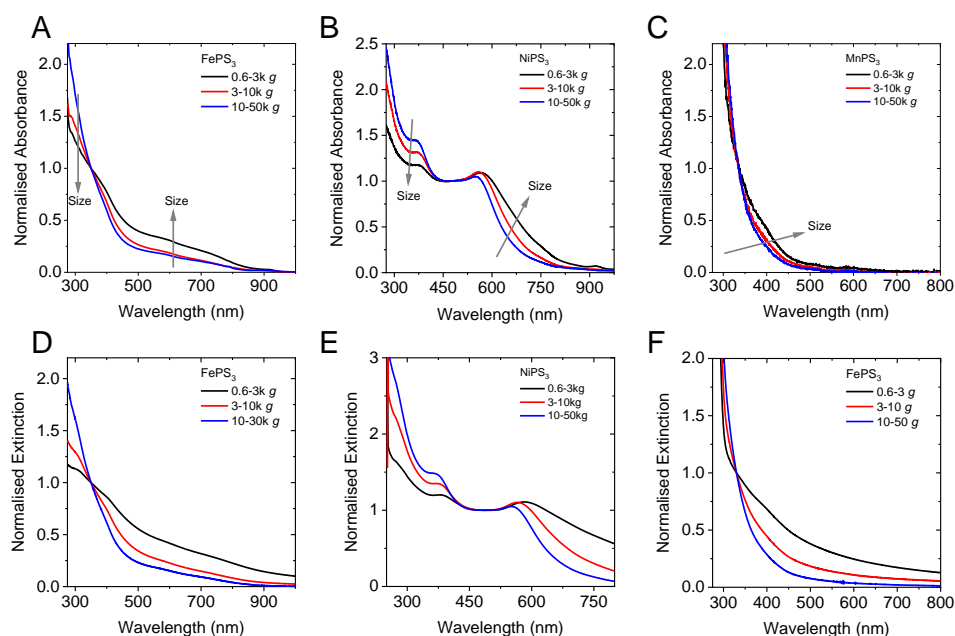


Figure A4.3-1.2: UV-Vis measurements of dispersions containing different sizes of MPS₃ nanosheets obtained from the second centrifugation cascade. (A-C) Normalised extinction spectra of NiPS₃ (A), FePS₃ (B) and MnPS₃ (C), respectively. The grey arrow indicates systematic changes with nanomaterial size. (D-F) Normalised absorbance spectra of NiPS₃ (D), FePS₃ (E) and MnPS₃ (F), respectively. See also in reference ¹¹ (NiPS₃).

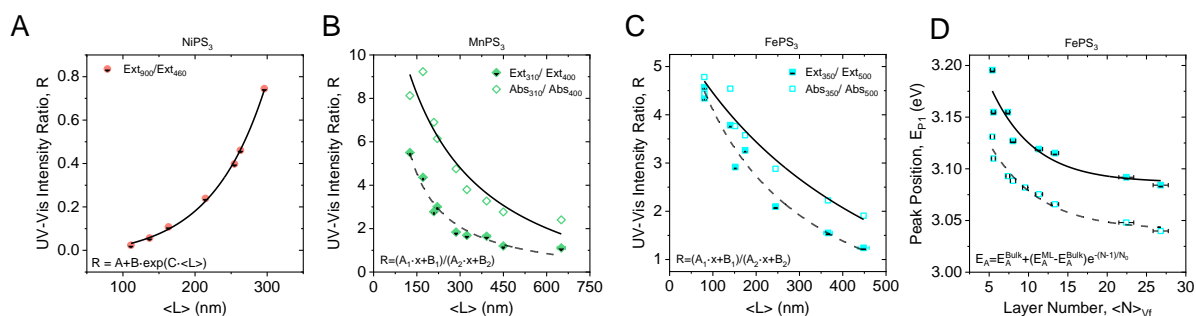
4.3-2 Additional metrics derived for MPS₃ nanosheets

Figure A4.3-2: Quantified changes optical spectra with material dimensions for different MPS₃ species. (A-C) Intensity ratios serve as metric for the lateral nanosheet size. **(A)** The extinction at 900 nm over 460 nm can be used to determine the nanosheet length of NiPS₃. **(B)** The extinction or absorbance ratio 310 nm/400 nm scales with the sheet length of MnPS₃. **(C)** The ratio 350 nm/500 nm scales with the sheet length of FePS₃. **(D)** Plot of the centre of mass peak positions as function of mean layer number extracted from extinction and absorbance spectra of FePS₃. The fit represents a metric for the nanosheet layer number and allows to extract the phenomenological decay constant (N_0) for excitonic resonances in FePS₃. See also in reference ¹¹ (NiPS₃).

Appendix 4.4:

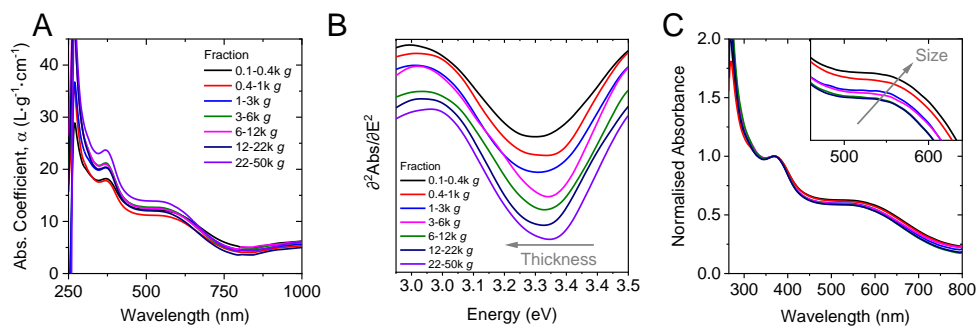
4.4-1 Absorbance measurements of exfoliated α -RuCl₃

Figure A4.4-1: Absorbance measurements of dispersions containing different sizes of α -RuCl₃ nanosheets. (A) Absorbance coefficient spectra for different nanosheet sizes. (B) Second derivative of the absorbance measurements shown in (A). The centre of mass peak position is used to identify changes of the resonance energy of optical transitions. The grey arrow indicates changes of the peak position with nanosheet layer number. (C) Normalised absorbance spectra of different nanosheet sizes. The grey arrow indicates systematic changes with nanosheet lateral size. Note, that the changes in the spectra are very subtle in case of α -RuCl₃ compared to other materials.

Appendix 4.6:

4.6-1 Optical properties of Anthracene and the monomer of 2D-Pol(1)

The optical spectra of 2D-Pol(1) strongly resemble patterns of small molecules. Hence, measurements of the optical extinction and the photoluminescence were performed on anthracene and on the monomer of 2D-Pol(1) for comparison. Indeed, the vibronic fine structure observed for 2D-Pol(1) can be attributed to excited states located at the anthracene rings (Figure A4.6-1)

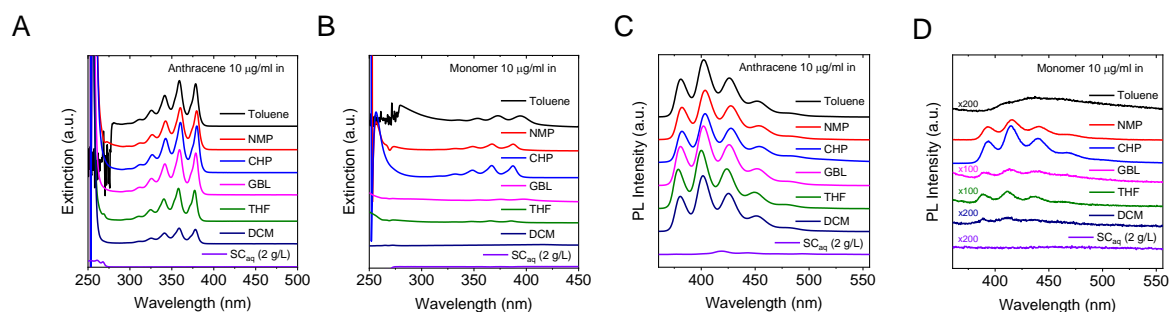


Figure A4.6-1: Optical spectra of small molecules integrated in the molecular structure of 2D-Pol(1). (A-B) Extinction spectra of anthracene (A) and the monomer of 2D-Pol(1) (B) in different solvents. (C-D) Photoluminescence spectra of anthracene (C) and the monomer of 2D-Pol(1) (D) in different solvents.

4.6-2 Extinction and absorbance spectra of different sizes of 2D-Pol(1)

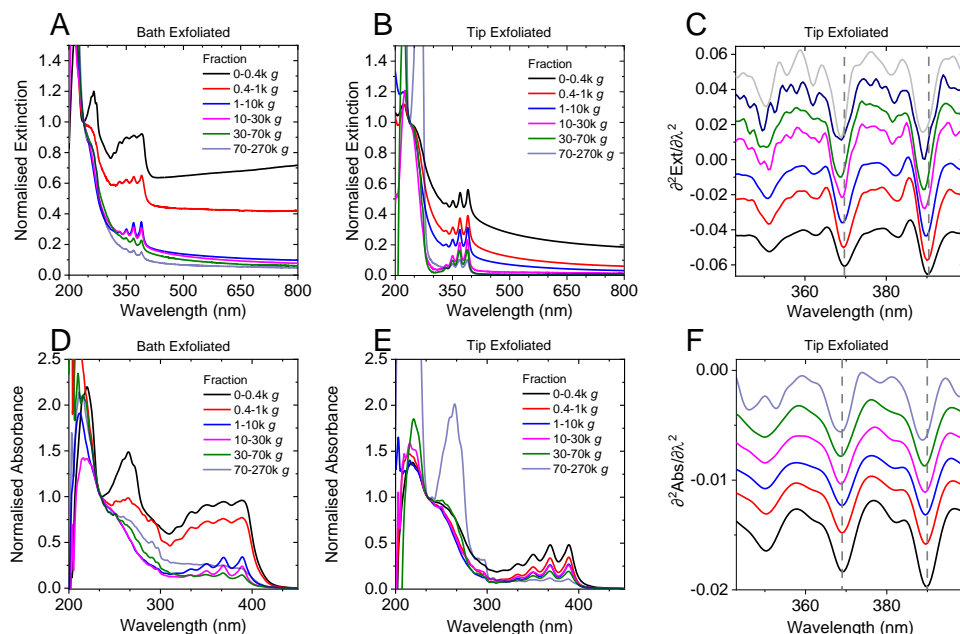


Figure A4.6-2: Extinction and absorbance spectra of 2D-Pol(1) exfoliated by bath and by tip sonication. (A-C) Extinction spectra and (D-F) absorbance spectra for different sizes of 2D-Pol(1). (A-B) Normalised extinction spectra for bath exfoliated (A) and tip exfoliated (B) 2D-Pol(1). (C) Second derivative of the extinction spectra of tip exfoliated samples. (D-E) Normalised absorbance spectra for bath exfoliated (A) and tip exfoliated (B) 2D-Pol(1).

Chapter 8 – Appendix

Pol(1). (F) Second derivative of the absorbance spectra of tip exfoliated samples. A slight blueshift of the features is observed with decreasing material thickness.

4.6-3 Photoluminescence of different sizes of 2D-Pol(1)

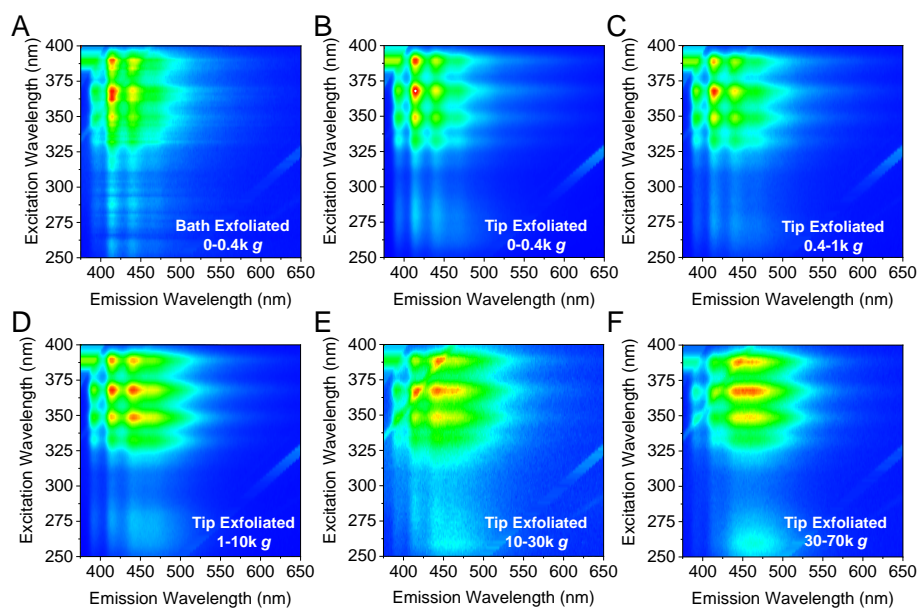


Figure A4.6-3.1: PLE maps of different sizes of 2D-Pol(1). (A-B) Comparison of a fraction from bath exfoliated (A) to tip exfoliated (B) nanosheets. (B-F) PLE maps of nanosheets with decreasing size from B \rightarrow F.

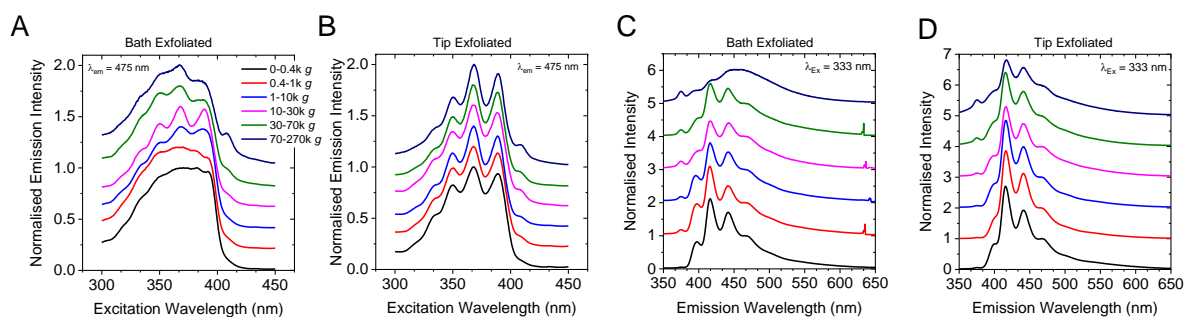


Figure A4.6-3.2: Photoluminescence excitation and emission spectra for different sizes of 2D-Pol(1). (A-B) PL excitation spectra for different nanosheet sizes prepared by bath- (A) and by tip-sonication (B). (C-D) PL emission spectra for different nanosheet sizes prepared by bath- (C) and by tip-sonication (D).

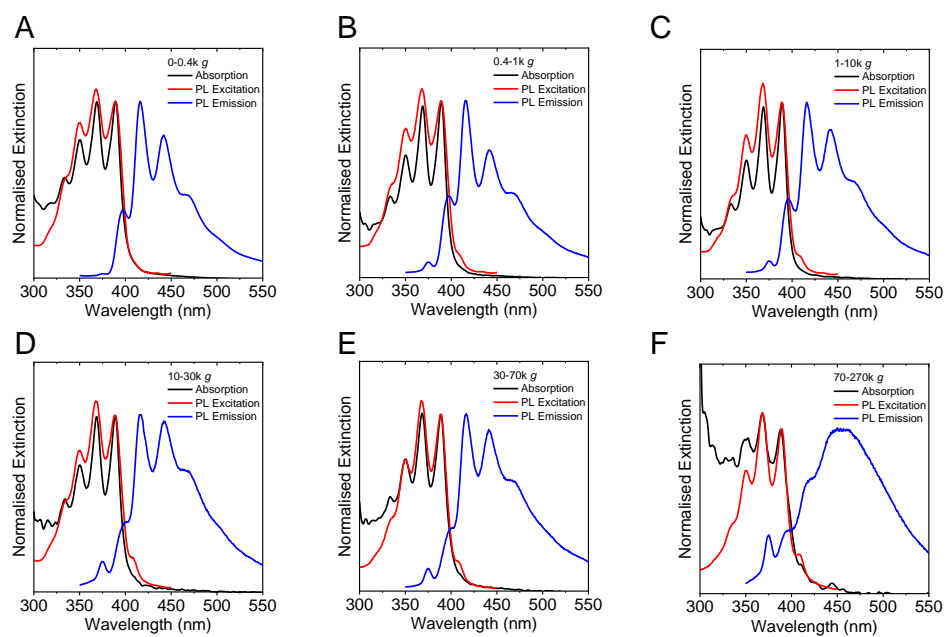


Figure A4.6-3.3: Normalised Absorbance, PL excitation and PL emission spectra for different sizes of 2D-Pol(1). (A-F) Spectra for nanosheets of decreasing size from A→F. The absorption and the excitation spectra overlap in every case.

4.6-4 Photoluminescence of different sizes of 2D-Pol(1)

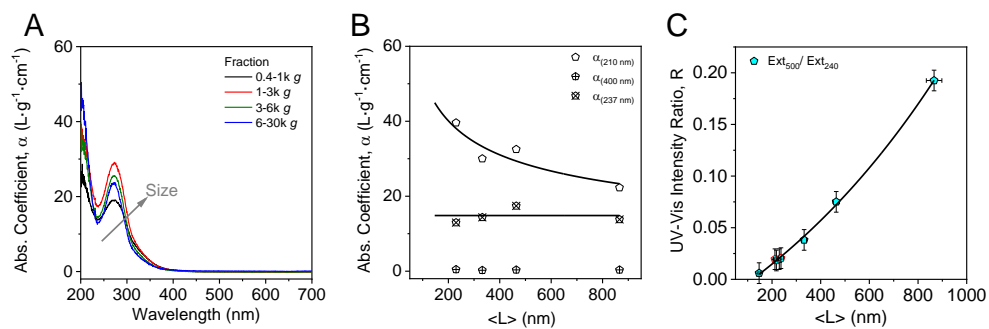


Figure A4.6-4: Optical properties of 2D-Pol(2N) nanosheets. (A) Size-dependent absorbance coefficient spectra show systematic changes with nanosheet dimensions. (B) Absorbance coefficients of 2D-Pol(2N) at different wavelengths. The absorbance coefficient remains approximately constant across all fractions at 400 nm. (C) Extinction intensity ratio at 500 nm over 240 nm scale with the lateral nanomaterial size. See also in reference ²³.

Appendix 4.7:

4.7-1 Optical properties of Anthracene and the monomer of 2D-Pol(1)

Supplementary data extracted from published work on changes of optical properties for exfoliated nanosheets of various materials was refitted to equation 28 and 29, respectively. The fits are shown below. (Figure A4.7-1).

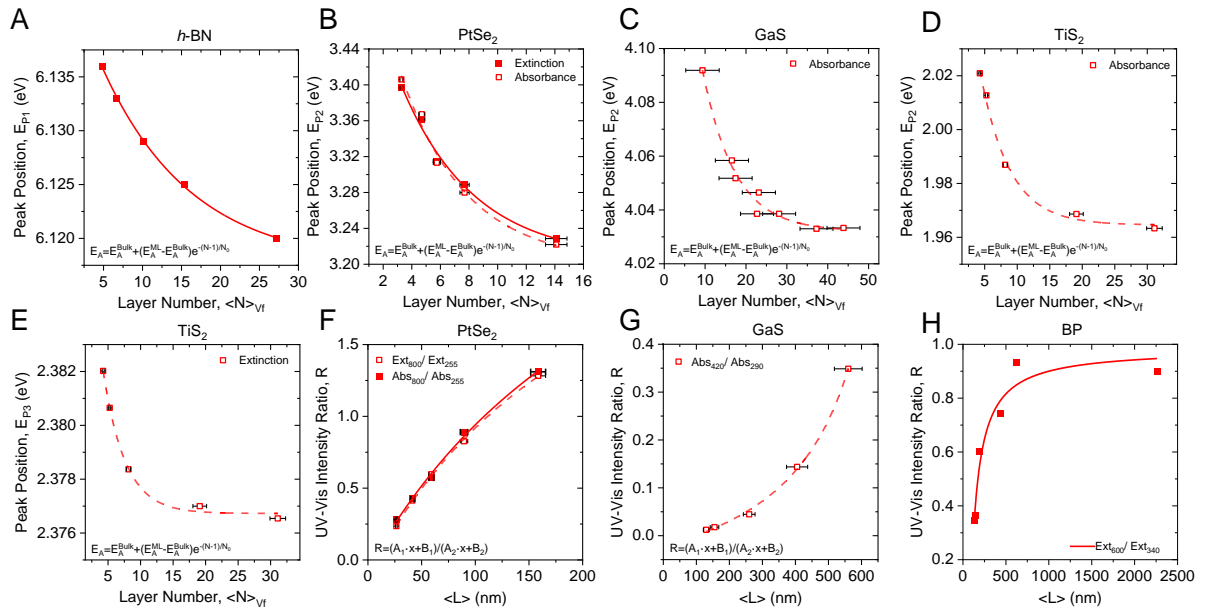


Figure A4.7-1: Literature values on size-dependent changes of optical properties. (A-E) Change of the UV-Vis peak positions as function of material thickness for *h*-BN (A),⁷² PtSe₂ (B),¹⁹² GaS (C)¹² and TiS₂ (D-E).¹⁹³ (F-H) Size-dependent changes of the UV-Vis intensity ratio for PtSe₂ (F),¹⁹² GaS (G)¹² and BP (H).¹²⁷

Appendix 5.1:

Changes of the optical spectra of dispersions containing nanosheets was observed over time in ambient conditions which were identified as effects from material decomposition. To address this in more detail, different sizes of nanosheets were kept at different temperatures and optical measurements were acquired in specific intervals of time. Supplementary data to discussions in Chapter 5 is shown below.

5.1-1 Optical characterisation of TMD nanosheets studied for material decomposition

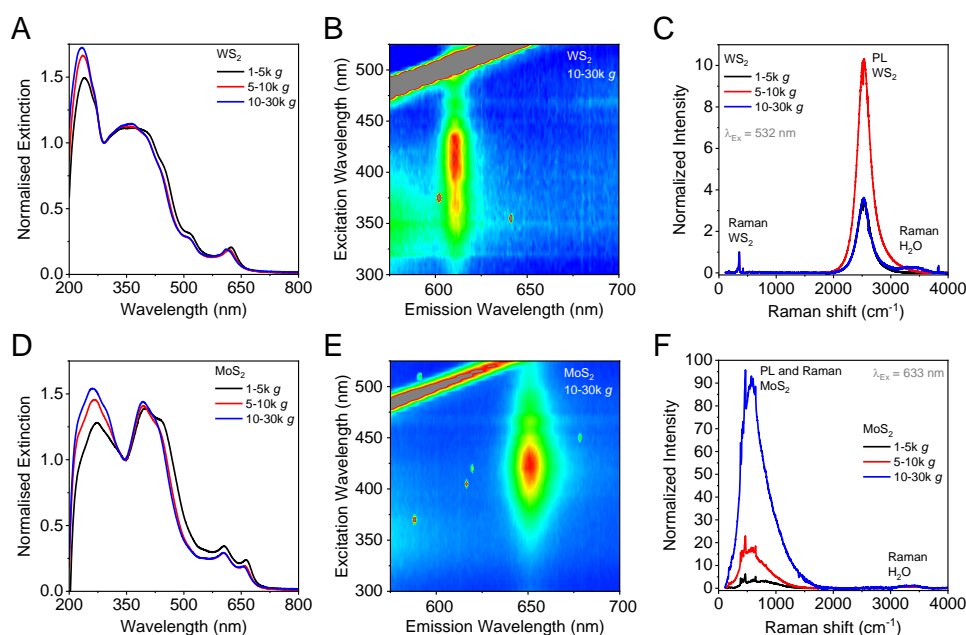


Figure A5.1-1.1: Optical characterisation of WS₂ and MoS₂ nanosheets used for decomposition studies. (A-C) Extinction (A), PLE (B) and Raman/PL (C) measurements acquired for WS₂. (D-F) Similar measurements as in (A-C) for MoS₂.

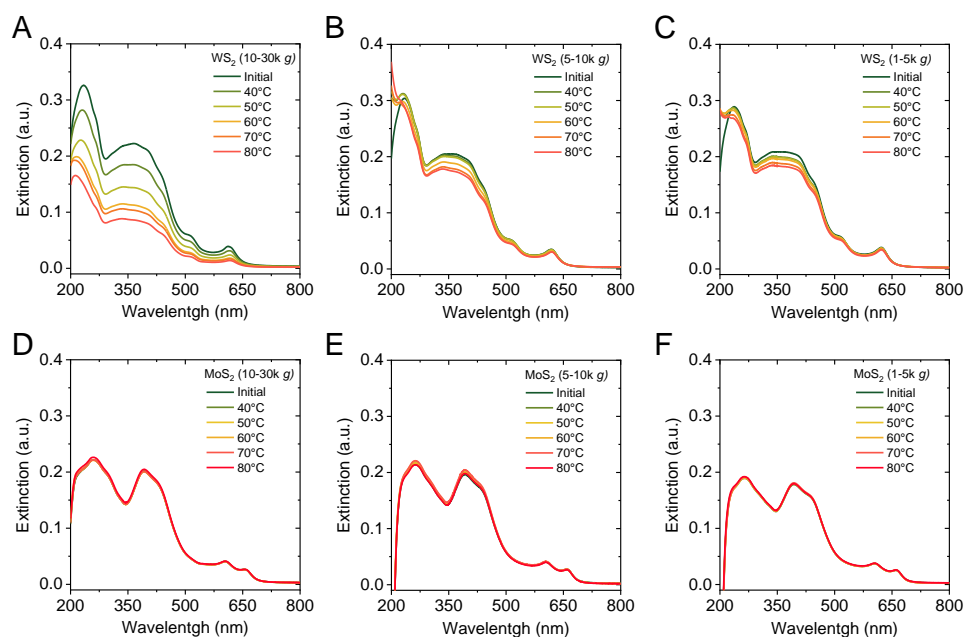


Figure A5.1-1.2: Extinction measurements of WS₂ and MoS₂ nanosheets. Measurements were acquired after storage of the dispersions at different temperatures for 400 minutes as indicated in the individual plots. (A-C) Different sizes of WS₂: (A) 10-30k g (*i.e.* small), (B) 5-10k g (*i.e.* medium) and (C) 1-5k g (*i.e.* large). (D-F) Different sizes of MoS₂: (D) 10-30k g (*i.e.* small), (E) 5-10k g (*i.e.* medium) and (F) 1-5k g (*i.e.* large).

5.1-2 Change of the photoluminescence as function of time for TMD nanosheets

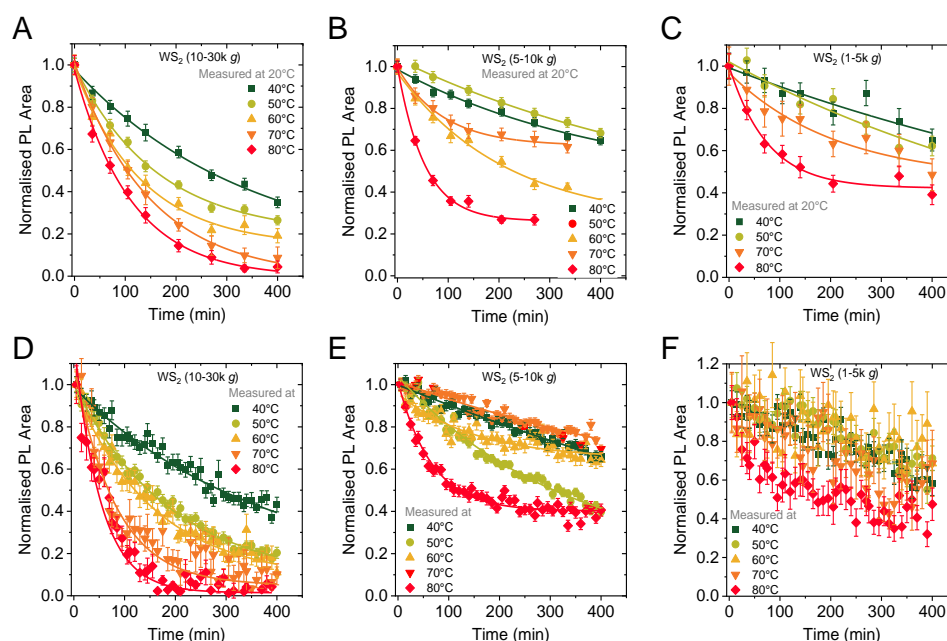


Figure A5.1-2.1: Evolution of the photoluminescence of WS₂ nanosheets over time for different temperatures. (A-C) PL area for different nanosheet sizes measured at 20°C after stirring at elevated temperatures as indicated in the individual plots. (D-F) PL area for different nanosheet sizes measured at elevated temperatures. (A, D) 10-30k g (*i.e.* small), (B, E) 5-10k g (*i.e.* medium) and (C, F) 1-5k g (*i.e.* large).

5.1-3 Impact of light on the TMD nanosheet decomposition

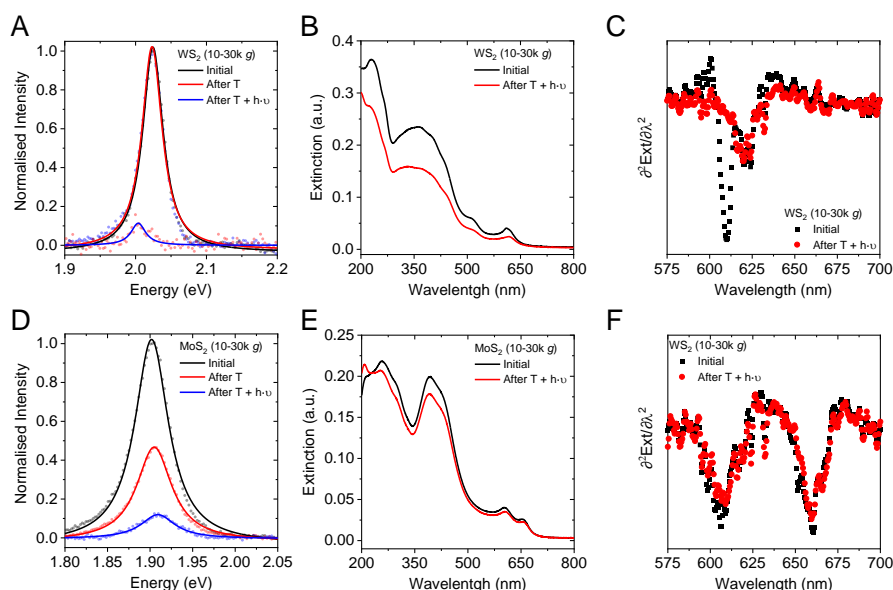


Figure A5.1-3: Optical response of nanosheets after temperature and illumination treatment. Initial spectra are shown in black, samples stirred at 80°C for 8 h are shown in blue and samples illuminated for 8 h (T ~50°C) are shown in red. (A-C) Measurements acquired for WS₂ (10-30k g). (D-F) Measurements acquired for MoS₂ (10-30k g). (A, D) PL emission spectra (B, E) Extinction spectra (C, F) Second derivative of the spectra shown in (B, E) in the region of the A-exciton.

Appendix 5.2:

5.2-1 Evolution of UV-Vis spectra of γ -InSe nanosheets at different temperatures

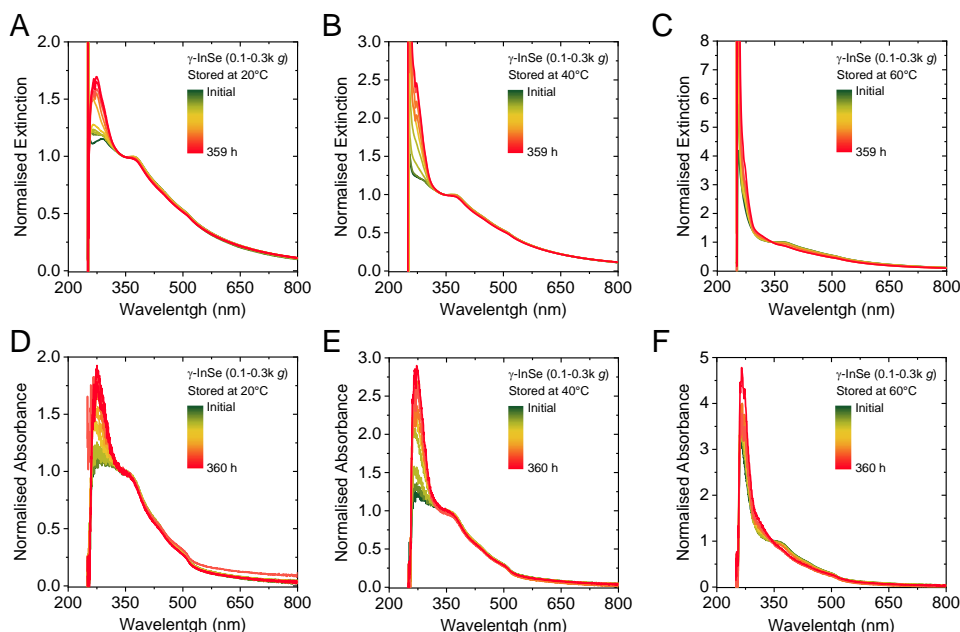


Figure A5.2-1.1: Extinction and absorbance spectra of γ -InSe nanosheets at different temperatures. (A-C) Normalised extinction spectra of relatively large (0.1-0.3k g) γ -InSe nanosheets. (D-F) Normalised absorbance

spectra of the same γ -InSe nanosheet fraction as in (A-C). Samples were kept at 20°C (A, D), 40°C (B, E) and 60°C (C, F) and measured over time.

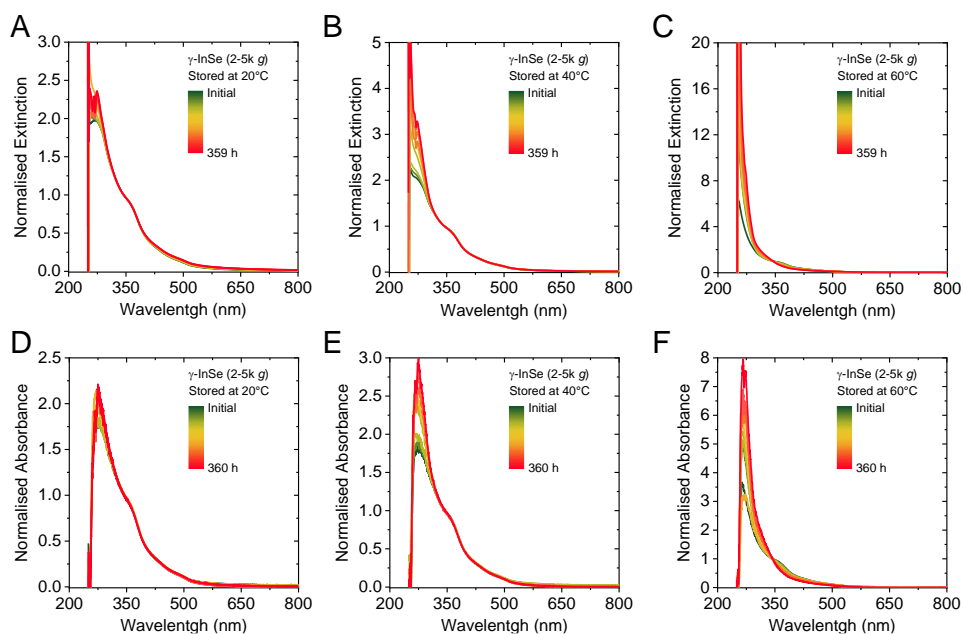


Figure A5.2-1.2: Extinction and absorbance spectra of γ -InSe nanosheets at different temperatures. (A-C) Normalised extinction spectra of relatively small (2-5k g) γ -InSe nanosheets. (D-F) Normalised absorbance spectra of the same γ -InSe nanosheet fraction as in (A-C). Samples were kept at 20°C (A, D), 40°C (B, E) and 60°C (C, F) and measured over time.

Appendix 5.3:

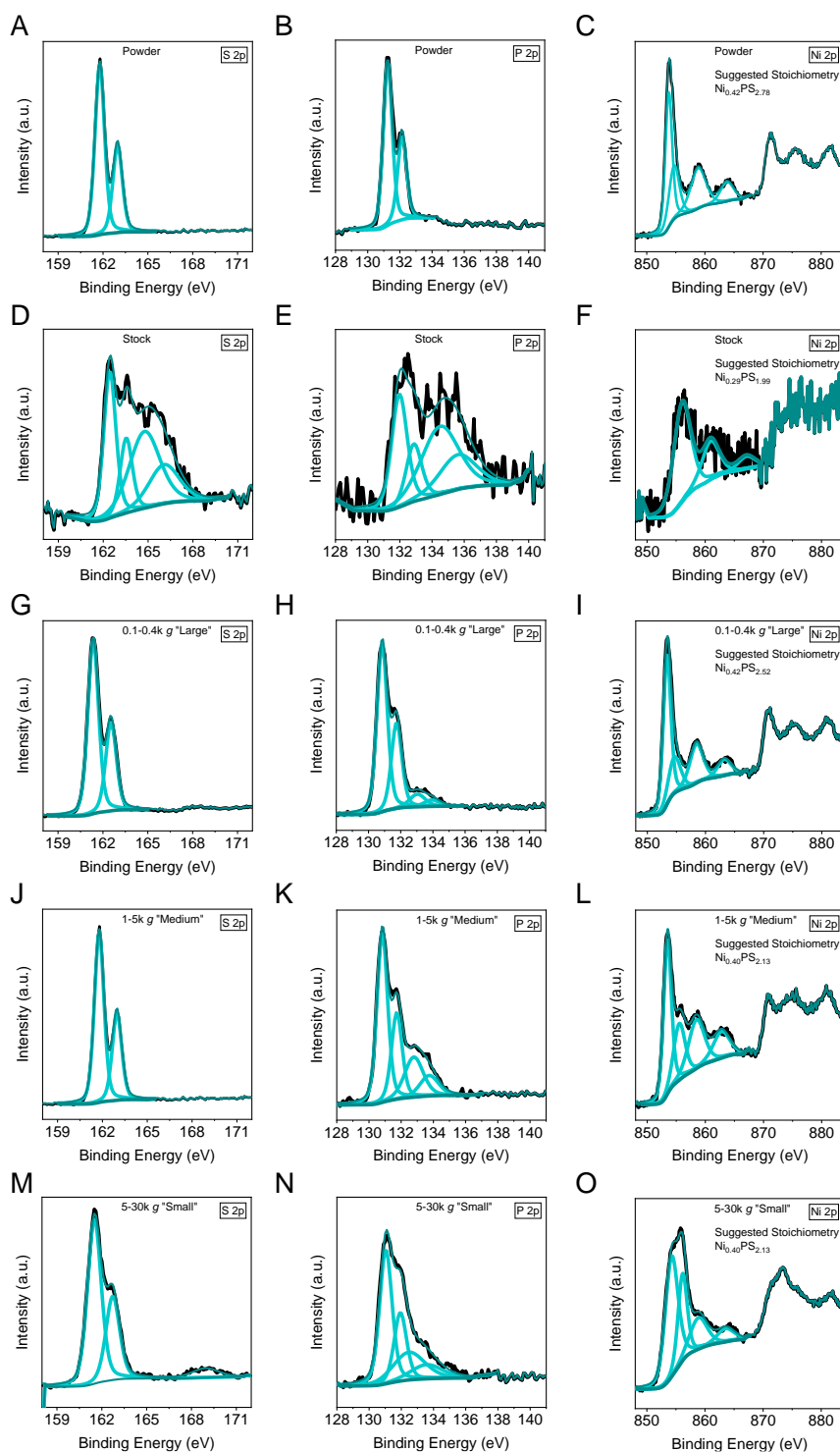
5.3-1 XPS measurements on exfoliated NiPS₃ nanosheets

Figure A5.3-1.1: XPS core level spectra of different sizes of NiPS₃. S 2p, P 2p and Ni 2p core level spectra of different material fractions are shown in the first, second and third column, respectively. (A-C) NiPS₃ powder, (D-F) stock dispersion, (G-I) large (0.1-0.4k g), (J-L) medium (1-5k g) and (M-O) small (5-30k g) nanosheets. See also in reference ¹¹.

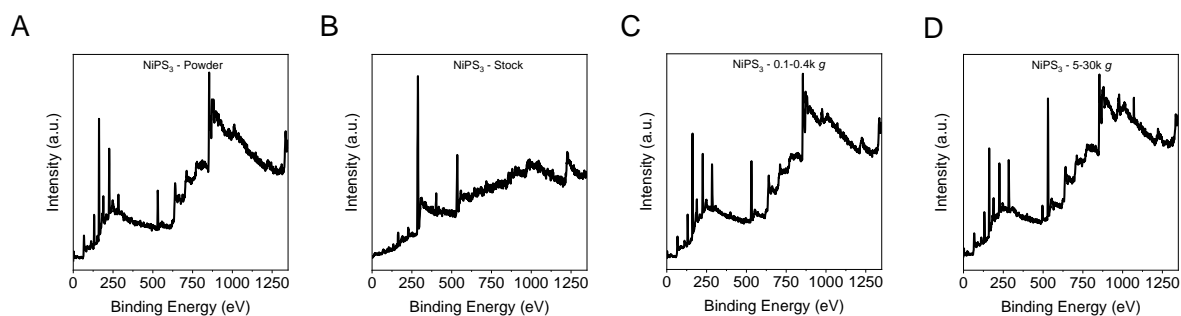


Figure A5.3-1.2: XPS survey scans for different sizes of NiPS₃. (A) NiPS₃ powder, (B) stock dispersion, (C) large (0.1-0.4k g) and (D) small (5-30k g) nanosheets. See also in reference ¹¹.

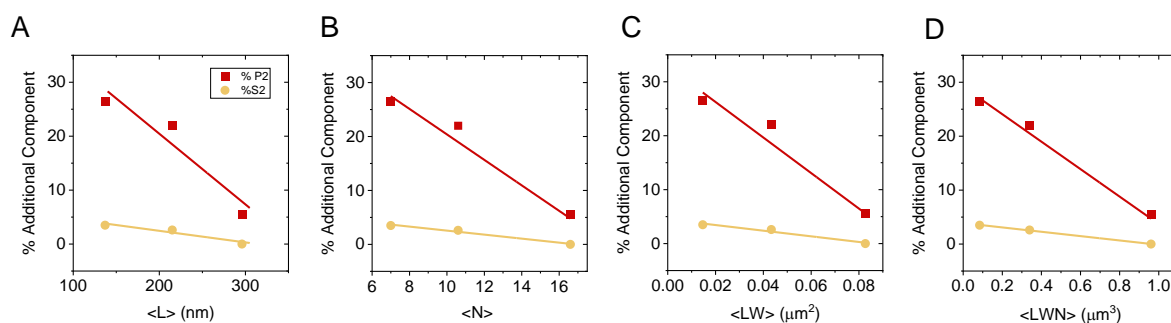


Figure A5.3-1.3: XPS oxide contribution in the S_{2p} and P_{2p} core level spectra of NiPS₃ samples. Evaluation of the additional P and S component with nanosheet dimensions allows to plot the percentage of the additional compound as function of nanosheet size $\langle L \rangle$ (A), thickness $\langle N \rangle$ (B), area $\langle LW \rangle$ (C) and volume $\langle LWN \rangle$ (D). The best correlation is given for nanosheet volume. See also in reference ¹¹.

5.3-2 TEM measurements on exfoliated MPS₃ nanosheets

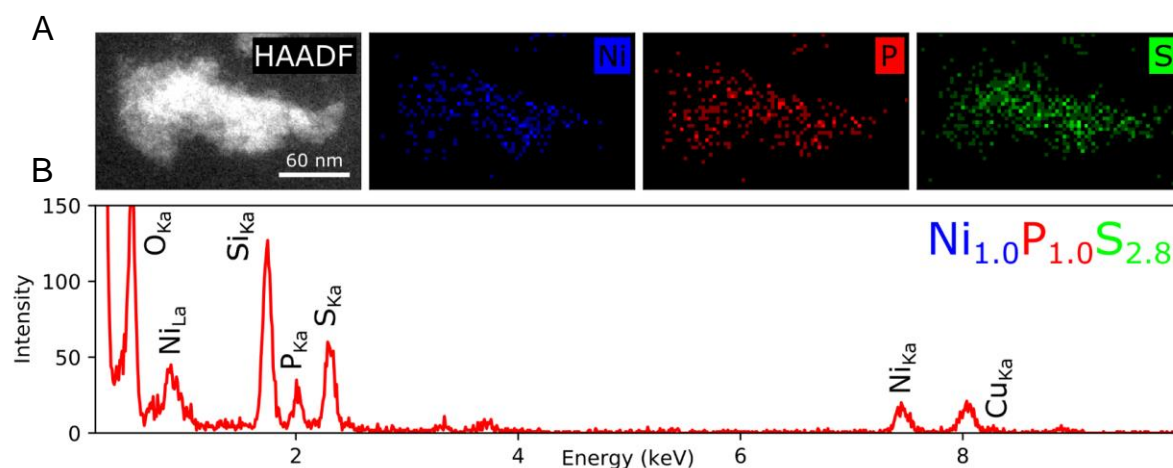


Figure A5.3-2.1: STEM-EDX of NiPS₃. (A) HAADF-STEM micrograph of a 200 nm flake and Ni, P, and S EDX maps of the same flake showing uniform distribution of each element throughout. (B) EDX spectrum from the entire flake which was used to determine atomic percent ratios 1:1:2.8 *via* the Cliff-Lorimer method. The few oxygen counts visible in the sum spectra are due to residual solvent and oxygen associated with the carbon support film. See also in reference ¹¹.

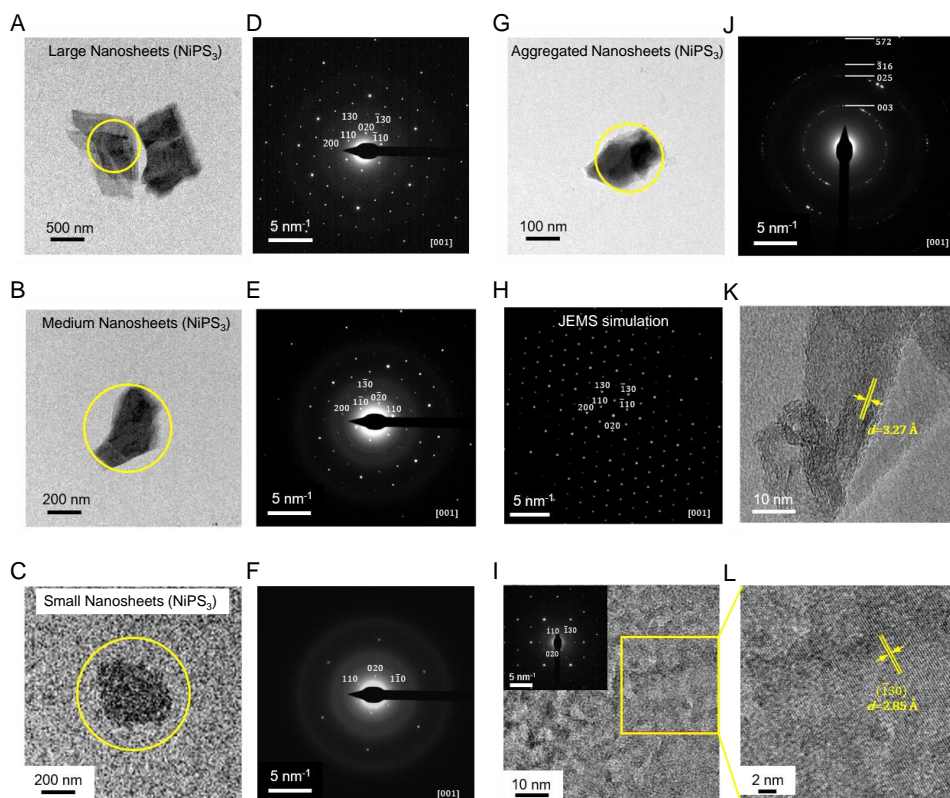


Figure A5.3-2.2: TEM measurements for different sizes of LPE NiPS₃ nanosheets. (A-C) show low magnification bright field images of different fractions of size-selected nanosheets with large- (A), medium- (B) and small- (C) sized sheets (0.6-3 k g, 3-10 k g and 10-30 k g, respectively). (D-F, and I inset) show the corresponding selected area electron diffraction pattern (SAED) viewed along the [001] direction revealing the single crystal nature of the nanosheets shown in (A-C). The yellow circle indicates the selected area for the diffraction measurement. Single crystal patterns match the expected pattern predicted from multislice simulations²⁴¹ (H). Aggregated or rotated nanosheets (G) show polycrystalline diffraction patterns (J). (K) shows a HRTEM image of a folded nanosheet, where the flake is locally oriented parallel to the electron beam allowing the number of atomic layers to be determined (14 with an interlayer distance of ~6.5 Å). (L, I) High resolution images reveal a high degree of crystallinity but also the presence of an amorphous surface layer. See also in reference ¹¹.

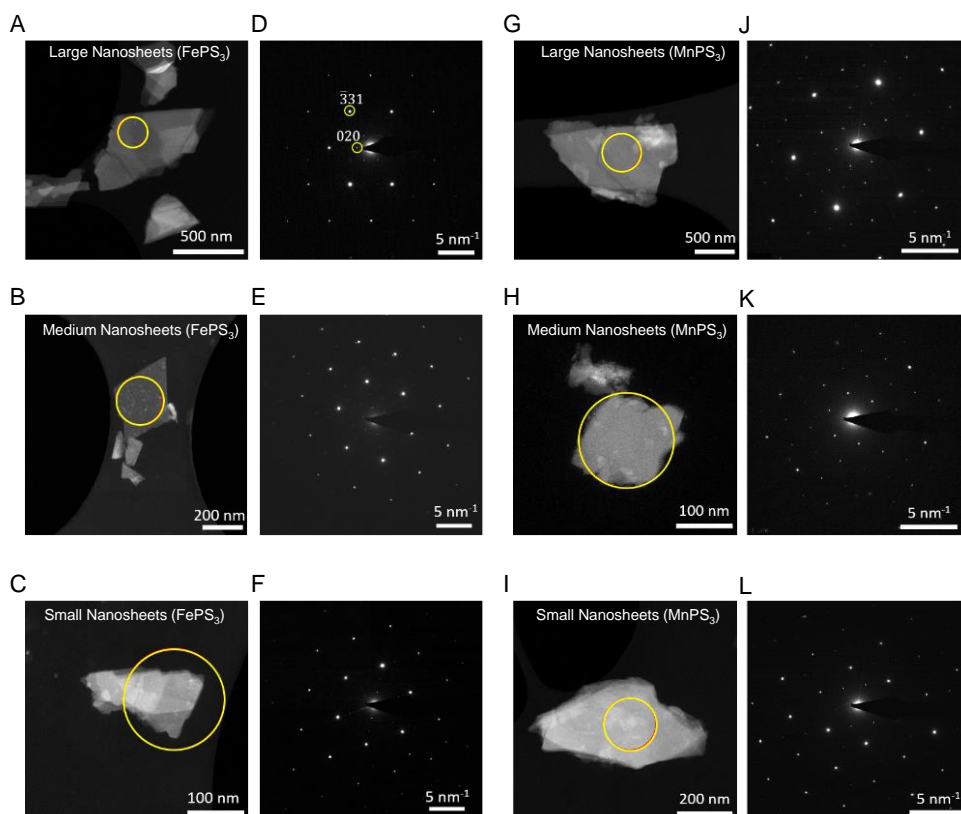


Figure A5.3-2.3: TEM measurements for different sizes of LPE FePS₃ and MnPS₃ nanosheets. (A-C) show low magnification bright field images of different fractions of size-selected nanosheets with large- (A), medium- (B) and small- (C) sized FePS₃ nanosheets (0.6-3 k g, 3-10 k g and 10-30k g, respectively). (D-F) show the corresponding selected area electron diffraction pattern (SAED) viewed along the [001] direction revealing the single crystal nature of the nanosheets shown in (A-C). (G-I) show low magnification bright field images of different fractions of size-selected nanosheets with large- (G), medium- (H) and small- (I) sized MnPS₃ nanosheets (0.6-3 k g, 3-10 k g and 10-30k g, respectively). (J-L) show the corresponding selected area electron diffraction pattern (SAED) viewed along the [001] direction revealing the single crystal nature of the nanosheets shown in (G-I). The yellow circle indicates the selected area for the diffraction measurement.

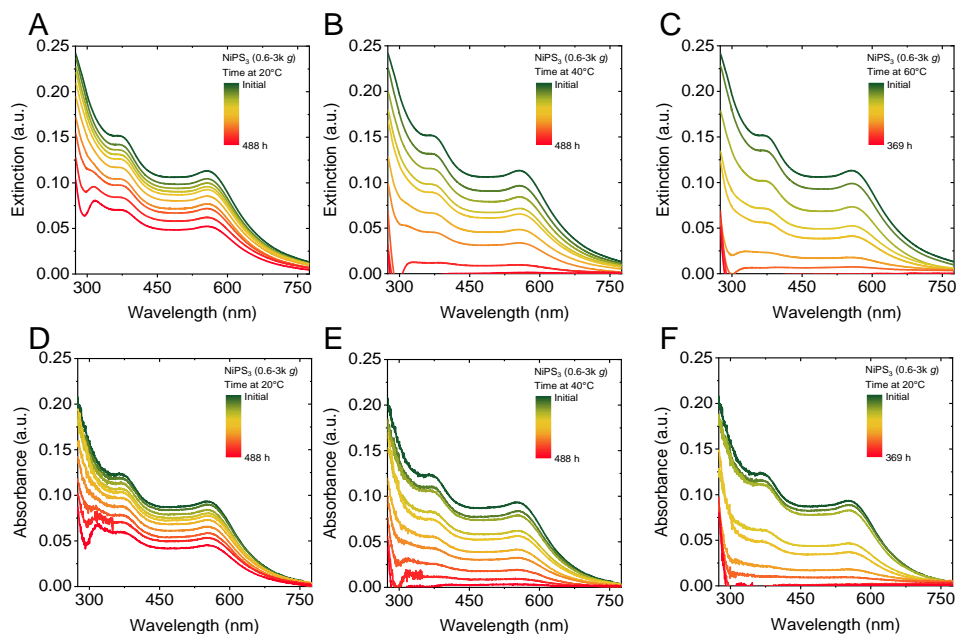
5.3-3 Evolution of UV-Vis spectra of MPS₃ nanosheets at different temperaturesNiPS₃:

Figure A5.3-3.1: UV-Vis spectra of NiPS₃ nanosheets measured at different times and temperatures. The upper row (A-C) shows extinction-, the lower row (D-F) absorbance spectra of large nanosheets (0.6-3k g) for different storage conditions. The spectra correspond to samples stored at 20, 40 and 60°C (from left to right). All spectra show changes over time. The optical density at 460 nm decreases in all cases systematically. The changes are more pronounced for elevated temperatures. See also in reference ¹¹.

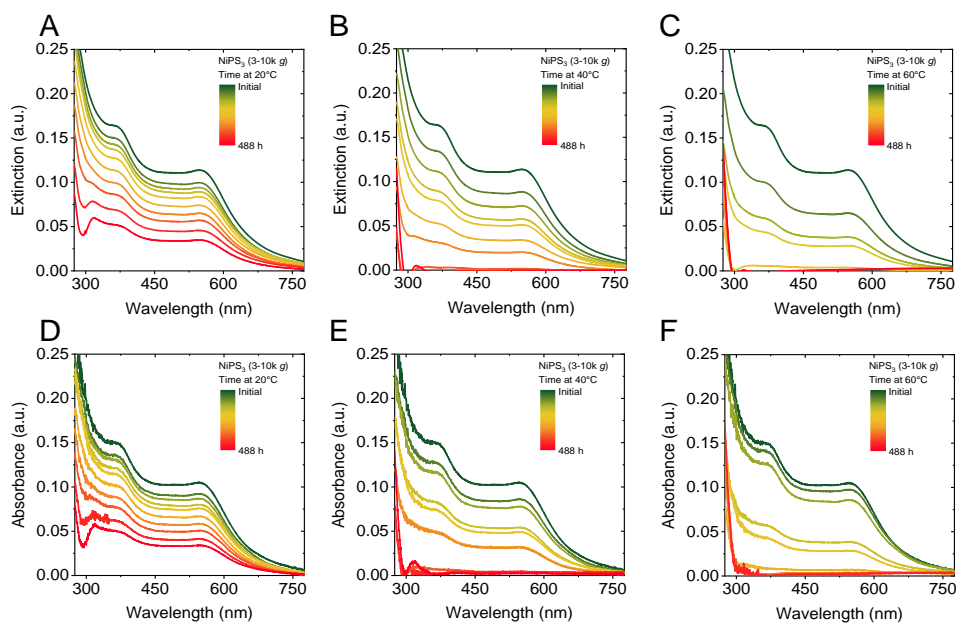


Figure A5.3-3.2: UV-Vis spectra of NiPS₃ nanosheets measured at different times and temperatures. The upper row (A-C) shows extinction-, the lower row (D-F) absorbance spectra of medium-sized nanosheets (3-10k g) for different storage conditions. The spectra correspond to samples stored at 20, 40 and 60°C (from left to right). All spectra show changes over time. The optical density at 460 nm decreases in all cases systematically. The changes are more pronounced for elevated temperatures. See also in reference ¹¹.

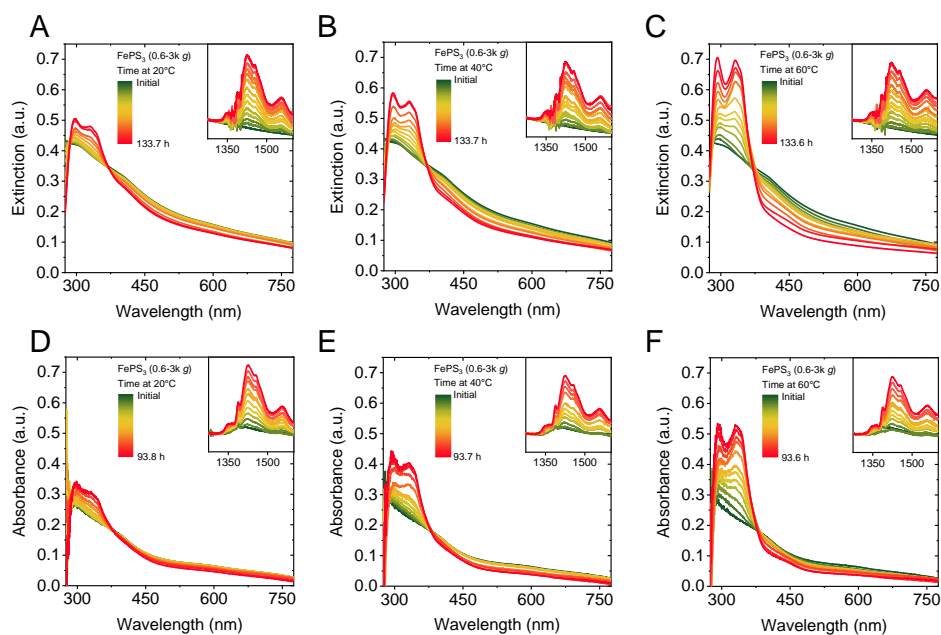
FePS₃:

Figure A5.3-3: UV-Vis spectra of FePS₃ nanosheets measured at different times and temperatures. The upper row (A-C) shows extinction-, the lower row (D-F) absorbance spectra of large nanosheets (0.6-3k g) for different storage conditions. The spectra correspond to samples stored at 20, 40 and 60°C (from left to right). All spectra show changes over time. The optical density at 400 nm decreases in all cases systematically. The changes are more pronounced for elevated temperatures.

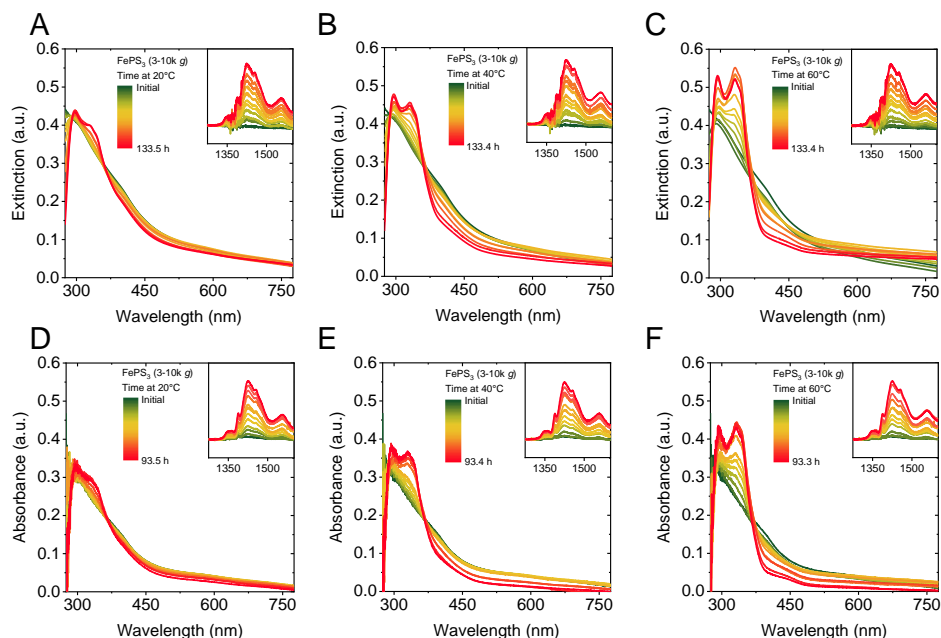


Figure A5.3-4: UV-Vis spectra of FePS₃ nanosheets measured at different times and temperatures. The upper row (A-C) shows extinction-, the lower row (D-F) absorbance spectra of medium-sized nanosheets (3-10k g) for different storage conditions. The spectra correspond to samples stored at 20, 40 and 60°C (from left to right). All spectra show changes over time. The optical density at 400 nm decreases in all cases systematically. The changes are more pronounced for elevated temperatures.

Chapter 8 – Appendix

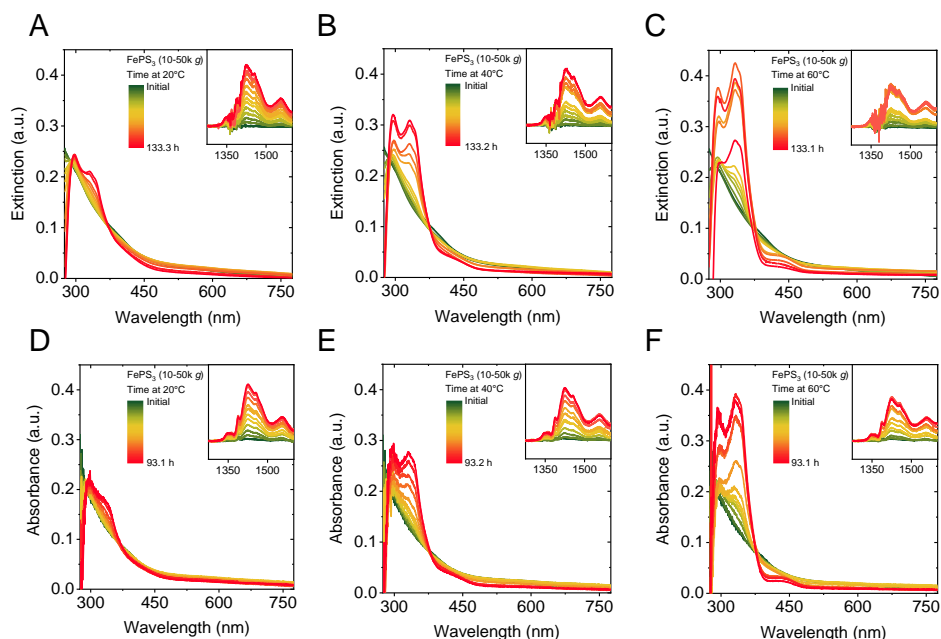


Figure A5.3-3.5: UV-Vis spectra of FePS₃ nanosheets measured at different times and temperatures. The upper row (A-C) shows extinction-, the lower row (D-F) absorbance spectra of small nanosheets (10-50k g) for different storage conditions. The spectra correspond to samples stored at 20, 40 and 60°C (from left to right). All spectra show changes over time. The optical density at 400 nm decreases in all cases systematically. The changes are more pronounced for elevated temperatures.

MnPS₃:

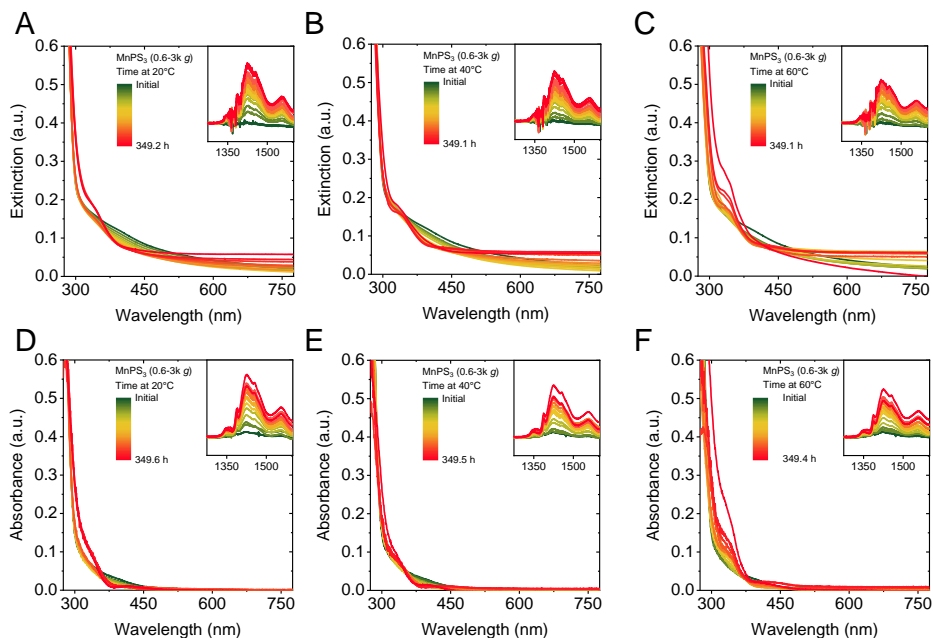


Figure A5.3-3.6: UV-Vis spectra of MnPS₃ nanosheets measured at different times and temperatures. The upper row (A-C) shows extinction-, the lower row (D-F) absorbance spectra of large nanosheets (0.6-3k g) for different storage conditions. The spectra correspond to samples stored at 20, 40 and 60°C (from left to right). All spectra show changes over time. The optical density at 400 nm decreases in all cases systematically. The changes are more pronounced for elevated temperatures.

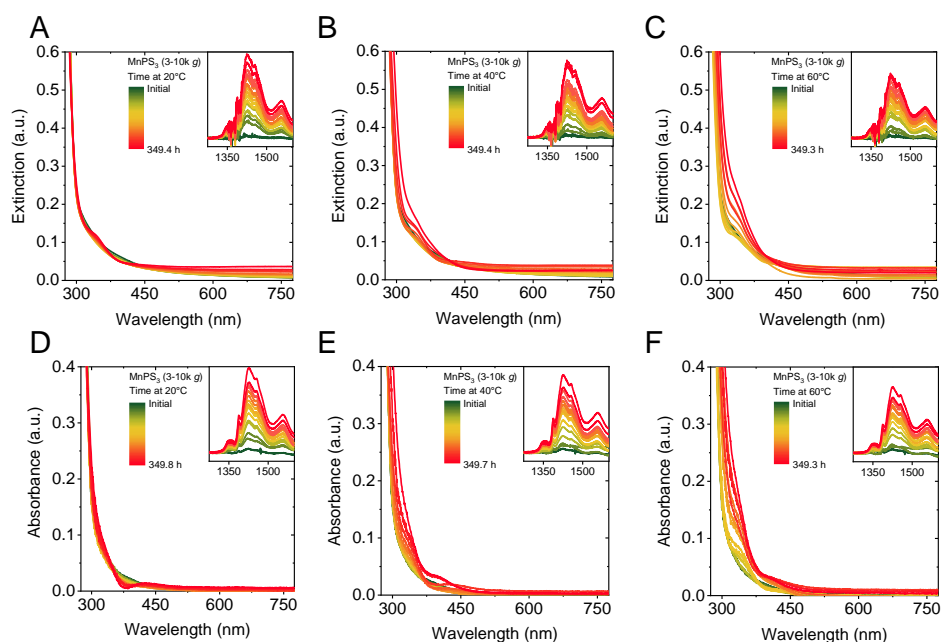


Figure A5.3-3.7: UV-Vis spectra of MnPS₃ nanosheets measured at different times and temperatures. The upper row (A-C) shows extinction-, the lower row (D-F) absorbance spectra of medium-sized nanosheets (3-10k g) for different storage conditions. The spectra correspond to samples stored at 20, 40 and 60°C (from left to right). All spectra show changes over time. The optical density at 400 nm decreases in all cases systematically. The changes are more pronounced for elevated temperatures.

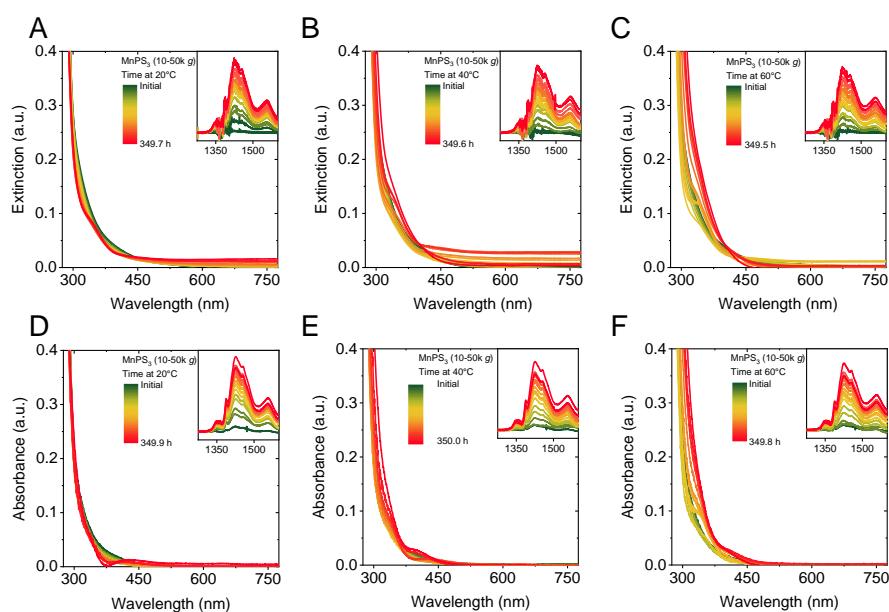


Figure A5.3-3.8: UV-Vis spectra of MnPS₃ nanosheets measured at different times and temperatures. The upper row (A-C) shows extinction-, the lower row (D-F) absorbance spectra of small nanosheets (10-50k g) for different storage conditions. The spectra correspond to samples stored at 20, 40 and 60°C (from left to right). All spectra show changes over time. The optical density at 400 nm decreases in all cases systematically. The changes are more pronounced for elevated temperatures.

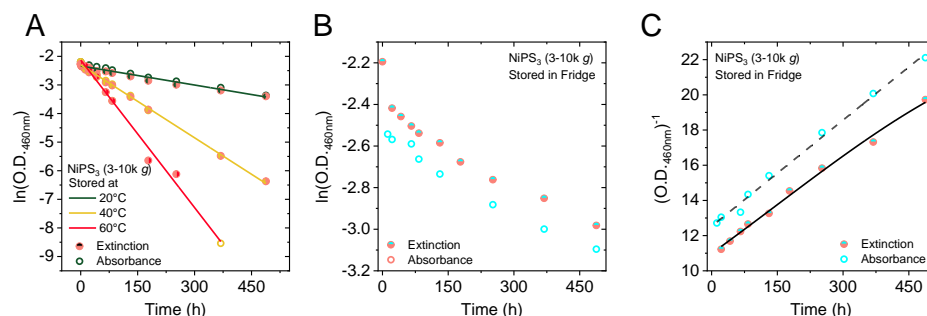
5.3-4 Decomposition of MPS₃ nanosheets at different temperaturesNiPS₃:

Figure A5.3-4.1: Degradation of NiPS₃ nanosheets (A) Natural logarithm of the extinction and absorption at 460 nm of the fraction containing small nanosheets stored at 20, 40 and 60°C, respectively as function of time. Data from both absorbance and extinction is included and falls on the same curve. Solid lines are linear fits to extract the degradation half-lives. (B) Plot of the natural logarithm of the extinction and absorption of NiPS₃ (3-10k g) nanosheets at 460 nm as function of time plotted for the sample stored in the refrigerator. No linearization of the data is observed. (C) Same data as in (B) plotted as inverse optical density at 460 nm as function of time. Linear fit suggests second order kinetics.

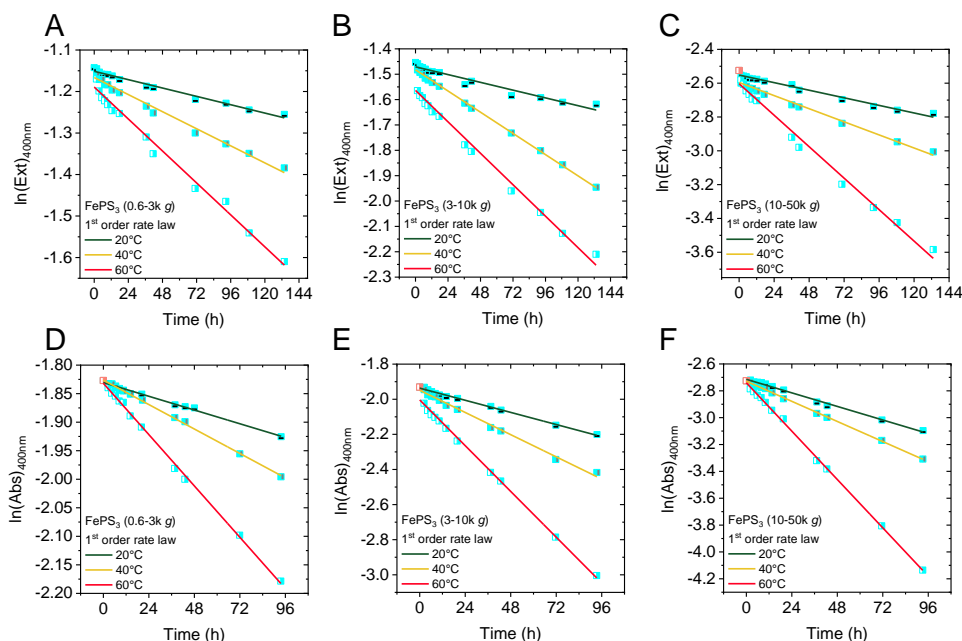
FePS₃:

Figure A5.3-4.2: Degradation of FePS₃ nanosheets. (A-F) Natural logarithm of the extinction (A-C) and absorption (D-F) at 400 nm of different fractions containing (from left to right) large (0.6-3k g), medium (3-10k g) and small (10-50k g) nanosheets stored at 20, 40 and 60°C, respectively as function of time. Solid lines are linear fits to extract the degradation half-lives.

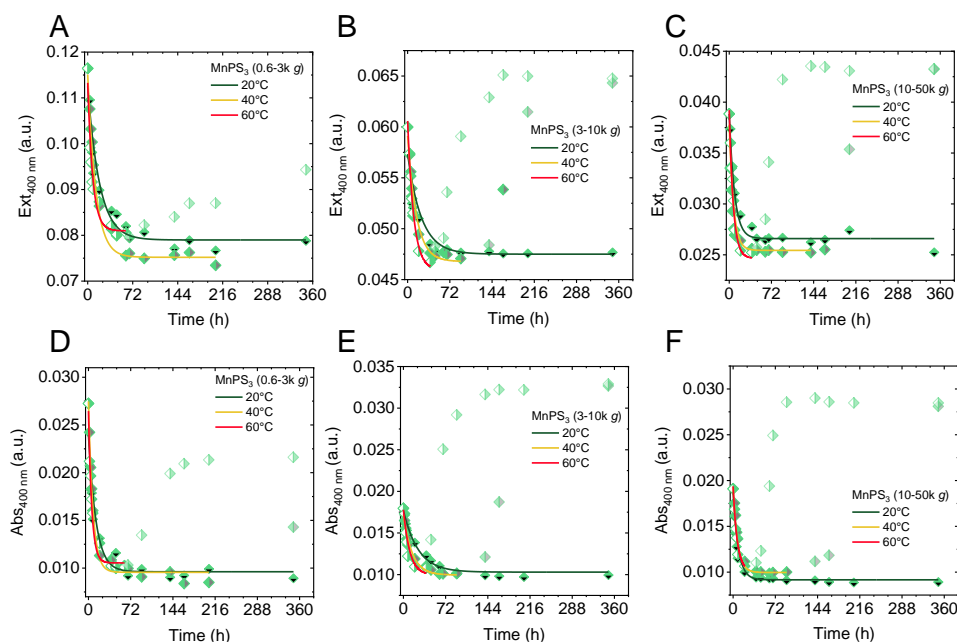
MnPS₃:

Figure A5.3-4.3: Degradation of MnPS₃ nanosheets. (A-F) Extinction (A-C) and absorption (D-F) at 400 nm of different fractions containing (from left to right) large (0.6-3k g), medium (3-10k g) and small (10-50k g) nanosheets stored at 20, 40 and 60°C, respectively as function of time. Solid lines are exponential fits to extract the degradation half-lives. Note, that no linearisation is observed for similar plots of the natural logarithm or the inverse optical density of MnPS₃.

5.3-5 Activation energy of MPS₃ nanosheets decomposition

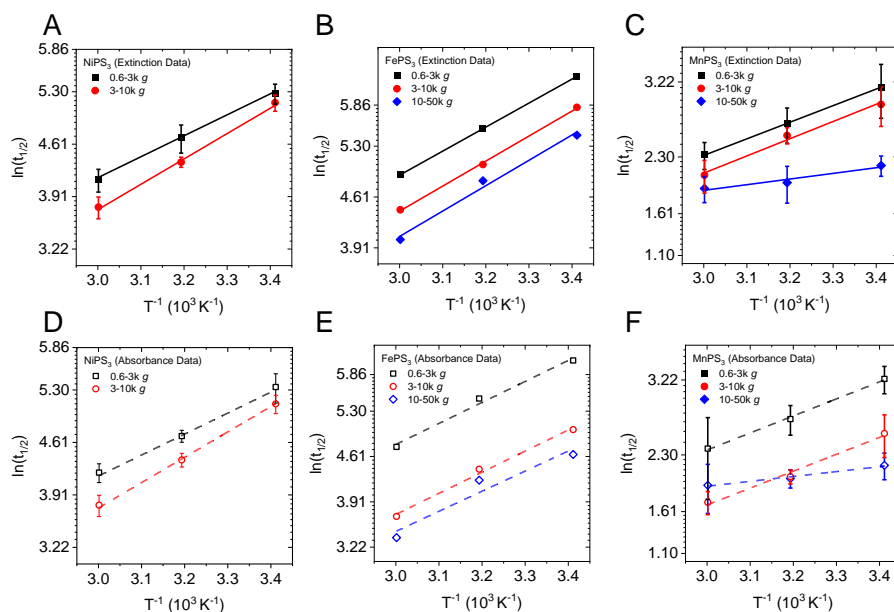


Figure A5.3-5.1: Arrhenius-type plots for the MPS₃ nanosheet degradation. (A-C) Plot of the half-lives from extinction measurements as a function of inverse temperature on a semi-ln scale for NiPS₃ (A), FePS₃ (B) and MnPS₃ (C), respectively. Lines are linear fits to approximate the activation energy of the degradation process. (D-F) Similar plots as in (A-C) for data extracted from absorbance measurements.

Chapter 8 – Appendix

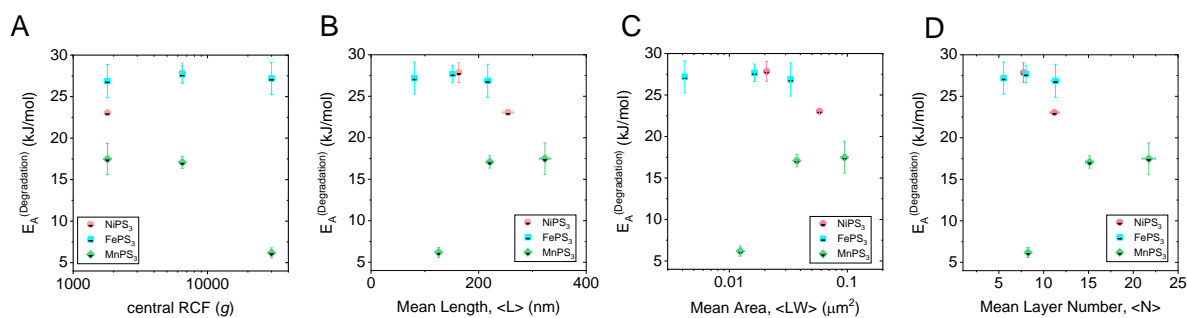


Figure A5.3-5.2: Size-dependence of the activation energy of NiPS₃, FePS₃ and MnPS₃ nanosheet decomposition. (A) Scaling of the activation energy with central centrifugal acceleration applied for material preparation. (B-D) Scaling of the activation energy with different average material dimensions: (B) Arithmetic mean length, $\langle L \rangle$ (C) arithmetic mean sheet area, $\langle LW \rangle$ and (D) arithmetic mean layer number, $\langle N \rangle$.

Appendix 5.4:

5.4-1 Evolution of UV-Vis spectra of α -RuCl₃ nanosheets at different temperatures

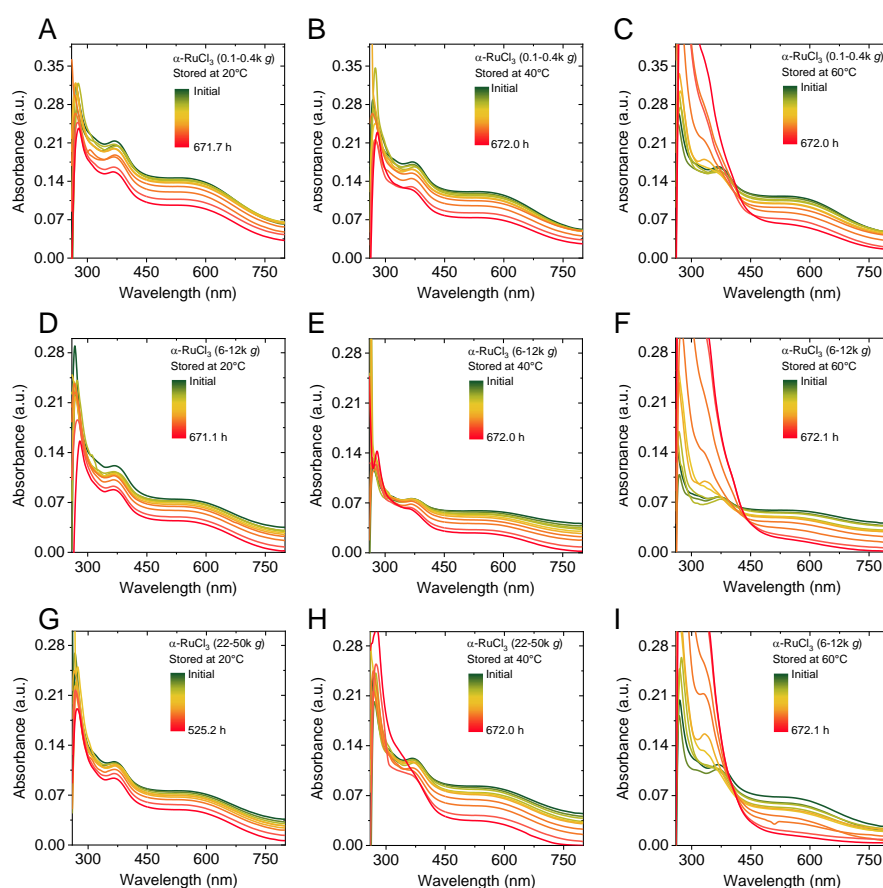


Figure A5.4-1: Absorbance of α -RuCl₃ nanosheets measured at different times and temperatures. The upper row (A-C) shows samples containing relatively large (0.1-0.4k g) nanosheets, the centre row (D-F) intermediate sized (6-12k g) and the lower row small-sized (22-50k g) nanosheets stored at 20, 40 and 60°C (from left to right), respectively. All spectra show changes over time. The optical density at 525 nm decreases in all cases systematically. The changes are more pronounced for elevated temperatures.

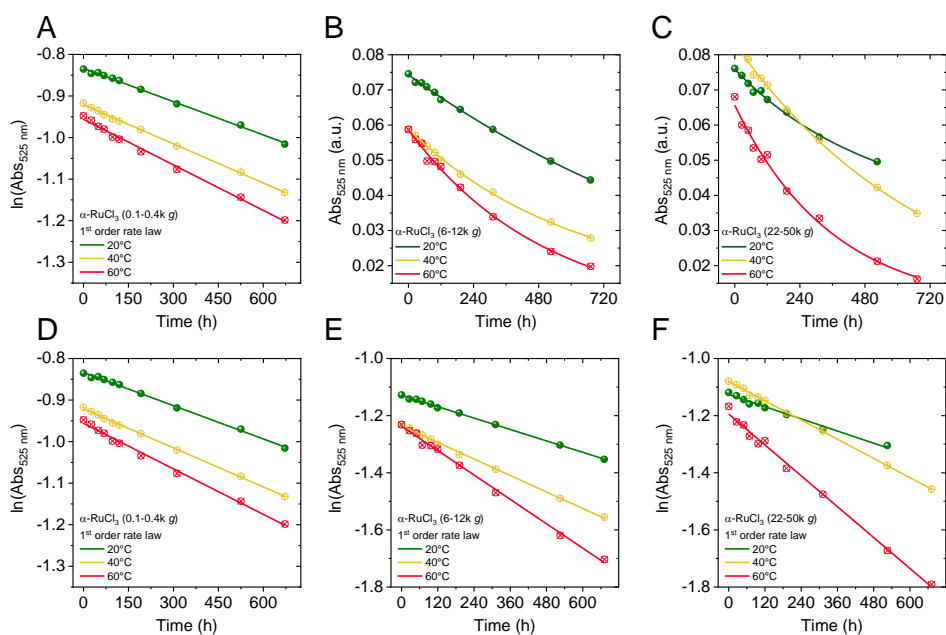
5.4-2 Decomposition of α -RuCl₃ nanosheets at different temperatures

Figure A5.4-2: Degradation of α -RuCl₃ nanosheets. (A-C) absorption at 525 nm of different fractions containing (from left to right) large (0.1-0.4k g), medium (6-12k g) and small (22-50k g) nanosheets stored at 20, 40 and 60°C, respectively as function of time. Solid lines are exponential fits for determination of the portion of reacted material. (D-F) Same data as in (A-C) plotted as natural logarithm of the absorption at 525 nm. Solid lines are linear fits to extract the degradation half-lives.

Appendix 5.5:

5.5-1 Evolution of UV-Vis spectra of CrTe₃ nanosheets

To account for nanosheet stability, extinction spectra of dispersions of size selected CrTe₃ nanosheets, stored in ambient conditions, were measured over time. Figure A5.5-1 shows the change of the extinction spectra of dispersions containing different sizes of nanosheets within one day.

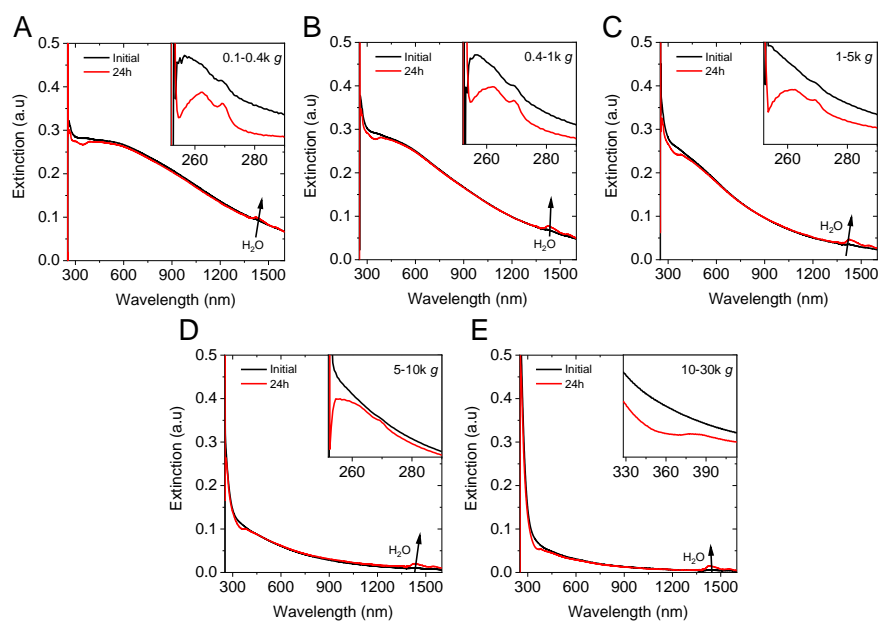


Figure A5.5-1: Extinction spectra of fresh and (1 day) aged CrTe₃ nanosheet dispersions. (A-E) UV-Vis measurements of dispersions containing different sizes of nanosheets (decreasing size and thickness from A→E) measured right after preparation and after aging 1 day under ambient conditions. In every case, additional features formed comparing the initial (black) to the aged (red) spectra. Two additional contributions arise between 250 and 280 nm for all nanosheet sizes. For the smallest nanosheets (E), an additional feature at ~385 nm develops. A water peak forms for all sizes as indicated by the black arrow.

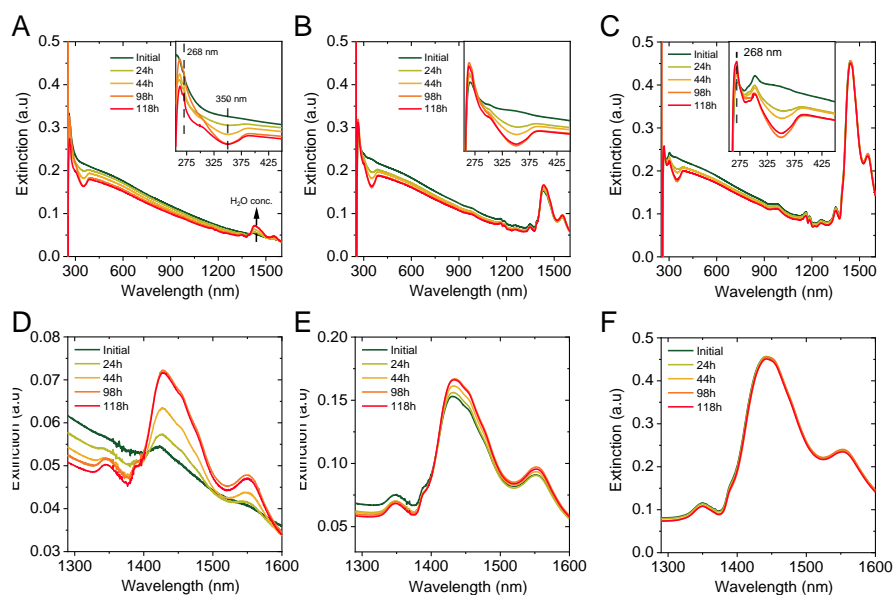
5.5-2 Role of water upon CrTe₃ nanosheet decomposition

Figure A5.5-2.1: Ageing of CrTe₃ nanosheet dispersions. (A) Extinction spectra of a freshly prepared stock dispersion of CrTe₃ nanosheets in CHP measured over time for storage in ambient conditions. The same development as shown for the size-selected samples (Figure A5.5-1:) can be observed. Additional features arise between 250 and 280 nm and a dip at 350 nm is formed. The water concentration is increasing over time as indicated by the black arrow. (B-C) Extinction spectra of the same dispersion as shown in (A) with different amounts of water added with the initial water concentration (from A → C) being 0, 3 and 10 vol%. The changes observed in (A) are apparent for the water titrated samples as well. (D-F) Zoom in to the water peak corresponding to the spectra shown in (A-C). The samples with an initial water concentration of 0 and 3 vol% (D and E) show a systematic increase of the water peak over time. The 10 vol% sample (F) shows only minor changes within the spectral range of the water peak.

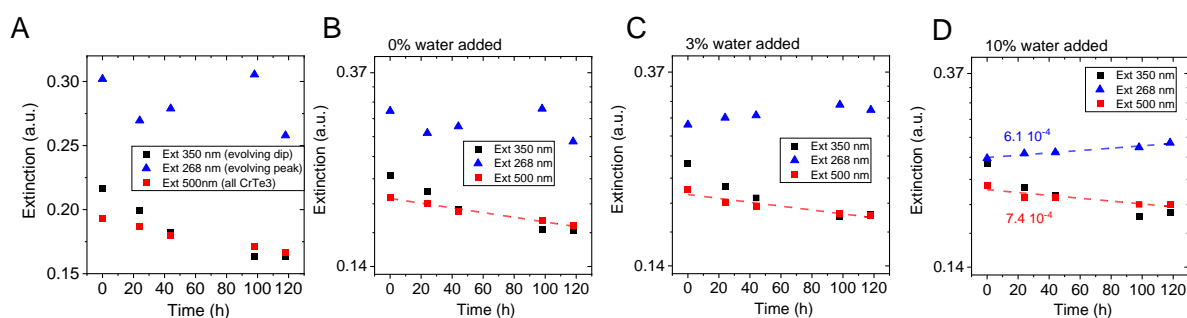


Figure A5.5-2.2: CrTe₃ degradation. (A) Change of the extinction intensities at 268, 350 and 500 nm followed over time for the initial CrTe₃ stock dispersion plotted on a linear scale. (B-D) The same wavelengths for samples of the same stock dispersion with 0, 3 and 10 vol% water added (from left to right) on a semi ln-scale. All samples show a linear decrease of the extinction at 500 nm which can be used to extract the decay time constant (assuming first order decay kinetics which are reasonable due to the observed linearization of the data on the semi-ln scale).

5.5-3 Relocalisation and remeasuring of nanosheets *via* AFM

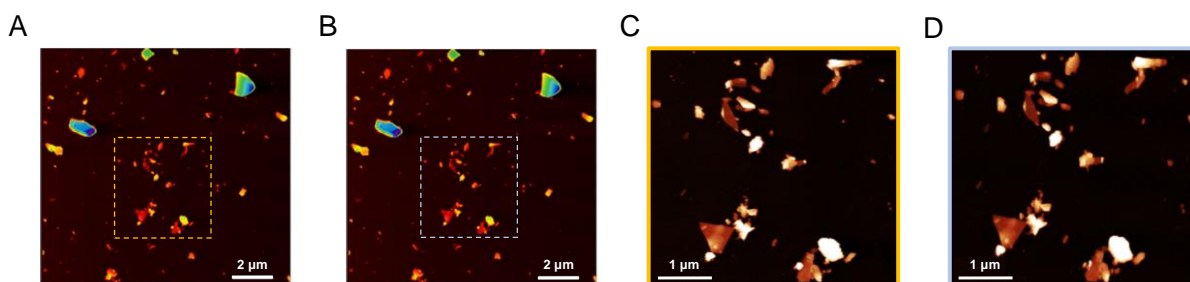


Figure A5.5-3: AFM images of a CrTe₃ stock sample. (A-B): Nanosheets recorded right after the exfoliation at different magnification. **(C-D):** The same nanosheets measured again after 2 days. No significant changes of the nanosheet morphology is observed within the time frame required for statistical AFM measurements.

9 Bibliography

1. Erogbogbo, F.; Lin, T.; Tucciarone, P. M.; LaJoie, K. M.; Lai, L.; Patki, G. D.; Prasad, P. N.; Swihart, M. T., On-Demand Hydrogen Generation using Nanosilicon: Splitting Water without Light, Heat, or Electricity. *Nano Letters* **2013**, *13* (2), 451-456.
2. Mikolajick, T.; Heinzig, A.; Trommer, J.; Pregl, S.; Grube, M.; Cuniberti, G.; Weber, W. M., Silicon nanowires – a versatile technology platform. *physica status solidi (RRL) – Rapid Research Letters* **2013**, *7* (10), 793-799.
3. Yang, Y.; Li, X., Giant piezoresistance of p-type nano-thick silicon induced by interface electron trapping instead of 2D quantum confinement. *Nanotechnology* **2010**, *22* (1), 015501.
4. Hernandez, Y.; Nicolosi, V.; Lotya, M.; Blighe, F. M.; Sun, Z.; De, S.; McGovern, I. T.; Holland, B.; Byrne, M.; Gun'Ko, Y. K.; Boland, J. J.; Niraj, P.; Duesberg, G.; Krishnamurthy, S.; Goodhue, R.; Hutchison, J.; Scardaci, V.; Ferrari, A. C.; Coleman, J. N., High-yield production of graphene by liquid-phase exfoliation of graphite. *Nature Nanotechnology* **2008**, *3* (9), 563-568.
5. Varrla, E.; Backes, C.; Paton, K. R.; Harvey, A.; Gholamvand, Z.; McCauley, J.; Coleman, J. N., Large-Scale Production of Size-Controlled MoS₂ Nanosheets by Shear Exfoliation. *Chemistry of Materials* **2015**, *27* (3), 1129–1139.
6. Paton, K. R.; Varrla, E.; Backes, C.; Smith, R. J.; Khan, U.; O'Neill, A.; Boland, C.; Lotya, M.; Istrate, O. M.; King, P.; Higgins, T.; Barwich, S.; May, P.; Puczkarski, P.; Ahmed, I.; Moebius, M.; Pettersson, H.; Long, E.; Coelho, J.; O'Brien, S. E.; McGuire, E. K.; Sanchez, B. M.; Duesberg, G. S.; McEvoy, N.; Pennycook, T. J.; Downing, C.; Crossley, A.; Nicolosi, V.; Coleman, J. N., Scalable production of large quantities of defect-free few-layer graphene by shear exfoliation in liquids. *Nat Mater* **2014**, *13* (6), 624-30.
7. Novoselov, K. S.; Geim, A. K.; Morozov, S. V.; Jiang, D.; Zhang, Y.; Dubonos, S. V.; Grigorieva, I. V.; Firsov, A. A., Electric Field Effect in Atomically Thin Carbon Films. *Science* **2004**, *306* (5696), 666-669.
8. Ueberricke, L.; Coleman, J. N.; Backes, C., Robustness of Size Selection and Spectroscopic Size, Thickness and Monolayer Metrics of Liquid-Exfoliated WS₂. *Phys. Status Solidi B* **2017**, *254* (11), 1700443.
9. Backes, C.; Hanlon, D.; Szydłowska, B. M.; Harvey, A.; Smith, R. J.; Higgins, T. M.; Coleman, J. N., Preparation of liquid-exfoliated transition metal dichalcogenide nanosheets with controlled size and thickness. *Journal of Visualised Experiments* **2016**, *118* (doi: 10.3791/54806).
10. Synnatschke, K.; Cieslik, P. A.; Harvey, A.; Castellanos-Gomez, A.; Tian, T.; Shih, C.-J.; Chernikov, A.; Santos, E. J. G.; Coleman, J. N.; Backes, C., Length and thickness dependent optical response of liquid-exfoliated transition metal dichalcogenides. *Chemistry of Materials* **2019**, *31* (24), 10049-10062.
11. Synnatschke, K.; Shao, S.; van Dinter, J.; Hofstetter, Y. J.; Kelly, D. J.; Grieger, S.; Haigh, S. J.; Vaynzof, Y.; Bensch, W.; Backes, C., Liquid exfoliation of Ni₂P₂S₆: Structural characterisation, size-dependent properties and degradation. *Chemistry of Materials* **2019**, *31* (21), 9127–9139.
12. Harvey, A.; Backes, C.; Gholamvand, Z.; Hanlon, D.; McAteer, D.; Nerl, H. C.; McGuire, E.; Seral-Ascaso, A.; Ramasse, Q. M.; McEvoy, N.; Winters, S.; Berner, N. C.; McCloskey, D.; Donegan, J.; Duesberg, G.; Nicolosi, V.; Coleman, J. N., Preparation of Gallium Sulfide Nanosheets

Chapter 9 – Literature

by Liquid Exfoliation and Their Application As Hydrogen Evolution Catalysts. *Chemistry of Materials* **2015**, 27 (9), 3483–3493.

13. John, B. B.; Andrew, H.; Ruiyuan, T.; Victor, V.-M.; Aideen, G.; Cian, G.; Madeleine, B.; Joshua, P.; Yanguang, L.; Jonathan, N. C., Liquid phase exfoliation of GeS nanosheets in ambient conditions for lithium ion battery applications. *2D Materials* **2020**.

14. Brent, J. R.; Lewis, D. J.; Lorenz, T.; Lewis, E. A.; Savjani, N.; Haigh, S. J.; Seifert, G.; Derby, B.; O'Brien, P., Tin(II) Sulfide (SnS) Nanosheets by Liquid-Phase Exfoliation of Herzenbergite: IV–VI Main Group Two-Dimensional Atomic Crystals. *Journal of the American Chemical Society* **2015**, 137 (39), 12689-12696.

15. Brent, J. R.; Savjani, N.; Lewis, E. A.; Haigh, S. J.; Lewis, D. J.; O'Brien, P., Production of few-layer phosphorene by liquid exfoliation of black phosphorus. *Chemical Communications* **2014**, 50 (87), 13338-13341.

16. Lin, S.; Chui, Y.; Li, Y.; Lau, S. P., Liquid-phase exfoliation of black phosphorus and its applications. *FlatChem* **2017**, 2, 15-37.

17. Gu, J.; Du, Z.; Zhang, C.; Ma, J.; Li, B.; Yang, S., Liquid-Phase Exfoliated Metallic Antimony Nanosheets toward High Volumetric Sodium Storage. *Advanced Energy Materials* **2017**, 7 (17), 1700447.

18. Stöter, M.; Rosenfeldt, S.; Breu, J., Tunable Exfoliation of Synthetic Clays. *Annual Review of Materials Research* **2015**, 45 (1), 129-151.

19. Wang, Y.; Zhang, Y.-Z.; Dubbink, D.; ten Elshof, J. E., Inkjet printing of δ -MnO₂ nanosheets for flexible solid-state micro-supercapacitor. *Nano Energy* **2018**, 49, 481-488.

20. Hanlon, D.; Backes, C.; Higgins, T. M.; Hughes, M.; O'Neill, A.; King, P.; McEvoy, N.; Duesberg, G. S.; Mendoza Sanchez, B.; Pettersson, H.; Nicolosi, V.; Coleman, J. N., Production of Molybdenum Trioxide Nanosheets by Liquid Exfoliation and Their Application in High-Performance Supercapacitors. *Chem. Mater.* **2014**, 26 (4), 1751-1763.

21. Harvey, A.; He, X.; Godwin, I. J.; Backes, C.; McAteer, D.; Berner, N. C.; McEvoy, N.; Ferguson, A.; Shmeliov, A.; Lyons, M. E. G.; Nicolosi, V.; Duesberg, G. S.; Donegan, J. F.; Coleman, J. N., Production of Ni(OH)₂ nanosheets by liquid phase exfoliation: from optical properties to electrochemical applications. *Journal of Materials Chemistry A* **2016**, 4 (28), 11046-11059.

22. Molina-Mendoza, A. J.; Giovanelli, E.; Paz, W. S.; Niño, M. A.; Island, J. O.; Evangeli, C.; Aballe, L.; Foerster, M.; van der Zant, H. S. J.; Rubio-Bollinger, G.; Agraït, N.; Palacios, J. J.; Pérez, E. M.; Castellanos-Gomez, A., Franckeite: a naturally occurring van der Waals heterostructure. *arXiv:1606.06651* **2016**.

23. Lange, R. Z.; Synnatschke, K.; Qi, H.; Huber, N.; Hofer, G.; Liang, B.; Huck, C.; Pucci, A.; Kaiser, U.; Backes, C.; Schlüter, A. D., Enriching and Quantifying Porous Single Layer 2D Polymers by Exfoliation of Chemically Modified van der Waals Crystals. *Angew. Chem. Int. Ed.* **2020**, 59, 5683–5695

24. Leubner, S.; Bengtsson, V. E. G.; Synnatschke, K.; Gosch, J.; Koch, A.; Reinsch, H.; Xu, H.; Backes, C.; Zou, X.; Stock, N., Synthesis and Exfoliation of a New Layered Mesoporous Zr-MOF Comprising Hexa- and Dodecanuclear Clusters as Well as a Small Organic Linker Molecule. *Journal of the American Chemical Society* **2020**, 142 (37), 15995-16000.

25. Bonaccorso, F.; Bartolotta, A.; Coleman, J. N.; Backes, C., 2D-Crystal-Based Functional Inks. *Advanced Materials* **2016**, 28 (29), 6136-6166.

26. Yi, M.; Shen, Z., Kitchen blender for producing high-quality few-layer graphene. *Carbon* **2014**, *78*, 622-626.
27. Varrla, E.; Paton, K. R.; Backes, C.; Harvey, A.; Smith, R. J.; McCauley, J.; Coleman, J. N., Turbulence-assisted shear exfoliation of graphene using household detergent and a kitchen blender. *Nanoscale* **2014**, *6*, 11810-11819.
28. Liu, L.; Shen, Z.; Yi, M.; Zhang, X.; Ma, S., A green, rapid and size-controlled production of high-quality graphene sheets by hydrodynamic forces. *RSC Advances* **2014**, *4* (69), 36464-36470.
29. Paton, K. R.; Varrla, E.; Backes, C.; Smith, R. J.; Khan, U.; O'Neill, A.; Boland, C.; Lotya, M.; Istrate, O. M.; King, P.; Higgins, T.; Barwich, S.; May, P.; Puczkarski, P.; Ahmed, I.; Moebius, M.; Pettersson, H.; Long, E.; Coelho, J.; O'Brien, S. E.; McGuire, E. K.; Sanchez, B. M.; Duesberg, G. S.; McEvoy, N.; Pennycook, T. J.; Downing, C.; Crossley, A.; Nicolosi, V.; Coleman, J. N., Scalable production of large quantities of defect-free few-layer graphene by shear exfoliation in liquids. *Nature Materials* **2014**, *13* (6), 624-630.
30. Furtado, C. A.; Kim, U. J.; Gutierrez, H. R.; Pan, L.; Dickey, E. C.; Eklund, P. C., Debundling and Dissolution of Single-Walled Carbon Nanotubes in Amide Solvents. *Journal of the American Chemical Society* **2004**, *126* (19), 6095-6105.
31. Hilding, J.; Grulke, E. A.; George Zhang, Z.; Lockwood, F., Dispersion of Carbon Nanotubes in Liquids. *Journal of Dispersion Science and Technology* **2003**, *24* (1), 1-41.
32. Utomo, A. T.; Baker, M.; Pacek, A. W., Flow pattern, periodicity and energy dissipation in a batch rotor–stator mixer. *Chemical Engineering Research and Design* **2008**, *86* (12), 1397-1409.
33. Bicca, S.; Barwich, S.; Boland, D.; Harvey, A.; Hanlon, D.; McEvoy, N.; Coleman, J. N., Exfoliation of 2D materials by high shear mixing. *2D Materials* **2018**, *6* (1), 015008.
34. Graf, A.; Zakharko, Y.; Schießl, S. P.; Backes, C.; Pfohl, M.; Flavel, B. S.; Zaumseil, J., Large scale, selective dispersion of long single-walled carbon nanotubes with high photoluminescence quantum yield by shear force mixing. *Carbon* **2016**, *105*, 593-599.
35. Hall, S.; Cooke, M.; Pacek, A. W.; Kowalski, A. J.; Rothman, D., Scaling up of silverson rotor–stator mixers. *The Canadian Journal of Chemical Engineering* **2011**, *89* (5), 1040-1050.
36. Karagiannidis, P. G.; Hodge, S. A.; Lombardi, L.; Tomarchio, F.; Decorde, N.; Milana, S.; Goykhman, I.; Su, Y.; Mesite, S. V.; Johnstone, D. N.; Leary, R. K.; Midgley, P. A.; Pugno, N. M.; Torrisi, F.; Ferrari, A. C., Microfluidization of Graphite and Formulation of Graphene-Based Conductive Inks. *ACS Nano* **2017**, *11* (3), 2742–2755.
37. Yi, M.; Li, J.; Shen, Z.; Zhang, X.; Ma, S., Morphology and structure of mono- and few-layer graphene produced by jet cavitation. *Applied Physics Letters* **2011**, *99* (12), 123112.
38. Rizvi, R.; Nguyen, E. P.; Kowal, M. D.; Mak, W. H.; Rasel, S.; Islam, M. A.; Abdelaal, A.; Joshi, A. S.; Zekriardehani, S.; Coleman, M. R.; Kaner, R. B., High-Throughput Continuous Production of Shear-Exfoliated 2D Layered Materials using Compressible Flows. *Advanced Materials* **2018**, *30* (30), 1800200.
39. Gutiérrez, M.; Henglein, A., Preparation of colloidal semiconductor solutions of MoS₂ and WSe₂ via sonication. *Ultrasonics* **1989**, *27* (5), 259-261.
40. Liu, W.-W.; Xia, B.-Y.; Wang, X.-X.; Wang, J.-N., Exfoliation and dispersion of graphene in ethanol-water mixtures. *Frontiers of Materials Science* **2012**, *6* (2), 176-182.
41. Halim, U.; Zheng, C. R.; Chen, Y.; Lin, Z.; Jiang, S.; Cheng, R.; Huang, Y.; Duan, X., A rational design of cosolvent exfoliation of layered materials by directly probing liquid–solid interaction. *Nature Communications* **2013**, *4* (1), 2213.

Chapter 9 – Literature

42. Alzakia, F. I.; Sun, W.; Pennycook, S. J.; Tan, S. C., Introducing Normalized Centrifugation for a More Accurate Thermodynamic Analysis of Molybdenum Disulfide Dispersions: A Study on Mixed Solvents of Alcohols and Amines with Water. *ACS Applied Materials & Interfaces* **2020**, *12* (2), 3096-3103.
43. Liang, K.-Y.; Yang, W.-D., Influence of ternary hydroalcoholic solvent on direct exfoliation concentration of graphite. *AIP Advances* **2018**, *8* (6), 065119.
44. Adilbekova, B.; Lin, Y.; Yengel, E.; Faber, H.; Harrison, G.; Firdaus, Y.; El-Labban, A.; Anjum, D. H.; Tung, V.; Anthopoulos, T. D., Liquid phase exfoliation of MoS₂ and WS₂ in aqueous ammonia and their application in highly efficient organic solar cells. *Journal of Materials Chemistry C* **2020**, *8* (15), 5259-5264.
45. Li, Z.; Young, R. J.; Backes, C.; Zhao, W.; Zhang, X.; Zhukov, A.; Tillotson, E.; Conlan, A. P.; Ding, F.; Haigh, S. J.; Novoselov, K. S.; Coleman, J. N., Mechanisms of Liquid-Phase Exfoliation for the Production of Graphene. *ACS Nano* **2020**, doi:10.1021/acsnano.0c03916.
46. Ji, L.-J.; Qin, Y.; Gui, D.; Li, W.; Li, Y.; Li, X.; Lu, P., Quantifying the Exfoliation Ease Level of 2D Materials via Mechanical Anisotropy. *Chemistry of Materials* **2018**, *30* (24), 8732-8738.
47. Backes, C.; Campi, D.; Szydłowska, B. M.; Synnatschke, K.; Ojala, E.; Rashvand, F.; Harvey, A.; Griffin, A.; Sofer, Z.; Marzari, N.; Coleman, J. N.; O'Regan, D. D., Equipartition of Energy Defines the Size–Thickness Relationship in Liquid-Exfoliated Nanosheets. *ACS Nano* **2019**, *13* (6), 7050-7061.
48. Backes, C.; Smith, R. J.; McEvoy, N.; Berner, N. C.; McCloskey, D.; Nerl, H. C.; O'Neill, A.; King, P. J.; Higgins, T.; Hanlon, D.; Scheuschner, N.; Maultzsch, J.; Houben, L.; Duesberg, G. S.; Donegan, J. F.; Nicolosi, V.; Coleman, J. N., Edge and Confinement Effects Allow in situ Measurement of Size and Thickness of Liquid-Exfoliated Nanosheets. *Nature Communications* **2014**, *5*, 4576.
49. Ott, S.; Wolff, N.; Rashvand, F.; Rao, V. J.; Zaumseil, J.; Backes, C., Impact of the MoS₂ Starting Material on the Dispersion Quality and Quantity after Liquid Phase Exfoliation. *Chemistry of Materials* **2019**, *31* (20), 8424-8431.
50. Cunningham, G.; Lotya, M.; Cucinotta, C. S.; Sanvito, S.; Bergin, S. D.; Menzel, R.; Shaffer, M. S. P.; Coleman, J. N., Solvent Exfoliation of Transition Metal Dichalcogenides: Dispersibility of Exfoliated Nanosheets Varies Only Weakly between Compounds. *ACS Nano* **2012**, *6* (4), 3468-3480.
51. Ferguson, A.; Caffrey, I. T.; Backes, C.; Coleman, J. N.; Bergin, S. D., Differentiating Defect and Basal Plane Contributions to the Surface Energy of Graphite Using Inverse Gas Chromatography. *Chemistry of Materials* **2016**, *28* (17), 6355-6366.
52. Auren, F.; Andrew, H.; Ian, J. G.; Shane, D. B.; Jonathan, N. C., The dependence of the measured surface energy of graphene on nanosheet size. *2D Materials* **2017**, *4* (1), 015040.
53. Hughes, J. M.; Aherne, D.; Coleman, J. N., Generalizing solubility parameter theory to apply to one- and two-dimensional solutes and to incorporate dipolar interactions. *Journal of Applied Polymer Science* **2013**, *127* (6), 4483-4491.
54. Marguerite Hughes, J.; Aherne, D.; Bergin, S. D.; O'Neill, A.; Streich, P. V.; Hamilton, J. P.; Coleman, J. N., Using solution thermodynamics to describe the dispersion of rod-like solutes: application to dispersions of carbon nanotubes in organic solvents. *Nanotechnology* **2012**, *23* (26), 265604.

55. Lyklema, J., The surface tension of pure liquids. Thermodynamic components and corresponding states. *Colloids and Surfaces. A: Physicochemical and Engineering Aspects* **1999**, *156*, 413-421.
56. Tsierkezos, N. G.; Filippou, A. C., Thermodynamic investigation of N,N-dimethylformamide/toluene binary mixtures in the temperature range from 278.15 to 293.15K. *The Journal of Chemical Thermodynamics* **2006**, *38* (8), 952-961.
57. Hansen, C. M., *The three dimensional solubility parameter and solvent diffusion coefficient : Their importance in surface coating formulation*. Danish Technical Press: Cph, 1967.
58. Hernandez, Y.; Lotya, M.; Rickard, D.; Bergin, S. D.; Coleman, J. N., Measurement of Multicomponent Solubility Parameters for Graphene Facilitates Solvent Discovery. *Langmuir* **2010**, *26* (5), 3208-3213.
59. Lotya, M.; Hernandez, Y.; King, P. J.; Smith, R. J.; Nicolosi, V.; Karlsson, L. S.; Blighe, F. M.; De, S.; Wang, Z.; McGovern, I. T.; Duesberg, G. S.; Coleman, J. N., Liquid Phase Production of Graphene by Exfoliation of Graphite in Surfactant/Water Solutions. *Journal of the American Chemical Society* **2009**, *131* (10), 3611-3620.
60. Lotya, M.; King, P. J.; Khan, U.; De, S.; Coleman, J. N., High-Concentration, Surfactant-Stabilized Graphene Dispersions. *ACS Nano* **2010**, *4* (6), 3155-3162.
61. Smith, R. J.; Lotya, M.; Coleman, J. N., The importance of repulsive potential barriers for the dispersion of graphene using surfactants. *New Journal of Physics* **2010**, *12*, 125008.
62. Vera-López, S.; Martínez, P.; San Andrés, M. P.; Díez-Pascual, A. M.; Valiente, M., Study of graphene dispersions in sodium dodecylsulfate by steady-state fluorescence of pyrene. *Journal of Colloid and Interface Science* **2018**, *514*, 415-424.
63. Vega-Mayoral, V.; Backes, C.; Hanlon, D.; Khan, U.; Gholamvand, Z.; O'Brien, M.; Duesberg, G. S.; Gadermaier, C.; Coleman, J. N., Photoluminescence from Liquid-Exfoliated WS₂ Monomers in Poly(Vinyl Alcohol) Polymer Composites. *Advanced Functional Materials* **2016**, *26* (7), 1028-1039.
64. Lin, C.-A. J.; Sperling, R. A.; Li, J. K.; Yang, T.-Y.; Li, P.-Y.; Zanella, M.; Chang, W. H.; Parak, W. J., Design of an Amphiphilic Polymer for Nanoparticle Coating and Functionalization. *Small* **2008**, *4* (3), 334-341.
65. Backes, C.; Hauke, F.; Hirsch, A., The Potential of Perylene Bisimide Derivatives for the Solubilization of Carbon Nanotubes and Graphene. *Advanced Materials* **2011**, *23* (22-23), 2588-2601.
66. Griffin, A.; Nisi, K.; Pepper, J.; Harvey, A.; Szydłowska, B. M.; Coleman, J. N.; Backes, C., Effect of Surfactant Choice and Concentration on the Dimensions and Yield of Liquid-Phase-Exfoliated Nanosheets. *Chemistry of Materials* **2020**, *32* (7), 2852-2862.
67. Smith, R. J.; King, P. J.; Lotya, M.; Wirtz, C.; Khan, U.; De, S.; O'Neill, A.; Duesberg, G. S.; Grunlan, J. C.; Moriarty, G.; Chen, J.; Wang, J.; Minett, A. I.; Nicolosi, V.; Coleman, J. N., Large-Scale Exfoliation of Inorganic Layered Compounds in Aqueous Surfactant Solutions. *Advanced Materials* **2011**, *23* (34), 3944-3948.
68. Najiminaini, M., Optical resonance transmission properties of nano-hole arrays in a gold film: effect of adhesion layer *Optics Express* **2011**, *19* (27), 11.
69. Svedberg, T.; Nichols, J. B., Determination of size and distribution of size of particles by centrifugal methods. *Journal of the American Chemical Society* **1923**, *45* (12), 2910-2917.
70. Backes, C.; Paton, K. R.; Hanlon, D.; Yuan, S.; Katsnelson, M. I.; Houston, J.; Smith, R. J.; McCloskey, D.; Donegan, J. F.; Coleman, J. N., Spectroscopic metrics allow in situ measurement

Chapter 9 – Literature

of mean size and thickness of liquid-exfoliated few-layer graphene nanosheets. *Nanoscale* **2016**, *8* (7), 4311-4323.

71. Backes, C.; Szydłowska, B. M.; Harvey, A.; Yuan, S.; Vega-Mayoral, V.; Davies, B. R.; Zhao, P.-l.; Hanlon, D.; Santos, E. J. G.; Katsnelson, M. I.; Blau, W. J.; Gadermaier, C.; Coleman, J. N., Production of Highly Monolayer Enriched Dispersions of Liquid-Exfoliated Nanosheets by Liquid Cascade Centrifugation. *ACS Nano* **2016**, *10* (1), 1589-1601.

72. Griffin, A.; Harvey, A.; Cunningham, B.; Scullion, D.; Tian, T.; Shih, C.-J.; Gruening, M.; Donegan, J. F.; Santos, E. J. G.; Backes, C.; Coleman, J. N., Spectroscopic Size and Thickness Metrics for Liquid-Exfoliated h-BN. *Chemistry of Materials* **2018**, *30* (6), 1998-2005.

73. Harvey, A.; Backes, C.; Boland, J. B.; He, X.; Griffin, A.; Szydłowska, B.; Gabbett, C.; Donegan, J. F.; Coleman, J. N., Non-resonant light scattering in dispersions of 2D nanosheets. *Nature Communications* **2018**, *9* (1), 4553.

74. Boland, J. B.; Harvey, A.; Tian, R.; Hanlon, D.; Vega-Mayoral, V.; Szydłowska, B. M.; Griffin, A.; Stimpel-Lindner, T.; Metel, S.; Nicolosi, V.; Duesberg, G.; Coleman, J. N., Liquid phase exfoliation of MoO₂ nanosheets for lithium ion battery applications. *Nanoscale Advances* **2019**, 1560-1570.

75. Hanlon, D.; Backes, C.; Doherty, E.; Cucinotta, C. S.; Berner, N. C.; Boland, C.; Lee, K.; Lynch, P.; Gholamvand, Z.; Harvey, A.; Zhang, S.; Wang, K.; Moynihan, G.; Pokle, A.; Ramasse, Q. M.; McEvoy, N.; Blau, W. J.; Wang, J.; Abellan, G.; Hauke, F.; Hirsch, A.; Sanvito, S.; O'Regan, D. D.; Duesberg, G. S.; Nicolosi, V.; Coleman, J. N., Liquid Exfoliation of Solvent-Stabilised Few-Layer Black Phosphorus for Applications Beyond Electronics. *Nature Communications* **2015**, *6*, 8563.

76. Hu, G.; Kang, J.; Ng, L. W. T.; Zhu, X.; Howe, R. C. T.; Jones, C. G.; Hersam, M. C.; Hasan, T., Functional inks and printing of two-dimensional materials. *Chemical Society Reviews* **2018**, *47* (9), 3265-3300.

77. Choi, J.-Y.; Alford, T. L.; Honsberg, C. B., Solvent-Controlled Spin-Coating Method for Large-Scale Area Deposition of Two-Dimensional Silica Nanosphere Assembled Layers. *Langmuir* **2014**, *30* (20), 5732-5738.

78. Backes, C.; Szydłowska, B. M.; Harvey, A.; Yuan, S.; Vega-Mayoral, V.; Davies, B. R.; Zhao, P. L.; Hanlon, D.; Santos, E. J.; Katsnelson, M. I.; Blau, W. J.; Gadermaier, C.; Coleman, J. N., Production of Highly Monolayer Enriched Dispersions of Liquid-Exfoliated Nanosheets by Liquid Cascade Centrifugation. *ACS Nano* **2016**, *10* (1), 1589-601.

79. Meselson, M.; Stahl, F. W.; Vinograd, J., Equilibrium sedimentation of macromolecules in density gradients. *Proceedings of the National Academy of Sciences* **1957**, *43* (7), 581.

80. Piazza, R.; Buzzaccaro, S.; Secchi, E.; Parola, A., On the general concept of buoyancy in sedimentation and ultracentrifugation. *Physical Biology* **2013**, *10* (4), 045005.

81. Kuang, Y.; Song, S.; Huang, J.; Sun, X., Separation of colloidal two dimensional materials by density gradient ultracentrifugation. *Journal of Solid State Chemistry* **2015**, *224*, 120-126.

82. Green, A. A.; Hersam, M. C., Solution Phase Production of Graphene with Controlled Thickness via Density Differentiation. *Nano Letters* **2009**, *9* (12), 4031-4036.

83. Zhu, J.; Kang, J.; Kang, J.; Jariwala, D.; Wood, J. D.; Seo, J.-W. T.; Chen, K.-S.; Marks, T. J.; Hersam, M. C., Solution-Processed Dielectrics Based on Thickness-Sorted Two-Dimensional Hexagonal Boron Nitride Nanosheets. *Nano Letters* **2015**, *15* (10), 7029-7036.

84. Kang, J.; Seo, J.-W. T.; Alducin, D.; Ponce, A.; Yacaman, M. J.; Hersam, M. C., Thickness sorting of two-dimensional transition metal dichalcogenides via copolymer-assisted density gradient ultracentrifugation. *Nat Commun* **2014**, *5*, 5478.
85. Kang, J.; Sangwan, V. K.; Wood, J. D.; Liu, X.; Balla, I.; Lam, D.; Hersam, M. C., Layer-by-Layer Sorting of Rhenium Disulfide via High-Density Isopycnic Density Gradient Ultracentrifugation. *Nano Letters* **2016**, *16* (11), 7216-7223.
86. Andrievski, R. A.; Glezer, A. M., Size effects in properties of nanomaterials. *Scripta Materialia* **2001**, *44* (8), 1621-1624.
87. Geim, A. K.; Novoselov, K. S., The rise of graphene. *Nature Materials* **2007**, *6* (3), 183-191.
88. Novoselov, K. S.; Geim, A. K.; Morozov, S. V.; Jiang, D.; Katsnelson, M. I.; Grigorieva, I. V.; Dubonos, S. V.; Firsov, A. A., Two-dimensional gas of massless Dirac fermions in graphene. *Nature* **2005**, *438* (7065), 197-200.
89. Pisana, S.; Lazzeri, M.; Casiraghi, C.; Novoselov, K. S.; Geim, A. K.; Ferrari, A. C.; Mauri, F., Breakdown of the adiabatic Born–Oppenheimer approximation in graphene. *Nature Materials* **2007**, *6* (3), 198-201.
90. Jiang, Z.; Zhang, Y.; Tan, Y. W.; Stormer, H. L.; Kim, P., Quantum Hall effect in graphene. *Solid State Communications* **2007**, *143* (1), 14-19.
91. Splendiani, A.; Sun, L.; Zhang, Y.; Li, T.; Kim, J.; Chim, C.-Y.; Galli, G.; Wang, F., Emerging Photoluminescence in Monolayer MoS₂. *Nano Letters* **2010**, *10* (4), 1271-1275.
92. Mak, K. F.; Lee, C.; Hone, J.; Shan, J.; Heinz, T. F., Atomically Thin MoS₂: A New Direct-Gap Semiconductor. *Physical Review Letters* **2010**, *105* (13), 136805.
93. Zhou, Q.; Chen, Q.; Tong, Y.; Wang, J., Light-Induced Ambient Degradation of Few-Layer Black Phosphorus: Mechanism and Protection. *Angewandte Chemie International Edition* **2016**, *55* (38), 11437-11441.
94. Velický, M.; Toth, P. S., From two-dimensional materials to their heterostructures: An electrochemist's perspective. *Applied Materials Today* **2017**, *8*, 68-103.
95. Li, Y.; Zhou, Z.; Zhang, S.; Chen, Z., MoS₂ Nanoribbons: High Stability and Unusual Electronic and Magnetic Properties. *Journal of the American Chemical Society* **2008**, *130* (49), 16739-16744.
96. Ratoi, M.; Niste, V. B.; Walker, J.; Zekonyte, J., Mechanism of Action of WS₂ Lubricant Nanoadditives in High-Pressure Contacts. *Tribology Letters* **2013**, *52* (1), 81-91.
97. Kim, J.; Kwon, S.; Cho, D.-H.; Kang, B.; Kwon, H.; Kim, Y.; Park, S. O.; Jung, G. Y.; Shin, E.; Kim, W.-G.; Lee, H.; Ryu, G. H.; Choi, M.; Kim, T. H.; Oh, J.; Park, S.; Kwak, S. K.; Yoon, S. W.; Byun, D.; Lee, Z.; Lee, C., Direct exfoliation and dispersion of two-dimensional materials in pure water via temperature control. *Nature Communications* **2015**, *6*, 9294.
98. Petó, J.; Ollár, T.; Vancsó, P.; Popov, Z. I.; Magda, G. Z.; Dobrik, G.; Hwang, C.; Sorokin, P. B.; Tapasztó, L., Spontaneous doping of the basal plane of MoS₂ single layers through oxygen substitution under ambient conditions. *Nature Chemistry* **2018**, *10* (12), 1246-1251.
99. Churchill, H. O. H.; Jarillo-Herrero, P., Phosphorus joins the family. *Nature Nanotechnology* **2014**, *9* (5), 330-331.
100. Gibaja, C.; Rodriguez-San-Miguel, D.; Ares, P.; Gómez-Herrero, J.; Varela, M.; Gillen, R.; Maultzsch, J.; Hauke, F.; Hirsch, A.; Abellán, G.; Zamora, F., Few-Layer Antimonene by Liquid-Phase Exfoliation. *Angewandte Chemie International Edition* **2016**, *55* (46), 14345-14349.
101. Klein, D. R.; MacNeill, D.; Lado, J. L.; Soriano, D.; Navarro-Moratalla, E.; Watanabe, K.; Taniguchi, T.; Manni, S.; Canfield, P.; Fernández-Rossier, J.; Jarillo-Herrero, P., Probing

Chapter 9 – Literature

magnetism in 2D van der Waals crystalline insulators via electron tunneling. *Science* **2018**, *360* (6394), 1218.

102. Weber, D.; Schoop, L. M.; Duppel, V.; Lippmann, J. M.; Nuss, J.; Lotsch, B. V., Magnetic Properties of Restacked 2D Spin 1/2 honeycomb RuCl₃ Nanosheets. *Nano Letters* **2016**, *16* (6), 3578-3584.

103. Mayorga-Martinez, C. C.; Sofer, Z.; Sedmidubský, D.; Huber, Š.; Eng, A. Y. S.; Pumera, M., Layered Metal Thiophosphite Materials: Magnetic, Electrochemical, and Electronic Properties. *ACS Applied Materials & Interfaces* **2017**, *9* (14), 12563-12573.

104. Island, J. O.; Steele, G. A.; Zant, H. S. J. v. d.; Castellanos-Gomez, A., Environmental instability of few-layer black phosphorus. *2D Materials* **2015**, *2* (1), 011002.

105. Grasseschi, D.; Bahamon, D. A.; Maia, F. C. B.; Neto, A. H. C.; Freitas, R. O.; de Matos, C. J. S., Oxygen impact on the electronic and vibrational properties of black phosphorus probed by synchrotron infrared nanospectroscopy. *2D Materials* **2017**, *4* (3), 035028.

106. Huang, Y.; Qiao, J.; He, K.; Bliznakov, S.; Sutter, E.; Chen, X.; Luo, D.; Meng, F.; Su, D.; Decker, J.; Ji, W.; Ruoff, R. S.; Sutter, P., Interaction of Black Phosphorus with Oxygen and Water. *Chemistry of Materials* **2016**, *28* (22), 8330-8339.

107. Abellán, G.; Lloret, V.; Mundloch, U.; Marcia, M.; Neiss, C.; Görling, A.; Varela, M.; Hauke, F.; Hirsch, A., Noncovalent Functionalization of Black Phosphorus. *Angewandte Chemie International Edition* **2016**, *55* (47), 14557-14562.

108. Geim, A. K.; Grigorieva, I. V., Van der Waals heterostructures. *Nature* **2013**, *499* (7459), 419-425.

109. Cai, Y.; Zhang, G.; Zhang, Y.-W., Electronic Properties of Phosphorene/Graphene and Phosphorene/Hexagonal Boron Nitride Heterostructures. *The Journal of Physical Chemistry C* **2015**, *119* (24), 13929-13936.

110. Kotsakidis, J. C.; Zhang, Q.; Vazquez de Parga, A. L.; Currie, M.; Helmerson, K.; Gaskill, D. K.; Fuhrer, M. S., Oxidation of Monolayer WS₂ in Ambient Is a Photoinduced Process. *Nano Letters* **2019**, *19* (8), 5205-5215.

111. Withers, F.; Del Pozo-Zamudio, O.; Mishchenko, A.; Rooney, A. P.; Gholinia, A.; Watanabe, K.; Taniguchi, T.; Haigh, S. J.; Geim, A. K.; Tartakovskii, A. I.; Novoselov, K. S., Light-emitting diodes by band-structure engineering in van der Waals heterostructures. *Nature Materials* **2015**, *14* (3), 301-306.

112. Bafaqeer, A.; Tahir, M.; Amin, N. A. S., Synergistic effects of 2D/2D ZnV₂O₆/RGO nanosheets heterojunction for stable and high performance photo-induced CO₂ reduction to solar fuels. *Chemical Engineering Journal* **2018**, *334*, 2142-2153.

113. Wu, F.; Li, Q.; Wang, P.; Xia, H.; Wang, Z.; Wang, Y.; Luo, M.; Chen, L.; Chen, F.; Miao, J.; Chen, X.; Lu, W.; Shan, C.; Pan, A.; Wu, X.; Ren, W.; Jariwala, D.; Hu, W., High efficiency and fast van der Waals hetero-photodiodes with a unilateral depletion region. *Nature Communications* **2019**, *10* (1), 4663.

114. Xia, M.; Yan, X.; Li, H.; Wells, N.; Yang, G., Well-designed efficient charge separation in 2D/2D N doped La₂Ti₂O₇/ZnIn₂S₄ heterojunction through band structure/morphology regulation synergistic effect. *Nano Energy* **2020**, *78*, 105401.

115. Mak, K. F.; Lee, C.; Hone, J.; Shan, J.; Heinz, T. F., Atomically Thin MoS₂: A New Direct-Gap Semiconductor. *Phys. Rev. Lett.* **2010**, *105* (13).

116. Ross, J. S.; Klement, P.; Jones, A. M.; Ghimire, N. J.; Yan, J. Q.; Mandrus, D. G.; Taniguchi, T.; Watanabe, K.; Kitamura, K.; Yao, W.; Cobden, D. H.; Xu, X. D., Electrically tunable

- excitonic light-emitting diodes based on monolayer WSe₂ p-n junctions. *Nature Nanotechnology* **2014**, *9* (4), 268-272.
117. Amani, M.; Lien, D. H.; Kiriya, D.; Xiao, J.; Azcatl, A.; Noh, J.; Madhvapathy, S. R.; Addou, R.; Santosh, K. C.; Dubey, M.; Cho, K.; Wallace, R. M.; Lee, S. C.; He, J. H.; Ager, J. W.; Zhang, X.; Yablonovitch, E.; Javey, A., Near-unity photoluminescence quantum yield in MoS₂. *Science* **2015**, *350* (6264), 1065-1068.
118. Niu, Y.; Gonzalez-Abad, S.; Frisenda, R.; Marauhn, P.; Drüppel, M.; Gant, P.; Schmidt, R.; Taghavi, N.; Barcons, D.; Molina-Mendoza, A.; de Vasconcellos, S.; Bratschitsch, R.; Perez De Lara, D.; Rohlfing, M.; Castellanos-Gomez, A., Thickness-Dependent Differential Reflectance Spectra of Monolayer and Few-Layer MoS₂, MoSe₂, WS₂ and WSe₂. *Nanomaterials* **2018**, *8* (9), 725.
119. Tonndorf, P.; Schmidt, R.; Böttger, P.; Zhang, X.; Börner, J.; Liebig, A.; Albrecht, M.; Kloc, C.; Gordan, O.; Zahn, D. R. T.; Michaelis de Vasconcellos, S.; Bratschitsch, R., Photoluminescence emission and Raman response of monolayer MoS₂, MoSe₂, and WSe₂. *Opt. Express* **2013**, *21* (4), 4908-4916.
120. Zhao, W. J.; Ghorannevis, Z.; Chu, L. Q.; Toh, M. L.; Kloc, C.; Tan, P. H.; Eda, G., Evolution of Electronic Structure in Atomically Thin Sheets of WS₂ and WSe₂. *ACS Nano* **2013**, *7* (1), 791-797.
121. Raja, A.; Chaves, A.; Yu, J.; Arefe, G.; Hill, H. M.; Rigosi, A. F.; Berkelbach, T. C.; Nagler, P.; Schuller, C.; Korn, T.; Nuckolls, C.; Hone, J.; Brus, L. E.; Heinz, T. F.; Reichman, D. R.; Chernikov, A., Coulomb engineering of the bandgap and excitons in two-dimensional materials. *Nature Communications* **2017**, *8*.
122. Backes, C., Ten Years of Liquid-phase Exfoliation of Layered Crystals – A Bright Future ahead? *CHIMIA International Journal for Chemistry* **2019**, *73* (6), 498-502.
123. Ebdon, J. R., Introduction to polymers (second edition) R. J. Young and P. A. Lovell Chapman and Hall, London, 1991. pp. 443, price £16.95. ISBN 0-412-30640-9 (PB); ISBN 0-412-30630-1 (HB). *Polymer International* **1992**, *27* (2), 207-208.
124. Brotons-Gisbert, M.; Andres-Penares, D.; Suh, J.; Hidalgo, F.; Abargues, R.; Rodríguez-Cantó, P. J.; Segura, A.; Cros, A.; Tobias, G.; Canadell, E.; Ordejón, P.; Wu, J.; Martínez-Pastor, J. P.; Sánchez-Royo, J. F., Nanotexturing To Enhance Photoluminescent Response of Atomically Thin Indium Selenide with Highly Tunable Band Gap. *Nano Letters* **2016**, *16* (5), 3221-3229.
125. Sánchez-Royo, J. F.; Muñoz-Matutano, G.; Brotons-Gisbert, M.; Martínez-Pastor, J. P.; Segura, A.; Cantarero, A.; Mata, R.; Canet-Ferrer, J.; Tobias, G.; Canadell, E.; Marqués-Hueso, J.; Gerardot, B. D., Electronic structure, optical properties, and lattice dynamics in atomically thin indium selenide flakes. *Nano Research* **2014**, *7* (10), 1556-1568.
126. Song, C.; Fan, F.; Xuan, N.; Huang, S.; Zhang, G.; Wang, C.; Sun, Z.; Wu, H.; Yan, H., Largely Tunable Band Structures of Few-Layer InSe by Uniaxial Strain. *ACS Applied Materials & Interfaces* **2018**, *10* (4), 3994-4000.
127. Hanlon, D.; Backes, C.; Doherty, E.; Cucinotta, C. S.; Berner, N. C.; Boland, C.; Lee, K.; Harvey, A.; Lynch, P.; Gholamvand, Z.; Zhang, S.; Wang, K.; Moynihan, G.; Pokle, A.; Ramasse, Q. M.; McEvoy, N.; Blau, W. J.; Wang, J.; Abellan, G.; Hauke, F.; Hirsch, A.; Sanvito, S.; O'Regan, D. D.; Duesberg, G. S.; Nicolosi, V.; Coleman, J. N., Liquid exfoliation of solvent-stabilized few-layer black phosphorus for applications beyond electronics. *Nature Communications* **2015**, *6* (1), 8563.

Chapter 9 – Literature

128. Ahmed, T.; Balendhran, S.; Karim, M. N.; Mayes, E. L. H.; Field, M. R.; Ramanathan, R.; Singh, M.; Bansal, V.; Sriram, S.; Bhaskaran, M.; Walia, S., Degradation of black phosphorus is contingent on UV–blue light exposure. *npj 2D Materials and Applications* **2017**, *1* (1), 18.
129. van Druenen, M.; Davitt, F.; Collins, T.; Glynn, C.; O'Dwyer, C.; Holmes, J. D.; Collins, G., Evaluating the Surface Chemistry of Black Phosphorus during Ambient Degradation. *Langmuir* **2019**, *35* (6), 2172-2178.
130. Illarionov, Y. Y.; Walzl, M.; Rzepa, G.; Knobloch, T.; Kim, J. S.; Akinwande, D.; Grasser, T., Highly-stable black phosphorus field-effect transistors with low density of oxide traps. *npj 2D Materials and Applications* **2017**, *1* (1), 23.
131. Politano, A.; Chiarello, G.; Samnakay, R.; Liu, G.; Gürbulak, B.; Duman, S.; Balandin, A. A.; Boukhvalov, D. W., The influence of chemical reactivity of surface defects on ambient-stable InSe-based nanodevices. *Nanoscale* **2016**, *8* (16), 8474-8479.
132. Backes, C.; Higgins, T. M.; Kelly, A.; Boland, C.; Harvey, A.; Hanlon, D.; Coleman, J. N., Guidelines for Exfoliation, Characterization and Processing of Layered Materials Produced by Liquid Exfoliation. *Chemistry of Materials* **2017**, *29* (1), 243-255.
133. Grieger, S.; Szydłowska, B. M.; Rao, V.; Steinmann, E.; Dodds, M.; Gholamvand, Z.; Duesberg, G. S.; Zaumseil, J.; Backes, C., Site-selective oxidation of monolayered liquid-exfoliated WS₂ by shielding the basal plane through adsorption of a facial amphiphile. *Angew. Chem. Int. Ed.* **2020**, *59* (33), 13785-13792.
134. Nacken, T. J.; Damm, C.; Walter, J.; Rüger, A.; Peukert, W., Delamination of graphite in a high pressure homogenizer. *RSC Advances* **2015**, *5* (71), 57328-57338.
135. Walter, J.; Nacken, T. J.; Damm, C.; Thajudeen, T.; Eigler, S.; Peukert, W., Determination of the Lateral Dimension of Graphene Oxide Nanosheets Using Analytical Ultracentrifugation. *Small* **2015**, *11* (7), 814-825.
136. Falciola, L.; Mussini, P. R.; Mussini, T.; Rossi, M., A Determination of Standard Potentials and Related Primary pH Standards in the 50 Mass Percent (N-Methyl-2-Pyrrolidinone + Water) Mixture at Various Temperatures. *Journal of Solution Chemistry* **2007**, *36* (8), 1037-1046.
137. Applebey, M. P., CCXI.—The viscosity of salt solutions. *Journal of the Chemical Society, Transactions* **1910**, *97* (0), 2000-2025.
138. William B. Smith, G. D. B., A study of aqueous sodium cholate by 2H nmr *Canadian Journal of Chemistry* **1981**, *59* (2), 5.
139. Ogilvie, S. P.; Large, M. J.; O'Mara, M. A.; Lynch, P. J.; Lee, C. L.; King, A. A. K.; Backes, C.; Dalton, A. B., Size selection of liquid-exfoliated 2D nanosheets. *2D Materials* **2019**, *6* (3), 031002.
140. Académie des sciences, C. n. d. l. r. s., *Comptes rendus hebdomadaires des séances de l'Académie des sciences*. publiés avec le concours du Centre national de la recherche scientifique par MM: Paris, 1894; Vol. 118 (1), p. 260-264.
141. Barj, M.; Sourisseau, C.; Ouvrard, G.; Brec, R., Infrared studies of lithium intercalation in the FePS₃ and NiPS₃ layer-type compounds. *Solid State Ionics* **1983**, *11* (2), 179-183.
142. Lifshitz, E.; Francis, A. H., Magnetic resonance and electronic spectroscopy of M₂P₂S₆ intercalation compounds. In *Chemical Physics of Intercalation*, Legrand, A. P.; Flandrois, S., Eds. Springer US: Boston, MA, 1987; pp 425-431.
143. Lagadic, I.; Lacroix, P. G.; Clément, R., Layered MPS₃ (M = Mn, Cd) Thin Films as Host Matrixes for Nonlinear Optical Material Processing. *Chemistry of Materials* **1997**, *9* (9), 2004-2012.

144. Gusmão, R.; Sofer, Z.; Pumera, M., Metal Phosphorous Trichalcogenides (MPCh₃): From Synthesis to Contemporary Energy Challenges. *Angewandte Chemie International Edition* **2019**, *58* (28), 9326-9337.
145. Harvey, A.; Backes, C.; Gholamvand, Z.; Hanlon, D.; McAteer, D.; Nerl, H. C.; McGuire, E.; Seral-Ascaso, A.; Ramasse, Q. M.; McEvoy, N.; Winters, S.; Berner, N. C.; McCloskey, D.; Donegan, J. F.; Duesberg, G. S.; Nicolosi, V.; Coleman, J. N., Preparation of Gallium Sulfide Nanosheets by Liquid Exfoliation and Their Application As Hydrogen Evolution Catalysts. *Chemistry of Materials* **2015**, *27* (9), 3483-3493.
146. Liu, X.; Zeng, J.; Yang, H.; Zhou, K.; Pan, D., V₂O₅-Based nanomaterials: synthesis and their applications. *RSC Advances* **2018**, *8* (8), 4014-4031.
147. Li, X.; Fang, Y.; Wang, J.; Wei, B.; Qi, K.; Hoh, H. Y.; Hao, Q.; Sun, T.; Wang, Z.; Yin, Z.; Zhang, Y.; Lu, J.; Bao, Q.; Su, C., High-Yield Electrochemical Production of Large-Sized and Thinly Layered NiPS₃ Flakes for Overall Water Splitting. *Small* **2019**, *15* (30), 1902427.
148. Barua, M.; Ayyub, M. M.; Vishnoi, P.; Pramoda, K.; Rao, C. N. R., Photochemical HER activity of layered metal phospho-sulfides and -selenides. *Journal of Materials Chemistry A* **2019**, *7* (39), 22500-22506.
149. Pethica, B. A.; Senak, L.; Zhu, Z.; Lou, A., Surface and colloidal properties of cyclic amides. 5. N-cyclohexyl-2-pyrrolidone–water mixtures aggregation in solution and adsorption at the air–solution interface. *Colloids and Surfaces A: Physicochemical and Engineering Aspects* **2001**, *186* (1), 113-122.
150. Klepp, K. O.; Ipser, H., On the phase CrTe₃. *Monatshefte für Chemie / Chemical Monthly* **1979**, *110* (2), 499-501.
151. Debbichi, M.; Debbichi, L.; Lebègue, S., Tuning the magnetic and electronic properties of monolayer chromium tritelluride through strain engineering. *Physics Letters A* **2020**, *384* (27), 126684.
152. Payamyar, P.; King, B. T.; Öttinger, H. C.; Schlüter, A. D., Two-dimensional polymers: concepts and perspectives. *Chemical Communications* **2016**, *52* (1), 18-34.
153. Wang, W.; Schlüter, A. A.-O., Synthetic 2D Polymers: A Critical Perspective and a Look into the Future. *Macromol. Rapid Commun* **2019**, *40* (1).
154. Kory, M. J.; Wörle, M.; Weber, T.; Payamyar, P.; van de Poll, S. W.; Dshemuchadse, J.; Trapp, N.; Schlüter, A. D., Gram-scale synthesis of two-dimensional polymer crystals and their structure analysis by X-ray diffraction. *Nature Chemistry* **2014**, *6* (9), 779-784.
155. Lange, R. Z.; Hofer, G.; Weber, T.; Schlüter, A. D., A Two-Dimensional Polymer Synthesized through Topochemical [2 + 2]-Cycloaddition on the Multigram Scale. *Journal of the American Chemical Society* **2017**, *139* (5), 2053-2059.
156. Bauer, S.; Stock, N., Hochdurchsatz-Methoden in der Festkörperchemie. Schneller zum Ziel. *Chemie in unserer Zeit* **2007**, *41* (5), 390-398.
157. Rowsell, J. L. C.; Yaghi, O. M., Metal–organic frameworks: a new class of porous materials. *Microporous and Mesoporous Materials* **2004**, *73* (1), 3-14.
158. Hou, Q.; Zhou, S.; Wei, Y.; Caro, J.; Wang, H., Balancing the Grain Boundary Structure and the Framework Flexibility through Bimetallic MOF Membranes for Gas Separation. *Journal of the American Chemical Society* **2020**, XXXX.
159. Waitschat, S.; Reinsch, H.; Arpacioğlu, M.; Stock, N., Direct water-based synthesis and characterization of new Zr/Hf-MOFs with dodecanuclear clusters as IBUs. *CrystEngComm* **2018**, *20* (35), 5108-5111.

Chapter 9 – Literature

160. Rönfeldt, P.; Reinsch, H.; Faßheber, N.; Terraschke, H.; Stock, N., Synthesis and Characterization of a Layered Scandium MOF Containing a Sulfone-Functionalized V-Shaped Linker Molecule. *European Journal of Inorganic Chemistry* **2020**, 2020 (13), 1147-1152.
161. Rabe, T.; Pewe, H.; Reinsch, H.; Willhammar, T.; Svensson Grape, E.; Stock, N., Influence of the substitution pattern of four naphthalenedicarboxylic acids on the structures and properties of group 13 metal–organic frameworks and coordination polymers. *Dalton Transactions* **2020**, 49 (15), 4861-4868.
162. Rönfeldt, P.; Ruser, N.; Reinsch, H.; Grape, E. S.; Ken Inge, A.; Suta, M.; Terraschke, H.; Stock, N., New Scandium-containing Coordination Polymers with Linear Linker Molecules: Crystal Structures and Luminescence Properties. *European Journal of Inorganic Chemistry* **2020**, 2020 (28), 2737-2743.
163. Wang, G.; Chernikov, A.; Glazov, M. M.; Heinz, T. F.; Marie, X.; Amand, T.; Urbaszek, B., Colloquium: Excitons in atomically thin transition metal dichalcogenides. *Rev. Mod. Phys.* **2018**, 90 (2).
164. O'Connell, M. J.; Bachilo, S. M.; Huffman, C. B.; Moore, V. C.; Strano, M. S.; Haroz, E. H.; Rialon, K. L.; Boul, P. J.; Noon, W. H.; Kittrell, C.; Ma, J. P.; Hauge, R. H.; Weisman, R. B.; Smalley, R. E., Band gap fluorescence from individual single-walled carbon nanotubes. *Science* **2002**, 297 (5581), 593-596.
165. Mak, K. F.; He, K. L.; Lee, C.; Lee, G. H.; Hone, J.; Heinz, T. F.; Shan, J., Tightly bound trions in monolayer MoS₂. *Nat. Mater.* **2013**, 12 (3), 207-211.
166. Li, Y. L.; Chernikov, A.; Zhang, X.; Rigosi, A.; Hill, H. M.; van der Zande, A. M.; Chenet, D. A.; Shih, E. M.; Hone, J.; Heinz, T. F., Measurement of the optical dielectric function of monolayer transition-metal dichalcogenides: MoS₂, MoSe₂, WS₂, and WSe₂. *Phys. Rev. B* **2014**, 90 (20).
167. Selig, M.; Berghauer, G.; Raja, A.; Nagler, P.; Schuller, C.; Heinz, T. F.; Korn, T.; Chernikov, A.; Malic, E.; Knorr, A., Excitonic linewidth and coherence lifetime in monolayer transition metal dichalcogenides. *Nature Commun.* **2016**, 7.
168. Kormanyos, A.; Burkard, G.; Gmitra, M.; Fabian, J.; Zolyomi, V.; Drummond, N. D.; Fal'ko, V., k.p theory for two-dimensional transition metal dichalcogenide semiconductors. *2D Mater.* **2015**, 2 (2).
169. Jin, Z. H.; Li, X. D.; Mullen, J. T.; Kim, K. W., Intrinsic transport properties of electrons and holes in monolayer transition-metal dichalcogenides. *Phys. Rev. B* **2014**, 90 (4).
170. Beal, A. R.; Hughes, H. P., Kramers-Kronig analysis of the reflectivity spectra of 2H-MoS₂, 2H-MoSe₂ and 2H-MoTe₂. *Journal of Physics C: Solid State Physics* **1979**, 12 (5), 881-890.
171. Beal, A. R.; Liang, W. Y.; Hughes, H. P., Kramers-Kronig analysis of the reflectivity spectra of 3R-WS₂ and 2H-WSe₂. *Journal of Physics C: Solid State Physics* **1976**, 9 (12), 2449-2457.
172. Evans, B. L.; Young, P. A., Exciton spectra in thin crystals: the diamagnetic effect. *Proceedings of the Physical Society* **1967**, 91 (2), 475-482.
173. Beal, A. R.; Liang, W. Y., EXCITONS IN 2H-WSE₂ AND 3R-WS₂. *J. Phys. C* **1976**, 9 (12), 2459-2466.
174. Ugeda, M. M.; Bradley, A. J.; Shi, S. F.; da Jornada, F. H.; Zhang, Y.; Qiu, D. Y.; Ruan, W.; Mo, S. K.; Hussain, Z.; Shen, Z. X.; Wang, F.; Louie, S. G.; Crommie, M. F., Giant bandgap renormalization and excitonic effects in a monolayer transition metal dichalcogenide semiconductor. *Nat. Mater.* **2014**, 13 (12), 1091-1095.

175. Chernikov, A.; Berkelbach, T. C.; Hill, H. M.; Rigosi, A.; Li, Y. L.; Aslan, O. B.; Reichman, D. R.; Hybertsen, M. S.; Heinz, T. F., Exciton Binding Energy and Nonhydrogenic Rydberg Series in Monolayer WS₂. *Phys. Rev. Lett.* **2014**, *113* (7).
176. Berkelbach, T. C.; Reichman, D. R., Optical and Excitonic Properties of Atomically Thin Transition-Metal Dichalcogenides. In *Annual Review of Condensed Matter Physics, Vol 9*, Sachdev, S.; Marchetti, M. C., Eds. 2018; Vol. 9, pp 379-396.
177. Stier, A. V.; Wilson, N. P.; Clark, G.; Xu, X. D.; Crooker, S. A., Probing the Influence of Dielectric Environment on Excitons in Monolayer WSe₂: Insight from High Magnetic Fields. *Nano Lett.* **2016**, *16* (11), 7054-7060.
178. Klingshirn, C. F., *Semiconductor Optics*. Springer-Verlag Berlin Heidelberg: 2007.
179. Splendiani, A.; Sun, L.; Zhang, Y. B.; Li, T. S.; Kim, J.; Chim, C. Y.; Galli, G.; Wang, F., Emerging Photoluminescence in Monolayer MoS₂. *Nano Lett.* **2010**, *10* (4), 1271-1275.
180. Song, C.; Huang, S.; Wang, C.; Luo, J.; Yan, H., The optical properties of few-layer InSe. *Journal of Applied Physics* **2020**, *128* (6), 060901.
181. Camassel, J.; Merle, P.; Mathieu, H.; Chevy, A., Excitonic absorption edge of indium selenide. *Physical Review B* **1978**, *17* (12), 4718-4725.
182. Giordani, S.; Bergin, S. D.; Nicolosi, V.; Lebedkin, S.; Kappes, M. M.; Blau, W. J.; Coleman, J. N., Debundling of Single-Walled Nanotubes by Dilution: Observation of Large Populations of Individual Nanotubes in Amide Solvent Dispersions. *The Journal of Physical Chemistry B* **2006**, *110* (32), 15708-15718.
183. Szydłowska, B. M.; Graf, A.; Kelly, A.; Blau, W. J.; Gather, M. C.; Zaumseil, J.; Backes, C., Preparation of WS₂-PMMA composite films for optical applications. *Journal of Materials Chemistry C* **2020**, *8*, 10805-10815.
184. Ogilvie, S. P.; Large, M. J.; Fratta, G.; Meloni, M.; Canton-Vitoria, R.; Tagmatarchis, N.; Massuyeau, F.; Ewels, C. P.; King, A. A. K.; Dalton, A. B., Considerations for spectroscopy of liquid-exfoliated 2D materials: emerging photoluminescence of N-methyl-2-pyrrolidone. *Scientific Reports* **2017**, *7* (1), 16706.
185. Bandurin, D. A.; Tyurnina, A. V.; Yu, G. L.; Mishchenko, A. A.-O.; Zólyomi, V.; Morozov, S. V.; Kumar, R. K.; Gorbachev, R. V.; Kudrynskyi, Z. R.; Pezzini, S.; Kovalyuk, Z. D.; Zeitler, U.; Novoselov, K. S.; Patanè, A.; Eaves, L.; Grigorieva, I. A.-O.; Fal'ko, V. I.; Geim, A. K.; Cao, Y., High electron mobility, quantum Hall effect and anomalous optical response in atomically thin InSe. (1748-3395 (Electronic)).
186. Dangol, R.; Dai, Z.; Chaturvedi, A.; Zheng, Y.; Zhang, Y.; Dinh, K. N.; Li, B.; Zong, Y.; Yan, Q., Few-layer NiPS₃ nanosheets as bifunctional materials for Li-ion storage and oxygen evolution reaction. *Nanoscale* **2018**, *10* (10), 4890-4896.
187. Light scattering by small particles. By H. C. van de Hulst. New York (John Wiley and Sons), London (Chapman and Hall), 1957. Pp. xiii, 470; 103 Figs.; 46 Tables. 96s. *Quarterly Journal of the Royal Meteorological Society* **1958**, *84* (360), 198-199.
188. Mandeep, S.; Enrico Della, G.; Taimur, A.; Sumeet, W.; Rajesh, R.; Joel van, E.; Edwin, M.; Vipul, B., Soft exfoliation of 2D SnO with size-dependent optical properties. *2D Materials* **2017**, *4* (2), 025110.
189. Kunnil, J.; Sarasanandarajah, S.; Chacko, E.; Reinisch, L., Fluorescence quantum efficiency of dry *Bacillus globigii* spores. *Optics express* **2005**, *13*, 8969-79.
190. Kasha, M., Characterization of electronic transitions in complex molecules. *Discussions of the Faraday Society* **1950**, *9* (0), 14-19.

Chapter 9 – Literature

191. He, G. S.; Qin, H.-Y.; Zheng, Q., Rayleigh, Mie, and Tyndall scatterings of polystyrene microspheres in water: Wavelength, size, and angle dependences. *J. Appl. Phys.* **2009**, *105* (2), 023110.
192. Szydłowska, B. M.; Hartwig, O.; Tywoniuk, B.; Hartman, T.; Stimpel-Lindner, T.; Sofer, Z.; McEvoy, N.; Duesberg, G. S.; Backes, C., Spectroscopic thickness and quality metrics for PtSe₂ layers produced by top-down and bottom-up techniques. *2D Materials* **2020**, *7* (4), 045027.
193. Vega-Mayoral, V.; Tian, R.; Kelly, A. G.; Griffin, A.; Harvey, A.; Borrelli, M.; Nisi, K.; Backes, C.; Coleman, J. N., Solvent exfoliation stabilizes TiS₂ nanosheets against oxidation, facilitating lithium storage applications. *Nanoscale* **2019**, *11* (13), 6206-6216.
194. Hess, L. H.; Jansen, M.; Maybeck, V.; Hauf, M. V.; Seifert, M.; Stutzmann, M.; Sharp, I. D.; Offenhäusser, A.; Garrido, J. A., Graphene Transistor Arrays for Recording Action Potentials from Electrogenic Cells. *Advanced Materials* **2011**, *23* (43), 5045-5049.
195. Finn, D. J.; Lotya, M.; Cunningham, G.; Smith, R. J.; McCloskey, D.; Donegan, J. F.; Coleman, J. N., Inkjet deposition of liquid-exfoliated graphene and MoS₂ nanosheets for printed device applications. *Journal of Materials Chemistry C* **2014**, *2* (5), 925-932.
196. Mahler, B.; Hoepfner, V.; Liao, K.; Ozin, G. A., Colloidal Synthesis of 1T-WS₂ and 2H-WS₂ Nanosheets: Applications for Photocatalytic Hydrogen Evolution. *Journal of the American Chemical Society* **2014**, *136* (40), 14121-14127.
197. Han, Y.; Wang, J.; Wan, H.; Wang, S.; Hu, H.; Xiao, T.-H.; Cheng, Z.; Liu, T., Solution processable transition metal dichalcogenides-based hybrids for photodetection. *Nano Materials Science* **2019**, *1* (4), 288-298.
198. Li, Y.; Zhang, J.; Huang, D.; Sun, H.; Fan, F.; Feng, J.; Wang, Z.; Ning, C. Z., Room-temperature continuous-wave lasing from monolayer molybdenum ditelluride integrated with a silicon nanobeam cavity. *Nature Nanotechnology* **2017**, *12* (10), 987-992.
199. Kang, N.; Paudel, H. P.; Leuenberger, M. N.; Tetard, L.; Khondaker, S. I., Photoluminescence Quenching in Single-Layer MoS₂ via Oxygen Plasma Treatment. *The Journal of Physical Chemistry C* **2014**, *118* (36), 21258-21263.
200. Canton-Vitoria, R.; Sayed-Ahmad-Baraza, Y.; Pelaez-Fernandez, M.; Arenal, R.; Bittencourt, C.; Ewels, C. P.; Tagmatarchis, N., Functionalization of MoS₂ with 1,2-dithiolanes: toward donor-acceptor nanohybrids for energy conversion. *npj 2D Materials and Applications* **2017**, *1* (1), 13.
201. Chen, X.; McDonald, A. R., Functionalization of Two-Dimensional Transition-Metal Dichalcogenides. *Advanced Materials* **2016**, *28* (27), 5738-5746.
202. Fabbri, F.; Dinelli, F.; Forti, S.; Sementa, L.; Pace, S.; Piccinini, G.; Fortunelli, A.; Coletti, C.; Pingue, P., Edge Defects Promoted Oxidation of Monolayer WS₂ Synthesized on Epitaxial Graphene. *The Journal of Physical Chemistry C* **2020**, *124* (16), 9035-9044.
203. Lin, Z.; Carvalho, B. R.; Kahn, E.; Lv, R.; Rao, R.; Terrones, H.; Pimenta, M. A.; Terrones, M., Defect engineering of two-dimensional transition metal dichalcogenides. *2D Materials* **2016**, *3* (2), 022002.
204. Martincová, J.; Otyepka, M.; Lazar, P., Is Single Layer MoS₂ Stable in the Air? *Chemistry – A European Journal* **2017**, *23* (53), 13233-13239.
205. Chen, J.; Walker, W. R.; Xu, L.; Krysiak, O.; She, Z.; Pope, M. A., Intrinsic Capacitance of Molybdenum Disulfide. *ACS Nano* **2020**, *14* (5), 5636-5648.
206. Knirsch, K. C.; Berner, N. C.; Nerl, H. C.; Cucinotta, C. S.; Gholamvand, Z.; McEvoy, N.; Wang, Z.; Abramovic, I.; Vecera, P.; Halik, M.; Sanvito, S.; Duesberg, G. S.; Nicolosi, V.; Hauke,

- F.; Hirsch, A.; Coleman, J. N.; Backes, C., Basal-Plane Functionalization of Chemically Exfoliated Molybdenum Disulfide by Diazonium Salts. *ACS Nano* **2015**, *9* (6), 6018-6030.
207. Zhou, W.; Zou, X.; Najmaei, S.; Liu, Z.; Shi, Y.; Kong, J.; Lou, J.; Ajayan, P. M.; Yakobson, B. I.; Idrobo, J.-C., Intrinsic Structural Defects in Monolayer Molybdenum Disulfide. *Nano Letters* **2013**, *13* (6), 2615-2622.
208. Arrhenius, S., Über die Reaktionsgeschwindigkeit bei der Inversion von Rohrzucker durch Säuren. *Zeitschrift für Physikalische Chemie* **1889**, *4U* (1), 226-248.
209. Boland, J. B.; Harvey, A.; Tian, R.; Hanlon, D.; Vega-Mayoral, V.; Szydłowska, B. M.; Griffin, A.; Stimpel-Lindner, T.; Metel, S.; Nicolosi, V.; Duesberg, G.; Coleman, J. N., Liquid phase exfoliation of MoO₂ nanosheets for lithium ion battery applications. *Nanoscale Advances* **2019**.
210. Zhang, C. J.; Pinilla, S.; McEvoy, N.; Cullen, C. P.; Anasori, B.; Long, E.; Park, S.-H.; Seral-Ascaso, A.; Shmeliov, A.; Krishnan, D.; Morant, C.; Liu, X.; Duesberg, G. S.; Gogotsi, Y.; Nicolosi, V., Oxidation Stability of Colloidal Two-Dimensional Titanium Carbides (MXenes). *Chem. Mater.* **2017**, *29* (11), 4848-4856.
211. Castellanos-Gomez, A.; Vicarelli, L.; Prada, E.; Island, J. O.; Narasimha-Acharya, K. L.; Blanter, S. I.; Groenendijk, D. J.; Buscema, M.; Steele, G. A.; Alvarez, J. V.; Zandbergen, H. W.; Palacios, J. J.; Zant, H. S. J. v. d., Isolation and characterization of few-layer black phosphorus. *2D Materials* **2014**, *1* (2), 025001.
212. Favron, A.; Gaufres, E.; Fossard, F.; Phaneuf-Lheureux, A.-L.; Tang, N. Y. W.; Levesque, P. L.; Loiseau, A.; Leonelli, R.; Francoeur, S.; Martel, R., Photooxidation and quantum confinement effects in exfoliated black phosphorus. *Nat. Mater.* **2015**, *14*, 826-832.
213. Kuo, C.-T.; Neumann, M.; Balamurugan, K.; Park, H. J.; Kang, S.; Shiu, H. W.; Kang, J. H.; Hong, B. H.; Han, M.; Noh, T. W.; Park, J.-G., Exfoliation and Raman Spectroscopic Fingerprint of Few-Layer NiPS₃ Van der Waals Crystals. *Sci. Rep.* **2016**, *6*, 20904.
214. El-Kemary, M.; Nagy, N.; El-Mehasseb, I., Nickel oxide nanoparticles: Synthesis and spectral studies of interactions with glucose. *Mater. Sci. Semicond. Process.* **2013**, *16* (6), 1747-1752.
215. Newman, R.; Chrenko, R. M., Optical Properties of Nickel Oxide. *Physical Review* **1959**, *114* (6), 1507-1513.
216. Withnall, R.; McCluskey, M.; Andrews, L., Absorption spectra of the phosphorus oxide (PO₂ and PO₃) radicals in solid argon. *The Journal of Physical Chemistry* **1989**, *93* (1), 126-129.
217. Modic, K. A.; McDonald, R. D.; Ruff, J. P. C.; Bachmann, M. D.; Lai, Y.; Palmstrom, J. C.; Graf, D.; Chan, M. K.; Balakirev, F. F.; Betts, J. B.; Boebinger, G. S.; Schmidt, M.; Lawler, M. J.; Sokolov, D. A.; Moll, P. J. W.; Ramshaw, B. J.; Shekhter, A., Scale-invariant magnetic anisotropy in RuCl₃ at high magnetic fields. *Nature Physics* **2020**.
218. Wulferding, D.; Choi, Y.; Do, S.-H.; Lee, C. H.; Lemmens, P.; Faugeras, C.; Gallais, Y.; Choi, K.-Y., Magnon bound states versus anyonic Majorana excitations in the Kitaev honeycomb magnet α -RuCl₃. *Nature Communications* **2020**, *11* (1), 1603.
219. Takeda, T.; Nagata, M.; Kobayashi, H.; Kanno, R.; Kawamoto, Y.; Takano, M.; Kamiyama, T.; Izumi, F.; Sleight, A. W., High-Pressure Synthesis, Crystal Structure, and Metal–Semiconductor Transitions in the Ti₂Ru₂O₇– δ Pyrochlore. *Journal of Solid State Chemistry* **1998**, *140* (2), 182-193.
220. Kraus, W.; Nolze, G., POWDER CELL– a program for the representation and manipulation of crystal structures and calculation of the resulting X-ray powder patterns. *Journal of Applied Crystallography* **1996**, *29* (3), 301-303.

Chapter 9 – Literature

221. Assebban, M.; Gibaja, C.; Fickert, M.; Torres, I.; Weinreich, E.; Wolff, S.; Gillen, R.; Maultzsch, J.; Varela, M.; Tan Jun Rong, S.; Loh, K. P.; Michel, E. G.; Zamora, F.; Abellán, G., Unveiling the oxidation behavior of liquid-phase exfoliated antimony nanosheets. *2D Materials* **2020**, *7* (2), 025039.
222. Sasaki, T.; Watanabe, M., Osmotic Swelling to Exfoliation. Exceptionally High Degrees of Hydration of a Layered Titanate. *Journal of the American Chemical Society* **1998**, *120* (19), 4682-4689.
223. Maluangnont, T.; Matsuba, K.; Geng, F.; Ma, R.; Yamauchi, Y.; Sasaki, T., Osmotic Swelling of Layered Compounds as a Route to Producing High-Quality Two-Dimensional Materials. A Comparative Study of Tetramethylammonium versus Tetrabutylammonium Cation in a Lepidocrocite-type Titanate. *Chemistry of Materials* **2013**, *25* (15), 3137-3146.
224. Bottari, G.; Herranz, M. Á.; Wibmer, L.; Volland, M.; Rodríguez-Pérez, L.; Guldi, D. M.; Hirsch, A.; Martín, N.; D'Souza, F.; Torres, T., Chemical functionalization and characterization of graphene-based materials. *Chemical Society Reviews* **2017**, *46* (15), 4464-4500.
225. Englert, J. M.; Röhr, J.; Schmidt, C. D.; Graupner, R.; Hundhausen, M.; Hauke, F.; Hirsch, A., Soluble Graphene: Generation of Aqueous Graphene Solutions Aided by a Perylenebisimide-Based Bolaamphiphile. *Advanced Materials* **2009**, *21* (42), 4265-4269.
226. Li, Y.; Lu, Y.; Adelhelm, P.; Titirici, M.-M.; Hu, Y.-S., Intercalation chemistry of graphite: alkali metal ions and beyond. *Chemical Society Reviews* **2019**, *48* (17), 4655-4687.
227. Benavente, E.; Santa Ana, M. A.; Mendizábal, F.; González, G., Intercalation chemistry of molybdenum disulfide. *Coordination Chemistry Reviews* **2002**, *224* (1–2), 87-109.
228. Yu, P.; Lowe, S. E.; Simon, G. P.; Zhong, Y. L., Electrochemical exfoliation of graphite and production of functional graphene. *Current Opinion in Colloid & Interface Science* **2015**, *20* (5), 329-338.
229. Kaur, H.; Tian, R.; Roy, A.; McCrystall, M.; Horvath, D. A.-O.; Lozano Onrubia, G.; Smith, R.; Ruether, M.; Griffin, A.; Backes, C. A.-O.; Nicolosi, V. A.-O.; Coleman, J. A.-O., Production of Quasi-2D Platelets of Nonlayered Iron Pyrite (FeS₂) by Liquid-Phase Exfoliation for High Performance Battery Electrodes. (1936-086X (Electronic)).
230. Kelly, A. G.; Hallam, T.; Backes, C.; Harvey, A.; Esmaeily, A. S.; Godwin, I.; Coelho, J.; Nicolosi, V.; Lauth, J.; Kulkarni, A.; Kinge, S.; Siebbeles, L. D. A.; Duesberg, G. S.; Coleman, J. N., All-printed thin-film transistors from networks of liquid-exfoliated nanosheets. *Science* **2017**, *356* (6333), 69.
231. He, J.; Wang, C.; Zhou, B.; Zhao, Y.; Tao, L.; Zhang, H., 2D van der Waals heterostructures: processing, optical properties and applications in ultrafast photonics. *Materials Horizons* **2020**, *7* (11), 2903-2921.
232. Ueberricke, L.; Coleman, J. N.; Backes, C., Robustness of Size Selection and Spectroscopic Size, Thickness and Monolayer Metrics of Liquid-Exfoliated WS₂. *physica status solidi (b)* **2017**, *254* (11), 1700443.
233. Filik, J.; Ashton, A. W.; Chang, P. C. Y.; Chater, P. A.; Day, S. J.; Drakopoulos, M.; Gerring, M. W.; Hart, M. L.; Magdysyuk, O. V.; Michalik, S.; Smith, A.; Tang, C. C.; Terrill, N. J.; Wharmby, M. T.; Wilhelm, H., Processing two-dimensional X-ray diffraction and small-angle scattering data in DAWN 2. *J. Appl. Crystallogr.* **2017**, *50* (3), 959-966.
234. Andersen, K.; Latini, S.; Thygesen, K. S., Dielectric Genome of van der Waals Heterostructures. *Nano Lett.* **2015**, *15* (7), 4616-4621.

235. Mortensen, J. J.; Hansen, L. B.; Jacobsen, K. W., Real-space grid implementation of the projector augmented wave method. *Phys. Rev. B* **2005**, *71* (3), 035109.
236. Winther, K. T.; Thygesen, K. S., Band structure engineering in van der Waals heterostructures via dielectric screening: the $G\uparrow\Delta$. **2017**, *4* (2), 025059.
237. Giannozzi, P.; Baroni S Fau - Bonini, N.; Bonini N Fau - Calandra, M.; Calandra M Fau - Car, R.; Car R Fau - Cavazzoni, C.; Cavazzoni C Fau - Ceresoli, D.; Ceresoli D Fau - Chiarotti, G. L.; Chiarotti G Fau - Cococcioni, M.; Cococcioni M Fau - Dabo, I.; Dabo I Fau - Dal Corso, A.; Dal Corso A Fau - de Gironcoli, S.; de Gironcoli S Fau - Fabris, S.; Fabris S Fau - Fratesi, G.; Fratesi G Fau - Gebauer, R.; Gebauer R Fau - Gerstmann, U.; Gerstmann U Fau - Gougoussis, C.; Gougoussis C Fau - Kokalj, A.; Kokalj A Fau - Lazzeri, M.; Lazzeri M Fau - Martin-Samos, L.; Martin-Samos L Fau - Marzari, N.; Marzari N Fau - Mauri, F.; Mauri F Fau - Mazzarello, R.; Mazzarello R Fau - Paolini, S.; Paolini S Fau - Pasquarello, A.; Pasquarello A Fau - Paulatto, L.; Paulatto L Fau - Sbraccia, C.; Sbraccia C Fau - Scandolo, S.; Scandolo S Fau - Sclauzero, G.; Sclauzero G Fau - Seitsonen, A. P.; Seitsonen Ap Fau - Smogunov, A.; Smogunov A Fau - Umari, P.; Umari P Fau - Wentzcovitch, R. M.; Wentzcovitch, R. M., QUANTUM ESPRESSO: a modular and open-source software project for quantum simulations of materials. (1361-648X (Electronic)).
238. Ridings, C.; Warr, G. G.; Andersson, G. G., Composition of the outermost layer and concentration depth profiles of ammonium nitrate ionic liquid surfaces. *Physical Chemistry Chemical Physics* **2012**, *14* (46), 16088-16095.
239. Nemes-Incze, P.; Osváth, Z.; Kamarás, K.; Biró, L. P., Anomalies in thickness measurements of graphene and few layer graphite crystals by tapping mode atomic force microscopy. *Carbon* **2008**, *46* (11), 1435-1442.
240. Zhang, P.; Zhao, F.; Long, P.; Wang, Y.; Yue, Y.; Liu, X.; Feng, Y.; Li, R.; Hu, W.; Li, Y.; Feng, W., Sonication-assisted liquid-phase exfoliated α -GeTe: a two-dimensional material with high Fe³⁺ sensitivity. *Nanoscale* **2018**, *10* (34), 15989-15997.
241. Stadelmann, P. A., EMS - a software package for electron diffraction analysis and HREM image simulation in materials science. *Ultramicroscopy* **1987**, *21* (2), 131-145.

Chapter 9 – Literature



**Eidesstattliche Versicherung gemäß § 8 der Promotionsordnung für die
Naturwissenschaftlich-Mathematische Gesamtfakultät der Universität Heidelberg /
Sworn Affidavit according to § 8 of the doctoral degree regulations of the Combined Faculty of Natural
Sciences and Mathematics**

1. Bei der eingereichten Dissertation zu dem Thema / **The thesis I have submitted entitled**
Liquid phase exfoliation and size-dependent properties of van der Waals crystals
handelt es sich um meine eigenständig erbrachte Leistung / **is my own work.**
2. Ich habe nur die angegebenen Quellen und Hilfsmittel benutzt und mich keiner unzulässigen Hilfe Dritter
bedient. Insbesondere habe ich wörtlich oder sinngemäß aus anderen Werken übernommene Inhalte als
solche kenntlich gemacht. / **I have only used the sources indicated and have not made unauthorised use of
services of a third party. Where the work of others has been quoted or reproduced, the source is always
given.**
3. Die Arbeit oder Teile davon habe ich wie folgt/bislang nicht¹⁾ an einer Hochschule des In- oder Auslands
als Bestandteil einer Prüfungs- oder Qualifikationsleistung vorgelegt. / **I have not yet/have already¹⁾
presented this thesis or parts thereof to a university as part of an examination or degree.**

Titel der Arbeit / **Title of the thesis:** Liquid phase exfoliation and size-dependent properties of van
der Waals crystals

Hochschule und Jahr / **University and year:** Heidelberg University, 2021

Art der Prüfungs- oder Qualifikationsleistung / **Type of examination or degree:** Dissertation

4. Die Richtigkeit der vorstehenden Erklärungen bestätige ich. / **I confirm that the declarations made above
are correct.**
5. Die Bedeutung der eidesstattlichen Versicherung und die strafrechtlichen Folgen einer unrichtigen oder
unvollständigen eidesstattlichen Versicherung sind mir bekannt. / **I am aware of the importance of a sworn
affidavit and the criminal prosecution in case of a false or incomplete affidavit.**

Ich versichere an Eides statt, dass ich nach bestem Wissen die reine Wahrheit erklärt und nichts verschwie-
gen habe. / **I affirm that the above is the absolute truth to the best of my knowledge and that I have not
concealed anything.**

Ort und Datum / **Place and date**

Unterschrift / **Signature**

¹⁾ Nicht Zutreffendes streichen. Bei Bejahung sind anzugeben: der Titel der andernorts vorgelegten Arbeit, die Hoch-
schule, das Jahr der Vorlage und die Art der Prüfungs- oder Qualifikationsleistung. / **Please cross out what is not appli-
cable. If applicable, please provide: the title of the thesis that was presented elsewhere, the name of the university, the
year of presentation and the type of examination or degree.**